Department of Applied Physics
School Of Applied Science

Surface-Atmosphere Interactions in the Thermal Infrared $(8 - 14\mu m)$

Brendon Kynnie McAtee

September 2003

Declaration

This thesis contains no material which has been accepted for the award of any other degree or diploma in any university.

To the best of my knowledge and belief this thesis contains no material previously published by any other person except where due acknowledgment has been made.

Signature:

Date: 7/10/03

Abstract

Remote sensing of land surface temperature (LST) is a complex task. From a satellite-based perspective the radiative properties of the land surface and the atmosphere are inextricably linked. Knowledge of both is required if one is to accurately measure the temperature of the land surface from a space-borne platform. In practice, most satellite-based sensors designed to measure LST over the surface of the Earth are polar orbiting. They scan swaths of the order of 2000 km, utilizing zenith angles of observation of up to 60°. As such, satellite viewing geometry is important when comparing estimates of LST between different overpasses of the same point on the Earth's surface.

In the case of the atmosphere, the optical path length through which the surface-leaving radiance propagates increases with increasing zenith angle of observation. A longer optical path may in turn alter the relative contributions which molecular absorption and emission processes make to the radiance measured at the satellite sensor. A means of estimating the magnitudes of these radiative components in relation to the viewing geometry of the satellite needs to be developed if their impacts on the at-sensor radiance are to be accurately accounted for.

The problem of accurately describing radiative transfer between the surface and the satellite sensor is further complicated by the fact that the surface-leaving radiance itself may also vary with sensor viewing geometry. Physical properties of the surface such as emissivity are known to vary as the zenith angle of observation changes. The proportions of sunlit and shaded areas with the field-of-view of the sensor may also change with viewing geometry depending on the type of cover (eg vegetation), further impacting the surface emissivity. Investigation of the change in surface-leaving radiance as the zenith angle of observation varies is then also important in developing a better understanding of the radiative interaction between the land surface and the atmosphere.

The work in this study investigates the atmospheric impacts using surface brightness temperature measurements from the ATSR-2 satellite sensor in combination

with atmospheric profile data from radiosondes and estimates of the downwelling sky radiance made by a ground-based radiometer. A line-by-line radiative transfer model is used to model the angular impacts of the atmosphere upon the surface-leaving radiance. Results from the modelling work show that if the magnitude of the upwelling and downwelling sky radiance and atmospheric transmittance are accurately known then the surface-emitted radiance and hence the LST may be retrieved with negligible error. Guided by the outcomes of the modelling work an atmospheric correction term is derived which accounts for absorption and emission by the atmosphere, and is based on the viewing geometry of the satellite sensor and atmospheric properties characteristic of a semi-arid field site near Alice Springs in the Northern Territory (Central Australia).

Ground-based angular measurements of surface brightness temperature made by a scanning, self calibrating radiometer situated at this field site are then used to investigate how the surface-leaving radiance varies over a range of zenith angles comparable to that of the ATSR-2 satellite sensor. Well defined cycles in the angular dependence of surface brightness temperature were observed on both diurnal and seasonal timescales in these data. The observed cycles in surface brightness temperature are explained in terms of the interaction between the downwelling sky radiance and the angular dependence of the surface emissivity. The angular surface brightness temperature and surface emissivity information is then applied to derive an LST estimate of high accuracy ($\approx$ 1 K at night and 1–2 K during the day), suitable for the validation of satellite-derived LST measurements.

Finally, the atmospheric and land surface components of this work are combined to describe surface-atmosphere interaction at the field site. Algorithms are derived for the satellite retrieval of LST for the nadir and forward viewing geometries of the ATSR-2 sensor, based upon the cycles in the angular dependence of surface brightness temperature observed *in situ* and the atmospheric correction term developed from the modelling of radiative transfer in the atmosphere. A qualitative assessment of the performance of these algorithms indicates they may obtain com-

parable accuracy to existing dual angle algorithms ($\approx$ 1.5 K) in the ideal case and an accuracy of 3–4 K in practice, which is limited by knowledge of atmospheric properties (eg downwelling sky radiance and atmospheric transmittance), and the surface emissivity. There are, however, strong prospects of enhanced performance given better estimates of these physical quantities, and if coefficients within the retrieval algorithms are determined over a wider range of observation zenith angles in the future.

Acknowledgements

Contents

List of Figures

xiii

List of Tables

Chapter 1

Introduction

Land Surface Temperature (LST) is a prime variable in Earth system science and climate studies on both global and regional scales (Running *et al.*, 1994). For the next generation of satellite-based sensors designed for such applications the desired accuracy of a global LST product is 1 K (Wan, 1999). The work in this thesis contributes towards reaching this goal through investigation of the underlying physical processes which drive radiative surface-atmosphere interactions.

For a satellite-based sensor viewing the land surface the at-sensor radiance is a combination of the surface-emitted radiance, atmospheric contributions from the upwelling and downwelling sky radiance and attenuation by the atmosphere. Further, the impacts of the land surface and atmosphere upon the measured signal are viewing angle dependent as well as temporally and spatially varying. The task of accurate remote sensing of LST therefore becomes quite complex. Because the bulk of satellite-derived measurements of LST covering the Earth's surface are made by scanning sensors such as the Advanced Very High Resolution Radiometer (AVHRR), Along Track Scanning Radiometer (ATSR) series of sensors, and more recently the Moderate Resolution Imaging Spectroradiometer (MODIS), the temporal, spatial and angular complexities mentioned above exist intrinsically within the task of accurate retrieval of LST from satellite-based sensors. The original contribution of this work to the satellite-based retrieval of LST is the investigation of

the angular nature of surface and atmospheric impacts upon the surface-emitted radiance.

The work in this thesis combines angular information unique to the ATSR series of satellite sensors, which possess a dual-view capacity allowing both a nadir and extreme zenith angle view (55°) of the same point upon the Earth's surface (Prata *et al.*, 1990; Mutlow *et al.*, 1999), with a continuous time series of *in situ* angular measurements of Surface Brightness Temperature (SBT) made by a scanning infrared radiometer installed at a field site instrumented for the validation of satellite-based measurements of LST in Central Australia spanning some seven months from the year 2000. The aim of this work is to develop methods for both the prediction and validation of satellite-based LST to a level of accuracy approaching 1 K. It is envisaged that such investigations as those detailed in this work will lead to a better understanding of the fundamental physical processes which govern radiative transfer between the land surface and the satellite and in doing so provide a basis for future improvements to the satellite remote sensing of LST on a global scale. The work comprising this thesis is divided as follows;

Chapter 2 of this thesis presents an overview of the current state of the science relating to the satellite-retrieval of LST. It discusses the important components of radiative transfer and approaches to solving the Radiative Transfer Equation (RTE) which allow LST to be estimated using remote sensing. It concludes with a description of the ATSR series of satellite sensors and suggests that the unique dual-look viewing capacity they possess may be utilized to extend understanding of the physical processes described by the RTE.

Chapter 3 describes two field sites instrumented for the calibration and validation of satellite-derived LST situated within different regions of Australia. The Amburla field site is situated in the Northern Territory, representing semi-arid conditions, while the Thangoo site is situated in the Kimberley Region of Western Australia and is representative of a sub-tropical climate. Satellite-derived and *in situ* data from these two sites are utilized in Chapters 4 and 5 to investigate how surface

and atmospheric properties impact the remote sensing of LST as the zenith angle of the satellite view of the surface increases.

Chapter 4 presents Surface Brightness Temperature (SBT) data acquired by the ATSR-2 satellite sensor over the two field sites and begins to account for the observed differences between the SBT measured by the nadir and forward viewing geometries of the ATSR-2 in terms of the angular nature of atmospheric impacts on the surface-leaving radiance. It describes how an atmospheric correction term may be developed and applied to satellite-derived SBT data to achieve and estimate of the LST based on knowledge of the atmospheric radiative components obtained using a radiative transfer model. Further, it describes a method via which *in situ* measurements of the downwelling sky radiance made by an infrared radiometer may be used to estimate downwelling and upwelling sky radiance and atmospheric transmittance at the scale of view of the satellite sensor and estimates the accuracy with which each of these radiative components may be known. Chapter 4 concludes by developing a generalized relation between the SBT and the magnitude of the atmospheric correction term for the nadir and forward views of the ATSR-2, and noting that the generalized relation may be modified for a particular surface type by characterizing the angular variation of the SBT and surface emissivity.

Chapter 5 begins by describing the scanning infrared radiometer installed at the field site in the Northern Territory for the purpose of validation of satellite-derived LST. It presents SBT data acquired by the scanning radiometer which show the existence of well-defined diurnal cycles in the angular distribution of SBT and shows how the results from a theoretical model for the surface emissivity may be applied to explain the observed angular distribution of SBT through the interaction of the downwelling sky radiance and surface emissivity as described by the RTE. It concludes by showing these results may be applied to; i) derive an LST validation product of accuracy approaching 1 K, and; ii) define LST retrieval algorithms for the nadir and forward viewing geometries of the ATSR-2 characteristic of the surface type and atmospheric conditions of the Amburla field site.

3

Chapter 2

Radiative Transfer

This chapter describes the underlying physics which permits the surface temperature of the Earth to be estimated via satellite-borne sensors. It discusses the formulation of the Radiative Transfer Equation (RTE), which describes the propagation of radiation from the surface of the Earth, through the atmosphere, to the satellite sensor. It defines the important variables within the framework of the RTE, with an emphasis on LST, and summarizes the current state of the science in relation to the estimation of these physical quantities, a knowledge of which allows the subsequent solution of the RTE for the land surface temperature. Finally, it discusses the suitability of the Along Track Scanning Radiometer (ATSR) series of satellites for the measurement of LST and how the novel viewing geometry of the instruments may improve the understanding of the radiative interaction between the land surface and the atmosphere.

2.1 The Radiative Transfer Equation

In the absence of an atmosphere, remote sensing of surface temperature would be a much simpler task. However, the presence of the Earth's atmosphere between the satellite and the surface impacts the surface-leaving radiance detected by the satellite sensor in numerous ways, making LST retrieval via satellite a complex

problem.

Collectively, the propagation of the surface-emitted radiance through the atmosphere to the satellite, and its interaction with the active constituents of the atmosphere, is termed '*radiative transfer*' and may be described by the RTE.

Following the notation of Prata (1993), the basic form of the RTE for a single channel, satellite-based TIR radiometer (8–14 μm) viewing a uniform surface through a non-scattering atmosphere, may be written;

$$I_\nu(\vec{s}) = \int_\nu R_\nu [\tau_\nu(\vec{s}) I_\nu^{surface}(\vec{s}) + I_\nu^{atmos}(\vec{s})] d\nu, \qquad (2.1)$$

where,

ν = wavenumber (cm^{-1}),

$\vec{s}$ = the vector in the direction of the optical path from the surface to the sensor ,

$I_\nu(\vec{s})$ = the radiance at the satellite sensor for wavenumber ν ($W/(cm^2.ster.cm^{-1})$),

R_ν = the normalised spectral response function of the sensor at wavenumber ν,

$\tau_\nu(\vec{s})$ = the transmittance in the direction of the optical path between the surface and the sensor at wavenumber ν,

$I_\nu^{surface}(\vec{s})$ = the surface-emitted radiance in the direction of the optical path at wavenumber ν ($W/(cm^2.ster.cm^{-1})$), and

$I_\nu^{atmos}(\vec{s})$ = the atmosphere-emitted radiance in the direction of the optical path at wavenumber ν ($W/(cm^2.ster.cm^{-1})$).

As in Prata (1993), it is assumed that the integration of the radiative quantities over the spectral response function may be replaced by monochromatic equivalents. This simplifies the notation for the following development of the RTE, however, in practice, the band-averaged quantities are used.

5

The radiance leaving the surface, $I_\nu^{surface}(\vec{s})$, is the sum of the surface-emitted radiance and the component of the Downwelling Sky Radiance (DWSR) reflected from the surface. This may be written;

$$I_\nu^{surface}(\vec{s}) = \varepsilon_\nu(\vec{s})B_\nu[T_s] + \frac{1}{\pi}\int_{\Omega^-} \vec{n}.\vec{s}\,\rho_\nu(\vec{s},\vec{s}')I_\nu^{sky}(\vec{s}')d\Omega(\vec{s}), \quad (2.2)$$

where,

T_s = the land surface temperature (K),

$B_\nu[T_s]$ = the blackbody equivalent radiance for T_s, defined via the

Planck Function $(W/(cm^2.ster.cm^{-1})$ (see Section 1.2.1),

Ω^- = the solid angle of the downward hemisphere,

$\vec{n}$ = the unit vector normal to the land surface,

$\vec{s}'$ = the vector from the origin of the DWSR to the surface,

$I_\nu^{sky}(\vec{s}')$ = the radiance from the sky in the direction defined by $\vec{s}'$ at wavenumber ν, and

$\rho_\nu(\vec{s},\vec{s}')$ = the surface reflectance in the direction of $\vec{s}$ for DWSR in the direction defined by $\vec{s}'$ at wavenumber ν.

When the temperature of the TIR penetration depth of the land surface is constant, Kirchhoff's law (Section 2.2.2.4) may be applied to replace the surface reflectance, $\rho_\nu(\vec{s},\vec{s}')$, in (2.2) (Salisbury et al., 1994; Snyder et al., 1998b; Korb et al., 1994) by;

$$\rho_\nu(\vec{s},\vec{s}') = 1 - \varepsilon_\nu(\vec{s}). \quad (2.3)$$

This substitution is made as the emissivity of the Earth's surface is high at wavelengths in the TIR and $\varepsilon_\nu(\vec{s})$ is already involved in (2.2) through the surface-emitted term. The substitution therefore minimizes the number of variables required

6

for the thorough description of the RTE. The validity of Kirchhoff's law is discussed more extensively in Section 2.2.2.4 .

Combining (2.2) and (2.3) allows the surface-leaving radiance at the surface to be expressed as;

$$I_\nu^{surface}(\theta) = \varepsilon_\nu(\theta)B_\nu[T_s] + [1 - \varepsilon_\nu(\theta)]I_\nu^{sky}(\theta'), \qquad (2.4)$$

where,

θ = the zenith angle at which the ground-based radiometer views the surface,

θ' = the zenith angle equivalent to *theta* but in the opposite azimuthal direction to that in which the radiometer looks.

It should be noted that, from this point onwards, vector notation of directional components is replaced with a description of directional components in terms of zenith angles (θ) as this notation relates more intuitively to the experimental component of the work for this thesis which deals with zenith angle effects upon the remote sensing of LST.

(2.4) is valid when the optical path length is short and there is little atmosphere between the surface and the sensor, such as for a ground based radiometer in dry conditions.

For the satellite, which views the Earth's surface through the entire atmosphere, there exist density profiles for water vapour and other absorbing gases in the atmospheric column from which a characteristic transmittance, τ_ν, measured at wavenumber ν (from height z to the top of the atmosphere), may be defined (Prabhakara et al., 1974; McMillin, 1975) according to the expression;

$$\tau_\nu(z, \infty, \theta) = exp[- \int_z^\infty k_\nu(z)u(z)sec(\theta)dz], \qquad (2.5)$$

where,

$\tau_\nu(z, \infty, \theta)$ = the atmospheric transmittance,

$k_\nu(z)$ = the absorption coefficient for the atmosphere which includes all active molecular species active at wavenumber ν (m^2/kg),

$u(z)$ = the water vapour profile (kg/m^2), and

z = the height (m).

In the Thermal Infrared (TIR) region (8–14 μm) of the electromagnetic spectrum, the principal component of the atmosphere which affects the radiance detected at the sensor is water vapour. The degree to which the signal is attenuated is dependent upon the amount, temperature and distribution of water vapour as well as the wavelength of radiation. Further, water vapour also emits in the TIR and the upwelling and downwelling components of this emission impact upon the radiance detected by the satellite sensor and must be accounted for in the appropriate form of the RTE. In a similar manner to (2.4), and using (2.1), the RTE for the satellite-based sensor may be expressed as;

$$I_v^{surface}(\theta) = [\varepsilon_\nu(\theta)B_\nu[T_s] + (1 - \varepsilon_\nu(\theta))I_\nu^{sky}(\theta')]\tau_\nu(\theta) + I_\nu^{atmos}(\theta), \qquad (2.6)$$

in which $I_\nu^{atmos}(\theta)$ represents the component of the Upwelling Sky Radiance (UWSR) which reaches the satellite sensor. The RTE in the form of (2.6) brings together the radiative components derived from both the surface and the atmosphere to describe the physical basis of the radiance sensed by a satellite-based sensor. The surface and atmospheric radiative components vary independently of each other and solving the RTE for the surface temperature, T_s in (2.6), requires an accurate estimate of the value of each of the physical variables as well as knowledge of their variability with changes in both land surface and atmospheric properties and viewing geometry.

8

In the following sections the definition, measurement and modelling of the important components of the RTE are discussed, leading to a summary of the literature relating to the solution of the RTE to obtain a remotely sensed estimate of the LST.

2.2 Components of Radiative Transfer

2.2.1 Surface Temperature

2.2.1.1 Definition

The thermodynamic temperature of a single molecule may be readily defined through its kinetic energy. However, for a surface viewed at a distance by a radiometer, kinetic energy is not an appropriate measure of temperature, and the best approximation of the thermodynamic temperature may be obtained via the radiative energy balance of the surface based on a measure of the surface-leaving radiance (Norman and Becker, 1995).

The physics of radiometrically measuring the temperature of a surface was described in Section 2.1 by (2.4) and (2.6) for the cases of *in situ* and satellite-based radiometers, respectively. The RTE for each of these cases is written in terms of radiance because, to be physically correct, the interaction between the TIR emission from the various components of the surface which constitute the at-sensor radiance must be described as a combination of the radiance contributions, rather than surface temperature. However, the blackbody temperature of the surface which is equivalent to the at-sensor radiance, $I_\nu^{surface}(\theta)$ in (2.4) and (2.6), termed the Brightness Temperature (BT) (Norman and Becker, 1995; Becker and Li, 1995), may be defined via the Planck Function (Menzel, 2001). For radiance measured in units of $W/(cm^2.ster.cm^{-1})$ the Planck Function may be written (Menzel, 2001) as;

$$I_\nu^{surface}(\theta) = \frac{c_1 \nu^3}{e^{\frac{c_2 \nu}{T}} - 1},$$

(2.7)

in which;

$$c_1 = 2hc^2,$$ (2.8)

and;

$$c_2 = \frac{hc}{k},$$ (2.9)

where,

T = brightness temperature,

ν = the wavenumber,

h = Planck's constant, 6.626713×10^{-34} J s

c = the speed of light, $2.99792458 \times 10^{-10}$ cm s^{-1}, and

k = the Boltzmann constant, 1.3807×10^{-23} J K^{-1}.

Similarly, the inverse Planck Function may be used to convert from radiance to BT, and may be written as (Menzel, 2001);

$$T = \frac{c_2 \nu}{[ln(\frac{c_1 \nu^3}{I_\nu^{surface}(\theta)} + 1)]}.$$ (2.10)

Although (2.10) is valid for a single wavenumber, by integrating over a specific wavenumber range and the response function of the radiometer, a BT may be defined which is equivalent to the band-averaged radiance measured by the radiometer. In the experimental component of the work for this thesis Look-Up Tables (LUTs) have been defined which simplify the process of conversion between radiance and

BT for a particular radiometer by calculating the band-averaged radiance over the range of BT which may be expected at the field site. These pre-defined relations may be easily accessed during computations involving the RTE and simply relate measured and modelled radiative quantities to the more intuitive description of the surface in terms of temperature.

The BT itself is defined as the temperature of a blackbody that emits the same radiance as that measured by the radiometer (Norman and Becker, 1995). Conversion of the BT to an estimate of the thermodynamic temperature of the surface then requires that the BT be corrected for; i) the surface emissivity, ii) the reflected DWSR component (when the surface emissivity is below unity) in (2.4), and; iii) the UWSR in the case of a satellite-based sensor, as given by (2.6). This correction process may be thought of as rearranging (2.4) and (2.6) so as to solve for $B_\nu[T_s]$, and subsequently T_s via the inverse Planck Function.

If the surface viewed by the radiometer is homogeneous and isothermal then, radiometrically, the temperature of the surface calculated after correcting the BT estimate may be defined as the Directional Radiometric Surface Temperature (DRST) (Norman and Becker, 1995). However, from a satellite remote sensing perspective, the surface of the Earth is rarely homogeneous. In practice, for a satellite view of the Earth, the closest approximation to a homogeneous surface is the sea surface because it is near-isothermal at the scale of view of the satellite (≈ 1 km^2 for near-nadir views of the AVHRR and ATSR sensors) and the Field-Of-View (FOV) of the satellite contains only water. Even so, the roughness of the sea surface may affect its homogeneous appearance at larger zenith angles (Masuda et al., 1988; Wu and Smith, 1997). Compared to the sea surface the land surface is heterogeneous to the extreme. It is generally comprised of different types of soils, rocks and vegetation, all of which may be of different sizes and scales. The topography of the land surface also varies much more significantly than the sea surface. As a result, for general applications of the remote sensing of the Earth's surface, the definition of surface temperature becomes much more complex than for the homogeneous case.

Due to the heterogeneity of the land surface, the DRST is not an appropriate definition of the LST. In fact, because for the case of the land surface there is "...not an equivalent blackbody with a given temperature yielding the same temperature at all wavelengths..." (Norman and Becker, 1995), LST must be defined radiometrically as the Ensemble Directional Radiometric Surface Temperature (EDRST) (Norman and Becker, 1995). For the case of the land surface, in the forms of the RTE given by (2.4) and (2.6) the quantity T_s is then an estimate of the EDRST, which itself is a radiometric estimate of the thermodynamic temperature of the land surface. Within Chapters 4 and 5 of this thesis the EDRST is referred to as the LST and is generally denoted by 'T_s' as in (2.4) and (2.6).

2.2.1.2 Radiometric Measurements of Brightness and Land Surface Temperature

Following the definition of BT and EDRST (LST) from the previous section, the radiance measured by a radiometer directed towards the land surface may be composed of contributions from many different sources, each possessing differing radiative properties. As such, the BT measured by the radiometer is a mean estimate of the BT of the ensemble of sources within its FOV. The EDRST may be subsequently defined after accounting for the emissivity of the radiative components within the FOV (see Section 2.2.2).

A pressing question in the context of the current research is how well radiometric measurements at the scale of the FOV of an *in situ* radiometer translate to the scale of the FOV of a satellite-based sensor. The scale of view of the standard infrared radiometers used for *in situ* measurements of BT and LST is of the order of 1 m² (McAtee *et al.*, 2002) for measurements made a few metres above the land surface, while the FOV of satellite-based sensors ranges from 90 m for the Advanced Spaceborne Thermal Emission and Reflection Radiometer (ASTER) to the order of 1 km² for sensors such AVHRR, ATSR-2 and MODIS (McAtee *et al.*, 2002). Work by Kustas *et al.* (1990) showed that measurements of BT made by

12

a hand held radiometer were representative of airborne radiometric measurements of dimensions at least up to an altitude of 150 metres, or a diameter of 40 m for circular FOV over crop-covered surfaces. Results from Prata (1994) suggest that; i) point measurements made by contact temperature sensors may agree with satellite-derived estimates of LST to within 1–2 K for uniform surfaces provided that such measurements are averaged over spatial scales large enough to capture any spatial variability of the terrain, and; ii) that the limit of accuracy of validation of satellite-derived estimates of LST may be an RMS error of approximately 1.5 K for fairly uniform grass and crop-covered sites. This limit is also suggested from the results from similar studies by Rustana et al. (1994a,b) and Sobrino et al. (1996).

At the smaller scale, the size of the FOV of the in situ radiometer compared to the dimensions of the individual radiative sources comprising the surface means that it is difficult to determine the radiative contributions from each individual source within the FOV of the radiometer. However, such detailed information may not be required from in situ measurements for applications such as the validation of satellite-derived LST, for which it may be sufficient to categorize components of the FOV of the radiometer into broad classes such as soil and vegetation/canopy. For the bare soil case, the radiance measured by a radiometer should be dependent only upon the radiative properties of the soil particles (Takashima and Masuda, 1987; Ishida et al., 1991; Lagouarde et al., 2000). For a surface covered by a vegetative canopy, if the dimensions of the vegetative canopy can be obtained, a composite radiometric surface temperature may be described via a geometrical-optical model describing the BT or LST observed by a remotely located sensor in terms of the proportions of soil and vegetation viewed by a satellite-based sensor for a given viewing geometry (Kimes et al., 1981; Kimes, 1983; Sobrino and Caselles, 1990; Sobrino et al., 1990; Kustas et al., 1990; Caselles et al., 1992; Friedl and Davis, 1994; Colton, 1996; Lagouarde et al., 2000). A similar analysis may also be applied to the case of forest-covered surfaces to determine how the dimensions of the canopy will impact the radiance measured by a satellite-based sensor for different

viewing geometries (Balick and Hutchinson, 1986; Lagouarde *et al.*, 1995; Jupp, 1998).

Since the majority of satellite-based estimates of LST are made by scanning sensors, it is important to observe how *in situ* measurements of LST vary under changing viewing geometry in order to begin to gauge the impacts which viewing geometry may have on satellite-based measurements. The angular variation of BT has been the focus of numerous studies, including those by Balick and Hutchinson (1986); Sobrino and Caselles (1990); Smith *et al.* (1997); Lagouarde *et al.* (1995) and Lagouarde *et al.* (2000) among others. Of most relevance to the research component of this thesis is the work of Lagouarde *et al.* (2000). They used a multi-angle radiometer installation to measure the change in BT of the land surface with increasing observation zenith angle for a number of land surface types including bare soil and an array of crop types. They observed asymmetry in the BT distributions about the nadir view, related to observational and solar geometry for the different crop types as well as for bare soils. The asymmetry for crop-covered surfaces was found to be more pronounced than for bare soil. However, of interest to the research for this thesis is that Lagouarde *et al.* (2000) were able to relate the change in BT they observed with increasing zenith angle for bare soils to the decrease in the surface emissivity with increasing zenith angle reported by Labed and Stoll (1991a) for similar soil types. This technique of analyzing the change in BT with zenith angle in relation to the decrease in surface emissivity was also used by Dozier and Warren (1982) in their studies of the impact of viewing angle on the radiative properties of snow surfaces. It is applied in the research for this thesis to *in situ* radiometric measurements of BT from a semi-arid field site in Central Australia in the Northern Territory.

As may be seen from the expressions for the RTE given previously in Section 2.1 by (2.4) and (2.6), it is difficult to distinguish between the contributions to changes in the observed BT from the surface emissivity and the LST. This section has discussed observations of changes in BT with zenith angle. The following section

14

discusses the surface emissivity and its role in radiative transfer in more detail.

2.2.2 Emissivity

2.2.2.1 Definition

As shown by (2.6), the surface emissivity, ε_ν, is fundamental to the radiometric measurement of LST. Even without consideration of the surface-reflected term in (2.4) and (2.6), ε_ν and T_s are coupled in such a way that independent information about ε_ν is required in order to solve the RTE for T_s (the EDRST defined previously). Without independent knowledge of ε_ν, (2.4) and (2.6) are underdetermined equations (Gillespie *et al.*, 1998), and T_s may not be evaluated.

In a similar fashion to the surface temperature, ε_ν should be defined depending on the target surface and the spatial scale of the measurement and viewing geometry (Norman and Becker, 1995; Becker and Li, 1995). The simplest definition of ε_ν is that for a single body at uniform temperature. Here, ε_ν is defined as the ratio of the radiance the body emits to the radiance it would emit if it were a perfect blackbody at the same thermodynamic temperature (Norman and Becker, 1995). Norman and Becker (1995) define this quantity as the r-emissivity, $\varepsilon_{r,\nu}$, and its value may be computed as the complement to the Directional-Hemispherical Reflectance (DHR) through Kirchhoff's Law (Section 2.2.2.4), as described by (2.3).

When dealing with a surface, it is necessary to define ε_ν in terms of an ensemble, as with the definition of EDRST. Because "... the ensemble of natural media at different temperatures is not simply related to a blackbody distribution at the same effective temperature ..." (Norman and Becker, 1995), the surface emissivity must be defined as the ratio of the radiance emitted from from an ensemble of natural media to the radiance emitted by the ensemble with the same temperature distribution assuming each element is a perfect blackbody. Norman and Becker (1995) term this the Ensemble Directional e-emissivity, $\varepsilon_{e,\nu}$. This quantity is purely theoretical and may not be directly measured. However, in practice, for measurement

15

and modelling purposes, the Ensemble Directional r-emissivity, $\varepsilon_{r,\nu}$, may be used. It is defined through (2.3) for the ensemble of media comprising the target surface. When the temperature distribution of the surface is uniform $\varepsilon_{e,\nu}$ and $\varepsilon_{r,\nu}$ become equal.

There is extensive literature concerning measurements and methods of extracting information on surface emissivity (which, strictly, should be termed the r-emissivity) and a summary of these are given in the following sections of this review of the literature.

2.2.2.2 Measurement

Due to its importance in the satellite sensing of LST (Becker, 1987), radiation budget (Prata et al., 1997), surface energy balance (Hall et al., 1992; Jupp, 1998) and applications, such as, mineral exploration and identification (Salisbury and Walter, 1989; Schmugge et al., 1991; Ninomiya et al., 1997), extensive measurements of emissivity have been made. There exist radiometric measurements of individual materials (Labed and Stoll, 1991b,a; Salisbury and D'Aria, 1992), various surface types (Masuda et al., 1988; Rees and James, 1992), soils (Sobrino and Cuenca, 1999) and vegetation (Labed and Stoll, 1991b; Sobrino and Caselles, 1993). The studies range from laboratory (Labed and Stoll, 1991a; Salisbury and D'Aria, 1992), field (Takashima and Masuda, 1987; Nerry et al., 990a,b; Rubio et al., 1997) and remotely sensed (Barton and Takashima, 1987; Ninomiya et al., 1997; Gillespie et al., 1998; Karnieli, 1999; Sobrino and Cuenca, 1999; Bower, 2001).

From a review of the literature on the measurement of surface emissivity, there are three methods which have been used repeatedly. The 'box' method has been applied to both laboratory (Labed and Stoll, 1991b) and field measurements Caselles et al. (1988); Labed and Stoll (1991b); Sobrino and Caselles (1993); Rubio et al. (1997). The technique essentially simulates an enclosure calculation (see Section 2.2.2.4).

The surface emissivity has also been estimated using a radiometric measure-

ment of the surface temperature, combined with an independent measurement of the surface temperature from a thermocouple or thermistor. Rees and James (1992) made laboratory measurements of the angular variation in the value of ε_ν in this way for water and ice surfaces. Barton and Takashima (1987) measured the emissivity of sand near Lake Eyre in northern South Australia. Sobrino and Cuenca (1999) also used this approach to determine the angular variation in emissivity for a range of surfaces. Similar angular measurements were made by Labed and Stoll (1991a) using a specrtoradiometer, with the samples being heated by an underlying heating plate.

The emissivity spectra of natural surfaces characterized by Salisbury and D'Aria (1992) and Ninomiya et al. (1997), the angular measurements of surface emissivity made by Bower (2001) and the investigations of the validity of Kirchhoff's Law by Salisbury et al. (1994) and Korb et al. (1994) were made at a much higher spectral resolution using the technique of interferometry (Bower, 2001). The instruments used in these experiments are able to measure the radiation scattered in all directions from the target, the DHR, and are related to the surface emissivity via Kirchhoff's Law, as given by (2.3) (Salisbury et al., 1994; Korb et al., 1994).

Because satellite TIR data are acquired over a range of zenith angles between 0 and 60° by scanning sensors such as AVHRR-2, MODIS and ATSR-2, knowledge of the variation in surface emissivity over this angular range is critical to the accuracy of large-scale measurements of LST. Barton and Takashima (1987) reported a decrease in ε_ν of the order of 2% between nadir and a zenith angle of 60°. Takashima and Masuda (1987) also reported only small decreases in the emissivities of quartz and Saharan dust over this angular range. The angular investigations carried out by Labed and Stoll (1991a) and Sobrino and Cuenca (1999) suggest decreases of between 3 and 5 % for soil types characterized by sand, clay and gravel. The emissivity of grass showed no decrease in surface emissivity with viewing angle. Bower (2001) reported similar decreases in the surface emissivity for a range of soil types. By far the largest decrease in surface emissivity with angle is exhibited by water

17

and ice surfaces (Masuda *et al.*, 1988; Rees and James, 1992). Both studies showed decreases of between 5 and 10% in the surface emissivity over the angular range 0 to 60° for pure water, seawater and ice. An unaccounted for decrease in ε_ν of the order of 2–3% will cause an underestimate in surface temperature measurement of 1K, while the error increases to as much as 4K for a 5–10% change, using the expressions derived by Becker (1987).

The consensus of the literature is that the bulk of emissivity values for terrestrial materials and surfaces in the TIR (8–14μm) are in the range $0.85 < \varepsilon_\nu < 0.99$ (Wan and Dozier, 1989). The results from various experiments are summarized in Table 2.1. In the 'Method' column, "1" represents the box method; '2' a radiometer with an independent surface temperature measurement; '3' modelling of optical properties; and '4', an airborne radiometer with independent surface temperature measurements. Rubio *et al.* (1997) records an extensive list of experimental emissivity measurements for various minerals, soil types and plant foliage. From Table 2.1, there obviously is a significant range of emissivity values for different surface types within the TIR. If unaccounted for, this variability has large effects on the accuracy of the measurement of LST. The target accuracy for the EOS/MODIS LST product is 1K (Wan, 1999). To meet this goal, the surface emissivity needs to be well known. In fact, Gillespie *et al.* (1998) suggest that in order to achieve a level of accuracy of 1 K for the ASTER instrument, aboard the EOS Terra platform, it is necessary to know the surface emissivity to an accuracy of ±0.015. Further, the emissivity estimates given in Table 2.1 were made at, or close to, nadir. The angular variation of ε_ν has been shown to be significant and this adds further complexity to the accurate estimation of LST from satellite sensors. For greatest accuracy of LST measurements from scanning satellite-based sensors, the surface emissivity needs to be continuously updated depending upon land surface type and viewing geometry. Given knowledge of these parameters, modelling of ε_ν may provide the most accurate data for minimizing the impact of uncertainty in ε_ν on the satellite measurement of LST.

Author(s)	Surface Type	Emissivity	wavelength range (μm)	Uncertainty	Method
Barton & Takashima (1986)[1]	sand	0.973	8–13	0.01	2
Takashima & Masuda (1987)[2]	quartz dust	0.86	10.5–11.5	0.01	3
”	”	0.93	11.5–12.5	0.05	”
”	Sahara dust	0.97	10.5–11.5	0.3	”
”	”	0.96	11.5–12.5	0.03	”
Masuda & Takashima (1988)[3]	pure water	0.987	8–13	-	3
”	sea water	0.987	”	-	”
Casselles & Sobrino (1988)[4]	orange tree	0.985	8–14	0.006	1
”	ground	0.957	”	0.007	”
Labed & Stoll (1991a)	very short grass	0.979	”	7.5E-3	1
”	tufts of grass	0.981	”	”	”
”	grassland	0.983	”	”	”
”	rushes	0.994	”	”	”
Schmugge et al (1991)	soil	0.946	10.1–11.5	1%	4
”	”	0.938	11.0–11.8	”	”
Rees & James (1992)[5]	water	0.973	8–14	0.002	2
”	water	0.969	”	”	”
”	ice	0.956	”	”	”
Sobrino & Caselles (1993)	red clay	0.957	8–14	0.006	1
”	brown loam	0.925	”	”	”
	orange tree (Navel)	0.985	”	0.005	”
”	” (Thompson)	0.983	”	”	”
”	green grass	0.972	”	0.008	”
”	yellow grass	0.945	”	0.012	”
Sobrino & Cuenca (1999)	water	0.974	”	-	2
”	sand	0.908	”	-	”
”	clay	0.947	”	-	”
”	slime	0.931	”	-	”
”	gravel	0.936	”	-	”

Table 2.1: List of radiometric surface emissivity estimates from previous studies. [1] Data read from line of best fit at $\theta = 0°$. [2] Average value over all grain sizes from measurements at $\theta = 7°$. [3] Average of all tabulated data for $\theta = 0°$ in $8 - 13\mu$m range. [4] Uncertainty is calculated from specified accuracy of measurement and spread of data. [5] Estimates made at $\theta = 5°$. − indicates no uncertainty given.

19

2.2.2.3 Modelling

The range in values of the surface emissivity, shown by the collection of studies from the previous section, reveal the variability in emissivity for different types of surfaces. As noted earlier, these measurements were typically made at normal incidence. Because satellite coverage is so vast and involves a range of viewing angles, the use of fixed emissivity values must limit the accuracy of satellite-LST retrieval. In order to improve the accuracy of global LST it is essential to be able to continuously redefine the value of ε_ν so that it is instantaneously appropriate for the type of land surface being viewed by the satellite (Snyder et al., 1998a), as well as for the viewing geometry for the scene. In situ measurements, as detailed in the previous section can help to achieve this, but their validity is localized as shown by the findings of Becker and Li (1990) and Labed and Stoll (1991b).

For increased accuracy of LST with global coverage, knowledge of the underlying physical principles which govern the emittance of radiation from the land surface is required in order to define the value of the surface emissivity. It is through modelling of these physical processes that such insights into the nature of surface emissivity may be gained. Although such work may be said to still be in its infancy, a number of approaches have been developed to date.

The fundamental science behind the description of radiative flux across a boundary viewed through an absorbing and scattering atmosphere, and the implications for the emissivity of a surface, is not new. There are numerous solutions to the differential equations which describe the radiative processes on a molecular level, but many are computationally complex, or else the constraints under which they are applicable limit their application (Joseph et al., 1976). Several computational methods for describing the spectral nature of the surface emissivity and reflectance, based on single particle scattering properties, have been developed for, and applied to, media ranging from silicate minerals (Conel, 1969; Takashima and Masuda, 1987) and various soil types (Ishida et al., 1991) to snow surfaces (Wiscombe and Warren, 1980; Warren and Wiscombe, 1980). In the work of Wiscombe and War-

ren a generalized framework for the spectral albedo is developed which predicts the asymmetry of molecular scattering in the atmosphere and at the boundary layer using the delta-Eddington approximation for describing the bulk radiative transfer (Joseph *et al.*, 1976), coupled with Mie scattering calculations at the snow surface. The model contains only observable parameters; the single scattering albedo and the asymmetry factor describing the proportions of forward and backscattering at the surface. Both these parameters are dependent upon the grain size of the surface and the wavelength of radiation. Knowledge of these parameters allows the model to be generalized to a range of surface types, and for this reason has been adopted in the experimental component of the work for this thesis described in Chapter 5. The reflectance of the surface, derived from this model, is related to the surface emissivity by (2.3), provided Kirchhoff's Law holds (Section 2.2.2.4). It is models such as that formulated by Wiscombe and Warren (1980), which describe radiative transfer at the particle level, that form the basis of models of surface emissivity.

Moving from the molecular level to the small-scale structure of the land surface, radiative interactions at the surface and particularly intra-canopy interactions have been modelled for many years in terms of the geometrical-optical properties of the scattering constituents of the surface/canopy (Otterman, 1981; Otterman *et al.*, 1992, 1995a,b; Colton, 1996; Francois *et al.*, 1997; Otterman *et al.*, 1999). Using such geometrical-optical models, classification-based emissivity schemes for remote sensing LST on a global scale have been developed, for example the work of Snyder *et al.* (1998a), which is designed for use with the TIR channels (31 and 32) of MODIS used in the split-window LST algorithm (Wan, 1999). In this case, from a combination of land cover classes derived from EOS/MODIS and the International Geosphere-Biosphere Program (IGBP) fourteen '*static*' landcover types have been defined, the properties of which are seasonally invariant. Further information from a vegetation and snow-cover index provides a dynamic component to the classification system, which modifies static properties on a pixel-by-pixel basis depending on time of year, latitude and longitude. In this way, the effects of seasonal variation

21

of bio-geophysical variables such as rainfall and plant growth, among others which impact surface radiative properties, may be accounted for within the scheme.

The radiative properties of the broad landcover classes are based upon Bi-directional Reflectance Distribution Function models (BRDF), for the visible spectrum (Roujean *et al.*, 1992) which have been extended into the TIR by Snyder and Wan (1998). The BRDF kernel models developed by Snyder and Wan (1998) describe the radiative interactions within a particular land surface type, and the surface emissivity is derived via knowledge of the the DHR and application of (2.3). The BRDF model for bare surfaces is derived from a rough-surface specular model for water and ice (Snyder and Wan, 1998), sparse vegetation cover from a spherical-planar geometrical-optical model (Li and Strahler, 1992), and for dense vegetation by a volumetric model developed by Roujean *et al.* (1992).

For eight out of the fourteen static classes defined, the variability in emissivity has been captured so that errors are approaching levels small enough to achieve the accuracy of 1K desired for MODIS LST using the split-window algorithm (Snyder *et al.*, 1998a). Together, these eight classes cover approximately 70% of the globe over an annual cycle, as well as the range of viewing angles for which satellite TIR data may be acquired (Snyder *et al.*, 1998a). The accuracy achieved so far is an encouraging result for global estimation of surface emissivity and LST.

Importantly, since scanning satellite-based sensors acquire the majority of remotely sensed data over the Earth's surface, the directional nature of the surface emissivity is embedded within the classification-based formulation for the surface emissivity, such as in the work of Snyder and Wan (1998). A more explicit model for directional emissivity is proposed by Li *et al.* (1999) in which it is shown that, for land surfaces with three-dimensional structure, such as vegetated surfaces, r-emissivity, as defined by Norman and Becker (1995), is not appropriate for solving the RTE when there are large temperature gradients within the vegetative canopy. Instead, an effective emissivity is proposed, such that;

$$\varepsilon_o = \varepsilon_{r,\nu} + \Delta\varepsilon_{GO}(\frac{T}{T_o}), \qquad\qquad (2.11)$$

where,

ε_o = the effective emissivity in given viewing direction,

$\varepsilon_{r,\nu}$ = the r-emissivity defined by Norman and Becker (1995),

T = the surface temperature for the viewing direction,

T_o = the effective surface temperature which is independent of viewing

direction, and

$\Delta\varepsilon_{GO}$ = a correction term to the r-emissivity derived from the difference

in temperature between the temperature of the scene, as measured

in the viewing direction, and the effective temperature of the

surface, T_o. Importantly, the reference temperature, T_o, is defined as the

temperature of the blackbody used to quantify the effective emissivity of the

surface.

Using this model, anisotropy in surface brightness temperature distribution with zenith angle, as reported by Balick and Hutchinson (1986); Sobrino and Caselles (1990); Smith *et al.* (1997); Jupp (1998) and Minnis and Khaiyer (2000) among others, may be interpreted as a change in the effective surface emissivity rather than the surface temperature, which remains characterized in the model by the directionally independent temperature, T_o. Such a model has possible applications to the analysis of TIR data acquired by the ATSR-2 (see Section 2.6 and Chapter 5) as it possesses a dual-look facility for viewing the same pixel at two different zenith angles. Further, the model also has implications for results from angular *in situ* measurements of surface emissivity and LST such as those of Sobrino and Cuenca (1999), as well as for the validation of satellite-derived LST using ground-based radiometric measurements, a component of the work for this thesis described in

23

Chapter 5.

In summary, the remote sensing of LST is a complex problem because of the coupling between the surface temperature and surface spectral emissivity within the surface emission term of the RTE as defined by (2.4) and (2.6). However, if an independent estimate of ε_ν may be obtained the LST may be evaluated. Whether such an estimate of the surface emissivity is derived via the modelling of radiative transfer, directional measurements, or classification of landcover types, continuous, accurate estimation remains a challenge in the field of remote sensing of LST. The experimental component of the work in this thesis, described in Chapter 5, builds upon the body of knowledge summarized in the previous few sections under the premise that a better understanding of the physical principles governing surface emissivity will allow its estimation accurately enough to meet the desired goals for remote sensing of LST in the future. In particular, the work utilizes the framework of the Wiscombe and Warren model and the concepts developed by Li *et al.* in the analysis of *in situ* data from an LST validation field site in Central Australia.

2.2.2.4 Kirchhoff's Law

Kirchhoff's Law, as given by (2.3), describes the radiative balance at the interface between two different media. As noted previously, the validity of Kirchoff's law is critical to the formulation of the RTE which describes the propagation of the surface-leaving radiance from the surface to the satellite sensor. It is best illustrated by perturbing thermodynamic equilibrium within an enclosure. Here, an enclosure is defined as having perfectly black inside walls, being isolated from its surroundings, and in thermodynamic equilibrium (Snyder *et al.*, 1998b).

If a radiative flux is emitted from an inside surface of the enclosure to a non-blackbody within the enclosure, in order to maintain thermal equilibrium;

$$\varepsilon(\theta_j, \phi_j) = 1 - \int_{2\pi} \rho(\theta_i, \phi_i; \theta_j, \phi_j) d\Omega_i, \, and \qquad (2.12)$$

24

$$\alpha(\theta_j, \phi_j) = 1 - \int_{2\pi} \rho(\theta_j, \phi_j; \theta_i, \phi_i) d\Omega_i, \qquad (2.13)$$

where,

$\varepsilon(\theta_j, \phi_j)$ = the emissivity of the non-blackbody,

$\alpha(\theta_j, \phi_j)$ = the absorptivity of the non-blackbody,

$\rho(\theta_j, \phi_j)$ = the DHR of the non-blackbody, and

$d\Omega_i$, = the the solid angle of the hemisphere.

θ_i, ϕ_i and θ_j, ϕ_j define the direction of the radiative flux.

Because the enclosure is in thermodynamic equilibrium (2.12) and (2.13) may be equated, giving;

$$\varepsilon(\theta_j, \phi_j) = \alpha(\theta_j, \phi_j). \qquad (2.14)$$

Through (2.14), the emissivity may now be defined as;

$$\varepsilon(\theta_j, \phi_j) = 1 - \int_{2\pi} \rho(\theta_j, \phi_j; \theta_i, \phi_i) d\Omega_i. \qquad (2.15)$$

The emissivity is therefore equal to the complement of the DHR (Section 2.2.2.1). Within the enclosure, the DHR and the Hemispherical-Directional Reflectance (HDR) are equal. However, in practice, the DHR must be used to quantitatively describe the reflectance because the radiance scattered from all directions from the surface of the target is required if Kirchhoff's law is to be applied to derive the surface emissivity from reflectance measurements (Salisbury et al., 1994).

In practice, as well, a real surface is very rarely in thermal equilibrium with its surroundings, as it is within the controlled enclosure. However, a freely radiat-

25

ing surface will still follow Kirchhoff's Law provided the energy states of the surface structure obey the Boltzman distribution (Salisbury *et al.*, 1994; Snyder *et al.*, 1998b). In other words, for Kirchhoff's Law to hold, it is important that the surface be isothermal, at least to the TIR penetration depth of the material (Korb *et al.*, 1994). If large thermal gradients exist within this layer, or indeed within layers of a canopy structure, Kirchhoff's law may be violated as the emitted radiance may appear to originate from more than one source, each with different temperatures. In such a case, the r-emissivity may not be defined (Snyder *et al.*, 1998b).

Salisbury *et al.* (1994), Korb *et al.* (1994) and Li *et al.* (1999) cite cases of large thermal gradients invalidating Kirchhoff's Law. However, the model for directional emissivity proposed by Li *et al.* (1999) defines a correction term to the r-emissivity (as defined by Kirchhoff's Law) which is derived from the existence of a thermal gradient within a vegetation canopy, as defined by (2.11). Using the formulation of Li *et al.* an effective temperature for the surface, which is constant for all viewing angles, may be defined irrespective of invalidation of Kirchhoff's law. This definition of a characteristic surface temperature proves useful in the analysis of the angular distribution of surface brightness temperatures and satellite-derived estimates of LST for utilizing radiometric ground-based measurements described in the experimental component of this thesis in Chapter 5.

2.2.3 Atmospheric Terms

The atmospheric terms in the RTE originate primarily from atmospheric water vapour emission and absorption. Water vapour is the main radiatively active constituent of the atmosphere in the TIR (Anding and Kauth, 1970) and the amount and vertical distribution of water vapour affects remotely sensed LST measurements (Sidran, 1980), with the major impacts on the surface-leaving radiance (in descending order of impact) being due to; i) attenuation by the atmosphere, which is described by the atmospheric transmittance, τ_ν, as defined by (2.5); ii) the UWSR, and; iii) the reflected DWSR component in the cases where the surface emissivity

is less than unity.

Although atmospheric effects add complexity to the task of accurately estimating land and sea surface temperature from space, pioneering work by Anding and Kauth (1970); Maul and Sidran (1972); Prabhakara $et\ al.$ (1974) and McMillin (1975) showed that properties of the atmosphere at specific wavelengths in the TIR could be harnessed so as to account for the impacts of atmospheric emission and absorption. In the earlier methods developed for estimating SST from space, such as the studies by Anding and Kauth (1970) and Maul and Sidran (1972), the atmosphere was characterized by vertical profiles of Pressure, Temperature and Relative Humidity (PTRH). The radiance reaching the satellite sensor was simulated using a radiative transfer model, and the combined effects of τ_ν and the UWSR upon the surface-leaving radiance were characterized. These studies showed that pairs of wavelengths could be defined within the TIR atmospheric windows, at around 9 and 11μm, such that there was a strong linear relationship between the simulated radiance that would be measured by the satellite sensor at each of the two wavelengths constituting a pair, over a range of surface temperatures. Because the same physical processes were acting at both of the selected wavelengths, but had a greater impact at wavelengths closer to 9μm, simultaneous measurement of the radiance at each wavelength could be used to estimate the magnitude of the water vapour emission and absorption.

Prabhakara $et\ al.$ (1974) expanded on the results of Anding and Kauth and Maul and Sidran, but assessed the atmospheric transmittance and atmospheric contribution of the UWSR to the at-sensor radiance separately, to show that; i) the spectral variability in the value of the absorption coefficient, k_ν, causes a difference in the transmittance, τ_ν, across wavelengths in the TIR, and; ii) there exist selected pairs of wavelengths within the TIR for which the average temperature of the atmosphere is equal (to within the order of ±0.1 K). Based on these two results, Prabhakara $et\ al.$ were able to define a linear relationship between the BT measured by the satellite sensor and k_ν, for a given wavelength. The fact that wavelength pairs could be de-

fined such that the mean temperature of the atmosphere was constant then allowed two simultaneous equations to be defined which could be solved for the true surface temperature, for a satellite-based sensor viewing through an atmosphere with known characteristics. McMillin (1975) then utilized the selected pairs of wavelengths noted by Prabhakara *et al.* to develop the Split-Window (SW) approach to the remote sensing of SST (see Section 1.3.2).

In these initial solutions to the problems posed to the remote sensing of SST by the complexities of the atmosphere Anding and Kauth, Maul and Sidran, Prabhakara *et al.* and McMillin regarded the sea surface as a blackbody having a surface emissivity of unity. In such cases there is no reflected DWSR component in the at-sensor radiance. However, when the surface emissivity drops below unity, as is the case for most real surfaces, the reflected DWSR component must be defined. From (2.4) and (2.6) in Section 1.1, the DWSR is denoted $I_\nu^{sky}(\theta')$, and may be defined as the sky radiance emitted downwards at a zenith angle equivalent to that at which a radiometer would view the surface to estimate the LST, but in the azimuthal direction opposite to that in which the radiometer looks. Strictly, under this definition, $I_\nu^{sky}(\theta')$ is a directional component of the hemispherical downwelling flux, F_ν^{sky} (W), and the surface must exhibit specular properties. The hemispherical downwelling flux may then be defined as;

$$F_\nu^{sky} = \int_0^{\frac{\pi}{2}} \int_0^{2\pi} I_\nu^{sky}(\theta', \phi) cos(\theta') sin(\theta') d\theta' d\phi, \qquad (2.16)$$

where,

θ' = the zenith angle of the incoming radiance, and

ϕ = the azimuth angle, and both angles are measured from the normal between the land surface and the sensor,

assuming the angular distribution of downwelling sky radiance is isotropic. Pro-

vided that this is the case, then evaluating (2.16) gives the hemispherical down-welling flux as;

$$F_\nu^{sky} = \pi I_\nu^{sky}(0, \phi), \qquad (2.17)$$

where $\pi I_\nu^{sky}(0,\phi)$ is the downwelling sky radiance at nadir.

For a surface possessing specular properties, the reflected component of the DWSR may then be defined as;

$$I_\nu^{sky}(\theta') = \frac{1}{\pi} F_\nu^{sky} sec(\theta'), \qquad (2.18)$$

where the reflected component of the DWSR is defined independently of the ϕ direction because the experimental work for this thesis, described in Chapters 4 and 5, focuses on zenith angle effects upon the remote sensing of LST without considering azimuthal variation.

From this summary of the atmospheric terms present within the RTE it is apparent that although it is the underlying physical properties of the atmosphere which make the remote sensing of land and sea surface temperature complex, these same physical properties, when utilized correctly, also provide the solutions to the RTE which allow SST and LST to be estimated via satellite remote sensing. The development of remote sensing techniques for effectively solving the RTE and thereby permitting estimation of SST and LST from space, up to the point at which the experimental component of the work for this thesis begins is described in the following sections.

2.3 Solving the RTE

2.3.1 The Split-Window Algorithm

The AVHRR sensor aboard the NOAA-7 satellite, launched in 1981, was the first instrument to possess a split-window in the TIR (channels 4 and 5) (McMillin and Crosby, 1984). It was designed for the satellite-based retrieval of SST, allowing the formulation of the SW algorithm derived by McMillin (1975) to be implemented operationally. The SW approach utilized the differential absorption in the atmospheric windows between 11 and 12μm (see Section 2.2.3) to effectively solve the RTE and derive an estimate of SST. Based on wavelengths within the TIR identified in earlier work by Anding and Kauth (1970); Maul and Sidran (1972) and Prabhakara et al. (1974), McMillin showed that the transmittances at two different wavelengths in the TIR could be described as linear combinations of each other. He expanded upon this result to show that the blackbody equivalent radiance for the surface temperature could be related to the surface-leaving radiances at each wavelength through the seemingly simple relation;

$$I_s = I_4 + \gamma(I_4 - I_5'),\qquad(2.19)$$

where,

I_s = the blackbody equivalent radiance from the surface,

I_4 = the measured radiance for channel 4 of the AVHRR,

I_5' = the equivalent radiance for channel 4 of the AVHRR for a given surface brightness temperature measured from channel 5, and

γ = a coefficient which is dependent upon the relative magnitudes of the atmospheric transmittance in channels 4 and 5.

The SW approach relies on; i) the two wavelengths being close together, ii)

there being a difference in atmospheric transmittance between them, and; iii) that the mean temperature of the atmosphere, $\overline{T}_a$, is equal for each of the chosen wavelengths. Earlier work by Prabhakara *et al.* (1974) showed that $\overline{T}_a$ varied by no more than 1K over the spectral interval 10.9–12.9μm, while Maul (1983) also reported that $\overline{T}_a$ may be considered uniform in this wavelength region, confirming the validity of the approach.

The derivation of (2.19) requires that the two channels, here denoted by wavenumbers ν_4 and ν_5, be close together so that the Planck radiance in one may described in terms of a linear combination of the other using a Taylor series expansion. The fact that $\overline{T}_a$ is constant between the two channels, allows the expansion to be written;

$$B(\nu_4, T) = B(\nu_4, \overline{T}_a) + \frac{dB(\nu_4, \overline{T}_a)}{dB(\nu_5, \overline{T}_a)}[B(\nu_4, T) - B(\nu_5, \overline{T}_a)]. \tag{2.20}$$

In the notation of McMillin and Crosby (1984), the RTE for a satellite-based sensor, as given previously by (2.6), may be written;

$$I(\nu_4, T, \theta) = B(\nu_4, T)\tau_s(\nu_4, \theta) + B(\nu_4, \overline{T}_a)[1 - \tau_s(\nu_4, \theta)], \tag{2.21}$$

where in (2.21), the emissivity is considered to be unity, τ_s is the transmittance from the surface to the top of the atmosphere, and the atmosphere-emitted radiance contribution to the at-sensor radiance is approximated over the entire atmospheric column using the mean value theorem (McMillin and Crosby, 1984).

Substituting (2.20) into (2.21) allows I_5' in (2.19) to be written;

$$I_5'(\nu_5, T, \theta) = B(\nu_4, T)\tau_s(\nu_4, \theta) + B(\nu_4, \overline{T}_a)[1 - \tau_s(\nu_4, \theta)]. \tag{2.22}$$

Because $\overline{T}_a$ is equal between ν_4 and ν_5, when (2.21) and (2.22) may be

equated, giving;

$$B(\nu_4, T_s) = I(\nu_4, T, \theta) + [I(\nu_4, T, \theta) - I'(\nu_5, T, \theta)][\frac{1 - \tau_s(\nu_4, \theta)}{\tau_s(\nu_4, \theta) - \tau_s(\nu_5, \theta)}].$$

(2.23)

(2.23) is an expanded form of (2.19), in which;

$$\gamma = \frac{1 - \tau_s(\nu_4, \theta)}{\tau_s(\nu_4, \theta) - \tau_s(\nu_5, \theta)}.$$

(2.24)

When T_4, T_5 and $\overline{T}_a$ are comparable (McMillin and Crosby, 1984), the Planck function may be accurately linearly approximated over the temperature range and an equivalent form of (2.19) may be written in terms of temperature as;

$$T_s = T_4 + \gamma(T_4 - T_5).$$

(2.25)

This approximation was considered by McMillin and Crosby (1984) to be less accurate than the corresponding radiance version, although the majority of SW algorithms use the form of (2.25) in preference to (2.19), as it is more intuitive to work with temperature rather than radiance, and, more importantly, data to validate the theoretical algorithms may be obtained more readily in the form of temperature rather than radiance (Prata, 1993).

The SW algorithm derived by McMillin is the simplest case of the more general form of the SW algorithm which may be written;

$$T_s = aT4 + b(T_4 - T_5) + c.$$

(2.26)

where, in the McMillin formulation, a = 1, b = γ, and c = 0.

SW algorithms are generally derived using either radiative transfer models and vertical atmospheric profiles, or statistical regression between coincident satellite and ground-based measurements of brightness temperature (Barton, 1995). Fixed coefficient equations for SST estimation, such as the original formulation by McMillin, were designed for global coverage and the coefficients in the algorithm implicitly incorporate the surface emissivity and atmospheric terms. Minnett (1990) showed that greater accuracy using the SW could be obtained if the coefficients were derived for specific climatologies, the trade-off for this, however, is that the range of application of the algorithm is decreased. Walton *et al.* (1998) showed that further improvement could be made using a non-linear algorithm. Barton (1995) lists the coefficients of a number of SST retrieval algorithms which reveals that there is a wide range in the values of the coefficients between algorithms due to the different approaches taken in accounting for atmospheric impacts upon the RTE and because the different algorithms were derived using data sets acquired from regions with differing climatologies. In general, using the SW approach, SST may be estimated with an accuracy of the order of 0.5–0.7 K.

The SW algorithm was initially applied to the sea surface as it was a more homogeneous target than the land surface. In order to simplify the physics of the SST retrieval problem, the sea surface was considered to be a perfect blackbody (McMillin, 1975; McMillin and Crosby, 1984). However, the need to measure global SST to greater accuracy led to more complex descriptions of the radiative transfer problem. In particular, a greater focus was placed on knowledge of the emissivity of the sea surface. Important work by Masuda *et al.* (1988) defined the decrease in the value of the sea surface emissivity as the zenith angle of the satellite view of the surface increased. Later work by Smith *et al.* (1996) and Wu and Smith (1997) showed that the roughness of the sea surface could also affect the surface emissivity under certain conditions.

As the complexity of the SW algorithm for SST estimation increased, the accu-

rate estimation of LST via remote sensing also became more viable. As with the SST case, the satellite-retrieval of LST was also limited in the early stages of remote sensing by knowledge of the surface emissivity. In fact, the variability in the emissivity of the land surface, due to its diverse spatial and compositional characteristics, remains an obstacle in the path of improving the accuracy with which LST may be estimated via satellite remote sensing to this day (Becker, 1987; Wan and Dozier, 1996; Li and Becker, 1993; Vidal, 1991; Kerr et al., 1992; Ottle and Stolle, 1993; Prata, 1993; Coll and Caselles, 1994; Coll et al., 1994; Prata, 1994).

In the first applications of the SW approach to LST, Price (1984) noted the existence of some of the difficulties in retrieving LST via satellite measurements to within ±1 K, particularly in relation to the surface emissivity, but did not require this level of accuracy for his work. Becker (1987) instigated investigations of the impact of the spectral nature of the surface emissivity upon the satellite retrieval of LST using the SW approach. He showed that the error in the estimate of LST, due purely to spectral differences in the surface emissivity between the two channels using the SW technique, may be given by;

$$\delta T \cong \frac{50(1-\varepsilon)}{\varepsilon} - \frac{300\Delta\varepsilon}{\varepsilon}, \tag{2.27}$$

where,

$\varepsilon = \frac{\varepsilon_4 + \varepsilon_5}{2}$, and

$\Delta\varepsilon = \varepsilon_4 - \varepsilon_5$.

Li and Becker (1993) expanded on this work to show that the error in LST due to error in emissivity measurement, δT, is given by;

$$\delta T = -52\delta\varepsilon - 110\delta(\Delta\varepsilon), \tag{2.28}$$

where,

$\delta\varepsilon$ = the error in the emissivity estimate for the two channels, and

$\delta(\Delta\varepsilon)$ = the difference in the surface emissivity between the two channels.

Their results showed that if $\delta\varepsilon = \delta(\Delta\varepsilon) = 1\%$, then the error in the LST retrieved using the SW technique will be greater than 1.6 K. Indeed, Wan and Dozier (1996) show that when using the SW approach it is necessary to know the surface emissivity to better than 0.01 if LST is to be estimated to within ± 1 K. This demonstrates that precise measurements of the surface emissivity are required for accurate results from the SW approach to LST estimation (see Section 2.2.2 for a more in-depth review of surface emissivity), and that knowledge of the surface emissivity is a limitation to the accuracy with which LST on a global scale may be retrieved using the techniques of satellite remote sensing.

The limitations imposed by knowledge of the surface emissivity on the accuracy with which the SW algorithm could be used to estimate LST, shown by Becker, led to further investigations of the LST retrieval problem. Prata (1993) noted that most of these approaches use a radiative transfer model such as LOWTRAN-6 (Wan and Dozier, 1989; Becker and Li, 1990; Ottle and Vidal-Madjar, 1992; Ottle and Stolle, 1993) or LOWTRAN-7 (Sobrino *et al.*, 1991; Coll and Caselles, 1994; Coll *et al.*, 1994; Rustana *et al.*, 1994a) to develop theoretical SW algorithms for LST retrieval. For a comprehensive review of SW algorithms the reader is directed to Becker and Li (1995) and Prata *et al.* (1995). Prata (1993) also noted that the problem of providing ground-truth data at the scale of view of satellite sensors, such as the AVHRR and ATSR-2 (≈ 1 km^2), had limited the amount of validation work which had been performed. Of the few studies undertaken to validate the SW algorithm with actual ground temperature measurements the results of Kerr *et al.* (1992); Caselles *et al.* (1992); Rustana *et al.* (1994b); Prata (1994) and Sobrino *et al.* (1996) showed that LST could be retrieved with an accuracy between 1 and 2.5 K in localized areas. On a global scale, Vidal (1991) estimated that LST could be estimated with an accuracy of the order of 3 K using the SW approach.

In the ongoing quest to improve the accuracy with which SST and LST may be estimated via the remote sensing, new retrieval methods are constantly being developed which utilize the newest satellite sensors and harness increasing computer power for data processing and analysis. Of particular interest to the remote sensing of SST during the past decade has been the development of the ATSR series of satellite sensors (Prata et al., 1990; Mutlow et al., 1994). These sensors were designed to retrieve SST to within ±0.3 K, utilizing a novel conical scan-mirror construction allowing a dual-look at the same point on the Earth's surface from two different viewing geometries. The ATSR series of sensors have facilitated the implementation of DA algorithms, most notably for SST retrieval (Mutlow et al., 1994; Zavody et al., 1995), but also for the estimation of LST (Sobrino et al., 1996). The DA approach to the solution of the RTE and its application to the remote sensing to SST and LST is described in the following section.

2.3.2 The Dual-Angle Algorithm

As early as 1975, McMillin (1975) noted in his work the possibility of developing a DA algorithm for satellite remote sensing of SST. However, it was impractical at the time as there were no satellite-based sensors able to view the same point on the Earth's surface simultaneously at two different zenith angles. But, with the launch of the first of the series of ATSR instruments in 1991, the DA approach to solving the RTE for the remote sensing of SST became feasible.

The ATSR series of satellite sensors possess a dual-look capability (Prata et al., 1990) (see Section 2.6), which permits two quasi-simultaneous views of the same pixel from different viewing geometries. The ATSR instrument was originally designed to measure SST to within ±0.3 K, utilizing the dual-look capacity to achieve better characterization of the atmosphere. Though the ATSR was designed primarily for SST measurement using a DA approach (Mutlow et al., 1994; Zavody et al., 1995), Prata (1993, 1994) and Sobrino et al. (1996) have also developed DA algorithms for the estimation of LST.

Using his SW formulation as a starting point, Prata (1993) derived a DA algorithm for channel 4 (the $11\mu m$ channel of the ATSR) as follows. The initial SW equation is written;

$$B_4[T_s] = \frac{1+\gamma}{\varepsilon_4}[\frac{1}{1+\gamma\tau_5\Delta\varepsilon}]I_4 - \frac{\gamma}{\varepsilon_5}[\frac{1}{1+(1+\gamma)\tau_4\Delta\varepsilon/\varepsilon_5}]I_4' + [\frac{1-\varepsilon_4-\gamma\tau_5\Delta\varepsilon}{\varepsilon_4+\gamma\tau_5\Delta\varepsilon}]\Delta\overline{I}\downarrow$$

(2.29)

where,

$B_4[T_s]$ = the Planck radiance in channel 4 for the surface temperature,

ε_4 = the surface emissivity for channel 4,

ε_5 = the surface emissivity for channel 5,

$\Delta\varepsilon = \varepsilon_4 - \varepsilon_5$,

τ_4 = the transmittance for channel 4,

τ_5 = the transmittance for channel 5,

$\gamma = \frac{1-\tau_4}{\tau_4-\tau_5}$,

I_4 = the radiance measured at the satellite in channel 4 for the surface brightness temperature T_4,

I_4' = the radiance measured at the satellite in channel 4 for the surface brightness temperature T_5, and

$\overline{I}\downarrow$ = the sky radiance difference between $\overline{I}_4\downarrow$ and $\Delta\overline{I}_4'\downarrow$.

If the following substitutions into (2.29) are made; i) $I_4=I_{\theta_1}$; ii) $I_4' = I_{\theta_2}$; iii) $\varepsilon_4 = \varepsilon_{\theta_1}$; iv) $\varepsilon_5 = \varepsilon_{\theta_2}$; v) $\tau_4 = \tau_{\theta_1}$ and vi) $\tau_5 = \tau_{\theta_2}$, where θ_1 is the nadir-view zenith angle of the satellite and θ_2 is the forward-view zenith angle of the satellite, then the DA equation may be written;

$$B_\nu[T_s] = [\frac{1 + \gamma_\theta}{\varepsilon_{\theta_1} + \gamma_\theta[1 - k_\nu w sec\theta_2]\Delta\varepsilon}]I_{\theta_1} - [\frac{\gamma_\theta}{\varepsilon_{\theta_2} + (1 + \gamma_\theta)[1 - k_\nu w sec\theta_1]\Delta\varepsilon}]I_{\theta_2},$$

(2.30)

in which;

$$\gamma_\theta = \frac{1}{\frac{cos\theta_1}{cos\theta_2} - 1},$$

(2.31)

and the transmittance has been approximated by;

$$\tau_\theta = 1 - k_\nu w sec\theta,$$

(2.32)

where k_ν is the absorption coefficient of the atmosphere at wavenumber ν, and w is the total absorber amount in the optical path from the surface to the top of the atmosphere.

In the formulation of (2.30), $B_\nu[T_s]$ is independent of the downwelling flux, and all quantities have an angular rather than a spectral dependence, removing the need for the Taylor series approximations devised by McMillin (1975) to relate brightness temperature measurements between different spectral channels via linear approximations of the Planck Function.

Accordingly, within the DA approach, emphasis is placed on obtaining information on how physical quantities such as the surface emissivity, UWSR, DWSR and atmospheric transmittance change with the increasing zenith angle of the satellite view of the surface. Of these quantities, however, only the variation of the surface emissivity with zenith angle has been studied extensively in relation to the remote sensing of surface temperature (Masuda et al., 1988; Barton and Takashima, 1987; Takashima and Masuda, 1987; Labed and Stoll, 1991a; Prata, 1993; Sobrino and

Cuenca, 1999; Bower, 2001) (see Section 2.2.2 for a more in depth discussion of the surface emissivity). Study of the angular variation of the atmospheric terms, for the most part, has been limited to investigation of the relationship between the water vapour content of the atmosphere and the transmittance, with little interest paid to variation of the UWSR and DWSR with increasing zenith angle. Most of these studies were conducted for the formulation of SW algorithms (McMillin, 1975; McMillin and Crosby, 1984; Sobrino *et al.*, 1991; Prata, 1993), and relate the decrease in the transmittance with increasing zenith angle to an increase in the water vapour content of the optical path proportional to the secant of the zenith angle, as in the DA algorithm developed by Prata. It is important to note, however, that the variation with zenith angle of the UWSR, and DWSR in the cases where ε is less than unity, is often included implicitly within retrieval algorithms through the angular variation of specific coefficients (Coll and Caselles, 1994; Coll *et al.*, 1994).

DA algorithms with a more explicit dependence of surface and atmospheric quantities have been developed by Sobrino *et al.* (1996). Using LOWTRAN-7 to model radiative transfer within the atmosphere, they developed coefficients with explicit dependence upon both the surface emissivity and the water vapour content of the atmosphere. The generalized form of their algorithm may be written;

$$T_s = T_n + \Delta T_{atmos} + \Delta T_{emis},\qquad(2.33)$$

where;

$$\Delta T_{atmos} = -\gamma_0 + \gamma_1(T_n - T_f),\qquad(2.34)$$

and;

$$\Delta T_{emis} = \gamma_2(1 - \varepsilon_n) - \gamma_3 \Delta \varepsilon_\theta. \tag{2.35}$$

In (2.33) and (2.34), T_n is the BT measured by the satellite in the nadir viewing direction and T_f the BT in the forward viewing direction of the ATSR sensor. From radiative transfer modelling, Sobrino *et al.* derived the coefficients γ_{0k} and γ_{1k} in (2.34) so as to minimize errors in the surface temperature retrieval. The coefficients γ_k, k=0,,3, are derived via a linear relation to the total vertical column water vapour in the atmosphere, W, given by;

$$\gamma_k = \gamma_{0k} + \gamma_{1k} W, \tag{2.36}$$

Although in their approach Sobrino *et al.* base the coefficients in their algorithm on the water vapour content of the optical path, the increase in W with increasing zenith angle means that increasing W acts as a surrogate for for increasing the zenith angle of the view of the satellite.

The impact of the surface emissivity on the initial BT measurement is described by (2.35), in which ε_n is the emissivity for the nadir view for a given channel, ε_f the emissivity for the forward view, and $\Delta \varepsilon = \varepsilon_n - \varepsilon_f$. The angular variation of the surface emissivity is parameterized *a priori* for the surface type under investigation.

Validation of the Sobrino *et al.* algorithm against ground-truth data showed that it was possible to retrieve LST to with ± 1.5 K. Importantly for the experimental component of the work for this thesis, the Sobrino *et al.* DA formulation begins to provide the freedom to investigate the variability and impact of each individual component of the RTE upon the accuracy of SST/LST retrieval. The results of Sobrino *et al.* suggest that treating the physical quantities comprising the RTE in a more explicit manner may improve the accuracy with which LST may be estimated via remote sensing. The framework of the DA algorithm, however, limits

40

the complexity with which each quantity within the RTE may be described. The use of radiative transfer modelling provides further scope to investigate the angular variation of each individual atmospheric term, while parameterizations of the angular variation of the surface emissivity such as those by Prata (1993) and Sobrino et al. (1996), as well as the measurements made by Takashima and Masuda (1987); Labed and Stoll (1991b); Sobrino and Cuenca (1999); Bower (2001) may aid in the description the impact of the surface terms on LST retrieval for different viewing geometries.

Obtaining independent knowledge of each of the physical quantities comprising the RTE, as mentioned above, permits the possibility of moving beyond a DA framework for the remote sensing of LST, towards a physically-based retrieval scheme based upon measurements from a single TIR channel of a satellite sensor combined with; i) atmospheric terms simulated using a radiative transfer model, and; ii) either modelled or measured values of the surface emissivity appropriate to the land surface viewed by the satellite sensor for a given viewing geometry. With this in mind, the following section discusses the development of single channel approaches to the remote sensing of SST/LST.

2.3.3 Single-Channel Approaches

Approaches to solving the RTE for land and sea surface temperature, such as the SW and DA methods discussed in the previous two sections, were initially adopted as it was necessary to minimize the computational load required to process global data sets during the early stages of satellite remote sensing of LST and SST. Advances in data transmission rates from satellites and computer processing power since that time now provide a greater opportunity to treat components of the radiative transfer equation individually, with the potential for physically-based retrievals to improve upon the accuracy with which LST and SST may be retrieved using empirically-based algorithms (Ma et al., 2002).

Many physically-based methods for the remote sensing of LST and SST have

41

been based on Single-Channel (SC) approaches. Such methods generally account for each of the atmospheric radiative components within the RTE individually, most commonly utilizing a good radiative transfer model with atmospheric profiles acquired by either satellite-based soundings or radiosonde measurements as input (Wan and Dozier, 1996). SC methods of LST and SST estimation may be roughly separated into three categories, although some methods may also utilize elements characteristic of another approach. These categories include; i) correction of the satellite-derived surface BT estimate or the radiance measured at the satellite sensor, based on an estimate of the transmittance obtained from a radiative transfer model, and an estimate of the mean temperature of the atmosphere (Price, 1983; Li and McDonnell, 1988); ii) 'reconstructed clear-column radiances' determined by estimating the individual radiative components through either measurements or via a radiative transfer model. The reconstructed clear-column radiance, which is an estimate of the surface-leaving radiance, may be subsequently converted to an estimate of the BT of the surface via the inverse Planck Function (see Section 2.2.1). (Susskind et al., 1984; Chedin et al., 1985; Ottle and Vidal-Madjar, 1992; Ottle and Stolle, 1993), and; iii) simultaneous retrieval of atmospheric terms, surface temperature and emissivity using sounding instruments (Li and Becker, 1993; Wan and Li, 1997; Ma et al., 2002).

In order to explicitly calculate each of the atmospheric radiative components within the RTE, radiative transfer models may be employed to simulate molecular interactions within layers of the atmosphere based on user-defined profiles of height, pressure, temperature, water vapour and concentrations of different molecular species. Since the inception of satellite remote sensing of sea and land surface temperature, a number of such models have been developed for studies of the impact of atmospheric parameters on the satellite-retrieval of LST and SST including LOWTRAN-6 (Kneizys et al., 1983), LOWTRAN-7 (Kneizys et al., 1988), MOD-TRAN (Berk et al., 1989), and LBLRTM (Clough et al., 1996).

Early SC formulations for estimating SST (Price, 1983; Li and McDonnell,

1988) utilized radiative transfer models, with PTRH profiles as input, to develop a simple formulation for a correction term to either the satellite-derived estimate of surface BT (Price, 1983) or the radiance measured at the satellite sensor (Li and McDonnell, 1988) in a single channel, based on the modelled atmospheric transmittance and an estimate of the mean temperature of the atmosphere. These techniques were able to estimate the SST to within ± 1 K under the assumption that the sea surface was a perfect blackbody.

By estimating each of the radiative components individually, Susskind *et al.* (1984); Chedin *et al.* (1985); Ottle and Vidal-Madjar (1992) and Ottle and Stolle (1993) obtained reconstructed clear column radiances for studies of both land and sea surface temperature. Susskind *et al.* (1984) combined simultaneous atmospheric soundings made by the High Resolution Infrared Sounder-2 (HIRS-2) and Microwave Sounding Unit (MSU) instruments to derive clear-column radiances. From these measurements they were able to estimate monthly averages of SST to within ± 0.5 K. Chedin *et al.* (1985) obtained a climatological SST of similar accuracy. They utilized atmospheric soundings made by the HIRS-2 and MSU instruments and combined these with predefined regression relations between observed radiances and co-located radiosonde measurements to estimate the DWSR, UWSR and atmospheric transmittance. Ottle and Vidal-Madjar (1992) and Ottle and Stolle (1993) obtained clear-column radiances using atmospheric profiles obtained from the NOAA TIROS-N Operational Vertical Sounder (TOVS) instrument as input to the radiative transfer model LOWTRAN-6 in their investigations of atmospheric impacts upon the satellite-retrieval of LST. Their SC approach agreed with results from SW algorithms for LST estimation to within an RMS error of 1.8 K. The more *'physio-statistical'* methods (Chedin *et al.*, 1985) for the simultaneous retrieval of atmospheric terms as well as surface temperature and emissivity employed by Wan and Li (1997) and Ma *et al.* (2002) utilize atmospheric data from the sounding channels of the MODIS instrument or the MODIS Airborne Simulator (MAS), and simulate radiative components using MODTRAN 1.3 in the work of Wan and Li

43

and a new transmittance model developed for the Advanced Microwave Sounding Unit (AMSU) in the work of Ma *et al.*. The algorithm proposed by Wan and Li, and extended by Ma *et al.*, is based upon changes in the physics of radiative transfer between day and nighttime scenarios which permit the separation of the surface emissivity and LST under the premise that the surface emissivity remains constant.

It is important to note that although the radiative components necessary to estimate LST using an SC approach may be accurately determined from radiative transfer models, the accuracy with which they may be modelled depends on the quality of the input information (Ottle and Vidal-Madjar, 1992; Ottle and Stolle, 1993; Li and Becker, 1993; Wan and Li, 1997; Teggi *et al.*, 1998; Ma *et al.*, 2002). For optimal results, work by Ottle and Vidal-Madjar (1992) and Teggi *et al.* (1998) shows that the input data from radiosonde launches should be collected spatially close to the area of interest, and at a time close to any surface measurements. Temperature discontinuities between the surface-air temperature estimate from the radiosonde and the true brightness temperature of the surface may also impact results derived from radiative transfer models (Sidran, 1980; Teggi *et al.*, 1998). A temperature discontinuity at the surface impacts the relative proportions of absorption and emission of the surface-leaving radiance by the boundary layer of the atmosphere and therefore simulations of the radiative components. In their work, Ottle and Vidal-Madjar (1992) found that radiosonde data was preferable to atmospheric information derived from the TOVS instrument for use as input to radiative transfer models over areas of the order of 50×50 km. However, the development in satellite sensors in the last decade does provides scope for more accurate atmospheric information to be derived from sounding instruments such as the AMSU and AIRS (Ma *et al.*, 2002).

In the experimental work for this thesis an SC approach to the estimation of LST is adopted because within the framework of such an algorithm it is possible to investigate the variation with viewing angle of each term within the RTE independently. The angular behaviour of the physical variables comprising the RTE is a focus of

the work which utilizes measurements from an *in situ* infrared scanning radiometer and analyzes these in conjunction with TIR satellite data from the ATSR-2 satellite sensor and atmospheric profile data derived from radiosonde profiles as input to the radiative transfer model LBLRTM. TIR data from the ATSR-2 is valuable in such an investigation because the sensor possesses a dual-look capability which allows the same point on the Earth's surface to be viewed from from two different viewing geometries. The ATSR-2 and it's application to this work are discussed in the following sections.

2.4 The Along Track Scanning Radiometer

2.4.1 History

The first of the Along Track Scanning Radiometer (ATSR) series of instruments was launched aboard the European Space Agency (ESA) ERS-1 satellite on the 17th July 1991. ATSR-1 possessed four channels, 12.0μm, 10.8μm, 3.7μm and 1.6μm, as well as boasting new design features which gave the instrument a stability and sensitivity superior to other operational space-borne sensors at the time such as the Advanced Very High Resolution Radiometer (AVHRR).

The new design features included low-noise infrared detectors, cooled to less than 95 K to minimize noise, continuous two-point onboard calibration of the infrared channels using high accuracy hot and cold blackbody calibration targets and '*along-track*' scanning, utilizing a conical scanning mirror permitting two views of the same point on the Earth's surface from different viewing geometries. The dual-angle capability of the ATSR allows the surface to be viewed along two different path lengths, providing extra information for increasing the accuracy of atmospheric correction. The combination of high radiometric accuracy together with the dual-angle view of the surface is designed to allow the instrument to acquire SST data sets to within the accuracy of ±0.3 K, set for climate change applications (WCRP,

45

1984).

The first ATSR instrument, ATSR-1, was put into hibernation in 1996. The second instrument, ATSR-2, was launched on the 21st April 1995 aboard the ESA ERS-2 satellite. It was designed so as to ensure the continuation of the high-accuracy global SST data set initially acquired by ATSR-1. The ATSR-2 sensor possesses the same design features as its predecessor, but has three additional channels located at 0.55μm, 0.67μm and 0.87μm, included primarily for the remote sensing of vegetation. Calibration of the near infrared and visible channels was enhanced through the addition of an onboard calibration system for these wavebands. The Advanced Along Track Scanning Radiometer (AATSR) is the next generation of ATSR instruments, and was successfully launched on the 1st March 2002. It has the same features as the ATSR-2 and once again, is designed to maintain the continuity of the high-accuracy global SST dataset acquired by the earlier ATSR instruments.

The high accuracy of radiometric data and the dual angle capability of the ATSR-2 are utilized in the experimental component of the work for this thesis described in Chapters 4 and 5.

2.4.2 ATSR-2 Orbital Information

The ERS-2 satellite, which carries the ATSR-2 instrument, possesses a near circular, retrograde, sun-synchronous orbit at an altitude of approximately 780 km. Its orbital period is approximately 100 minutes and the sub-satellite velocity across the Earth's surface is 6.7 kms^{-1}. The south-bound equator-crossing time (descending node) is around 1030 hrs local solar time, and the north-bound equator crossing (ascending node) is at 2230 hrs local solar time. Global coverage may range from the three day repeat cycle to 35 and 168 day cycles for more comprehensive global coverage (Mutlow *et al.*, 1999).

In order to keep the nadir and forward views aligned, the sensor principally operates in '*yaw steering*' mode, whereby it slowly oscillates about its yaw axis in order to compensate for the Earth's rotation during the time lag between the

Feature	Wavelength (μm)	Bandwidth	ATSR-1	ATSR-2/AATSR	Detector Type
Chlorophyll	0.55	20 nm	N	Y	Si
Vegetation Index	0.67	20 nm	N	Y	Si
Vegetation Index	0.87	20 nm	N	Y	Si
Cloud Clearing	1.6	0.3μm	Y	Y	PV InSb
SST retrieval	3.7	0.3μm	Y	Y	PV InSb
SST retrieval	10.8	1.0μm	Y	Y	PC CMT
SST retrieval	12.0	1.0μm	Y	Y	PC CMT

Table 2.2: Spectral channels of the ATSR-1, ATSR-2 and AATSR. Taken from Mutlow *et al.* (1999).

nadir and forward views. This yaw axis compensation is crucial for the accuracy of co-location between the nadir and forward views of the sensor. During optimal operation, the two views may be co-located to with ±1 pixel (Mutlow *et al.*, 1999).

2.4.3 Specifications and Instrument Performance

ATSR-1 possessed only four spectral channels. This has been increased to seven for the ATSR-2 and AATSR, diversifying the range of applications of the sensor. The spectral channels utilized by each sensor are shown in Table 2.2, taken from Mutlow *et al.* (1999).

As the sensor was primarily designed for SST measurement, the TIR and NIR channels may saturate over land. The radiometric data are generally 12 bit, though this is dependent upon the mode of operation.

The data rate from the ATSR-2 is dependent upon the allocation of resources of accompanying instruments. The minimum data rate is 320 kbs^{-1} and the maximum rate may be as high as 680 kbs^{-1}. The telemetry is mainly shared with the Ac-

tive Microwave Instrument (AMI). The AMI acquires substantially more data over ocean than over land. This complements the ATSR-2 which ideally requires greater resources over land since this is when the visible channels are most useful. At night, the telemetry is dedicated to the thermal channels.

Pre-launch sensitivity checks of the ATSR-2's onboard blackbodies for TIR calibration were made against external reference targets and showed agreement to within 10 mK. The cooler maintains the instrument at a temperature of 81 ± 1 K with very little variation over the orbital cycle. The high level of sensitivity of the instrument, and the low operating temperature allow the noise equivalent error in temperature (NEΔT) measurement to be kept low. When viewing a scene where the surface temperature is 270K the NEΔTs in the 3.7μm, 11μm and 12μm channels are 50, 21 and 25 mK respectively. These values slightly increase as the surface temperature increases as shown in Table 2.3, which compares the instrument performance of ATSR-1 and ATSR-2. The table shows that the ATSR-2 is calibrated to high accuracy and stable, and is superior to the earlier sensor. Figure 4.10a in Section 4.2.2 shows the response function for the 11 and 12 μm channels of ATSR-2.

In general ATSR-2 has performed to its specifications. However, some '*scan-jitter*' due to small deviations in the scan rate of the sensor have been noted. Irregularities in the scan mirror lock have caused some data in forward scenes to '*slip*', but this affects no more than 1% of the ATSR-2 data set and ground processing of the data may detect and flag any occurrences of data misregistration. These quality control procedures ensure that the nadir and forward view data used in this work is well geolocated and co-located.

2.4.4 Viewing Geometry and Geolocation

The ATSR is a scanning radiometer that scans across-track, as do other instruments such as AVHRR, but its defining feature is its ability to scan along-track in its direction of motion. It is this unique feature of the ATSR series of instruments which makes the ATSR-2 data useful for the research applications described later in this

Variable	Parameter	ATSR-1	ATSR-2
Cooler Temperature	Long term variation	90–110K	81 ±1K (1995–1999)
	Orbital variation	±1K	±0.1K
NEΔT (at 300K)	11.0 μm	60mK (March 1995)	46mK (March 1995)
	12.0 μm	130mK (March1995)	36mK (March 1995)
FOV	11.0 & 12.0 μm	Some non-uniformity	Some non-uniformity but better than ATSR-1 Better co-aligned than ATSR-1
	1.6 & 3.7 μm	Fairly Uniform	All very uniform Better co-aligned than ATSR-1
	0.55, 0.67 & 0.87 μm	N/A	Very uniform

Table 2.3: Extract from the ATSR1/2 User Guide (Mutlow *et al.*, 1999) which compares the performance of ATSR-1 and ATSR-2

thesis (Chapters 4 and 5).

The viewing geometry of the ATSR instruments is shown in Figure 2.1. Across-track, the conical scanning mirror captures two 500 km wide swaths, one at the nadir view, typically in the zenith angle range 0–20°, and the other at the forward view at a zenith angle of approximately 55°. The radiance measurement for each pixel is integrated over the 75μs time period for which the instrument views each pixel during the scan. There is a temporal lag of approximately 150 s between the nadir and forward swaths. The viewing geometry is such that although both swaths

cover 500 km across the Earth's surface, the nadir swath contains 555 pixels and the forward only 371. Consequently, the pixels in the forward scan are larger than those in the nadir scan. At the sub-satellite point, for the nadir scan, the instantaneous field of view (IFOV) of the ATSR-2 is 1km×1km, while for the forward swath, the IFOV at the sub-satellite point is 1.5km×2.5km. The dimension and orientation of the pixels from the two scans are shown in Figures 2.2a and b, adapted from Prata *et al.* (1990). In Figure 2.2b, pixel 500 is the pixel at the sub-satellite point of the nadir scan. Close to the sub-satellite point, for sequential nadir scans, in the along-track direction, the pixels fit closely together and are undistorted. In the cross-track

ATSR-1/2 Viewing Geometry
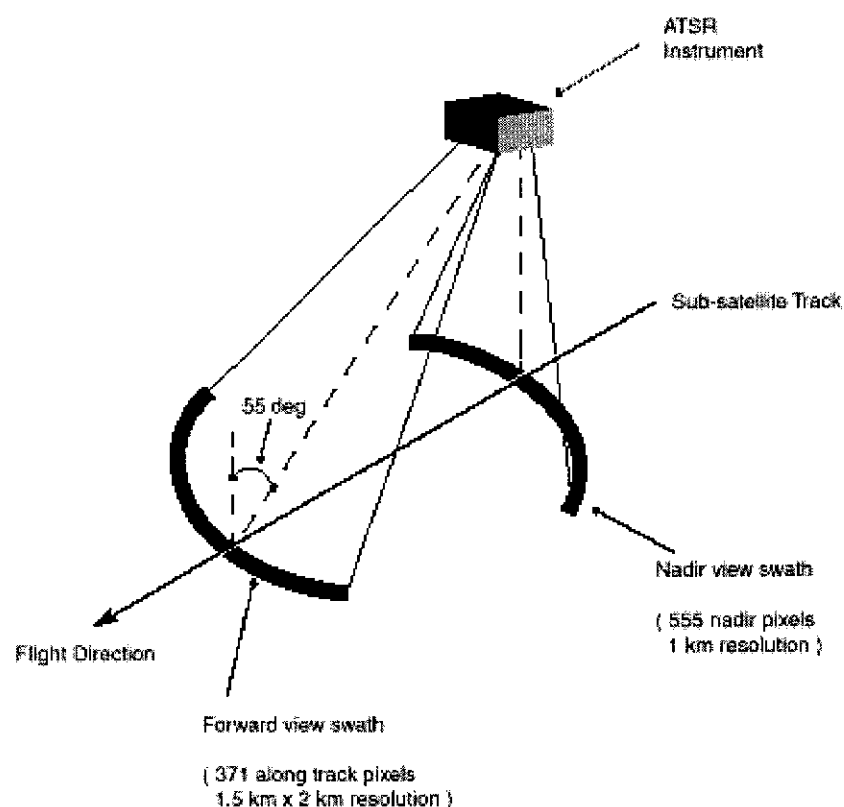
Figure 2.1: Viewing geometry of the ATSR series of sensors. The nadir and forward swaths both cover the same distance across the Earth's surface. The forward swath contains fewer pixels and they are of larger area than for the nadir case. Taken from Mutlow *et al.* (1999).

50

direction, pixels narrowly overlap and are slightly elongated. For the forward view, pixel 1501, at the sub-satellite point, is significantly elongated in the along-track direction, and broadened in the across-track direction. Figure 2.2b shows that in the forward viewing direction, pixels are slightly elongated and narrowly overlap in the along-track direction near the sub-satellite point. In the across-track direction the pixels are broadened, there is overlap between adjacent pixels, and also some offset between adjacent across-track pixels in the along-track direction. The same effects are evident in the forward view geometry for pixels at extreme zenith angles, though each is more pronounced than for the near sub-satellite point case.

Though there is overlap between pixels in both the nadir and forward viewing geometries, and the FOV of the sensor increases with zenith angle, the geolocation process remaps all pixels into a $1km \times 1km$ grid. Mapping pixels of area larger than $1km^2$ to this spatial resolution causes unfilled pixels in the geolocated image, which are filled using a nearest neighbour approach. The process geolocates the data to an accuracy of ± 1 pixels when the navigation systems of the satellite are fully functional (Mutlow et al., 1999). The yaw steering mode of the satellite is critical to obtaining optimum geolocation/co-location, which may be degraded when this mode is not in use. For the ATSR-2 sensor, periods when the geolocation/co-location of the sensor is below optimum are noted in updates on the status of the sensor on the ATSR homepage (ATSR Homepage, 2002). There were found to be no problems with the geolocation/co-location of the sensor over the period in 2000 from which ATSR-2 data were used in the experimental component of this thesis.

2.4.5 Instrument Applications

The ATSR series of satellite sensors are highly calibrated and possess a unique dual-angle viewing capacity which allows the same point of the Earth's surface to be observed at two different zenith angles. The primary application of these instruments is to measure SST for ongoing climate monitoring (Mutlow et al., 1994). Other applications include studies of sea ice, volcanoes, clouds, vegetation and land surface

temperature (Prata, 1993). It is in this latter capacity that this research utilizes TIR data from the ATSR-2.

The information obtained through the ATSR-2's dual-angle view is applied in this research with the aim of extending the understanding of the physical process described by the RTE. In particular, the research focuses on investigating the change with zenith angle of the magnitude of the radiance emanating from the land surface and relating it to the change in the value of the individual physical variables comprising the RTE (see Sections 2.2.1–2.2.3).

The review of the literature presented in the current chapter began by summarizing radiative transfer in the TIR, and developing the RTE to describe the propagation of TIR radiation from the surface of the Earth to; i) a ground-based sensor, and; ii) a satellite-based sensor. The state of the science concerning the definition, measurement and modelling of the physical variables fundamental to the remote sensing of LST was then described. In summary, the remote sensing of LST/SST is made complex by the coupling of the surface temperature and emissivity in the surface emission term of the RTE. In order to accurately measure LST/SST remotely it is then necessary to have an accurate estimate of the surface emissivity. This fact makes achieving the global remote sensing of LST to within 1 K a difficult task, as the surface emissivity may vary between 0.85 and 0.99 depending on land surface characteristics (see Table 2.1 from Section 2.2.2.2. Further complexity is added to the problem when the effects of the atmosphere upon the surface-leaving radiance are considered. The surface-leaving radiance is attenuated by the atmosphere, and also contaminated by components of the UWSR and DWSR by the time it reaches the the satellite sensor.

The discussion was then extended to incorporate the knowledge of the physical variables comprising the RTE into an overview of methodologies for the measurement of LST/SST from satellite-based sensors. The SW approach, developed by McMillin (1975), was the first operational algorithm for remote sensing of SST. Utilizing measurements at two different wavelengths, McMillin developed regres-

sion equations that allowed calculation of a correction term which could be applied to one of the SST estimates so as to account for atmospheric effects. In early remote sensing of SST, the sea surface was assumed to be a perfect blackbody. Later versions of the SW approach became more complex as the surface emissivity was included, and the accuracy with which SST could be retrieved on a global scale was increased to between 0.5–0.7 K by such modifications. At the same time, global LST could only be retrieved to within 3 K because of the variability of the land surface.

McMillin also suggested the possibility of using two views of the sea surface at different zenith angles, rather than different wavelengths, to remotely measure SST via satellite. Such a technique only became feasible, however, during the last decade, with the launch of the ATSR series of instruments. The DA algorithms developed for use with data from the ATSR instruments were also, for the most part, regression-based. This meant that surface emissivity and atmospheric effects were included implicitly, within the majority of algorithms for the retrieval of LST and SST, through the regression-derived coefficients in a retrieval equation. More recent DA algorithms developed by Sobrino et $al.$ (1996) began to include surface emissivity and atmospheric terms more explicitly in their formulations, permitting greater investigation of the impact of each individual term within the RTE on the accuracy of LST/SST retrieval. In their work Sobrino et $al.$ report retrieving LST to within ± 1.5 K. The most scope for the investigation of the individual terms of the RTE is, however, permitted by SC methods of satellite remote sensing. Under an SC approach, each individual component of the RTE may be estimated independently and included together within a description of the RTE in order to reconstruct clear-column radiances. Such radiances may then be related to the LST/SST via the inverse Planck Function. In contrast to SW and DA algorithms, an SC approach allows the variation with zenith angle of each individual component of the RTE to be addressed explicitly. Because most remotely sensed LST data is acquired by scanning instruments, which may utilize zenith angles of up to 60°, the variation of

the surface and atmospheric terms within the RTE with zenith angle is important in the understanding of the surface-atmosphere interactions described by the RTE.

Through the analysis of ATSR-2-derived LST data, in combination with coincident multi-angle *in situ* measurements in the TIR made by a ground-based scanning radiometer, and modelling of radiative transfer within the atmosphere using an atmospheric transmittance model, it is possible to separate the zenith angle variation of the at-sensor radiance into atmospheric and surface components. The surface-emitted component of the at-sensor radiance may then be calculated through the RTE and subsequently used to accurately estimate the LST via the inverse Planck Function.

Primarily, the experimental work for this thesis, described in the following chapters, will focus on accurately estimating the surface-emitted component of the radiance measured at the sensor, at multiple zenith angles, with emphasis on the impact of; i) the radiative components of the atmosphere in Chapter 4, and; ii) the surface spectral emissivity and LST in Chapter 5.

In line with these investigations, the objectives of this research are then to; i) develop a better theoretical understanding of the radiative interactions between the surface and the atmosphere, ii) apply this knowledge of the fundamental physical principles which govern surface-atmosphere interaction to the development of a methodology for deriving an LST product suitable for the validation of satellite-based retrieval of LST, to a level of accuracy approaching 1K, and; iii) the derivation of a set of physically-based algorithms for the satellite retrieval of LST.
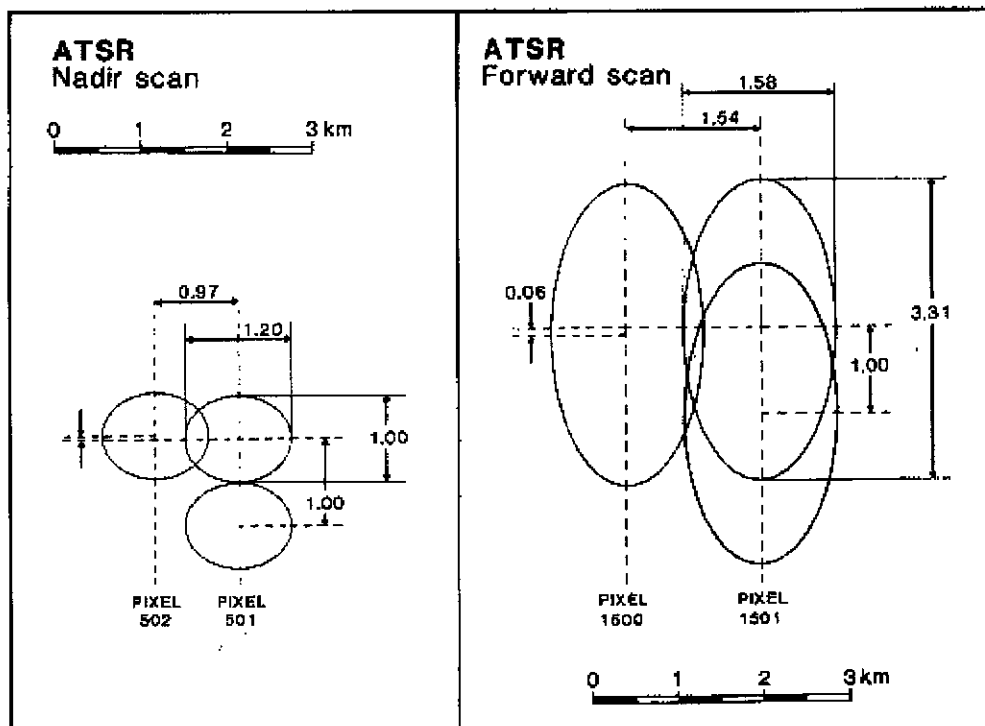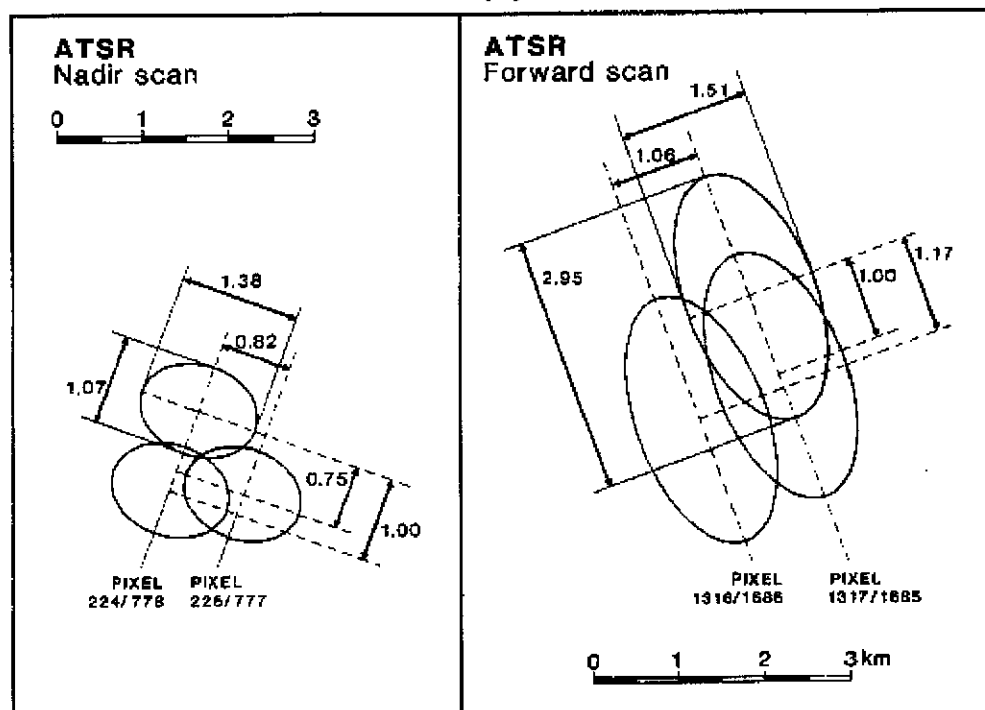
Figure 2.2: Dimensions and geolocation of pixels from the nadir and forward swaths of the ATSR. Taken from Prata *et al.* (1990)

Chapter 3

CIGSN Field Sites

3.1 Overview of Field Sites

CSIRO Atmospheric Research (CAR) has established a number of field sites within Australia for the purposes of calibration and validation (CAL/VAL) of current and proposed satellites, with the ultimate aim of improving the performance of Global Climate Models (GCMs) (Prata *et al.*, 1997, 1998). The LST component of such CAL/VAL experiments deals with the TIR emission from the Earth's surface, with particular applications to polar-orbiting satellite sensors such as MODIS (Wan, 1999), ATSR-2 and AATSR (Prata, 1993; Sobrino *et al.*, 1996), AVHRR-2 (Becker and Li, 1995; Prata *et al.*, 1995; Coll and Caselles, 1997), and has implications geostationary satellite-sensors such as the Visible and Infrared Spin Scan Radiometer (VISSR) aboard Geostationary Meteorological Satellite-5 (GMS-5) (Prata and Cechet, 1999) and the Geostationary Operational Environmental Satellite (GOES). (Minnis and Khaiyer, 2000).

Physical criteria for selection of field sites are that they must be flat, be relatively uniform at the scale of view of the satellite (≈ 1 km^2), so that it is feasible to relate *in situ* measurements to satellite observations. Ideally, the sites should also possess a high probability of clear skies. There are also logistical criteria which cover aspects such as access to the sites, power, communications and budgetary constraints.

In order to establish the next generation of global LST algorithms it is necessary to validate results over the range of climatologies which can be expected, with high quality *in situ* radiometric measurements. The Continental Integrated Ground Truth Site Network (CIGSN) sites in drier areas such as Hay in New South Wales (Uardry) and the Alice Springs site in the Northern Territory (Amburla) have been operating for a number of years. However, CAL/VAL data in more humid regions, in which the precipitable water (PW) in the atmosphere is often greater than 3 cm, are scarce. For this reason, the Thangoo site near Broome, in the Kimberley region of Western Australia, was chosen to compliment the sites already established in the drier areas. Thangoo is situated in a sub-tropical region, and is generally humid all year round, but especially during the wet season from October-April.

The CIGSN sites are instrumented with a CAR custom-built data acquisition, logging and transmission system. They are instrumented to measure LST, surface albedo, and long and short wave irradiance and exitance. Of particular interest to the experimental work in this thesis are the sites at Amburla and Thangoo stations, which have also been instrumented with scanning radiometers, with the aim of investigating the angular distribution of surface brightness temperatures. When combined with knowledge of the surface emissivity, which may also be derived from field measurements, and its variation with viewing angle, the directional LST distribution may also be obtained. These measurements have direct applications to the validation of LST retrieval algorithms for scanning satellite sensors such as MODIS, ATSR-2/AATSR and AVHRR-2.

Characterizing the surface-atmosphere interaction is a major part of validation of satellite-derived LST. The Amburla and Thangoo field sites represent considerably different climatic regimes, and accordingly, also possess different surface characteristics. Investigations of the relationship between LST at the scale of view of the ground-based scanning radiometer and the satellite for these two different scenarios, may provide useful information that will benefit future global LST measurements, and aid in realizing the goal of 1K accuracy for global LST datasets

(Wan, 1999).

3.2 Amburla Station

Amburla Station (23.39°S, 133.12°E, 620 m elevation) is located approximately 100 km WNW of Alice Springs in the Northern Territory. The area of the field site is roughly 12km×30km. Figure 3.1 shows the location of the site in an image acquired from the ATSR-2 during a descending overpass on the 6 June 2000. The image is produced using IDL code developed by Dr. A.J. Prata, based upon the SADIST-2 processing code (Bailey, 1995). The field site is marked in the image by the white cross. The location of the field site within Australia is shown in Figure 3.1b. Figure 3.1c shows the relative position of the forward and nadir scans of the ATSR-2, and the solar position (represented by the two black regions) at the time of the scans.

Table 3.1 shows monthly averages of climate data, which characterize the climate of the central Australian region. The region is hot during the day in summer, and mild in winter, and is particularly dry all year round. What little rain does fall is spread consistently throughout the year. As a consequence of the arid climate, there is very little vegetation, mainly Mitchell grass, which is fairly evenly distributed over the surface, and reaches no more than 20cm in height. The field site itself is flat and quite uniform (Prata and Cechet, 1999), but there are ranges of hills in the surrounding area, which can be made out in Figure 3.1. Over geological timescales these have contributed to the soils characteristic of the area which are generally sandy and iron-rich, with a high quartz content (Northcote and Wright, 1983).

Figure 3.2 shows a characteristic view of the Amburla field site from late August of 2000. Even at the end of winter, the grassy vegetation appears very dry. The scanning radiometer installation can be seen in the figure. It is comprised of a TASCO radiometer, housed in PVC piping at the top of the pole. It is powered by the attached solar panel, and transmits data back to the central site a few hundred metres away. The TASCO radiometer and other instrumentation at the site is described in

	Jan	Feb	Mar	Apr	May	Jun	Jul	Aug	Sep	Oct	Nov	Dec
Mean daily max temp ($^\circ$C)	36.2	34.9	32.6	27.9	22.9	19.8	19.5	22.4	26.9	30.8	33.6	35.4
Mean daily min temp ($^\circ$C)	21.3	20.7	17.5	12.6	8.4	5.3	4.1	6.1	10.2	14.8	17.8	20.2
Mean 9am rel. hum. (%)	34	39	40	45	57	65	60	47	35	31	30	30
Mean 3pm rel. hum. (%)	21	25	23	26	33	35	31	25	20	20	19	20
Mean monthly rain (mm)	35.1	44.4	32.0	18.5	19.8	14.6	14.5	10.4	9.0	21.6	24.7	36.6
Mean no. of clear days	13.7	12.4	17.3	16.8	15.7	16.9	21.3	22.7	21.2	18.2	14.0	13.7
Max wind gust (km hr^{-1})	121	122	104	78	121	95	91	97	100	104	174	131

Table 3.1: Monthly climatological data for Alice Springs, derived from daily radiosonde data. Extracted from the Bureau of Meteorology website (Bureau of Meteorology, 2001).

more detail in Section 5.1.

Figure 3.3 shows the variation in PW in the atmosphere between June and September in 2000, derived from daily radiosonde profiles acquired at Alice Springs airport. The maximum value of the PW in the data is approximately 2 cm. This shows that the atmosphere is particularly dry, and that the climatic regime is vastly different to the Thangoo field site region (see Figures 3.7 and 3.8a,b in Section 3.3). Because the atmosphere is so dry the atmospheric transmittance is much greater, and the UWSR and DWSR from the atmosphere are much smaller than for the humid conditions typical of the Thangoo field site.

The characteristic atmospheric transmittance for the Amburla site, over the same period as the PW data in Figure 3.3, for which there is coincident ATSR-2 data, is shown in Figure 3.4a. The atmospheric transmittance, calculated via the Line By Line Radiative Transfer Model (LBLRTM) (Clough et al., 1996) using radiosonde profile data from Alice Springs airport is plotted for both the nadir view of the ATSR-2. The data show that even for the forward view (an observation zenith angle $\approx 55^\circ$) of the satellite, the transmittance rarely ranges below 0.9. The large decrease in the atmospheric transmittance, evident around Julian day 196 and 199 is due to the influence of cloud and is a relatively rare occurrence at the Amburla site.

ATSR-2 over AUSTRALIA
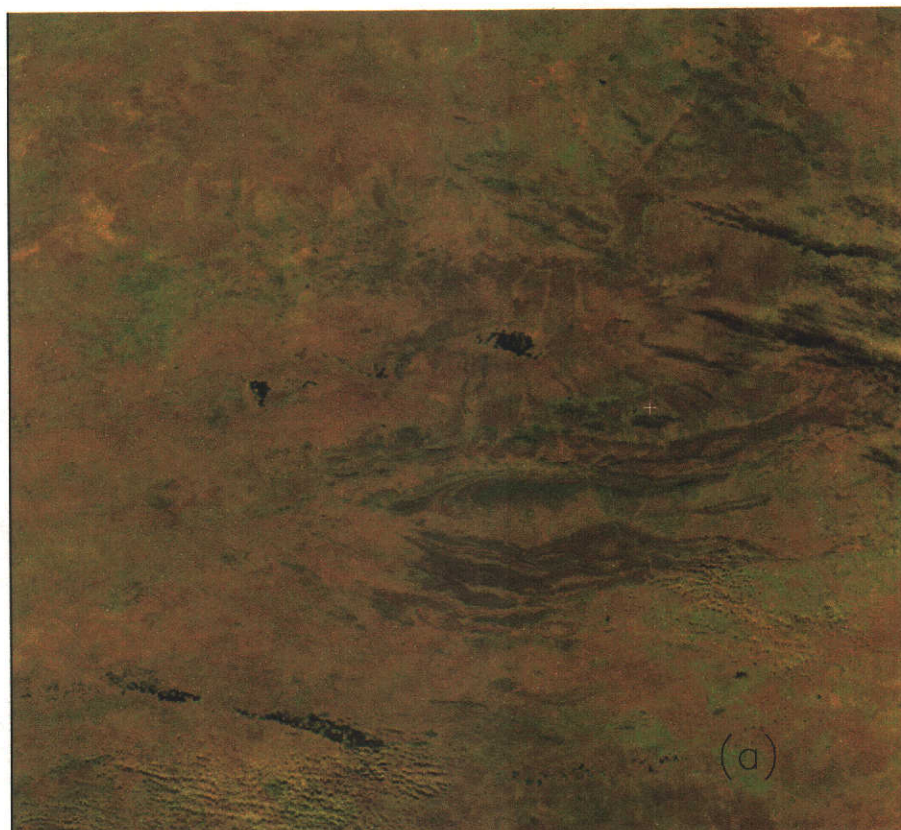
The Image: Amburla, NT (Day)

Product name:0024_D-0006060030-22650-000813-2av321.GBT-TVLXC
Acquisition time:06-JUN-2000 01:26:20.041
Latitudes: -24.96   -25.99   -20.47   -21.50
Longitudes:129.05   133.99   130.24   135.03
Channel assignments: Red: 1.60 μm [0 : 9000] Green: 0.87 μm [0 : 7000] Blue: 0.67 μm [0 :18000]

CSIRO DIVISION OF ATMOSPHERIC RESEARCH   Acknowledgements; Data courtesy ESA; processed by RAL, UK.
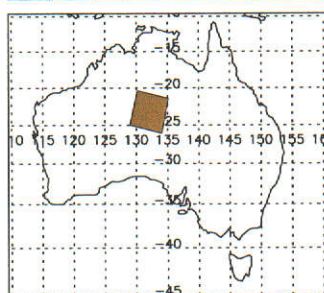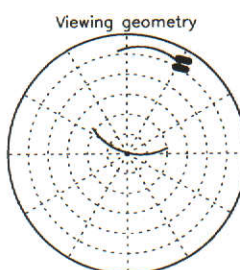
(b)   (c)

Figure 3.1: a) Image of the Central Australia region acquired from a descending pass of the ATSR-2 at approximately 1030 hrs local time. The location of the Amburla field site is represented in the image by the white cross. b) Location of the field site within Australia. c) Polar plot showing viewing geometry of the satellite and the solar geometry.

60

Figure 3.2: Photograph of the Amburla field site in late August of 2000 showing typical land surface cover. The scanning radiometer installation is visible in the background.
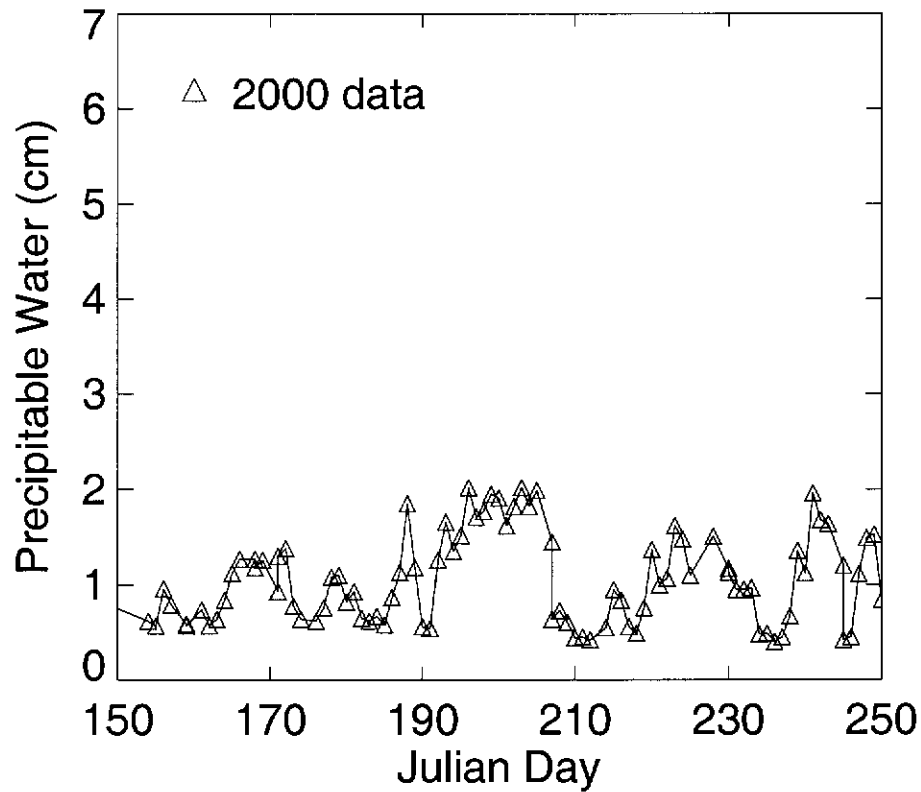
Figure 3.3: Plot of precipitable water over Amburla during 2000 derived from daily radiosonde data.

Figure 3.4b shows the DWSR over the same period as in Figure 3.4a (note, Figure 3.4b is also representative of the UWSR because it is generally only a few percent larger than the downwelling).

Figure 3.4b shows that, at the Amburla field site, the atmosphere is typically dry. The contributions from the atmosphere to the at-sensor radiance measured by a radiometer are therefore small and the surface-leaving radiance comprises the bulk of the measured signal. In contrast, for more humid climates, such as that which is characteristic of the Thangoo field site, the atmospheric emitted contributions are much larger and often approach the magnitude of the surface-leaving radiance. It is the varying proportions of the radiance contributions from the surface and atmo-
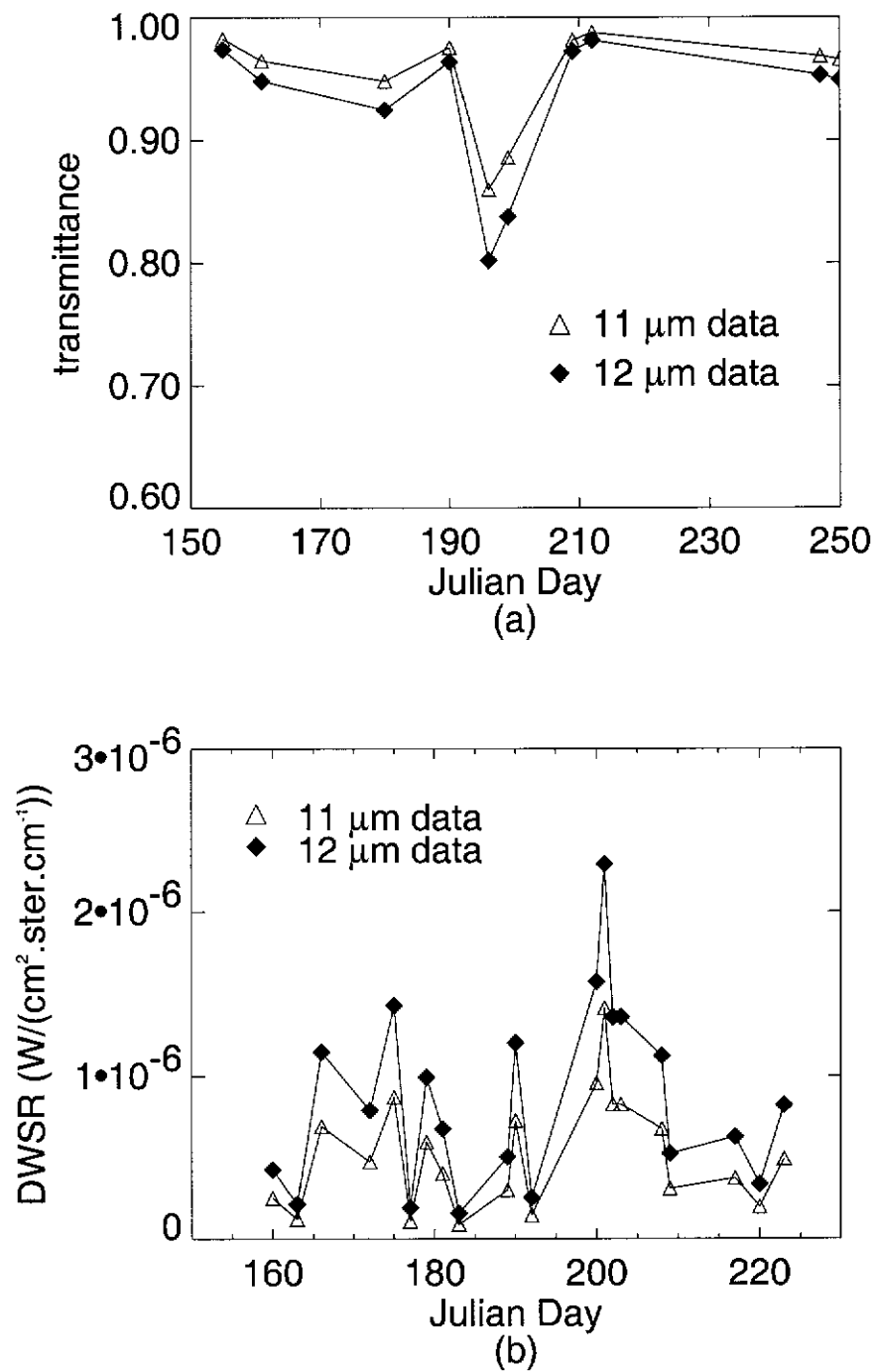
Figure 3.4: Simulated band-averaged transmittance data for the 11 and 12μm channels of the ATSR-2 for days in June-September of 1998 for which there are coincident ATSR-2 and radiosonde data. a) transmittance values for the 11 and 12μm channels of the ATSR-2. The transmittance for both the nadir and forward views of the satellite overpass are plotted. b) DWSR values for the same days and channels as in (a), but for the vertical only.

sphere that the process of atmospheric correction must be able to account for, in order to measure LST with high accuracy. When variability in the surface emissivity is also considered the full range of surface-atmosphere interactions as described by the RTE are then involved in the complex problem of accurately estimating LST remotely.

At the Amburla field site, both satellite and *in situ* data have been acquired for analysis in the experimental component of this thesis. These datasets are complimentary in nature, and when combined, provide some interesting insights into the interaction between the land surface and the atmosphere.

Importantly for the analysis of satellite-derived and *in situ* measurements described later in Chapters 4 and 5, although the climate averages for Alice Springs from Table 3.1 show that rainfall may be expected to be low throughout the year in Central Australia, in October, November and December rainfall was particularly high and there were an unusually high number of wet days. Rainfall for each month totalled between 50 and 200 mm (Bureau of Meteorology, Northern Territory, 2001). This should be noted for future reference, as rainfall may impact the analysis of data from the field site, and potentially cause the results derived for these months in this work to be unrepresentative of the usually dry conditions at these times of the year.

3.3   Thangoo Station

Thangoo Station (122.354° E, 18.181° S, 10m elevation) is located approximately 40 km, by line-of-sight, south east of Broome in the Kimberley region of Western Australia. It is primarily a cattle station and stretches 30 km inland from the coast, where it borders onto Roebuck Bay, and 70 km north-south, beginning some 30 km south of Broome. The total area of the station is of the order of 500 000 acres, though the uniform target area identified by Prata *et al.* (1998) is only 10km × 10km, and is located about five km from the coast, inland of the tidal plain. Figure

3.5a shows an image of part of the Kimberley region of Western Australia acquired from a descending pass of the ATSR-2 about 1030 hrs local time on the 15 July 1998. The image is produced using IDL code developed by Dr. A.J. Prata, based upon the SADIST-2 processing code (Bailey, 1995). The location of the Thangoo field site is marked by a white cross in the image. The location of the field site within Australia is shown in Figure 3.5b. Figure 3.5c shows the relative position of the forward and nadir scans of the ATSR-2, and the solar position (represented by the two black regions) at the time of the scans.

Roebuck plain, on which the station is situated, is low-lying (0–10 m elevation), and due to the large tidal range of the area, the vegetation ranges from mangrove swamps and grassy plains nearer to the coast, to the characteristic acacia (wattle) a few kilometers further inland. The acacia (up to 5m in height) shown in Figure (3.6) is the dominant vegetation in the area of the field site. The soil in the area is characterized by red-coloured siliceous sandy soil, with areas of darker calcareous soils closer to the coastal fringe (Northcote and Wright, 1983).

Climatological data, derived from daily radiosondes released from Broome airport, taken from (Prata *et al.*, 1998), are given in Table 3.2. The data show that the majority of rainfall occurs during the period from December to March, but that from May to October there are between 15 and 22 clear days per month which are suitable for remote sensing applications. The humidity is noticeably high, particularly during the wet season. Figure 3.7 shows that the PW in the atmosphere during the period November to April is frequently between 5 and 6 cm. The figure shows PW data from the second half of 1998 and the first half of 1999 derived from radiosonde profiles and plotted against the Julian day of the year. Significant variation in PW loading on a daily basis is evident, and the transition between the wet and dry seasons is particularly clear. The combination of high moisture levels and warm temperatures in this type of climate makes remote sensing of LST difficult, particularly at extreme zenith angles, because of the proportions of surface and atmosphere-emitted radiance comprising the signal measured by the satellite

ATSR-2 over AUSTRALIA
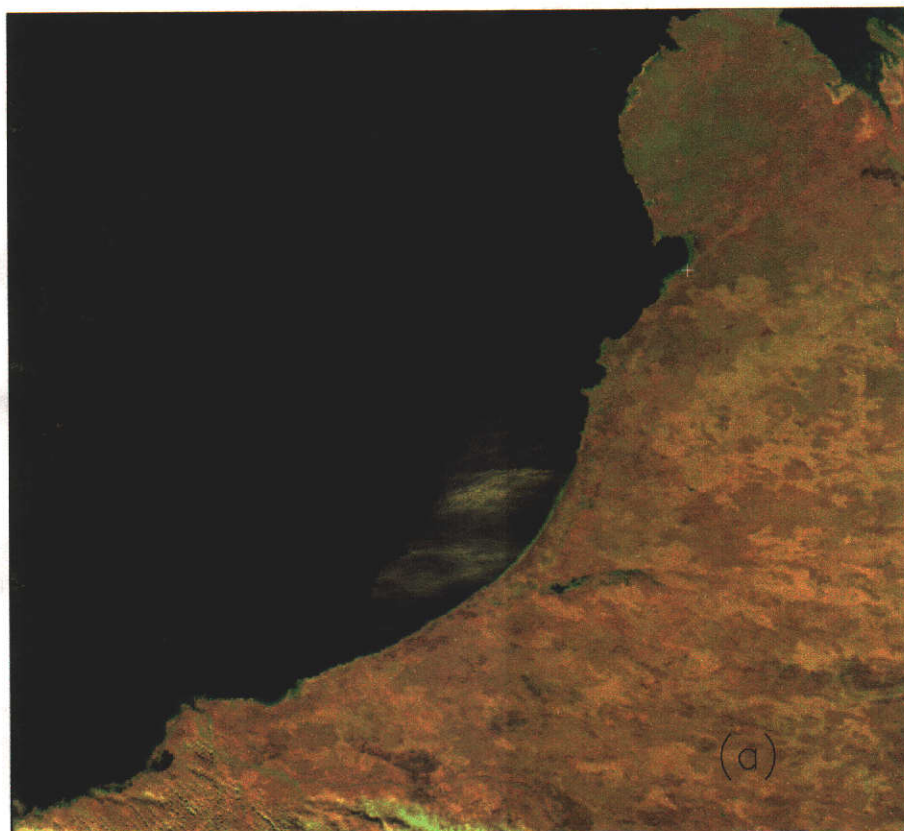
The Image: Thangoo, WA (Day)

Product name:9813_D-9807150119-22139-9B0807-2av302.GBT-TVLXC
Acquisition time:15-JUL-1998 02:13:54.643
Latitudes: -20.47   -21.50   -15.98   -16.99
Longitudes:118.03   122.82   119.16   123.83
Channel assignments: Red: 1.60 μm [0 : 9000] Green: 0.87 μm [0 : 7000] Blue: 0.67 μm [0 :18000]

CSIRO DIVISION OF ATMOSPHERIC RESEARCH   Acknowledgements: Data courtesy ESA; processed by RAL, UK.

Viewing geometry
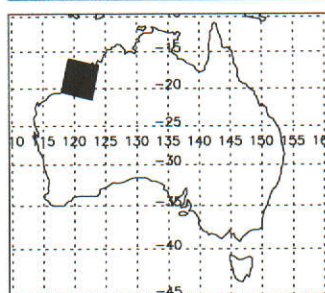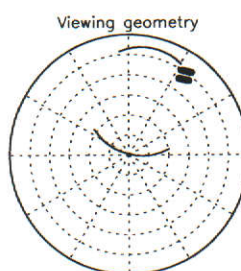
(b)   (c)

Figure 3.5: a) Image of the Broome region acquired from a descending pass of the ATSR-2 at approximately 1030 hrs local time. The location of the Thangoo field site is represented in the image by the white cross. b) Location of the field site within Australia. c) Polar plot showing viewing geometry of the satellite and the solar geometry.

	Jan	Feb	Mar	Apr	May	Jun	Jul	Aug	Sep	Oct	Nov	Dec
Mean daily max temp (°C)	33.4	33.0	34.0	34.3	31.5	29.1	28.7	30.2	31.8	32.9	33.6	33.9
Mean daily min temp (°C)	26.2	26.0	25.4	22.5	18.3	15.3	13.6	15.0	18.4	22.2	25.0	26.4
Mean 9am rel. hum. (%)	70	73	69	55	48	48	46	44	48	53	57	64
Mean 3pm rel. hum. (%)	65	66	58	43	38	36	33	33	42	52	56	61
Mean monthly rain (mm)	177.7	166.0	89.0	23.0	31.0	18.3	4.3	1.7	1.5	1.4	8.4	46.6
Mean no. of clear days	3.6	3.1	8.1	13.5	15.3	18.1	20.2	21.5	20.2	18.5	14.5	7.8
Max wind gust (km hr^{-1})	141	161	147	100	71	85	68	87	71	82	85	134

Table 3.2: Monthly climatological data for Broome, derived from daily radiosonde data. Taken from (Prata et al., 1998)

sensor. The atmosphere-emitted radiance in this region is often of the same magnitude as the surface-emitted signal, and at off-nadir viewing angles, the atmospheric component of the signal may be larger than the contribution from surface.

The atmospheric water vapour is the source of atmosphere-emitted TIR radiance, and is largely responsible for the attenuation of the surface-emitted signal. Figure 3.8a shows simulated band-averaged transmittance values for the 11 and 12μm channels of the ATSR-2 for days between June and December in 1998 where there is coincident radiosonde data. The transmittance values were derived using the Line By Line Radiative Transfer Model (LBLRTM) (Clough et al., 1996), using radiosonde data from Broome airport as input. The spectral transmittance data derived from LBLRTM were averaged over the response function of the appropriate channel of the ATSR-2 satellite sensor in order to calculate the band-averaged transmittance for each channel.

Figure 3.8b shows simulated DWSR for the same dates as in Figure 3.8a. Comparison of Figures 3.8a and b with the PW data shown in Figure 3.7 shows that the atmosphere-emitted TIR radiance is proportional to the PW loading in the atmosphere, and that the transmittance is inversely proportional. The variability in the data shown by Figures 3.7, and 3.8a,b suggest that for remote sensing of LST in subtropical conditions, atmospheric correction data (eg radiosonde profiles) need to

be collected regularly, at least on a daily basis.

3.3.1 Environmental Impacts

Although field sites such as Thangoo are capable of producing much needed validation data for remote sensing of LST in tropical and sub tropical regions, the environment is harsh upon instrumentation. The high humidity, and often torrential rain, is detrimental to the electronics which acquire, log and transmit *in situ* data. As well, the fire regime of northern Australia is such that bushfires burn on vast scales through the region during the dry season. During November of 1999 Thangoo station was ravaged by fire, and the homestead itself was in danger of being destroyed. Cyclone activity is also common off the Kimberley coast. In March 2000 cyclone Rosita crossed the coast at Thangoo station, destroying a nearby holiday resort and causing damage to Broome itself, as well as to the field site installation at the station. Due to these unforeseen acts of nature, little *in situ* data has been collected from Thangoo station to this time. This is disappointing from the perspective of validation of LST. However, there is the prospect that datasets covering the regeneration of the site, and the spectral contrasts observed due to the burning and change in land cover could prove to be of interest to other studies in the future. In the experimental work for this thesis, however, analysis of data from the Thangoo site is limited to remotely sensed data acquired by the ATSR-2 satellite sensor, without the complimentary *in situ* data obtained from scanning radiometer measurements as for the Amburla field site.

Figure 3.6: One of the scanning TASCO radiometer installations at the Thangoo field site, erected amongst characteristic vegetation for the site.
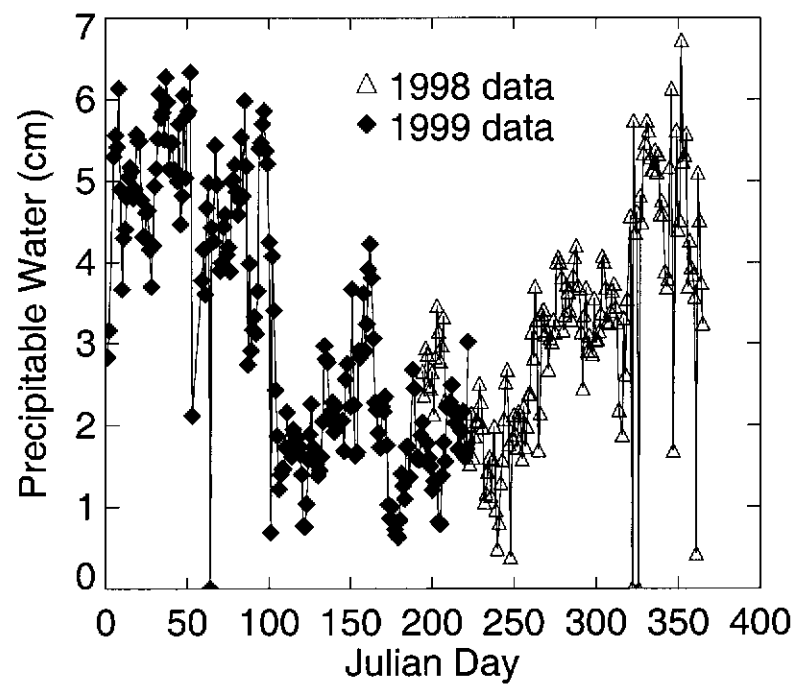
Figure 3.7: Plot of precipitable water over Broome during 1998 and 1999 derived from daily radiosonde data.
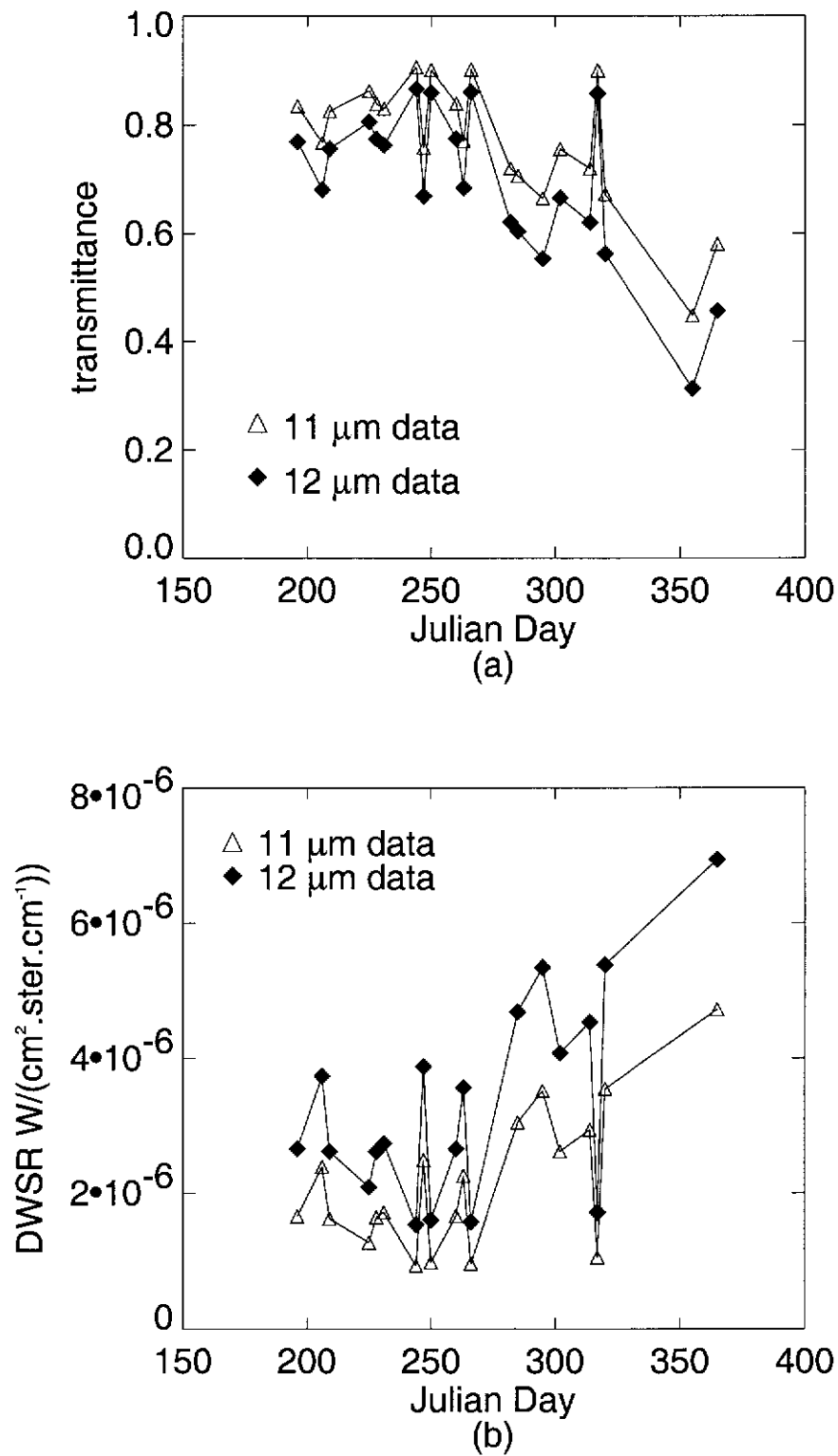
Figure 3.8: a) Band-averaged transmittance values for the 11 and 12μm channels of the ATSR-2 for days in June-December of 1998 for which there are coincident ATSR-2 and radiosonde data. b) Band-averaged downwelling sky radiance (W/cm^2.ster.cm^{-1}) for the same days and channels as in a).

Chapter 4

Surface-Atmosphere Interaction

For the next generation of global LST products, the desired accuracy is ± 1 K (Wan, 1999). Currently, one of the best estimates of the Surface Brightness Temperature (SBT) of the Earth may be obtained to an accuracy of ± 0.05 K by the ATSR-2 satellite sensor (Mutlow *et al.*, 1999). Although SBT and LST are different physical quantities, LST may be calculated from the SBT by emissivity and atmospherically correcting satellite-derived SBT data. Both these quantities limit the accuracy with which LST may be estimated from space. A key challenge for remote sensing of LST is then to define the magnitude of the atmospheric correction term accurately enough to achieve 1 K accuracy for global satellite-retrieval of LST. The current chapter describes a single channel approach (Section 2.3.3) to LST estimation utilizing TIR data acquired by the ATSR-2 satellite sensor over two LST validation field sites in different parts of Australia. The approach is based upon modelling radiative transfer between the land surface and the satellite sensor in terms of three key radiative components; i) the DWSR; ii) the UWSR, and; iii) the atmospheric transmittance, using a line-by-line radiative transfer model. From the modelling work, linear relationships between the magnitude of the atmospheric correction term and; i) the surface emissivity, and; ii) the SBT are demonstrated. Given knowledge of the atmospheric state and the surface emissivity appropriate to the satellite view of the land surface, the magnitude of the atmospheric correction term may be predicted .

4.1 Satellite-Derived Surface Brightness Temperature

The ATSR-2 acquires TIR data in the 11μm (channel 4) and 12μm (channel 5) regions of the electromagnetic spectrum. The response functions for these channels are shown in Figure 4.10a in Section 4.2.2. Due to the closeness of their respective spectral positioning within the 8–12 μm atmospheric window, and the similarity of the spectral response functions for each channel, the two channels meet the requirements for application of the Split-Window (SW) approach for estimating LST (Section 2.5.1). The dual-view capability of the ATSR-2 also facilitates application of the DA algorithms (Section 2.5.2).

Because of the similar characteristics of the two TIR channels, the Surface Brightness Temperature(s) (SBT) measured in each channel are also similar. Figures 4.1 to 4.3 illustrate the closeness of the SBTs in the 11 and 12μm channels for day and night ATSR-2 overpasses. The triangles represent channel 4 temperatures (T_4) and the circles represent channel 5 (T_5). The SBT data are plotted against the zenith angle of the satellite view, and each colour represents data from an ATSR-2 overpass on a different day/night. Each data value is the average of a 3×3 pixel array centred on the position of the respective field site. For the work with ATSR-2 data, averaging over 3×3 has been performed in order to allow for possible geolocation error (± 1 pixel (Mutlow *et al.*, 1999)) in the position of the central pixel between the nadir and forward views of the sensor.

There is no real structure apparent in the data, which is to be expected, since SBT measurements made on different days are independent of each other. The data have been plotted in Figures 4.1 to 4.3 to show the total collection of SBT data derived from the ATSR-2 satellite sensor used in the experimental component of this thesis. In the following sections of the current chapter these data will be used in the analysis of atmospheric effects upon the surface-leaving radiance, as it propagates through the atmosphere to the satellite sensor. The data in Figures 4.1 to 4.3 have not been screened for cloud contamination and so contain some data which
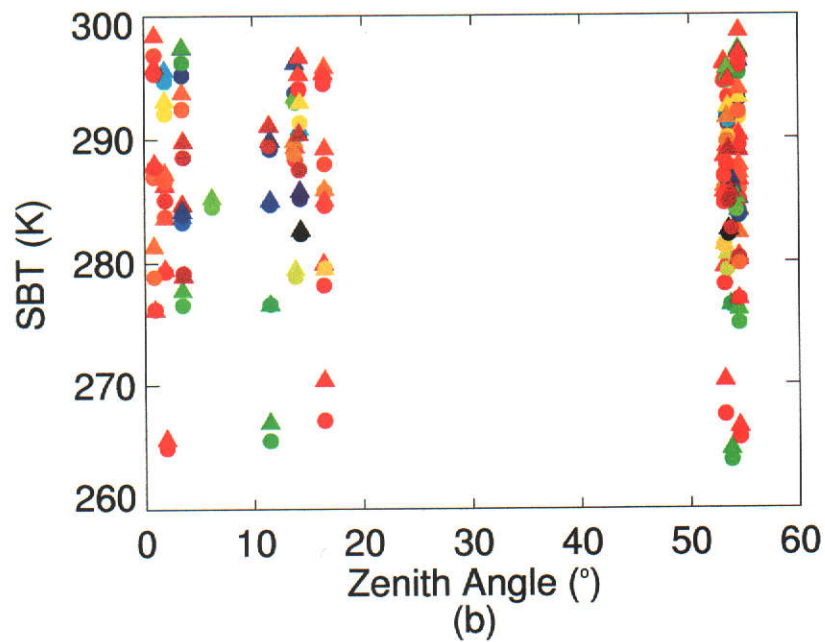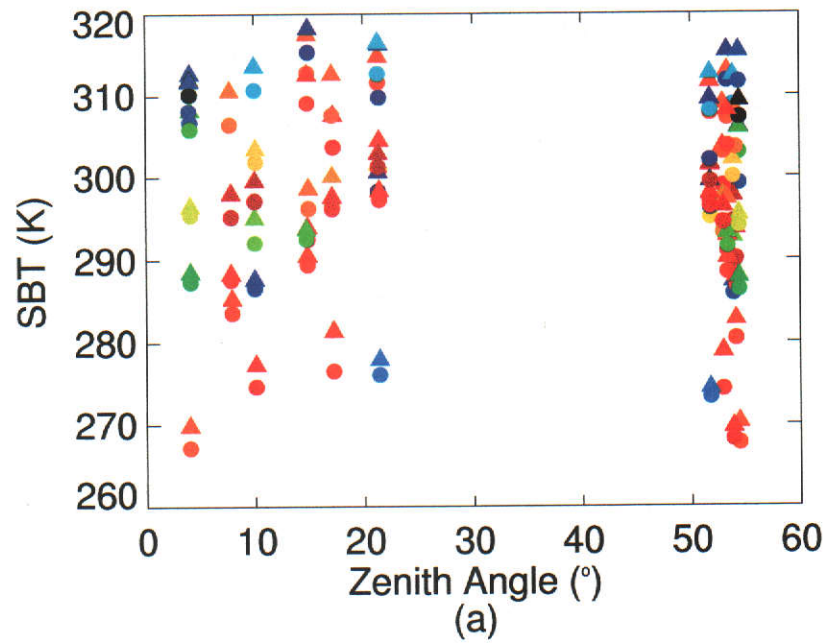
Figure 4.1: Surface brightness temperatures derived from ATSR-2 during 1998 for a) day, and b) nighttime overpasses of the Amburla field site. Triangles show $11\mu m$ data. Circles show $12\mu m$ data. Each colour represents an overpass from a different day/night.

will be excluded from analysis in later stages of this work.

The analysis of atmospheric effects on the surface-leaving radiance begins in the following Section with the investigation of the impact of observation zenith angle on SBT data derived from the ATSR-2.

4.1.1 Angular Effects

It is well known that radiance measured at a satellite sensor varies with zenith angle, due to atmospheric effects (eg McMillin, 1975; Maul, 1983; Sobrino *et al.* 1991), and that the surface emissivity also varies with angle (Masuda *et al.*, 1988; Labed and Stoll, 1991a; Sobrino and Cuenca, 1999). However, as is shown by the figures earlier in this chapter, it is difficult to identify the impact of these variables purely by examining satellite-derived SBT. More insight into the impact which the atmospheric transmittance and the surface emissivity have on the SBT measured by the satellite sensor as the zenith angle increases may be gained by analysing the difference in SBT, here termed dBT, between the SBT measured for the nadir and forward views of ATSR-2. Figures 4.4, 4.5 and 4.6 show such dBT data acquired over the Amburla and Thangoo field sites. In the figures, the measured dBT data are plotted against the difference in zenith angle (forward minus nadir) between the two views. Figures 4.4 and 4.5 show dBT data for the Amburla site for 1998 and June to September of 2000 respectively. Figure 4.6 shows data acquired over the Thangoo field site during 1998 only. Data for the Amburla field site from 2000 were included because they coincide with the *in situ* SBT data sets acquired by the scanning radiometer installed at the site. These data are discussed in Chapter 5.

Figure 'a' in each plot shows day time data, and 'b' in each plot shows nighttime data. In the plots the 11μm data are shown by diamond shaped symbols and the 12μm data by circles. The data are once again the average of a 3×3 array centred on the field site coordinates, and the error bars represent one standard deviation of the data in the array. As for the earlier plots (Figures 4.1 to 4.3), no cloud screening has been performed on the data at this stage and the plots show the total data set
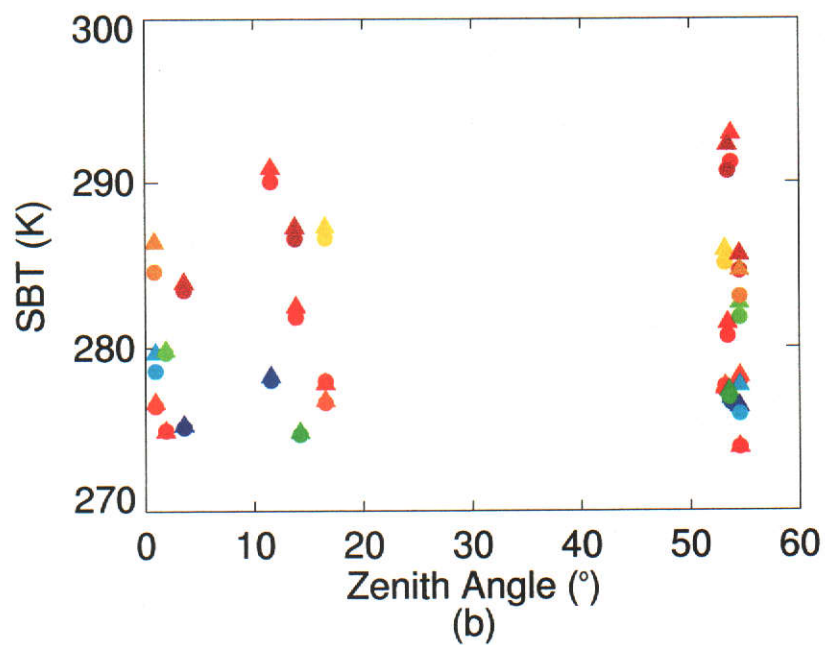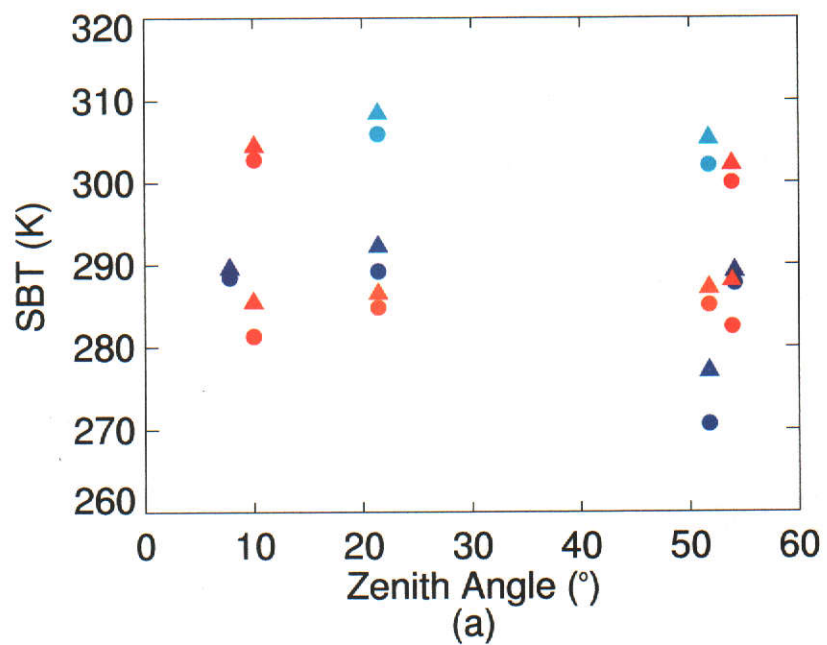
Figure 4.2: Surface brightness temperatures derived from ATSR-2 during 2000 for a) day, and b) nighttime overpasses of the Amburla field site. Triangles show 11μm data. Circles show 12μm data. Each colour represents an overpass from a different day/night.
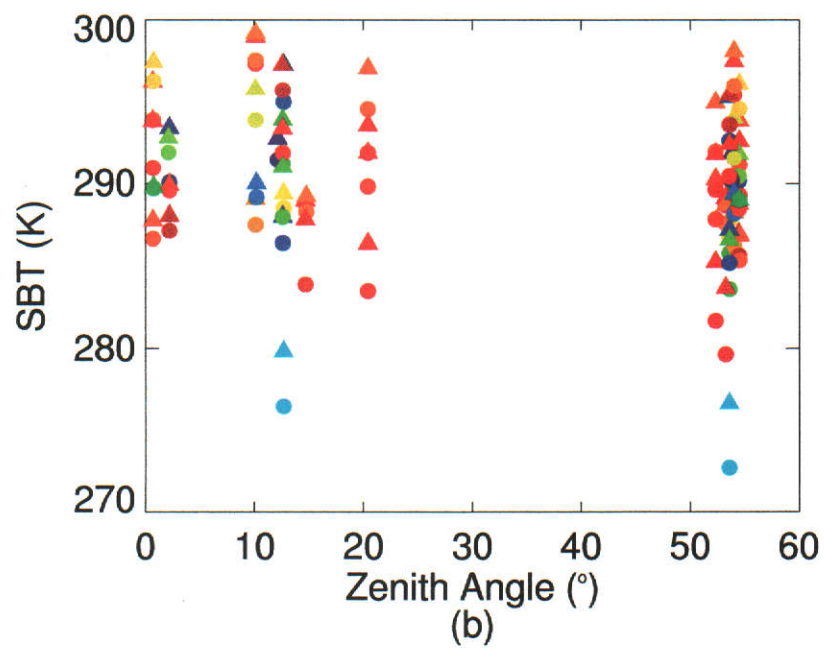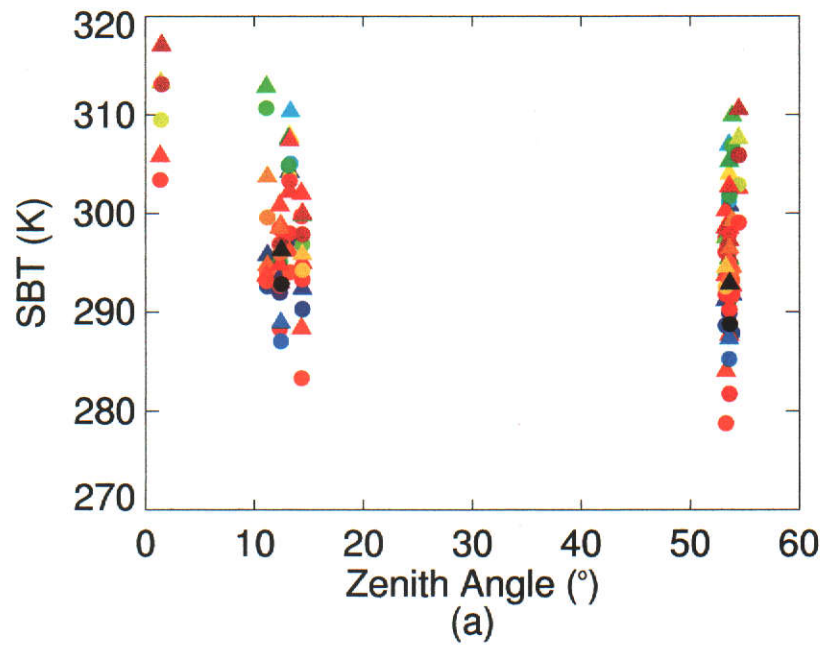
Figure 4.3: Surface brightness temperatures derived from ATSR-2 during 2000 for a) day, and b) nighttime overpasses of the Thangoo field site. Triangles show 11μm data. Circles show 12μm data. Each colour represents an overpass from a different day/night.

from which cloud-free data will later be extracted.

There is almost no trend with viewing angle evident in the data, except in Figure 4.6a, where the magnitude of the dBT increase with zenith angle difference. However, the range of zenith angles of the observations is limited (especially in Figure 4.5a) such that no solid conclusions about the variation of SBT with angle can be drawn by inspection.

Though there are no obvious relationships in the dBT data when plotted against difference in zenith angle, as in Figures 4.4 to 4.6, a more interesting picture emerges when the dBT data are plotted against the Julian day of the year of acquisition. When plotted in this way, some seasonal variation in the magnitude of the dBT data is evident.

In Figure 4.7a, which shows daytime dBT data for the Amburla site, incorporating both 1998 and 2000 data. The magnitude of the data represented by the trend line, which is a three-point moving average (plotted in red), decreases noticeably to between 0 and 2 K for Julian days between 150 and 250, which coincides with the winter months of the year. At the start and end of the year, in summer, the magnitude of the dBT data is closer to 4K. In Fig 4.7b, the nighttime data, there seems to be little variation in dBT throughout the year, with the majority of data falling in the range between 2 and -2K. This nighttime result is interesting, as the range of the dBT data plotted in the figure agrees with the results from the surface emissivity modelling work described in Chapter 5. It suggests that the nighttime angular distribution of surface emissivity captured in the *in situ* modelling work also describes satellite measurements, and that the observed angular distribution is applicable all year round, and at least in the time period encompassing 1998 to 2000.

In Figure 4.8b, a similar distribution to that in Figure 4.7 is evident in the daytime dBT data from the Thangoo field site, shown in Figure 4.8a. At this site, Julian days 150-250 correspond to the dry season. There is more scatter in the Thangoo data, but, again, the data seem to converge towards a difference of 4 K at the start and end of the year, and to a minimum between 0 and 2 K mid-year. Unlike the
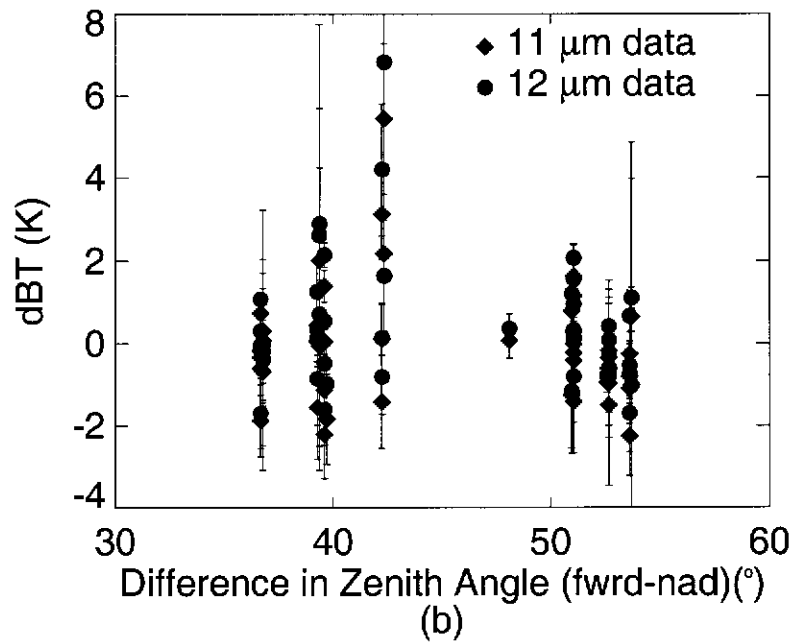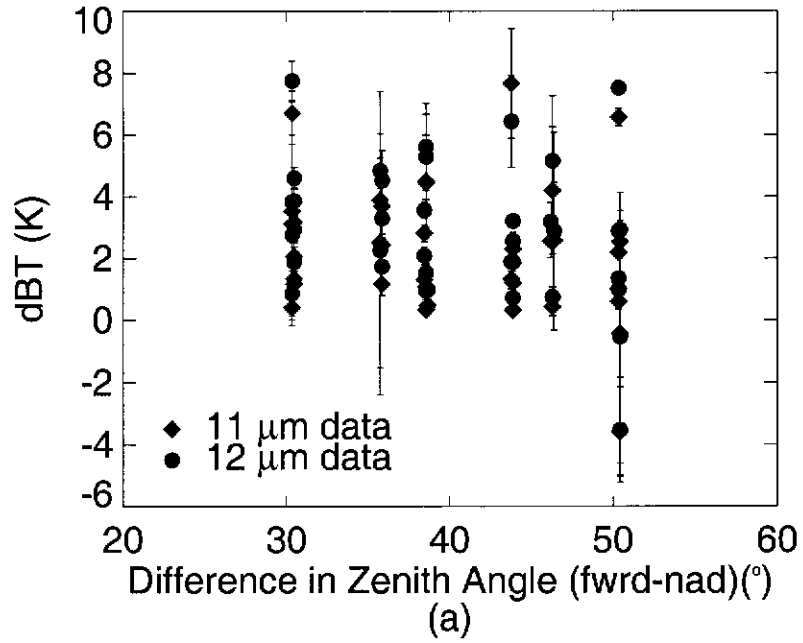
Figure 4.4: Differences in surface brightness temperatures between the nadir and forward views of ATSR-2, acquired during 1998 for a) day, and b) nighttime over-passes of the Amburla field site. Diamonds show the average dBT of a 3×3 pixel array centred on the Amburla field satellite at 11μm. Circles show 12μm data. The error bars show one standard deviation of the data.
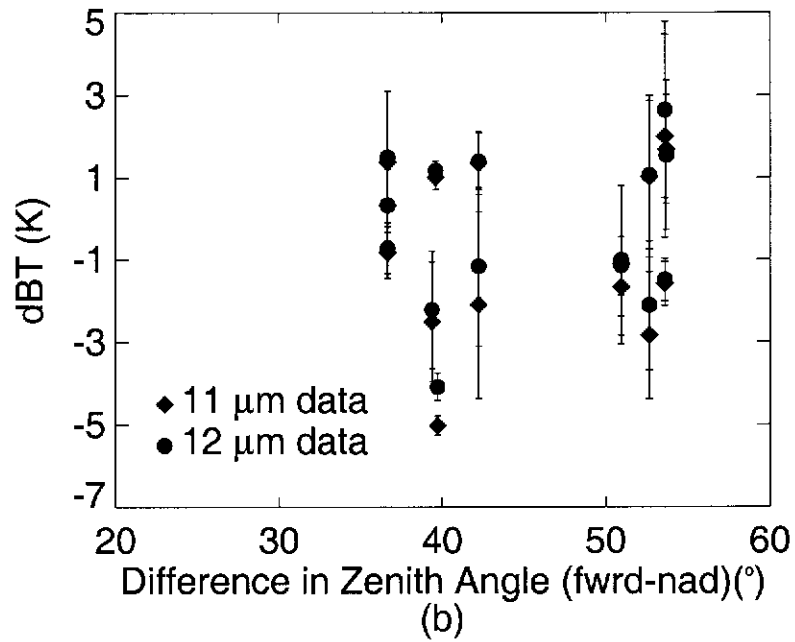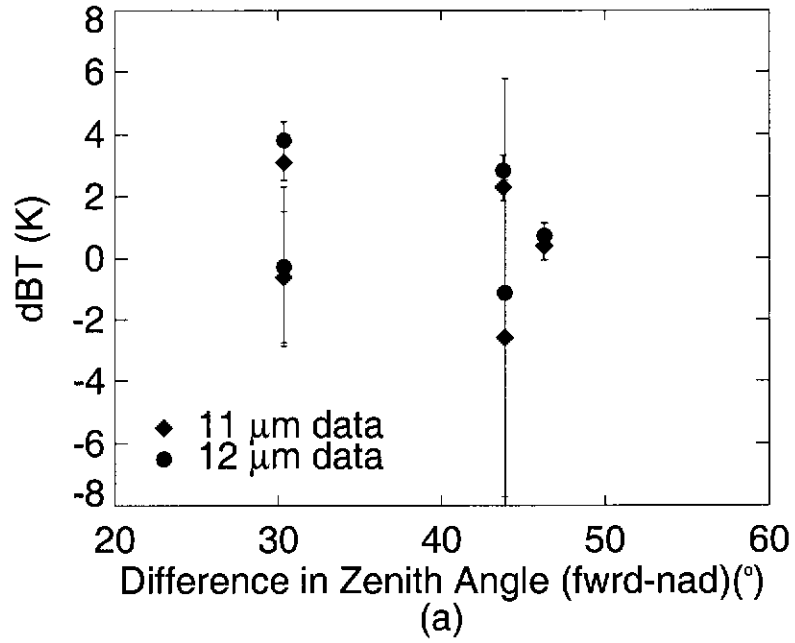
Figure 4.5: Differences in surface brightness temperatures between the nadir and forward views of ATSR-2, acquired between June and September 2000 for a) day, and b) nighttime overpasses of the Amburla field site. Diamonds show the average dBT of a 3×3 pixel array centred on the Amburla field satellite at $11 \mu m$. Circles show $12 \mu m$ data. The error bars show one standard deviation of the data.
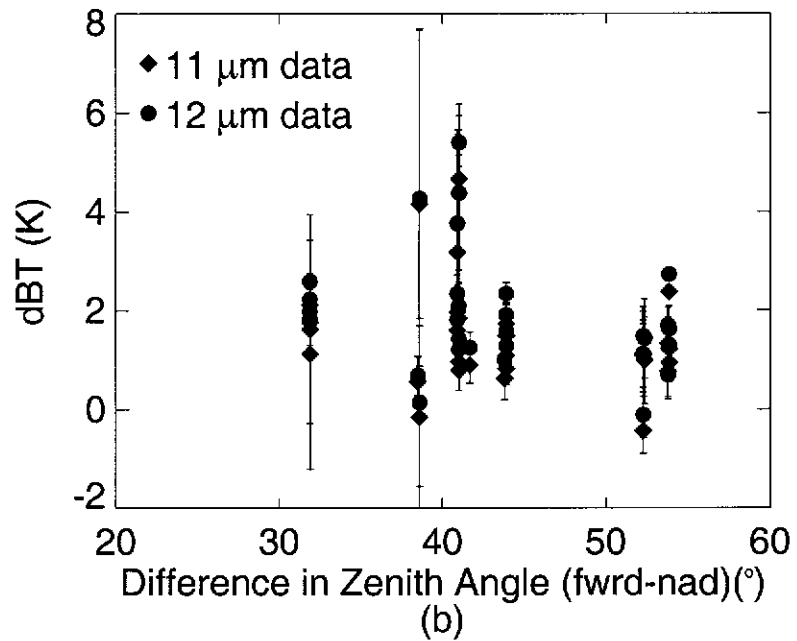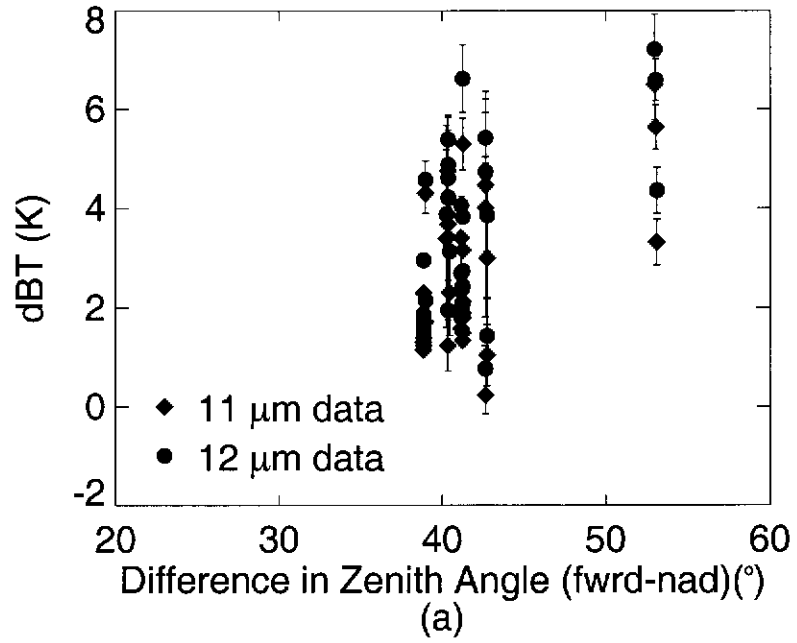
Figure 4.6: Differences in surface brightness temperatures between the nadir and forward views of ATSR-2, acquired during 1998 for a) day, and b) nighttime overpasses of the Thangoo field site. Diamonds show the average dBT of a 3×3 pixel array centred on the Thangoo field satellite at $11\mu m$. Circles show $12\mu m$ data. The error bars show one standard deviation of the data.

Amburla site, however, Figure 4.8b also shows some seasonal variation at night, with dBT values decreasing during the dry season. This minimum may be due to the decrease in atmospheric PW during the dry season as shown in Fig 3.7, which causes a smaller differential in the transmittance between the two viewing angles. The change may also be related to variation in the properties of surface vegetation which must flower and seed also has a seasonal cycle.

The amount of information to be gleaned from the plots of raw SBT in Figures 4.1 to 4.6 is limited since the amount of data is small and angular atmospheric and surface effects remain embedded within the data. The interactions between the underlying physical processes become more apparent once atmospheric effects are considered through atmospheric correction of the data, and by accounting for surface effects through improving understanding of the relationships between solar-sensor viewing geometry and the angular distribution of SBT and the surface emissivity. It is interesting that seasonal trends in the dBT data are evident, particularly in the day time data shown in Figures 4.7 and 4.8. The plot of the Amburla data shows similarities to the seasonal variation in the BT distributions captured by the *in situ* scanning radiometer at the site (see Chapter 5). This is suggests that the small scale angular BT distributions translate to the scale of satellite measurements. This is encouraging for the use of the *in situ* data in validation studies of satellite-derived LST, and it provides the motivation for the more detailed study of the angular distribution of SBT and dBT data which follows in the remainder of this chapter and in Chapter 5.

4.2 Atmospheric Correction

The process of atmospheric correction of remotely sensed surface temperature accounts for the impact of atmospheric emitted and absorbed radiance on the signal measured at the satellite. The at-sensor radiance comprises contributions from the surface and the atmosphere, both directly and reflected from the Earth's surface.
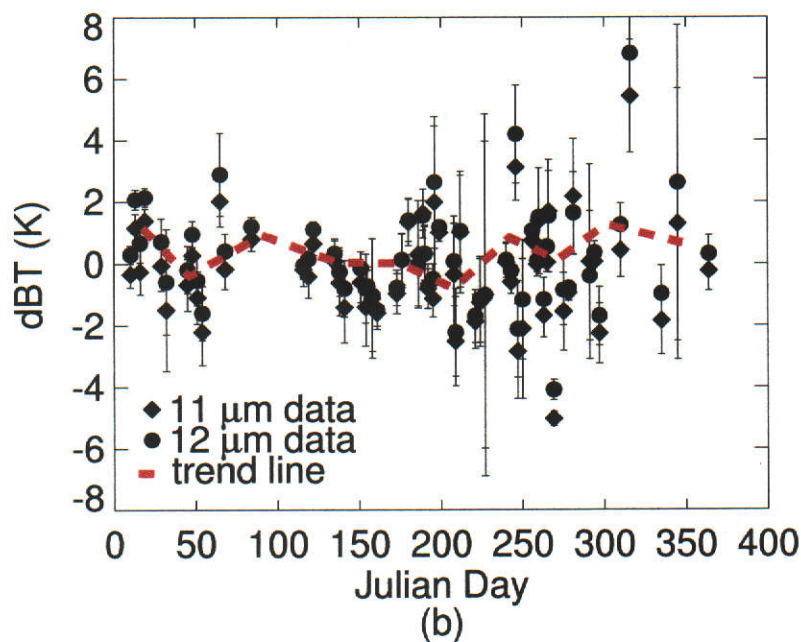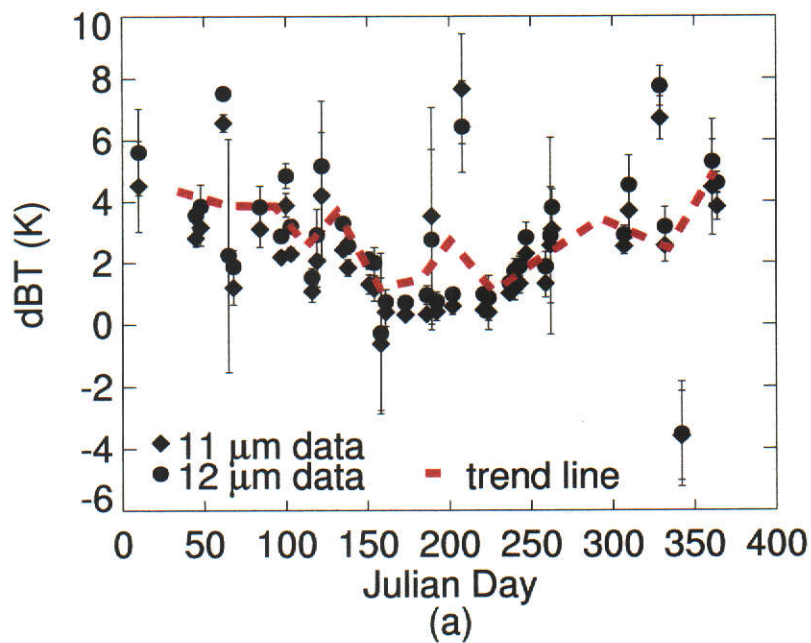
Figure 4.7: Differences in surface brightness temperatures between the nadir and forward views of ATSR-2, acquired during 1998 and 2000 for a) day, and b) night-time overpasses of the Amburla field site plotted against Julian day of acquisition. Diamonds show the average dBT of a 3×3 pixel array centred on the Amburla field satellite at $11\mu m$. Circles show $12\mu m$ data. The error bars show one standard deviation of the data. The dashed red line is a three-point moving average.
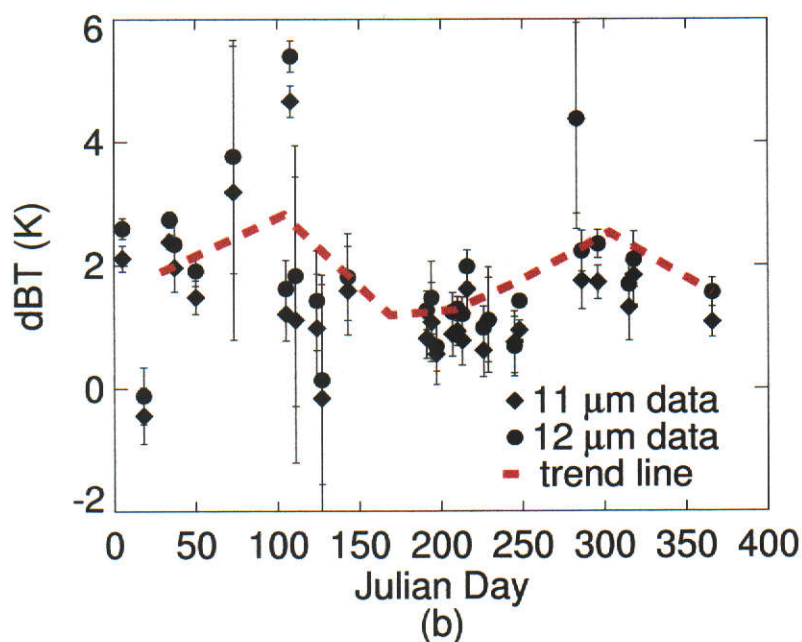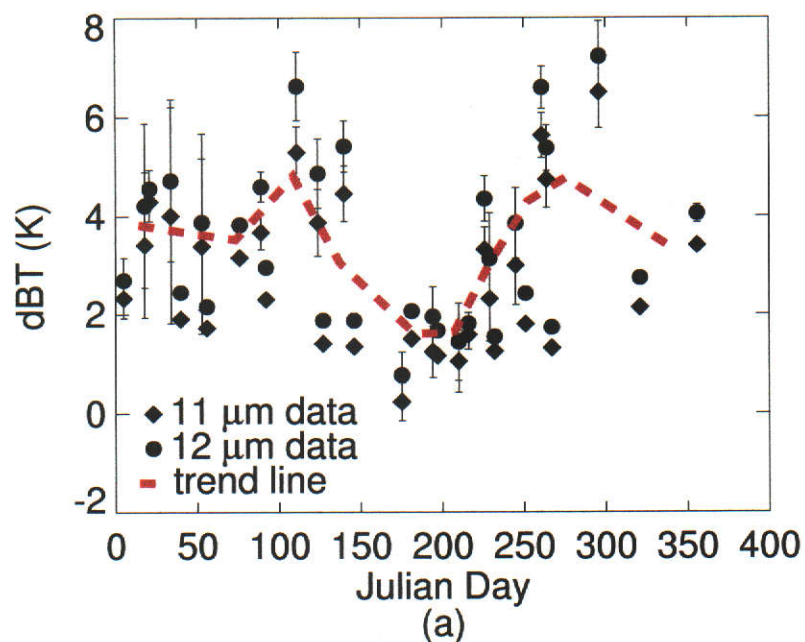
Figure 4.8: Differences in surface brightness temperatures between the nadir and forward views of ATSR-2, acquired during 1998 for a) day, and b) nighttime overpasses of the Thangoo field site plotted against Julian day of acquisition. Diamonds show the average dBT of a 3×3 pixel array centred on the Thangoo field satellite at $11\mu m$. Circles show $12\mu m$ data. The error bars show one standard deviation of the data. The error bars show one standard deviation of the data. The dashed red line is a three-point moving average.

Because of the reflected component, surface properties become involved in the atmospheric correction process through the surface-reflected term, as given in (2.4) and (2.6). The SW (Section 2.3.1) and DA (Section 2.3.2) algorithm approaches to surface temperature estimation combine atmospheric and surface information into an equation in order to retrieve the true surface temperature.

Atmospheric correction may also be performed by estimating the magnitudes of the individual radiative components (described in Section 2.2.3), by adopting a single channel approach (Price, 1983; Susskind et al., 1984; Chedin et al., 1985; Ottle and Vidal-Madjar, 1992; Li and Becker, 1993; Wan and Dozier, 1996; Wan and Li, 1997; Ma et al., 2002). However, as noted by Ottle and Vidal-Madjar (1992) and Teggi et al. (1998), atmospheric profile data must be representative of the atmospheric conditions at the time of acquisition of satellite data. In this work, atmospheric profile data for the Amburla and Thangoo field sites are derived respectively from radiosondes launched daily from the Alice Springs and Broome airports at 0830 hrs and 0700 hrs respectively. The Alice Springs and Broome airports are respectively 25 km and 80 km from the respective field sites,a fact that is discussed in more detail in Section 4.2.4

4.2.1 A Radiative Component Approach to Atmospheric Correction

Using radiosonde-derived atmospheric profile data as input to a radiative transfer model, such as LBLRTM (Clough et al., 1996), allows the determination of the magnitude of the radiative components involved in the atmospheric correction of remotely sensed LST data.

Using LBLRTM version 5.2-2, with input derived from radiosondes launched from the Broome airport, simulations (this section, Table 4.1, 4.2) have shown that, using the Radiative Component (RC) approach to SC atmospheric correction (Section 2.3.3), it is possible to retrieve the surface temperature to within ±0.01K over

the range of surface temperatures typical of the Thangoo field site, for the range of viewing angles utilized by a scanning satellite sensor (0 to 60°). This result is obtained in the ideal case, for which it is assumed the atmospheric profile used in the model perfectly describes the atmospheric state between the sensor and the surface, and that the surface emissivity is also known exactly. In order to estimate the magnitude of the radiative components, namely the upwelling and downwelling sky radiance and the atmospheric transmittance, the LBLRTM model is executed over the waveband of the channel for which the simulation is required (eg the 11 and 12μm channels of the ATSR-2), at the default resolution of $0.01\mathrm{cm}^{-1}$. For the 11 and 12μm channels, this generates approximately 16000 and 20000 spectral radiance/transmittance values respectively.

Using the RC approach, the formulation for atmospheric correction is;

$$B(T_s)(\nu, \theta) = \frac{B(T_{sat})(\nu, \theta) - (B(T_{sky}) \uparrow (\nu, \theta)_{\epsilon=1.0} + B(T_{sky})_{ref}(\nu, \theta))}{\epsilon(\nu, \theta)\tau(\nu, \theta)}, \quad (4.1)$$

in which;

$$B(T_{sky})_{ref}(\nu, \theta) = \tau(\nu, \theta)(1 - \epsilon(\nu, \theta))(B(T_{sky}) \downarrow (\nu, \theta'), \quad (4.2)$$

where,

υ = wavenumber,

θ = zenith angle at which the reflected component leaves the surface,

θ' = zenith angle at which the downwelling sky radiance impacts upon the surface,

T_s = the surface temperature,

$B(T_s)(\nu, \theta)$ = the blackbody equivalent radiance for the surface temperature, at a given wavenumber and zenith angle,

$B(T_{sat})(\nu, \theta)$ = the blackbody equivalent at-sensor radiance for the surface

temperature, at a given wavenumber and zenith angle,

$B(T_{sky}) \uparrow (\nu, \theta)_{\epsilon=1.0}$ = the upwelling sky radiance at a given wavenumber and zenith angle,

$B(T_{sky}) \downarrow (\nu, \theta')$ = the downwelling sky radiance for at a given wavenumber and zenith angle,

$B(T_{sky})_{ref}(\nu, \theta)$ = the downwelling sky radiance reflected from the surface at a given wavenumber and zenith angle,

$\tau(\nu, \theta)$ = the atmospheric transmittance at a given wavenumber and zenith angle, and

$\epsilon(\nu, \theta)$ = the surface emissivity at a given wavenumber and zenith angle.

(4.1) is essentially derived by rearranging the RTE, as described by (2.6), and is expressed in terms of the radiative components which may be simulated using LBLRTM. It is for this reason that the upwelling sky radiance term in (4.1) is denoted $\epsilon = 1.0$. Using LBLRTM, the UWSR and the reflected DWSR component must be calculated separately, and the UWSR component must be simulated with the surface emissivity set to unity (i.e zero reflectance), so that there is no contribution from the reflected DWSR component to the simulated UWSR. Application of (4.1) produces spectral values of the surface-emitted radiance over the waveband used. The spectral data may then be integrated over the spectral response function of the appropriate channel in order to obtain a band-averaged estimate of the surface-emitted radiance, which subsequently may be converted to an equivalent surface temperature via an LUT. The surface temperature calculated in this way is an estimate of the EDRST defined by Norman and Becker (1995) (see Section 2.2.1.2). The EDRST itself is the closest radiometric approximation of the thermodynamic temperature of the land surface. In this chapter, as well as in Chapter 5, this quantity is referred to as the LST.

Table 4.1 contains an extract of the spectral data used in a simulation study to confirm the validity and accuracy of the RC method. The data are for the 12μm

87

channel of the ATSR-2, for retrieval through a U.S. Standard Tropical Atmosphere, with a surface temperature of 280 K and a surface emissivity of 0.98, at nadir viewing. The tropical atmosphere was chosen as it is the most problematic scenario for satellite-retrieval of LST, and as such represents an upper limit on the accuracy of the RC method of atmospheric correction.

In the table, the column headed '$B(T_{sat})$' contains the simulated at-sensor radiance data, the column '$B(T_{sky})$ ↑' contains the simulated UWSR data, the column '$B(T_{sky})$ ↓' the simulated downwelling and the column '$B(T_{sky})_{ref}$' the simulated downwelling sky radiance reflected from the surface. Each of the surface-leaving radiance components is defined in the viewing direction of the sensor, however, the DWSR, prior to impacting the surface, is defined at an equivalent zenith angle θ', but in the direction towards the surface rather than the sensor. As such, it is assumed for the simulation that the surface exhibits specular properties. In the simulation, the value of $B(T_{sky})_{ref}$ may be calculated via (4.2). In order to calculate $B(T_{sky})_{ref}$ correctly, using the LBLRTM model, the simulation of $B(T_{sky})$ ↑ should be performed once with the surface emissivity set to unity, so that there is no contribution from the surface-reflected term. It should then be repeated using the appropriate value of the surface emissivity. The difference in the value of $B(T_{sky})$ ↑ between these two estimates gives the correct result for $B(T_{sky})_{ref}$. The column headed "$B(T_s = 280K)$" contains the blackbody equivalent radiance, derived via a LUT for the 12μm channel of the ATSR-2, for a surface temperature of 280 K at a wavenumber resolution of 0.01cm^{-1}.

If the RC technique, using (4.1), successfully retrieves the surface temperature; then the assumed values in the '$B(T_s = 280K)$' column should be equal to those in the column headed '$B(T_s)_{calc}$', which are atmospherically corrected at-sensor radiances calculated by using the simulated radiative components in (4.1). To calculate the retrieved value of T$_s$, the spectral radiance data in the $B(T_s)_{calc}$ column are band-averaged over the spectral response function of the 12μm channel of the ATSR-2, and this result is then converted to a temperature via the LUT for the

12μm channel of the sensor. Examination of Table 4.1 reveals that the data in the two columns show slight differences in the fourth decimal place, which equates to an accuracy of ± 0.01K in the temperature range of 280–320K. This result is quoted in Table 4.2.

Table 4.2 contains data that confirm the RC simulation, for a prescribed atmosphere and spectral surface emissivity, retrieves the surface temperature to within ± 0.01 K, for assumed surface temperatures ranging between 280 K (at nadir viewing with surface emissivity equal to 0.98) and 320 K (at zenith angle 60° , with surface emissivity equal to 0.98). The column headed 'T_s' contains the surface temperature specified in the model at the outset. The column '$B(T_s)$' contains the equivalent blackbody radiances for this temperature, derived from the LUT for the 12μm channel of the ATSR-2. The '$B(T_s)_{calc}$' column contains the band-averaged spectral data output from LBLRTM. Together, the data in the table confirm that the RC technique is capable of retrieving the surface temperature to within ± 0.01 K, under ideal conditions. Though the data in Table 4.2 are for the 12μm channel, the RC method is equally applicable, and comparable accuracy can be expected, in other wavebands of the ATSR-2, such as the 11μm channel. As well, the TIR channels of other satellite sensors, and *in situ* instruments such as the TASCO radiometer installed at the Amburla field site, should perform comparably if well calibrated and with comparable radiometric resolution.

In practice, radiosonde data are subject to errors in the measurement of temperature and water vapour. Further, the sonde launch time is often offset from the satellite overpass time, leading to uncertainty in the estimate of the near-surface atmospheric conditions. The accuracy of radiosonde estimates of temperature and humidity are assessed in Section 4.2.3 using data obtained from Broome airport, near the Thangoo field site. The impact of spatial offsets between the location of launch and the ascent of a radiosonde and the site of subsequent application of the data to the RC method of atmospheric correction, are quantified in Section 4.2.4 using radiosonde data from the Alice Springs airport and *in situ* measurements of

Wave No. (cm^{-1})	$B(T_{sat})$	$B(T_{sky})\uparrow$	$B(T_{sky})\downarrow$	$B(T_{sky})_{ref}$	τ	$B(T_s = 280K)$	$B(T_s)_{calc}$
748.53	1.207E-05	8.810E-06	9.248E-06	5.544E-08	2.998E-01	1.0902E-05	1.0902E-05
748.54	1.207E-05	8.810E-06	9.248E-06	5.544E-08	2.998E-01	1.0902E-05	1.0902E-05
748.55	1.207E-05	8.810E-06	9.247E-06	5.544E-08	2.998E-01	1.0902E-05	1.0901E-05
748.56	1.207E-05	8.810E-06	9.247E-06	5.545E-08	2.998E-01	1.0902E-05	1.0901E-05
748.57	1.207E-05	8.809E-06	9.247E-06	5.545E-08	2.998E-01	1.0902E-05	1.0901E-05
748.58	1.207E-05	8.809E-06	9.246E-06	5.545E-08	2.998E-01	1.0901E-05	1.0901E-05
748.59	1.207E-05	8.809E-06	9.246E-06	5.545E-08	2.999E-01	1.090E-05	1.090E-05
748.60	1.207E-05	8.808E-06	9.245E-06	5.545E-08	2.999E-01	1.0901E-05	1.0901E-05
748.61	1.207E-05	8.808E-06	9.245E-06	5.545E-08	2.999E-01	1.0901E-05	1.0901E-05
748.62	1.207E-05	8.808E-06	9.245E-06	5.545E-08	2.999E-01	1.0901E-05	1.0901E-05
748.63	1.207E-05	8.807E-06	9.244E-06	5.546E-08	2.999E-01	1.0901E-05	1.0900E-05
748.64	1.207E-05	8.807E-06	9.244E-06	5.546E-08	3.000E-01	1.0901E-05	1.0900E-05
748.65	1.207E-05	8.807E-06	9.244E-06	5.546E-08	3.000E-01	1.090E-05	1.090E-05
748.66	1.207E-05	8.806E-06	9.243E-06	5.546E-08	3.000E-01	1.091E-05	1.0900E-05
748.67	1.207E-05	8.806E-06	9.243E-06	5.546E-08	3.000E-01	1.090E-05	1.090E-05
748.68	1.207E-05	8.806E-06	9.243E-06	5.546E-08	3.000E-01	1.0900E-05	1.0900E-05
748.69	1.207E-05	8.805E-06	9.242E-06	5.546E-08	3.001E-01	1.0900E-05	1.0900E-05
748.70	1.207E-05	8.805E-06	9.242E-06	5.547E-08	3.001E-01	1.0900E-05	1.0900E-05
748.71	1.207E-05	8.805E-06	9.242E-06	5.547E-08	3.001E-01	1.0900E-05	1.0900E-05
748.72	1.207E-05	8.804E-06	9.241E-06	5.547E-08	3.001E-01	1.0900E-05	1.0899E-05
748.73	1.207E-05	8.804E-06	9.241E-06	5.547E-08	3.001E-01	1.0900E-05	1.0899E-05
748.74	1.207E-05	8.804E-06	9.241E-06	5.547E-08	3.001E-01	1.0900E-05	1.0899E-05
748.75	1.206E-05	8.804E-06	9.240E-06	5.547E-08	3.002E-01	1.0899E-05	1.0899E-05
748.76	1.206E-05	8.803E-06	9.240E-06	5.547E-08	3.002E-01	1.0899E-05	1.0899E-05
748.77	1.206E-05	8.803E-06	9.239E-06	5.547E-08	3.002E-01	1.0899E-05	1.0899E-05
748.78	1.206E-05	8.803E-06	9.239E-06	5.548E-08	3.002E-01	1.0899E-05	1.0899E-05
748.79	1.206E-05	8.802E-06	9.239E-06	5.548E-08	3.002E-01	1.0899E-05	1.0898E-05
748.80	1.206E-05	8.802E-06	9.238E-06	5.548E-08	3.003E-01	1.0899E-05	1.0898E-05
748.81	1.206E-05	8.801E-06	9.238E-06	5.548E-08	3.002E-01	1.0899E-05	1.0898E-05
748.82	1.206E-05	8.801E-06	9.237E-06	5.548E-08	3.002E-01	1.0899E-05	1.0898E-05
748.83	1.206E-05	8.800E-06	9.237E-06	5.548E-08	3.002E-01	1.0898E-05	1.0898E-05
748.84	1.206E-05	8.800E-06	9.236E-06	5.548E-08	3.002E-01	1.0898E-05	1.0898E-05
748.85	1.206E-05	8.800E-06	9.236E-06	5.548E-08	3.002E-01	1.0898E-05	1.0898E-05
748.86	1.206E-05	8.800E-06	9.236E-06	5.548E-08	3.002E-01	1.0898E-05	1.0898E-05
748.87	1.206E-05	8.79E-06	9.235E-06	5.548E-08	3.002E-01	1.0898E-05	1.0897E-05
748.88	1.206E-05	8.799E-06	9.235E-06	5.549E-08	3.002E-01	1.0898E-05	1.0897E-05
748.89	1.206E-05	8.799E-06	9.235E-06	5.549E-08	3.002E-01	1.0898E-05	1.0897E-05
748.90	1.206E-05	8.798E-06	9.234E-06	5.549E-08	3.002E-01	1.0897E-05	1.0897E-05
748.91	1.206E-05	8.798E-06	9.234E-06	5.549E-08	3.002E-01	1.0897E-05	1.0897E-05
748.92	1.206E-05	8.798E-06	9.234E-06	5.549E-08	3.002E-01	1.0897E-05	1.0897E-05
748.93	1.206E-05	8.797E-06	9.233E-06	5.549E-08	3.002E-01	1.0897E-05	1.0897E-05
748.94	1.206E-05	8.797E-06	9.233E-06	5.549E-08	3.002E-01	1.0897E-05	1.0896E-05
748.95	1.206E-05	8.797E-06	9.233E-06	5.549E-08	3.002E-01	1.0897E-05	1.0896E-05
748.96	1.206E-05	8.796E-06	9.232E-06	5.550E-08	3.002E-01	1.0897E-05	1.0896E-05
748.97	1.206E-05	8.796E-06	9.232E-06	5.550E-08	3.002E-01	1.0897E-05	1.0896E-05
748.98	1.206E-05	8.796E-06	9.231E-06	5.550E-08	3.002E-01	1.0896E-05	1.0896E-05
748.99	1.206E-05	8.795E-06	9.231E-06	5.550E-08	3.002E-01	1.0896E-05	1.0896E-05
749.00	1.206E-05	8.795E-06	9.231E-06	5.550E-08	3.002E-01	1.0896E-05	1.0896E-05
749.01	1.206E-05	8.795E-06	9.230E-06	5.550E-08	3.002E-01	1.0896E-05	1.0895E-05
749.02	1.206E-05	8.794E-06	9.230E-06	5.550E-08	3.002E-01	1.0896E-05	1.0895E-05
749.03	1.206E-05	8.794E-06	9.230E-06	5.551E-08	3.002E-01	1.0896E-05	1.0895E-05
749.04	1.206E-05	8.794E-06	9.229E-06	5.551E-08	3.002E-01	1.0896E-05	1.0895E-05
749.05	1.206E-05	8.793E-06	9.229E-06	5.551E-08	3.002E-01	1.0895E-05	1.0894E-05
749.06	1.206E-05	8.793E-06	9.229E-06	5.551E-08	3.002E-01	1.0894E-05	1.0894E-05
749.07	1.206E-05	8.793E-06	9.228E-06	5.551E-08	3.002E-01	1.0894E-05	1.0894E-05

Table 4.1: Extract of spectral radiance and transmittance data showing agreement to at least 3 decimal places between the spectral radiance for T_s=280.00 K, derived from the LUT for the 12μm channel of the ATSR-2 (column B(T_s)=280 K), and the simulated spectral radiance at the sensor (column B(T_s)$_{calc}$), after applying the RC method of atmospheric correction using (4.1).

T_s	$B(T_s)_{LUT}$	θ (°)	ϵ	$B(T_s)_{calc}$	$T_{s\ calc}$
280.00	$9.6947E^{-6}$	0	1.0	$9.69352E^{-6}$	279.99
280.00	"	0	0.98	$9.69351E^{-6}$	279.99
320.00	$1.66895E^{-5}$	60	1.0	$1.6687E^{-5}$	279.99
320.00	"	60	0.98	$1.66911E^{-5}$	320.01

Table 4.2: Accuracy of retrieval of surface temperature using the RC method over the range of surface temperatures expected at the Thangoo field site, for the range of viewing angles utilized by scanning satellite sensors.

the DWSR from the Amburla field site.

The simulation described in this section assumes that the surface exhibits specular properties. However, the land surface is rarely perfectly specular, and often exhibits BRDF properties in the visible spectrum (Roujean et al., 1992), for which there may exist similar Bi-directional Emission Distribution Function (BEDF) effects in the TIR (Jupp, 1998; Snyder and Wan, 1998). Such effects will impact the measurement of LST from space, and in order to better understand the interactions between the atmosphere and the land surface the radiative properties of the Amburla field site are investigated extensively in Chapter 5.

4.2.2 Modelling Radiative Components

For satellite applications such as atmospheric correction of ATSR-2-derived SBT, using the RC approach, the radiative components in the TIR band are required to be estimated. In this work, the algorithm for modelling the radiative components, namely the DWSR, UWSR and the atmospheric transmittance, is based upon the regression relation between the DWSR measured by the zenith sky-view of the *in situ* TASCO radiometer, situated at the Amburla field site, and coincident modelled estimates of the DWSR for the TIR channels of the ATSR-2, derived from radiosonde measurements of the vertical temperature and humidity profiles of the atmosphere. This regression approach to atmospheric correction, between the *in situ* DWSR data and modelled radiative components derived from LBLRTM, has been adopted in this work in order to at least partially compensate for the shortcom-

ings of the two individual sets of atmospheric data. The *in situ* radiometric DWSR measurements have the advantage of being continuous, and so some knowledge of the atmospheric state may be gained at the exact times of the overpasses of the ATSR-2 above the field site. However, the DWSR estimate derived from the *in situ* radiometer gives no information on the vertical atmospheric profile, the UWSR or the atmospheric transmittance. Further, the *in situ* DWSR estimate is recorded over different spectral intervals than those of the ATSR-2 TIR channels. The modelling approach allows estimation of the DWSR, UWSR and atmospheric transmittance for any given spectral interval, so radiative components may be simulated for the TASCO radiometer as well as the TIR channels of the satellite sensor.

In contrast, the profile data used as input to LBLRTM are derived from sondes launched at a fixed time, which do not necessarily coincide with satellite overpasses of the field site, and the sonde launch site is also approximately 80 km from the Amburla field site. Thus, in order to form the best dataset possible for atmospheric correction of satellite-derived SBT data over the Amburla field site, a regression relation between the *in situ* and modelled DWSR is defined, so that the DWSR, UWSR and atmospheric transmittance, modelled using LBLRTM, may be estimated from the single measurement of the DWSR made by the *in situ* radiometer. In this way, the magnitude of the individual radiative components may be estimated for the time of the overpasses of the ATSR-2, and at the location of the Amburla field site. The regression approach used also permits the accuracy with which each radiative component may be estimated to be assessed. This is important when the magnitudes of radiative components estimated in this way are applied to the atmospheric correction of satellite-derived LST data, particularly in validation studies.

The initial relation for estimating the DWSR is defined for nadir viewing. Further regression relations are then developed which describe the increase in the magnitude of the modelled DWSR for the ATSR-2 TIR channels as the zenith angle of the satellite view of the surface increases. In the final step, regression relations are developed to describe the magnitude of the UWSR and atmospheric transmittance

using the modelled value of the DWSR for the ATSR-2 TIR channels. Figure 4.9 shows the sequence of regression equations composing the algorithm for deriving the radiative components for the nadir view (θ_n) of the ATSR-2 in the 11μm channel. The method is the same for other viewing angles and wavebands, although the value of the coefficients of the regression equations will vary between sensors and viewing geometries. It is important to note that the first step in the algorithm depicted in Figure 4.9 is to show that a strong correlation exists between ground-based estimates of the DWSR from the *in situ* radiometer at the Amburla field site and the DWSR modelled using LBLRTM (with vertical atmospheric profile data derived from radiosondes launched from the Alice Springs airport). It is the DWSR modelled using this combination of radiosonde and *in situ* measurements which forms the basis of the regression equations developed to estimate the UWSR and atmospheric transmittance for use in the RC method of atmospheric correction of satellite-derived SBT data (the method for which was described for the ideal case in the previous section). This important initial step also quantifies the accuracy with which the radiative components may be estimated using this regression-based approach, and is described in more detail in Section 4.2.4.

Figure 4.10 shows the relative spectral response of the 11 and 12μm channels of ATSR-2 and the TASCO radiometer and the regression relations between the modelled, radiosonde-based, DWSR for the 11 and 12μm channels of the ATSR-2 and the ground-based TASCO radiometer. This is the second step in the flow diagram shown in Fig 4.9. The fit between the TASCO radiometer-derived data and both the 11 and 12μm data is strongly linear (r^2=0.983 for the 11μm and r^2=0.986 for the 12μm channel), with only a small amount of scatter evident so that the error introduced by the use of the regression relations is small. The gradient of the fit varies noticeably in the two figures and there is a substantial offset between the simulated TASCO data and the simulated 11 and 12μm data. Both of these features are due to the differences in the spectral location within the TIR part of the spectrum and the breadth of the spectral response of the sensors shown in Figure 4.10. The

$$TASCO_{in\ situ}DWSR \rightarrow TASCO_{modelled}\ DWSR$$

$$TASCO_{modelled}DWSR \rightarrow ATSR - 2_{11\mu m}DWSR$$

determine ratio between $ATSR - 2_{11\mu m}DWSR$
at $\theta = 0$ and at θ_n

$$ATSR - 2_{11\mu m}(\theta_n)DWSR \rightarrow ATSR - 2_{11\mu m}(\theta_n)UWSR$$

$$ATSR - 2_{11\mu m}(\theta_n)DWSR \rightarrow ATSR - 2_{11\mu m}(\theta_n)\ \tau$$
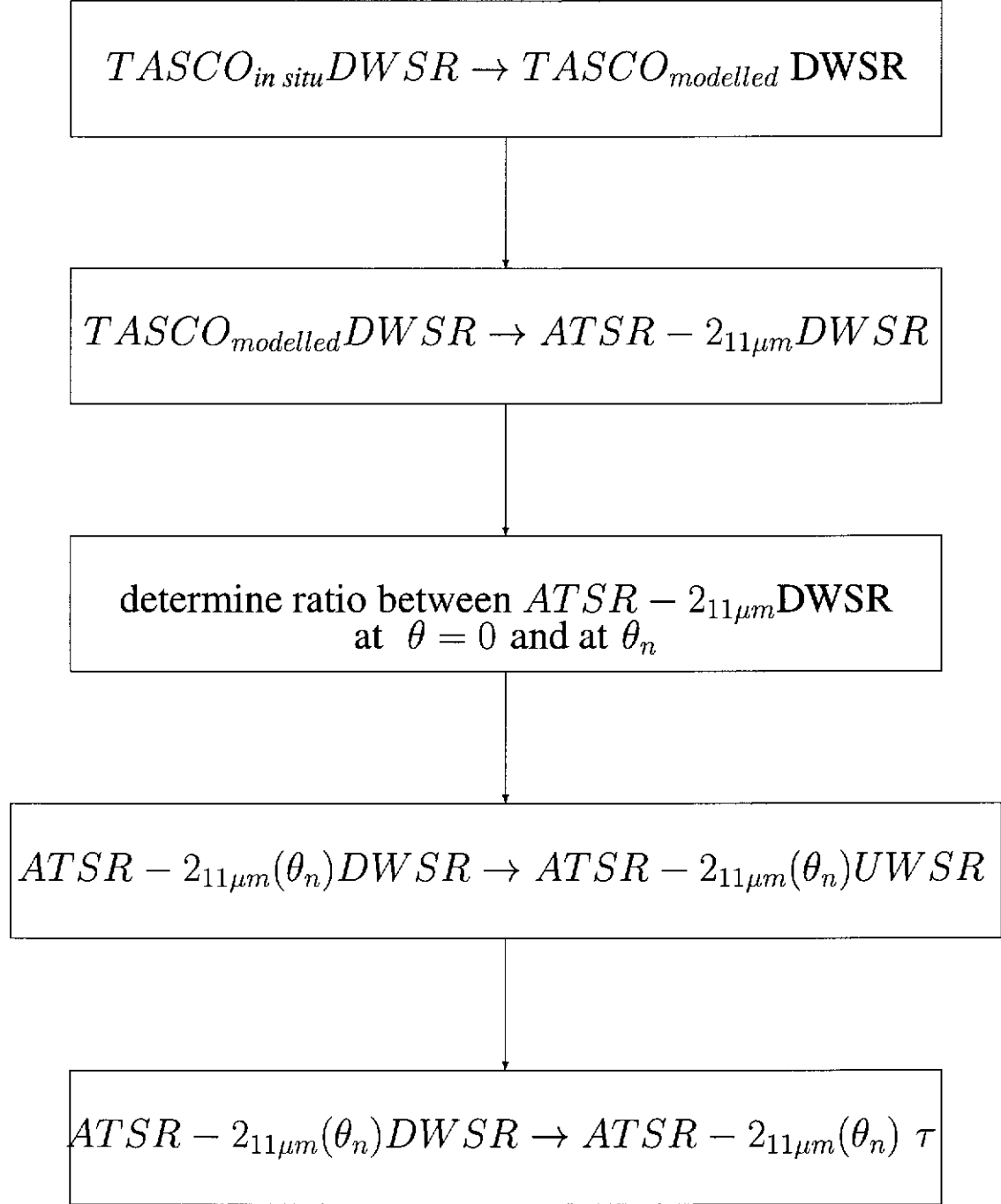
Figure 4.9: Flow diagram showing sequence of regression equations used to estimate radiative components for the 11μm channel of ATSR-2 based on measurements of the DWSR derived from the *in situ* TASCO radiometer.
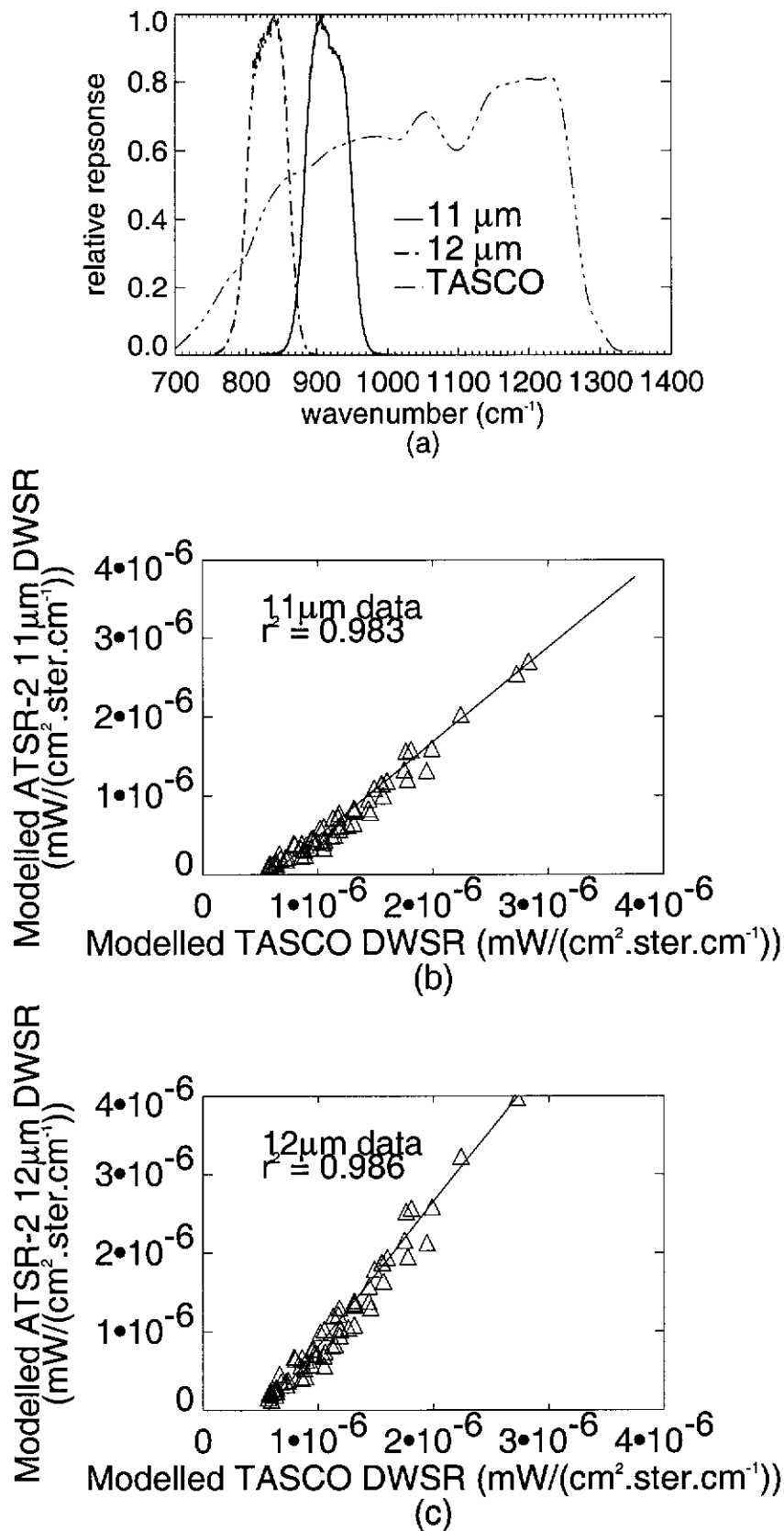
Figure 4.10: The relative response functions of the 11 and 12 μm channels of ATSR-2 and the TASCO radiometer and their impact on the estimation of the DWSR. (a) The 11 and 12 μm channels of the ATSR-2 overlaid by the response function of the TASCO radiometer. (b) Regression relationship between simulated 11 μm DWSR and the TASCO DWSR estimate. (c) Regression relationship between simulated 12 μm DWSR and the TASCO DWSR estimate.

11 and 12μm channels of the ATSR-2 are centred in window regions where the impact of water vapour upon the TIR signal is minimal. However, because the spectral response function of the *in situ* radiometer is much broader than that of the ATSR-2 channels, there is a greater contribution of atmosphere-emitted radiance from those spectral regions outside the TIR window regions contained within the *in situ* estimate of the DWSR. These regions are excluded from the ATSR-2 TIR bands, hence the DWSR measured by the *in situ* radiometer is larger than the equivalent estimates recorded by the TIR channels of the satellite sensor. This difference in DWSR is apparent in figures 4.10a and b in the form of the the offset in the line of regression between the modelled TASCO-derived DWSR and the modelled DWSR for the 11 and 12μm channels of the ATSR-2.

Because the TASCO radiometer installed at the Amburla field site only views the sky vertically, a further relation between the magnitude of the DWSR for vertical viewing and off-nadir zenith angles must be defined in order to accommodate the varying observational geometries utilized by scanning satellite sensors. The relation describing the change in the DWSR with viewing angle on a given day is dependent upon the magnitude of the nadir estimate. Figure 3.4b in Section 3.2 shows that there is variability in this estimate of the magnitude of the DWSR on a daily basis. This suggests that a fixed-coefficient relation dependent upon the magnitude of the DWSR may not give the most accurate estimates of the off-nadir DWSR. However, the ratio between the magnitude of the DWSR for vertical viewing and viewing at larger zenith angles is nearly independent of the nadir estimate of the DWSR. In order to minimize the error in estimating the magnitude of the off-nadir DWSR, a well-defined regression relation may be developed which is based upon the ratio of the relative magnitudes of the DWSR to the nadir estimate, at increasing zenith angles, as shown in Figure 4.11. For Figure 4.11, the DWSR was modelled using LBLRTM with vertical atmospheric profile data derived from 21 radiosondes launched between June and December 2000, 3 sondes from each month. For each sonde the DWSR was modelled at zenith angles of 0, 20, 40 and 60°, cov-

ering the scan angle range of the ATSR-2. The figure shows that for atmospheric profiles characteristic of the Amburla site, the magnitude of the DWSR increases in a non-linear fashion as the zenith angle increases. This is an interesting result as the radiative components, in particular the atmospheric transmittance, are generally considered to be linearly related to the cosine of the zenith angle (Maul, 1983; Sobrino et al., 1991; Prata, 1993). However, Sobrino et al. (1991) also present results from modelling of radiative transfer which show that for a downwards-looking instrument the atmospheric transmittance between the ground and an arbitrary level in the atmosphere varies in a quadratic fashion with increasing zenith angle. As shown in Figure 4.12, there is a strong linear relationship between the DWSR and the atmospheric transmittance, so that the fit of the regression line to the DWSR data in Figure 4.11, which estimates the ratio between the magnitude of the DWSR at a given zenith angle and the nadir estimate, may also be given a quadratic form. These relations for the 11 and 12μm channels of ATSR-2 then allow the DWSR at any zenith angle to be modelled with negligible error, based upon the nadir DWSR estimate.

Further regression relations may be derived using LBLRTM to relate the DWSR estimated from step 3 in Figure 4.9, to the UWSR (step 4 in Figure 4.9) and the atmospheric transmittance (step 5) in each waveband. The relations for the 11 and 12μm channels of the ATSR-2 are shown in Figures 4.12a and b. These regression relations are also very strongly linear (r^2 >0.99), and add only negligible error to the estimates of the UWSR and atmospheric transmittance. In Figures 4.12a and b, the data are plotted independently of zenith angle, as it is only the magnitude of the DWSR which is important when modelling the UWSR and atmospheric transmittance using this approach. As such, these relations may be applied to estimate the UWSR and transmittance from the DWSR irrespective of viewing angle.

The sequence of regression equations represented by Figure 4.9 for the 11 and 12μm channels of the ATSR-2, from which all of the radiative components necessary to apply the RC method of atmospheric correction to satellite-derived TIR data
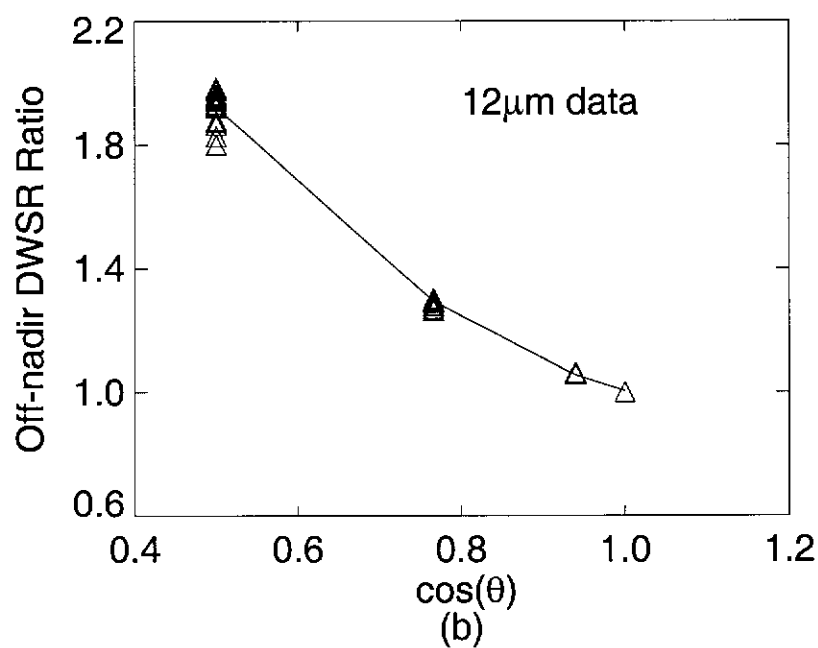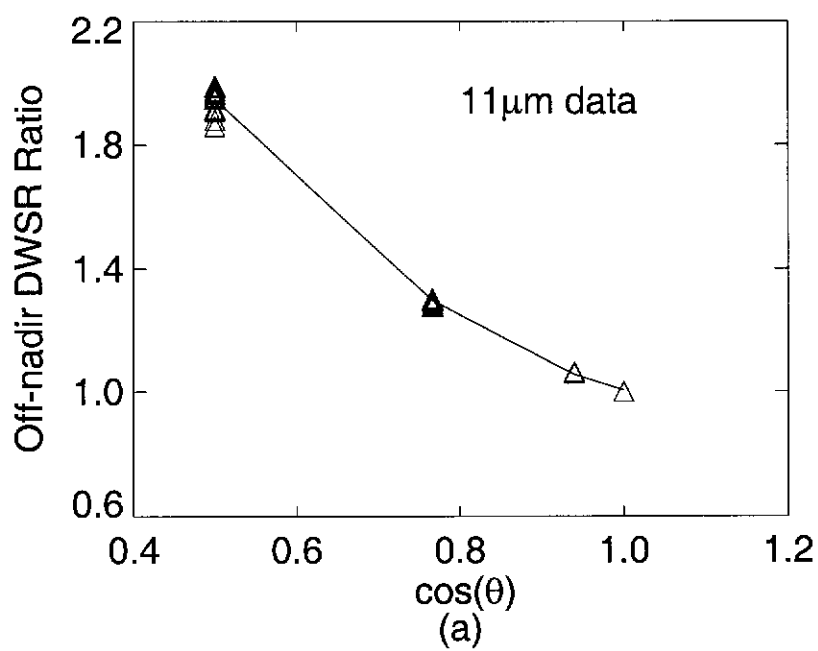
Figure 4.11: Regression relationships for determining the ratio between the modelled DWSR at nadir and at increasing zenith angles for the 11 and 12μm channel of ATSR-2.
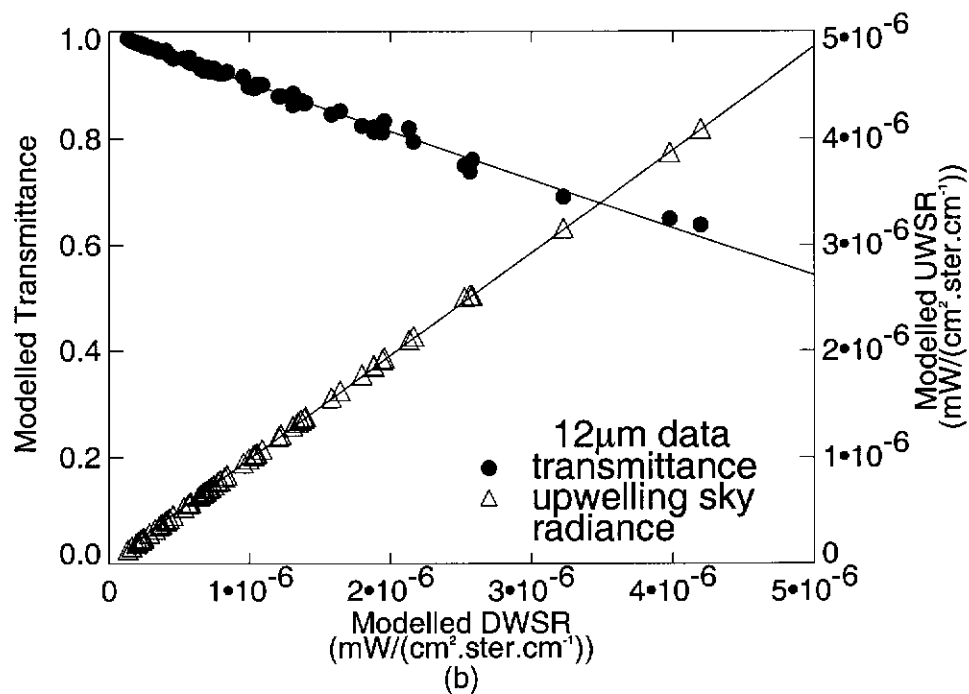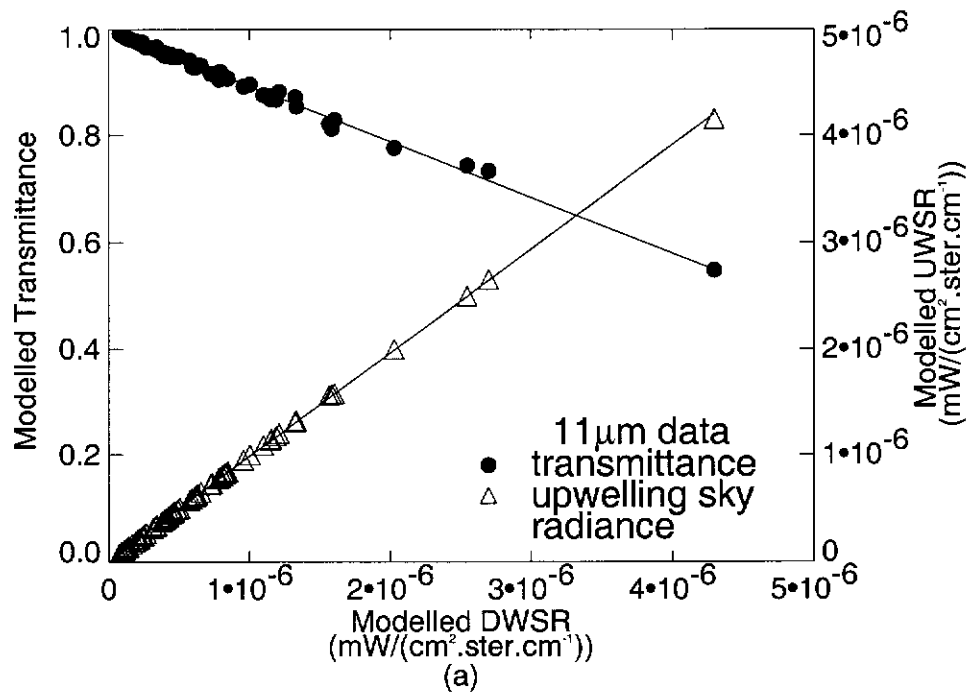
Figure 4.12: Regression relationships for estimating the UWSR and transmittance from the DWSR for a) the 11 and b) 12μm channels of ATSR-2.

may be derived, are;

<u>11μm</u>

$TASCO_{modelled}$ DWSR to modelled $ATSR - 2_{11\mu m}$ DWSR at $\theta = 0°$;

$B(T_{sky})_{11\mu m} \downarrow_{modelled} = 1.1961 \times B(T_{sky})_{TASCO} \downarrow_{modelled} -7.0793E - 7.$

$B(T_{sky})_{11\mu m} \downarrow_{modelled}$ at $\theta = 0°$ to $B(T_{sky})_{11\mu m} \downarrow_{modelled}$ at zenith angle θ;

ratio = 2.368 $cos\theta^2$ - 5.436 $cos\theta$ + 4.073,

$B(T_{sky})_{11\mu m} \downarrow_{modelled} (\theta) = ratio \times B(T_{sky})_{11\mu m} \downarrow_{modelled} (\theta = 0°).$

$B(T_{sky})_{11\mu m} \downarrow_{modelled} (\theta) to B(T_{sky})_{11\mu m} \uparrow_{modelled} (\theta)$;

$B(T_{sky})_{11\mu m} \uparrow_{modelled} (\theta) = 0.9750 \times B(T_{sky})_{11\mu m} \downarrow_{modelled} (\theta) + 1.069E - 9.$

$B(T_{sky})_{11\mu m} \downarrow_{modelled} (\theta)$ to $\tau_{11\mu m\,modelled}(\theta)$;

$\tau_{11\mu m\,modelled}(\theta) = -104193.469 \times B(T_{sky})_{11\mu m} \downarrow_{modelled} (\theta) + 0.996.$

<u>12μm</u>

$TASCO_{modelled}$DWSR to modelled$ATSR - 2_{12\mu m}$DWSR at $\theta = 0°$;

$B(T_{sky})_{12\mu m} \downarrow_{modelled} = 1.8332 \times B(T_{sky})_{TASCO} \downarrow_{modelled} -1.1087E - 6.$

$B(T_{sky})_{12\mu m} \downarrow_{modelled}$ at $\theta = 0°to B(T_{sky})_{12\mu m} \downarrow_{modelled}$ at zenith angle θ;

ratio = 2.279 $cos\theta^2$ - 5.247 $cos\theta$ + 3.979,

$B(T_{sky})_{12\mu m} \downarrow_{modelled} (\theta) = ratio \times B(T_{sky})_{12\mu m} \downarrow_{modelled} (\theta = 0°).$

$B(T_{sky})_{12\mu m} \downarrow_{modelled} (\theta)$ to $B(T_{sky})_{12\mu m} \uparrow_{modelled} (\theta)$;

$B(T_{sky})_{12\mu m} \uparrow_{modelled} (\theta) = 0.968 \times B(T_{sky})_{12\mu m} \downarrow_{modelled} (\theta) + 2.2332E - 8.$

$B(T_{sky})_{12\mu m} \downarrow_{modelled} (\theta)$ to $\tau_{12\mu m\,modelled} (\theta)$;

$\tau_{12\mu m\,modelled}(\theta) = -90546.82 \times B(T_{sky})_{12\mu m} \downarrow_{modelled} (\theta) + 0.995.$

The algorithms for modelling the radiative components described in this section will be applied to the investigation of the process of atmospheric correction of LST data derived from the ATSR-2 satellite sensor over the Amburla field site, using the RC approach to atmospheric correction, in Section 4.2.5. Importantly, however, in Section 4.2.1, the RC method was only validated under ideal conditions, for which case the RC approach was shown to be accurate to within ±0.01 K. In practice, however, the value of the radiative components will not be known exactly, and it is

therefore necessary to derive an estimate of the uncertainty with which they may be known, in order to evaluate the accuracy of the RC method of atmospheric correction under realistic conditions. The following two sections define the accuracy with which the radiative components may be known when estimated using the combination of radiative transfer modelling and *in situ* data as described in this section.

4.2.3 Accuracy of Radiosonde Data

For the Thangoo and Amburla field sites, the main source of atmospheric data applicable to atmospheric correction of satellite TIR data are radiosonde profiles. The problem with such data is that they are acquired some distance from the field sites, and at times which do not coincide with the overpass of the ATSR-2 satellite. Both of these factors degrade the quality of information contained in the profiles for purposes of atmospheric correction. However, the remote location of the field sites make frequent *in situ* radiosonde launches impractical, such that the radiosonde data derived from sondes launched at the Broome and Alice Springs airports are the most practical data sources for characterizing the atmospheric structure for the total atmospheric column on a continual basis. Given this fact, it is necessary to clarify the accuracy with which radiosonde data can characterize the atmospheric vertical structure at the field sites, particularly for validation studies of satellite-derived LST.

The radiosonde measures both the atmospheric temperature and the atmospheric dew point temperature, from which the relative humidity may be determined. The accuracy with which radiative components may be simulated using radiosonde data as input to a radiative transfer model, such as LBLRTM (Clough *et al.*, 1996), is fundamentally dependent upon the accuracy with which the radiosonde measures temperature and humidity. Using the technical specifications for the Vaisala RS80 model of radiosonde, obtained from CSIRO Atmospheric Research (Cechet, 2001), the uncertainty in temperature measurement may be calculated from a combination of uncertainty deriving from the resolution and reproducibility of temperature measurements, and the repeatability of calibration of the instrument, to be $\pm 0.5°$ C.

This level of uncertainty is applicable to each temperature measurement, and may be propagated through the calculations from which the water vapour mixing ratio is calculated for input to LBLRTM. The mixing ratio is calculated from the radiosonde data by applying an algorithm used by the Bureau of Meteorology in Perth, Western Australia (van Burgel, 1999).

In estimating the uncertainty in the main LBLRTM input quantities, it has been assumed that the impact of uncertainty in pressure and height measurements on the upwelling and downwelling atmosphere-emitted radiance and the transmittance is negligible. The uncertainty in the radiative components, due essentially to the uncertainty in temperature measurement, has been calculated using 20 radiosonde profiles, launched from the Broome airport between June and December 1998. Broome data was chosen because, as the atmosphere is generally humid, the derived uncertainties in the radiative components will form an upper limit applicable to radiosonde data from other areas such as Amburla.

From the original 20 radiosondes, 83 input files to LBLRTM were generated, which encompass the range of zenith angles used by the ATSR-2. It is assumed that the largest atmosphere-emitted radiance and the smallest transmittance values will be obtained when the atmosphere is warmest and most humid, and that the smallest atmosphere-emitted radiance and largest transmittance occur in the coolest and driest conditions. Hence, to estimate the magnitude of the uncertainty in the radiative components, for each of the 83 input files the radiosonde-measured temperatures were edited such that the uncertainty calculated from the technical specifications ($\pm 0.5°C$) was added to each temperature reading in the file to simulate the warmest possible atmosphere, and a second set of input files were generated by subtracting the uncertainty in temperature, to simulate the coolest possible atmosphere. For the warmer case, the water vapour mixing ratio was positively incremented by the uncertainty calculated for the mixing ratio, so as to simulate the warmest, most humid atmosphere. For the cooler case, the water vapour mixing ratio was decremented, so as to simulate the driest, coolest atmosphere possible. Using these files as input

Upwelling Sky Radiance				
	ΔRC_T	ΔRC_W	ΔRC_{total}	(%)
11μm	1.314E-8	2.892E-7	2.896E-7	7.9
12μm	1.841E-7	2.826E-7	3.373E-7	9.2
Downwelling Sky Radiance				
	ΔRC_T	ΔRC_W	ΔRC_{total}	(%)
11μm	1.443E-8	2.720E-7	2.724E-7	7.2
12μm	3.357E-7	3.637E-7	4.950E-7	12.7
Transmittance				
	ΔRC_T	ΔRC_W	ΔRC_{total}	(%)
11μm	0.003	0.025	0.025	3.7
12μm	0.004	0.026	0.026	4.0

Table 4.3: Estimated magnitude of uncertainty in DWSR, UWSR ($mW/(cm^2.ster.cm^{-1})$) and atmospheric transmittance derived from radiosonde profiles using the radiative transfer model LBLRTM. Uncertainties are derived from instrument error in the measurement of atmospheric temperature and humidity. ΔRC_{total} represents the absolute uncertainty in each radiative component. The column headed "%" is the percentage uncertainty relative to the mean value of each radiative component over the 20 days of the investigation.

to LBLRTM gives the extremes of the possible range of magnitudes of the radiative components, given the level of uncertainty in the temperature and humidity measurements. The results of this process are summarized in Table 4.3.

In the table, 'ΔRC_T' and 'ΔRC_W' represent components of uncertainty arising from the radiosonde estimates of temperature and humidity respectively. They are treated as independent quantities, and the total uncertainty associated with the estimate of each radiative component, 'ΔRC_{total}', namely the upwelling and downwelling sky radiance and the atmospheric transmittance, are then given by the equation (Kirkup, 1994);

$$\Delta RC_{total} = ((\Delta RC_T)^2 + (\Delta RC_W)^2)^{1/2}, \qquad (4.3)$$

where,

ΔRC_{total} = the maximum possible absolute error in the estimate of each ra-

diative component in units of that quantity (eg for downwelling sky radiance the units are $mW/(cm^{-2}.ster.cm^{-1})$,

ΔRC_T = the maximum possible error in the modelled radiative component due to uncertainty in the radiosonde temperature estimate, and

ΔRC_W = the maximum possible error in the modelled radiative component due to uncertainty in the radiosonde humidity estimate.

In the table, the column headed '%' is the percentage uncertainty relative to the mean value of each radiative component over the 20 days of the investigation. The percentage uncertainty quoted in Table 4.3 for each of the radiative components may be considered to be representative of the measurement uncertainty associated with the use of radiosonde measurements of temperature and humidity in LBLRTM. The characteristic atmosphere for the Thangoo field site was chosen for the study as it is often very humid, particularly in the wet season. As such, the results in Table 4.3 form an upper bound on the estimate of the uncertainty in the radiative components simulated using the radiative transfer model.

In Section 4.2.5, the RC method of atmospheric correction is applied to SBT data acquired by the ATSR-2 in order to estimate the size of the correction which should be applied to the data so as to accurately account for atmospheric effects. The accuracy of such a correction is dependent upon how well the value of the radiative components are known, both in terms of the uncertainty in the actual measurements made by the radiosonde, and how representative the radiosonde measurements are of the vertical atmospheric profile over the geographical location of the field site. This section has discussed the uncertainty in the radiosonde measurements themselves. The following section examines how representative the radiosonde-derived vertical atmospheric profile is of the atmospheric structure over the Amburla field site due to both spatial and temporal differences between when the sonde is launched at the Alice Springs airport, some 80 km distant, and when the data are applied in the analysis of *in situ* SBT measurements at the field site. Such an

analysis is also important in quantifying the accuracy with which firstly radiative components and subsequently an atmospheric correction term may be defined using the available atmospheric data.

4.2.4 Spatial and Temporal Variability of Atmospheric Structure

At the Thangoo field site atmospheric information is limited. Radiosondes launched on a daily basis from the Broome airport, approximately 25 km distant, are the only regular source of atmospheric data. Using the radiosonde data alone, it is not possible to derive any information on the spatial or temporal relationship between the atmospheric structure at the Thangoo field site and the airport, which is important if such data are to be used in the atmospheric correction of satellite-derived SBT data from the field site. In order to do this, *in situ* instrumentation is required so that comparisons between the atmospheric structure derived from the radiosonde and from the field site, at the time of the airport sonde launch, can be made. At the Amburla field site, situated some 80 km distant from the Alice Springs airport, the scanning infrared radiometer provides comparison data by utilizing the zenith sky-view, which the radiometer makes once every cycle, to measure the DWSR. At times coincident with radiosonde launches, the *in situ* DWSR data may be compared to the equivalent downwelling radiance simulated using the radiosonde data as input to LBLRTM, for the waveband of the TASCO radiometer. Analysis of such coincident data estimates the temporal variability of the atmospheric thermodynamic structure at both the radiosonde launch site and the field site location, as well as quantifying the spatial variability in atmospheric properties when *in situ* measurements are taken at times coincident with the launch of a sonde. It is important to note that, by itself, the radiosonde-derived DWSR estimates only take into account atmospheric structure from the surface to between 10 and 20 km. Statistical averages of the vertical extent of the atmosphere sampled by radiosonde compiled

by Maher and Lee (1977), between 1957 and 1975 from meteorological data for the Alice Springs airport, show that the sonde ascent the atmosphere is closer to 30 km. To compensate for this difference in vertical coverage, the radiosonde profiles of temperature and humidity used in this work have been extended to the upper boundary of the atmosphere (taken to be an atmospheric pressure of 10 mb) using the monthly climatological averages given by Maher and Lee (1977).

Figure 4.13 shows the correlation between the *in situ* measurement of DWSR at 0830, 1030 and 2330 hrs local time, and the DWSR modelled using LBLRTM, with atmospheric profile data from the radiosonde launched at 0830 hrs from the Alice Springs airport, as input. The figure shows a good correlation between the *in situ* TASCO radiometer data and the DWSR modelled using LBLRTM, for the coincident time of the launch of the radiosonde. Figure 4.13a suggests acceptable spatial correspondence (r^2=0.695) between the atmospheric structure over the airport and the field site, at coincident times of *in situ* DWSR measurement and radiosonde launch. As the offset between the time of the radiosonde launch and the *in situ* DWSR measurement increases, the correlation between the two DWSR datasets decreases. There is only a small decrease in the value of the correlation coefficient between Figure 4.13a, at 0830 hrs local time, and Figure 4.13b, at 1030 hrs ($r^2 = 0.625$), which is a positive result for atmospheric correction of LST data derived from the descending pass overpass of the Amburla field site by ATSR-2 (approximately 1030 hrs, local time). Although there is a 9 hour offset between the ascending overpass of ATSR-2 at 2330 hrs (local time) and the radiosonde launch at 0830 hrs (local time) the following morning, the value of the correlation coefficient ($r^2 = 0.713$) between the *in situ* and modelled estimates of the DWSR, as shown by Figure 4.13c, is very similar to the correlation coefficient between the *in situ* and modelled DWSR data for 0830 hrs. This results suggests that during the night and early morning the properties of the atmosphere may be consistent over large spatial scales, and that changes in the atmospheric state occur slowly. In part, this arises from using clear sky satellite data sets which, significantly, will avoid

passage of frontal systems. In the morning, as solar heating begins to impact the radiative properties of the land surface and atmosphere, the correlation coefficient between the *in situ* and modelled data begin to decrease more rapidly. Interestingly, the launch of the radiosonde at 0830 hrs coincides with the time when solar heating begins to initiate changes to the angular distribution of surface brightness temperature measured by the scanning radiometer at the Amburla field site. The evolution of the diurnal cycle of SBT from the Amburla field site is analysed extensively in Chapter 5.

Together, the data plotted in Figures 4.13a, b and c show that the correlation between the atmospheric state measured by the radiosonde and that inferred from measurements of DWSR made by the *in situ* radiometer is nearly constant during the night, but degrades as the day progresses and the surface and atmosphere warm. The least squares analysis provides an estimate of the uncertainty in the modelled radiative components and quantifies the impact of using atmospheric profiles in the atmospheric correction process that may be offset both spatially and temporally. The regression approach allows the impact of the changing atmospheric state to be evaluated for atmospheric conditions common to the Amburla field site, which is important when determining how accurately LST at the field site may be estimated by satellite sensors.

For this work, such differences between the *in situ* and modelled estimates of the DWSR may be characterized by a least squares regression between the *in situ* and modelled DWSR data. The results suggest that the combination of *in situ* and radiosonde data is suitable for use as the basis of the RC method of atmospheric correction for remotely sensed LST data. However, due to the location and time of the launch of radiosondes, there is significant uncertainty associated with the estimation of the magnitude of each of the radiative components using the regression approach. Table 4.4 summarizes the uncertainty in the estimation of the DWSR, UWSR and atmospheric transmittance from the regression approach. The estimates of uncertainty are given in the table as a percentage of the mean value of each radia-
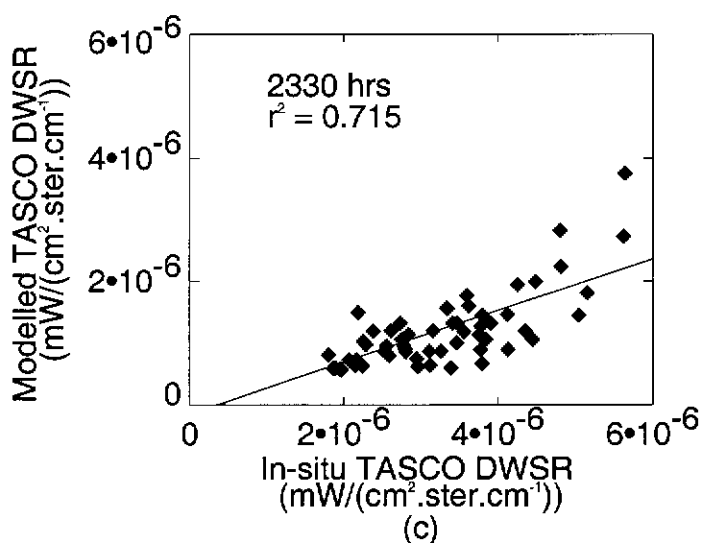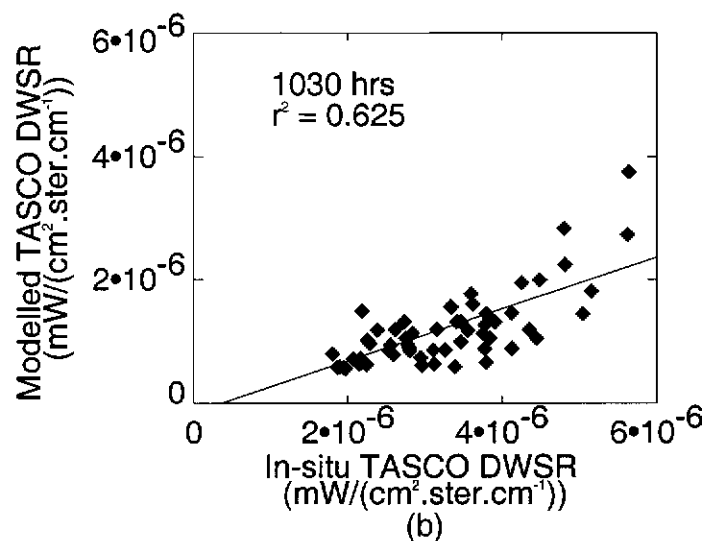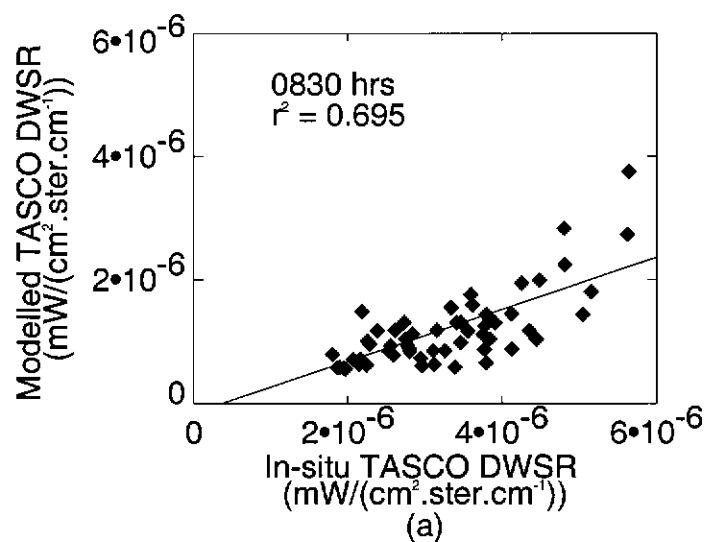
Figure 4.13: Regression relations between *in situ* and modelled TASCO DWSR estimates at a) the time of the radiosonde launch (0830 hrs), b) the time of the descending ATSR-2 overpass 2 hours later (1030 hrs), and c) the time of the ATSR-2 ascending pass 9 hours earlier (2330hrs).

108

tive component for the period of study between June and December 2000, for which there were *in situ* measurements of the DWSR and radiosonde measurements of the vertical atmospheric profile at the time of the launch of the radiosonde and of the overpass of the field site by the ATSR-2 satellite sensor. The data in the table are for the time of the ascending overpass of the field site by the ATSR-2. The night-time uncertainty estimates are given as they are generally a few tenths of a percent larger than the daytime estimates for the descending overpass of the ATSR-2 because the mean values of UWSR and DWSR are lower at night and the percentage error is therefore slightly higher (the percentage error in the transmittance is therefore slightly underestimated, however, the difference is negligible). The data in Table 4.4 represent an upper bound on the uncertainty in the estimates of each radiative component.

To define the total uncertainty in the DWSR, UWSR and atmospheric transmittance, when these radiative components are estimated using the combination of *in situ* measurements of the DWSR from the Amburla field site and modelling of radiative transfer, with radiosonde-derived atmospheric profile data as input, the uncertainty estimates for each radiative component given in Table 4.4 may be added to the uncertainty estimates in Table 4.3. These estimates of uncertainty are derived from the accuracy with which the radiosonde instrumentation is able to measure the atmospheric temperature and humidity. The total uncertainty associated with the estimation of each radiative component is give in Table 4.5. Again, the estimates are expressed as a percentage of the mean value of each radiative component for conditions representative of the Amburla field site. Clearly, the spatial and temporal offsets between the *in situ* data acquisition and the radiosonde launch have the largest impact on the estimates of the DWSR, UWSR and atmospheric transmittance. Fortunately, the spatial and temporal offsets do not affect the estimates of the transmittance as much as the DWSR and UWSR. This is a favourable result for the atmospheric correction process, as the atmospheric transmittance is a coefficient of the surface-leaving radiance and may therefore have large effects on the at-sensor

109

	Downwelling Sky Radiance (%)	Upwelling Sky Radiance (%)	Transmittance (%)
11μm	15.2	15.6	0.5
12μm	8.3	11.9	3.3

Table 4.4: Estimated magnitude of uncertainty in DWSR and UWSR $(\mathrm{mW/(cm^2.ster.cm^{-1})})$ and transmittance due to spatial and temporal variability of atmospheric structure, derived from the set of regression equations for the 11 and 12μm channels of the ATSR-2.

	Downwelling Sky Radiance (%)	Upwelling Sky Radiance (%)	Transmittance (%)
11μm	22.4	23.5	4.2
12μm	21.0	21.1	4.8

Table 4.5: Estimated total relative uncertainty in in DWSR and UWSR $(\mathrm{mW/(cm^2.ster.cm^{-1})})$ and transmittance due to the combination of uncertainty in radiosonde measurements and spatial and temporal variability of atmospheric structure, for the 11 and 12μm channels of the ATSR-2.

radiance if its value is not well known.

In the ideal case, it would be desirable to use more accurate estimates of the radiative components in the RC approach to atmospheric correction. For example this could be achieved in the future by launching radiosondes from the location of the Amburla field site coincident with satellite-overpass times. Alternatively, a multi-sensor approach (Ma *et al.*, 2002) to remote sensing of LST which combines data collected simultaneously by a number of different sensors aboard the same satellite platform (eg. NASA's *'Terra'* satellite (NASA, 2002)) could be employed. For the present, however, this work is confined to the use of the regression approach to model the DWSR, UWSR and atmospheric transmittance. This provides the best estimate available of these quantities important in the atmospheric correction process.

The preceding sections in this chapter have described the RC approach to atmospheric correction, defined an algorithm in which the necessary radiative components for this approach may be modelled, and assessed the accuracy with which

each of these radiative components may be known, using a combination of *in situ* measurements of the DWSR and modelling of radiative transfer, with vertical atmospheric profile data derived from radiosondes as input to the radiative transfer model LBLRTM. In the following section these techniques are applied in a study of the RC approach to atmospheric correction for LST data derived from ATSR-2 TIR LST data for the Thangoo and Amburla field sites.

4.2.5 Magnitude of Atmospheric Correction

The process of atmospheric correction is performed on satellite-based estimates of the SBT so as to derive an accurate estimate of the LST. Following the definition given by Norman and Becker (1995) (see Section 2.2.1), this is the closest possible radiometric estimate of the thermodynamic temperature of the land surface. Earlier in this chapter, the RC approach to atmospheric correction was described, which utilizes modelled estimates of the DWSR, UWSR and atmospheric transmittance derived from the radiative transfer model LBLRTM. In this section, the study of the atmospheric correction of the SBT data from the Amburla and Thangoo field sites, shown in Section 4.1, utilizing the RC approach as given by (4.1), begins by describing the radiative interaction between the land surface and the atmosphere. By investigating the change in the magnitude of the atmospheric correction term with the change in other physical variables, such as the surface emissivity, as well as the value of the satellite-derived SBT itself, an explanation for the observed form of the seasonal variation of dBT in Section 4.1 (Figures 4.7 and 4.8) emerges.

In this work, the magnitude of the atmospheric correction term is denoted 'ΔT_{AC}', and is defined as the difference between the LST, determined by converting the result from (4.1) to a brightness temperature via a LUT, and the SBT measured by the satellite sensor for the appropriate channel of the sensor. In terms of the temperature estimates used in (4.1), the equation for ΔT_{AC} may be written as;

$$\Delta T_{AC} = T_{sat} - T_S, \qquad\qquad (4.4)$$

where,

ΔT_{AC} = the magnitude of the atmospheric correction term,

T_{sat} = the SBT estimate made by the satellite, and

T_S = the LST estimate for the satellite measurement after

atmospherically correcting T_{sat} using (4.1).

As shown by (4.1), the magnitude of the atmospheric correction term is dependent upon both the atmospheric radiative components, namely the DWSR, UWSR and atmospheric transmittance, as well as the surface emissivity. In order to illustrate the dependence of ΔT_{AC} upon the surface emissivity, the average magnitude of ΔT_{AC} for 3×3 pixel arrays centred upon the location of the Amburla and Thangoo field sites, for both the nadir and forward views in the 12μm channel of the ATSR-2, were calculated for a series of day and nighttime overpasses of each field site. It is important to note that, although the work described in this section concentrates on data from the 12μm channel of the ATSR-2, the approaches described are equally valid for the 11μm channel of the ATSR-2, as well as the TIR channels of other satellite sensors. Data for the 12μm channel has been chosen to illustrate the outcomes of the investigation into atmospheric correction described in this section, because the magnitude of atmospheric correction is largest in the 12μm TIR channel, and, as such, the results are upper-bound estimates of the impact of the atmosphere upon the satellite-retrieval of LST.

The mean of the ΔT_{AC} values derived from the collection of overpasses of each field site, by the ATSR-2 satellite sensor, are plotted for the Amburla site in Figure 4.14 and for the Thangoo site in Figure 4.15. The data for each site are further separated into day (Figures 4.14a, 4.15a, 4.16a and 4.17a) and night (Figures

4.14b, 4.15b, 4.16b and 4.17b) in order to assess the impact of the atmosphere on the surface-leaving radiance under the different conditions characteristic of each of the two field sites. For both field sites, the investigation shows that ΔT_{AC} may be linearly related to both the surface emissivity and the SBT.

In Figures 4.14 and 4.15, the value of ΔT_{AC} is shown to be linearly related to the surface emissivity. For the plots of SBT data from the 12μm channels of ATSR-2, for which the satellite overpass is coincident with a radiosonde launch, have been atmospherically corrected using (4.1). The surface emissivity was incremented between 0.90 and 1.00 in steps of 0.02, and at each value of the surface emissivity the mean of ΔT_{AC}, calculated via (4.4), was obtained for the set of SBT data from the satellite overpasses, for both the nadir and forward views of the sensor. In each of the figures the uncertainty in the data, represented by the error bars, is calculated by propagating the uncertainty in the modelled estimates of each of the radiative components (see Table 4.5 in the previous section) through the calculation of ΔT_{AC} described by (4.1) and (4.4). For the Amburla site, using the estimates of the uncertainty in the radiative components given in Table 4.5, the uncertainty in the value of ΔT_{AC} is 3–4 K. Without consideration of the spatial and temporal contribution to the uncertainty in the estimate of each radiative component, when the uncertainty is due only to the measurement accuracy of the radiosonde instrumentation (see Table 4.3 in Section 4.2.3) gives an uncertainty of 2.5–3.5 K for estimates of ΔT_{AC} is obtained. For the Thangoo field site, the atmosphere is more humid, and as a result the DWSR and UWSR are larger and the atmospheric transmittance is lower. Consequently, the uncertainty in estimates of ΔT_{AC} for the Thangoo site are larger than for the Amburla site. Using the uncertainty estimates given in Table 4.5 for the Thangoo case (though the calculation of the contribution of the spatial and temporal differences between the radiosonde launch site and time to the total uncertainty are strictly only valid for the Amburla site, they are used in the Thangoo case in lieu of similar data), the uncertainty in the estimation of ΔT_{AC} is 4.5–9.5 K. Using the estimates of the uncertainty in the radiative components from Table 4.3,

the analysis gives 3.5–7.5 K. In general, to derive ΔT_{AC} in humid conditions to the same level of accuracy as in arid/semi-arid conditions requires that the magnitude of each radiative component be known much more exactly.

It is also worth noting that, for the two field sites, assuming an uncertainty of half that stated for each radiative component in Table 4.3 gives an estimate of the uncertainty in ΔT_{AC} to within 1.5–2 K for the Amburla, and an uncertainty estimate of 2–4 K for the Thangoo field site. Such a level of accuracy for vertical atmospheric profile data may be potentially achievable from new satellite sensors such as the Atmospheric Infrared Sounder (AIRS) (BAE Systems, 2002). The application of such high quality atmospheric data to atmospheric correction algorithms, such as those described in this thesis, has the potential to markedly improve the accuracy with which ΔT_{AC} may be estimated using this approach in the future.

In Figures 4.14a and b, data from the Amburla field site for 1998 and 2000 are combined to describe the atmospheric correction process in low PW scenarios. Because the transmittance is generally high, and the atmospheric contributions (the UWSR and surface-reflected DWSR) to the at-sensor radiance are small in such conditions, the atmospheric correction process results in a negative value of ΔT_{AC}. This means that the atmospherically corrected estimate of the LST is warmer than that of the initial SBT retrieved by the satellite, which is also the case for the more humid Thangoo case, although, as will be discussed, the humidity of the subtropical atmosphere noticeably impacts the atmospheric correction process and thereby the estimation of ΔT_{AC}.

The major factor which influences the magnitude of ΔT_{AC} using the RC approach is the choice of surface emissivity. Figures 4.14 and 4.15 show that ΔT_{AC} may vary by up to 6 K over the range of surface emissivity from 0.90 to 1.00. For a given value of the surface emissivity the impact on the magnitude of ΔT_{AC} of the change in the value of the radiative components between the nadir and forward zenith viewing angles of the ATSR-2 sensor is small, being less than 2 K at $\epsilon = 0.90$. However, of importance for remote sensing of LST is the way in which the changes in the
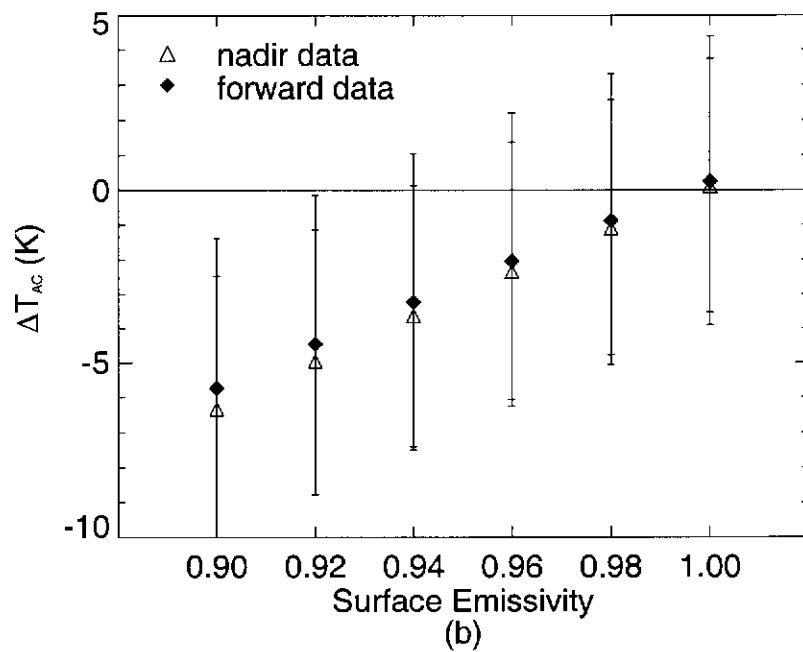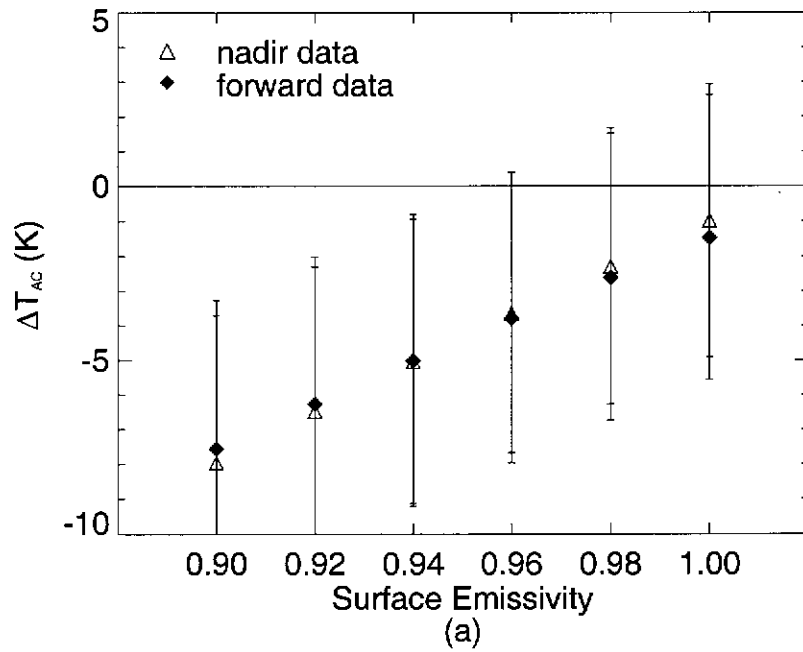
Figure 4.14: The magnitude of the atmospheric correction term, ΔT_{AC} , derived using $12\mu m$ ATSR-2 data from 2000 and plotted against the surface emissivity for a) day, and b) nighttime overpasses of the Amburla field site. Triangles show nadir data. Filled diamonds show forward view data.

115
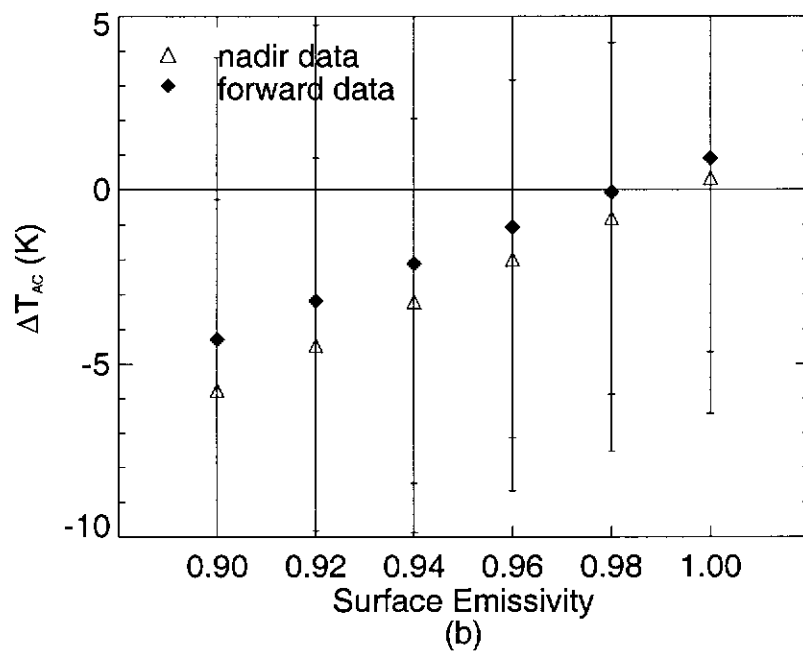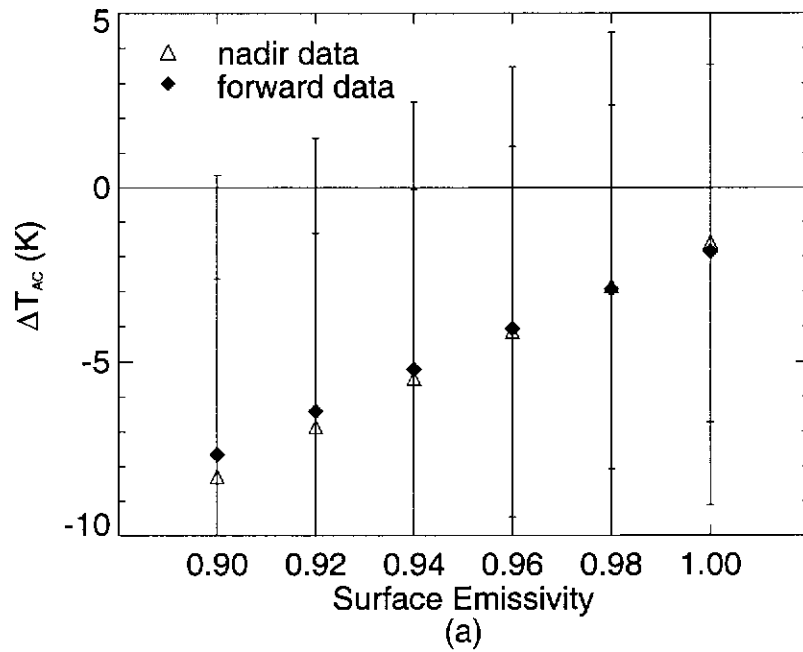
Figure 4.15: The magnitude of the atmospheric correction term, ΔT_{AC}, derived using 12μm ATSR-2 data from 1998 and plotted against the surface emissivity for a) day, and b) nighttime overpasses of the Thangoo field site. Triangles show nadir data. Filled diamonds show forward view data.

magnitude of the radiative components affect the rate of change of ΔT_{AC} with the surface emissivity between the nadir and forward views of the satellite sensor.

During the day, for the Amburla field site (Figure 4.14a) the change in ΔT_{AC} over the range in surface emissivity values is greater for the nadir view than that for the forward view. This occurs because as the surface emissivity decreases, the relative impact of the atmospheric radiative components upon the value of ΔT_{AC} increases. The DWSR and UWSR are larger at off-nadir zenith angles and the atmospheric transmittance is smaller, hence the combined atmospheric component of ΔT_{AC} is larger. In this low emissivity scenario, for the forward view of the ATSR-2 sensor, the impact of the reflected DWSR component upon the value of ΔT_{AC} is maximized, since the magnitude of the DWSR increases quadratically with the cosine of the zenith angle (see Section 4.2.2). Consequently, because the surface-reflected DWSR and the UWSR act to increase the at-sensor radiance, the magnitude of ΔT_{AC} for the nadir view of the satellite sensor, at lower values of the surface emissivity, is larger than that for the forward view, at the equivalent surface emissivity. Assuming that the LST is constant for all zenith viewing angles, the nadir satellite estimate of the SBT will be cooler than the forward estimate. In the higher surface emissivity scenario, however, the impact of the DWSR upon ΔT_{AC}, through the surface reflected component, is not as great. Hence, for this case, the magnitude of ΔT_{AC} for the nadir view becomes less than the magnitude of ΔT_{AC} for the forward view of the sensor. The nadir SBT estimate is subsequently warmer than the estimate from the forward view of the sensor, at equivalent values of the surface emissivity. Although the difference between ΔT_{AC} in the nadir and forward viewing directions in Figure 4.14a is small compared to the uncertainty estimate the trend in the results from the figure is important for the construction of DA algorithms for LST retrieval (Prata, 1993; Sobrino et al., 1996) since they show that it may not always be assumed that nadir estimates of SBT will be warmer than SBT estimates made by the satellite sensor at larger zenith angles. This point is further illustrated by Figure 4.14b, in which ΔT_{AC} is plotted against the surface emissivity

for nighttime overpasses of the Amburla field site by the ATSR-2 sensor. The figure shows that, at night, the nadir estimate of SBT from ATSR-2 are slightly cooler than the estimate of SBT from the forward view. In relation to Figure 4.14b it is important to note, however, that the average values of ΔT_{AC} plotted in the figure are somewhat dependent upon the SBT estimates from the nadir and forward views of ATSR-2. This fact may be generalized to each of the plots of surface emissivity versus ΔT_{AC} in Figures 4.14 and 4.15. The impact of the SBT upon estimation of ΔT_{AC} is discussed in more detail later in this section.

Figures 4.15a and b show ΔT_{AC} plotted against the surface emissivity for ATSR-2 data from the Thangoo site. For the daytime case, shown in Figure 4.15a, it is apparent that the magnitude of ΔT_{AC} is larger, at the same value of the surface emissivity, than the equivalent value of ΔT_{AC} for the Amburla site from Figure 4.14a. This principally is due to the lower atmospheric transmittance of the humid atmosphere which is characteristic of the Thangoo site. In general, this explains why the magnitude of the atmospheric correction term is larger for subtropical satellite TIR data than for the arid/semi-arid case. Figure 4.15a also shows that for a given surface emissivity, when compared to the more arid case of the Amburla site, shown in Figure 4.14a, the magnitude of ΔT_{AC} for the forward case is smaller relative to the nadir estimate. This is due to the fact that the reflected DWSR and the UWSR components are the major causes of the differences between the magnitude of ΔT_{AC} for the nadir and forward cases. Because the magnitude of the DWSR and UWSR are larger at the Thangoo site than the Amburla site, the contribution of the surface-reflected DWSR and the UWSR to the at-sensor signal, which acts to partially offset the attenuation of the surface-leaving signal by the atmosphere, is increased. Hence, the offset between ΔT_{AC} for the nadir and forward views, at a given surface emissivity is smaller for the Thangoo site than for the Amburla site.

This effect is even more noticeable in the nighttime data from the Thangoo field site shown in Figure 4.15b. The figure shows that the nadir estimate of SBT is always cooler than the forward estimate of SBT at night, and that the magnitude of

ΔT_{AC} for the forward view may be up to 2 K smaller than the nadir estimate due to the impact of the surface-reflected DWSR and the UWSR. Though the DWSR and UWSR accentuate the offset between the nadir and forward estimates of ΔT_{AC}, in order to fully explain why the magnitude of ΔT_{AC} for the forward view is smaller than for the nadir view in the nighttime plots of ΔT_{AC} for the two field sites, it is necessary to consider the dependence of ΔT_{AC} upon the SBT itself, as well as the choice of surface emissivity used in the atmospheric correction process.

ΔT_{AC} is plotted against estimates of SBT derived from the ATSR-2 satellite sensor for the Amburla field site in Figure 4.16, and for the Thangoo site in Figure 4.17. As was the case for Figures 4.14 and 4.15, the estimates of ΔT_{AC} for the nadir and forward channels of ATSR-2 are derived from overpasses of the two field sites for which there were coincident radiosonde launches. In Figures 4.16 and 4.17 the estimates of ΔT_{AC} were once again derived using the RC approach to atmospheric correction. However, this time, the estimates of ΔT_{AC} from each overpass have been averaged over a range of emissivity values between 0.90 and 1.0, and are plotted against SBT estimates from the nadir and forward views of the ATSR-2 sensor. Figures 4.16 and 4.17 show that there are very strong correlations between both the nadir and forward-view estimates of SBT and the value of ΔT_{AC} .

Figure 4.16a shows the strongly linear relationships between the SBT and ΔT_{AC} estimates for the nadir ($r^2 = -0.914$) and forward ($r^2 = -0.877$) views of the land surface of the Amburla field site during the day. This plot explains why it is possible for SBT data from the nadir view of the surface to be cooler than for the forward view. It shows that below an SBT of approximately 290 K the magnitude of ΔT_{AC} for the nadir case is larger than ΔT_{AC} for the forward case. This indicates that the nadir SBT estimate made by the satellite will be cooler than the forward estimate, assuming the LST is independent of the zenith angle of the satellite view of the surface. When the SBT estimate is greater than 290 K the nadir estimate is then warmer than the forward estimate. This is the most common case for the daytime scenario since the SBT at the Amburla site is usually warmer than 290 K, at

119
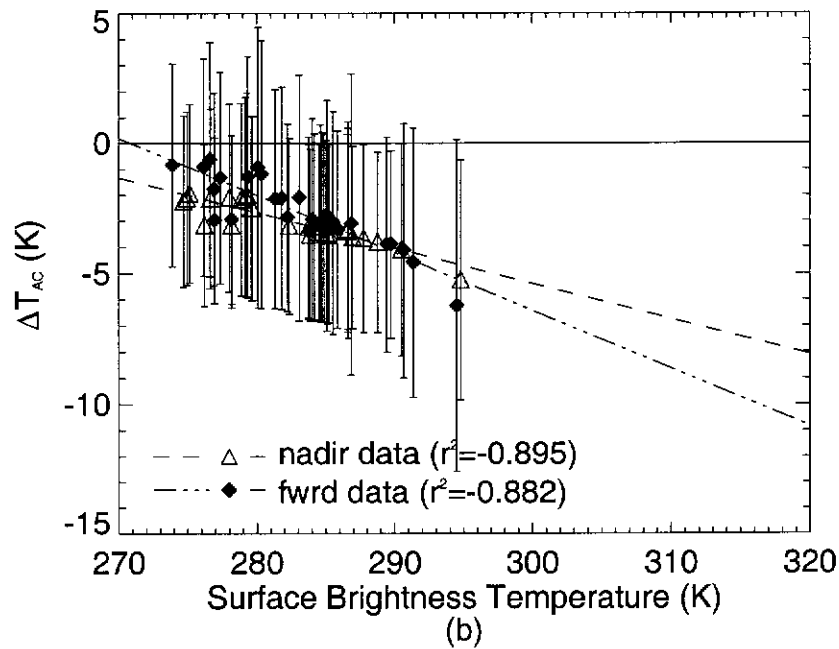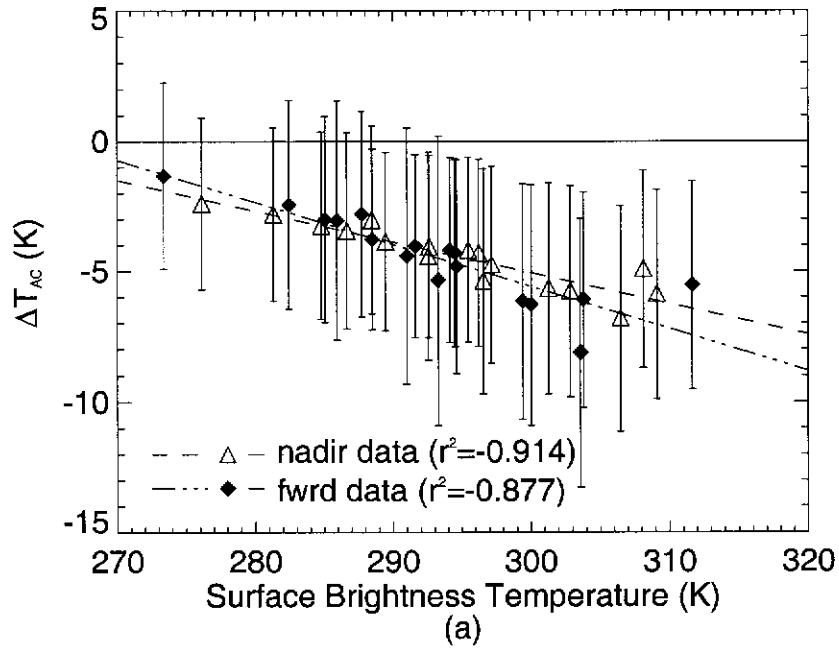
Figure 4.16: The magnitude of the atmospheric correction term, ΔT_{AC}, derived using ATSR-2 data from 1998 and 2000 and plotted against the surface brightness temperature for a) day, and b) nighttime overpasses of the Amburla field site. Triangles show nadir data. Filled diamonds show data from the forward view.

least during the middle part part the day. However, the descending pass of ATSR-2 occurs at approximately 1030 hrs local time, and it is often the case, particularly in winter, that the land surface is still heating up at this time and may not have reached the 290 K threshold by the time of the overpass of the ATSR-2. Consequently, the nadir estimate may be cooler than the forward estimate on occasion, and any LST algorithm used for LST retrieval at this time should be derived with this fact in mind.

Figure 4.16b shows the nighttime scenario for the Amburla field site. The relationship between SBT and ΔT_{AC} are again strong for both the nadir ($r^2 = -0.895$) and the forward ($r^2 = -0.882$) views of the surface. The lines of best fit of the data are similar to those for data acquired during the day. In Figure 4.16 the SBT threshold at which the nadir estimate will be cooler than the forward estimates is perhaps slightly lower than the 290 K for the daytime, however, the interesting fact for the nighttime case is that the majority of the SBT estimates made by the satellite sensor lie below this threshold. This is the reason that the magnitude of ΔT_{AC} for the nadir case is larger than that for the forward case, as noted previously in Figure 4.14. The relationships between SBT and ΔT_{AC}, shown by Figures 4.16a and b, suggest that to achieve the greatest accuracy of LST retrieval different algorithms are required for day and nighttime operation in order to account for the changing properties of the atmosphere and surface between day and night, which result in variation of the magnitude of ΔT_{AC} between the nadir and forward views of the satellite sensor. For the Amburla site, the change in ΔT_{AC} with SBT between day and nighttime conditions is not great. For the nadir view, the difference in ΔT_{AC} between day and night is close to 0 K for nadir and 1 K for the forward view at cooler SBT estimates, and 1 K for nadir and up to 2 K for the forward view for the warmer SBT estimates possible during the day.

Figure 4.17 shows the relationship between ΔT_{AC} and SBT for the Thangoo field site. These two figures only contain data from 1998, resulting in fewer data points than for the Amburla study, particularly at night when atmospheric conditions

limit the number of clear overpasses. During the day at the Thangoo site, Figure 4.17a again shows strong correlations between ΔT_{AC} and SBT ($r^2 = -0.949$ for nadir and $r^2 = -0.935$ for the forward case). The gradients of the lines of best fit are noticeably steeper than for the Amburla site. This is due to the more humid atmosphere and the changes this causes to the DWSR, UWSR and atmospheric transmittance. The threshold at which the magnitude of ΔT_{AC} for the nadir view becomes larger than ΔT_{AC} for the forward view is around 293 K for the Thangoo site during the day. The morning overpass of the ATSR-2 occurs at approximately 1030 hrs local time, so it is again possible that the SBT may be cooler than this threshold at the time of the satellite overpass, most commonly in the dry season between April and August.

For the Thangoo site at night, shown in Figure 4.17b, the number of data is limited and the relationship between SBT and ΔT_{AC} for both the nadir ($r^2 = -0.542$) and the forward ($r^2 = -0.409$) cases is not as well defined as a result. However the figure still shows a similar form to the plots from Figures 4.16a,b and 4.17a. Again, at night, the SBT data mostly lie below then threshold (about 297 K from the figure), so that the nadir satellite estimate of SBT may be expected to be cooler than for the forward view, as was suggested by Figure 4.15b. The increased steepness of the lines of best fit, compared to the Amburla case, mean that at extremes of surface temperature the differences between ΔT_{AC} for the nadir and forward cases will be larger. From Figures 4.17a and b the difference in ΔT_{AC} between day and night may be up to 1 K for the nadir and 1–2 K for the forward case for cool SBT estimates, while for warmer SBT estimates the difference in ΔT_{AC} between day and night predictions may be 2–3 K for nadir and as much as 5 K for the forward view. It is therefore even more important than for the semi-arid case that satellite-based LST algorithms are derived with high regard having been paid to the atmospheric and surface properties specific to the Thangoo field site in order to retrieve LST with the greatest accuracy in subtropical conditions.

Interestingly, Figures 4.17a and b also show that under some conditions, it may
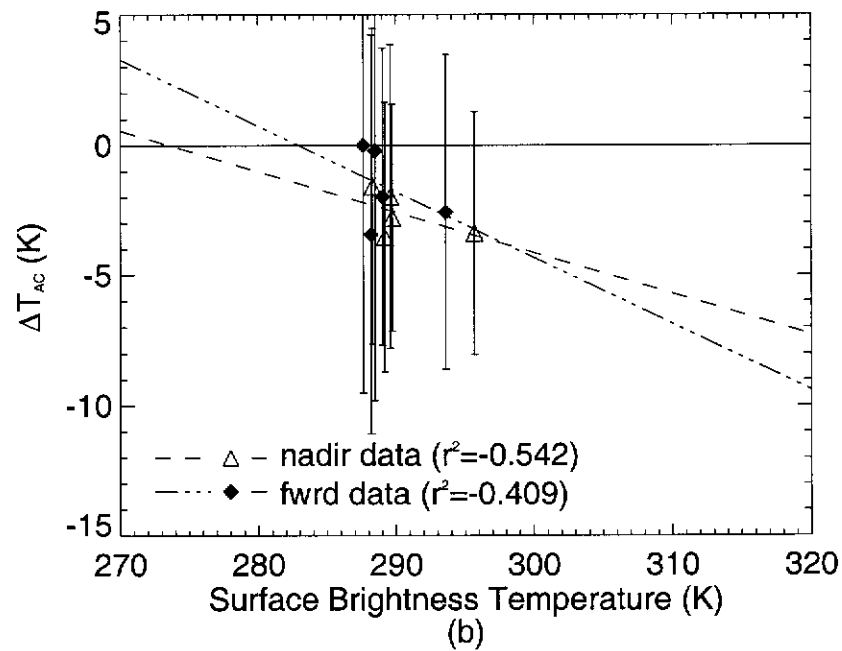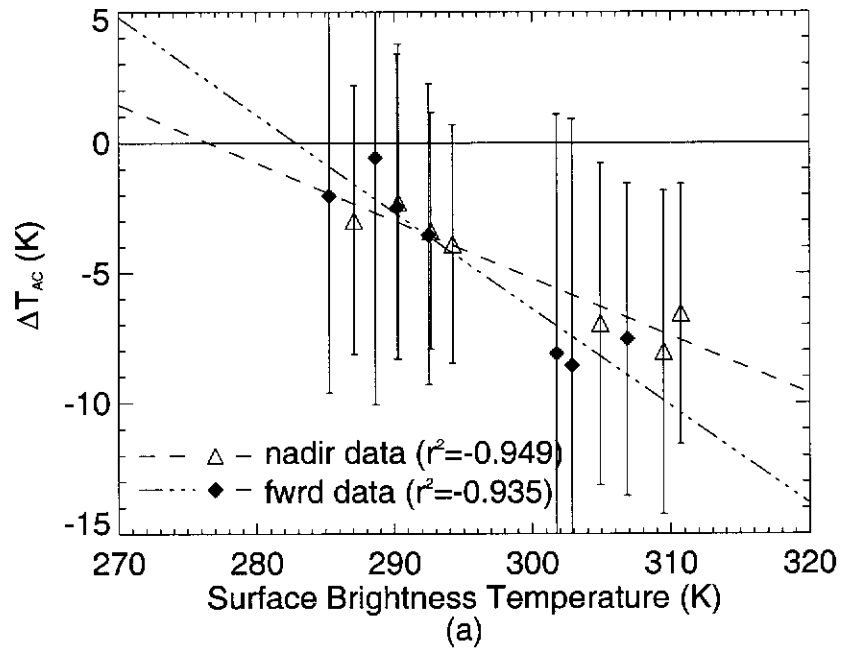
Figure 4.17: The magnitude of the atmospheric correction term, ΔT_{AC}, derived using ATSR-2 data from 1998 and plotted against the surface brightness temperature for a) day, and b) nighttime overpasses of the Thangoo field site. Triangles show nadir data. Filled diamonds show data from the forward view.

be just possible for the value of ΔT_{AC} to become positive. The figures show that for very cool SBT, ΔT_{AC} may become positive, because in these cases, the amount of surface-emitted radiance attenuated by the atmosphere is less than the radiance contribution supplied by the atmosphere to the at-sensor signal. Hence, after the atmospheric correction process, which accounts for the radiative components, the LST estimate is cooler than the initial SBT estimate made by the satellite sensor. Figures 4.16 b for the Amburla site, and Figure 4.15b for the Thangoo site, show that this may occur only at high values of the surface emissivity. Figures 4.17a and b show that the occurrence of positive values of ΔT_{AC} is limited to nighttime conditions the when the temperature is low at the Thangoo site. It is important to note that it is possible for conditions to exist such that ΔT_{AC} will be positive for SBT derived from satellite sensors, although this should rarely happen at the two field sites discussed here, both because the sites are too warm for this to occur, and because the surface emissivity is too far below unity. Of greater importance to satellite-based LST retrieval, however, is that the lines of best fit between ΔT_{AC} and SBT, from which ΔT_{AC} may be estimated, are dependent upon the range of surface emissivity values over which ΔT_{AC} in Figures 4.16 and 4.17 are averaged. Increasing the surface emissivity tends to shift the value of ΔT_{AC} towards zero, while decreasing the surface emissivity shifts the value of ΔT_{AC} away from zero, increasing the magnitude of the atmospheric correction term. Figures 4.16 and 4.17 give a generalized estimate of a simple linear equation for estimating ΔT_{AC} for satellite data, which is applicable over a wide range of surface emissivities. As the surface emissivity estimate is improved, the equation for predicting ΔT_{AC} given an SBT estimate becomes more accurate. It is likely, from work such as that by Takashima and Masuda (1987) and Sobrino and Cuenca (1999), that there exists a significant difference between the values of the surface emissivity for the zenith angles of the nadir and forward views of ATSR-2. In practice, it is only once the value of the surface emissivity at these angles is accurately estimated, that the observed differences between the nadir and forward-view estimates of SBT made by the ATSR-2, depicted in

124

Figures 4.7 and 4.8 may be explained. The differences between the SBT estimates from the nadir and forward views of the ATSR-2 sensor, revealed by these figures, cannot be explained solely in terms of atmospheric impacts. The surface emissivity structure also needs to be understood in order to explain the seasonal distribution of dBT data plotted in these figures. The instrumentation installed at the Amburla field site, such as the scanning infrared radiometer, was designed for exactly this purpose. Chapter 5 of this thesis details the analysis of *in situ* data from the Amburla field site, and links the results from *in situ* investigations to the results from this chapter.

Chapter 4 of this thesis began to investigate the physical basis of the distribution of both SBT and subsequently dBT data characteristic of the Amburla and Thangoo field sites. It is clear from the seasonal distribution of dBT data given in Section 4.1.1 that both atmosphere and surface effects impact the retrieval of LST from the ATSR-2 satellite sensor. The focus of this chapter has been to investigate the impact of atmospheric effects upon the satellite retrieval of LST under different atmospheric conditions, specifically; i) the characteristically dry, semi-arid conditions of the Amburla field site in the Northern Territory, and; ii) the subtropical conditions of the Thangoo field site in the Kimberley region of the far North West of Australia.

In Section 4.1, SBT estimates derived from the TIR channels of the ATSR-2 were presented for the Amburla field site in Figures 4.1 and 4.2, and for the Thangoo field site in Figure 4.3. The data plotted in these figures showed that; i) there was substantial variation in the SBT for both field sites on a daily basis; ii) there was no straight forward relationship between the SBT estimates from the nadir and forward views of the satellite, and; iii) the angular coverage of the ATSR-2 satellite sensor for particular geographic locations is limited. These figures did not, however, provide much insight into the physical processes impacting the satellite retrieval of LST. In Section 4.1.1, plots of the difference between the SBT estimate from the nadir and forward views of the ATSR-2, termed dBT data, for the Amburla field site, (Figures 4.4 and 4.5) and for the Thangoo site (Figure 4.6) were presented

with the intent of beginning to quantify the change in satellite-derived estimates of SBT with viewing angle. Again, there did not appear to be any obvious relationship between these data and the difference in zenith angle between the nadir and forward views of the ATSR-2 sensor. However, when the dBT data were plotted against the Julian day of their acquisition (Figures 4.7 and 4.8), seasonal patterns in the data began to emerge. A definite mid-year minimum was shown to exist in the data acquired during the day at both the Amburla and Thangoo field sites, and also for the Thangoo data acquired during the night. The minimums in the dBT data coincide with the winter months at the Amburla field site and with the dry season at the Thangoo site. Such variation hints that there are seasonally varying physical processes impacting the data, and provides the inspiration to examine the radiative properties of the surface and atmosphere in relation to satellite retrieval of LST.

The investigation of the radiative properties of the atmosphere commenced in Section 4.2.1, based upon the radiative transfer equation given by (2.6) in Section 2.1, and the use of a single channel approach to atmospheric correction of remotely sensed data, as discussed in Section 2.3.3. In Section 4.2.1, the important radiative components in the atmospheric correction process used to estimate T_s, as described by (4.1), were simulated using the radiative transfer model LBLRTM with data from vertical atmospheric profiles derived from radiosonde launches as input. This simulation study, conducted with atmospheric data from the Thangoo field site, showed that using the RC approach to atmospheric correction from Section 4.2.1, it was possible to retrieve the LST (T_s) in (4.1) to with ± 0.01 K, under ideal conditions. Importantly, the surface was assumed to exhibit spectral properties, and the reflected DWSR component was calculated from the directional DWSR for the zenith angle of the satellite view of the surface. In order to apply this approach to the investigation of the angular distribution of ATSR-2 SBT estimates, the DWSR, UWSR and atmospheric transmittance had to be estimated. Section 4.2.2 described the development of an algorithm for estimating each of these quantities for the 11 and 12μm channels of ATSR-2, based upon a combination of *in situ* measurements

126

of the DWSR made by the TASCO radiometer installed at the Amburla field site, measurements of the vertical temperature and moisture profiles form radiosondes launched from the Alice Springs airport, and modelling radiative transfer between the surface and the satellite using LBLRTM. Regression relations were defined allowing each of the necessary radiative components to be estimated from the *in situ* DWSR estimate at the scale of view of the satellite sensor for the times of the ascending (night) and descending (morning) overpasses of the field site by ATSR-2.

Prior to applying the RC approach, utilizing the radiative components estimated via the regression relations, to the investigation into atmospheric correction of satellite-derived LST data from the two field sites, the accuracy with which the radiative components to be used in the RC could be estimated was assessed in Sections 4.2.3 and 4.2.4. The uncertainty in the measurement of the vertical temperature and moisture profiles from the radiosonde instrument specifications was used to model the expected uncertainty in each of the radiative components. Table 4.3 in Section 4.2.3 showed that an error of approximately 10% could be expected in the modelled estimates of the DWSR and UWSR based upon the measurement uncertainty of the radiosonde instrumentation, while an error of around 4% could be expected in the estimate of the transmittance. In Section 4.2.4, spatial and temporal differences between the geographical location of the radiosonde launch site and the time of launch of the radiosonde and the estimate of the DWSR made by the *in situ* radiometer were also assessed. For the times of both the day and nighttime overpasses of the field site by ATSR-2 sensor, these differences increased the uncertainty with which the magnitude of the DWSR and UWSR could be known to approximately 20% and the transmittance to 5%.

Finally, in Section 4.2.5, the dependence of the magnitude of the atmospheric correction term, ΔT_{AC}, defined by (4.4), upon the surface emissivity (Figures 4.14 and 4.15) and the initial SBT estimates (Figures 4.16 and 4.17) was investigated. These results showed that the magnitude of ΔT_{AC} was dependent upon both the surface emissivity and the SBT. For both cases, strong regression relations with very

high correlation coefficients ($r^2 \approx 0.90$) were established for daytime conditions for both field sites and also nighttime conditions at he Amburla field site (nighttime satellite data from the Thangoo field site was limited and the correlation between SBT and ΔT_{AC} was not as strong) which allows the prediction of ΔT_{AC} given an estimate of SBT. Important results from the analysis of the dependence of ΔT_{AC} on SBT are that; i) there are slightly different equations for predicting ΔT_{AC} from SBT for the nadir and forward views of the satellite sensor, and; ii) there exists an SBT threshold below which the magnitude of ΔT_{AC} is greater for the nadir case than for the forward case. This implies that it is possible, particularly at night, for the nadir estimate of SBT made by the ATSR-2 to be cooler than the forward estimate, a result which is not intuitive, and which should be considered in the derivation and application of algorithms for the satellite retrieval of LST. Currently, although the plots of SBT versus ΔT_{AC} show well defined regression relations, the accuracy with which ΔT_{AC} may be predicted is limited to 3–4 K for the Amburla field site and 4.5–9.5 K for the Thangoo site, based upon the uncertainty within each of the radiative components used in the RC approach to produce the equations. Simulations have, however, shown that the accuracy with which ΔT_{AC} may be estimated improves when the radiative components are known more exactly. Vertical atmospheric profile data from satellite sensors such as the Atmospheric Infrared Sounder (AIRS) (BAE Systems, 2002) may potentially increase the accuracy of ΔT_{AC} to 1–2 K.

The linear equations for estimating ΔT_{AC} which may derived from Figures 4.16 and 4.17 in Section 4.2.5 are for the generalized case only. Without specific knowledge of the surface emissivity the best estimate of ΔT_{AC} may not be obtained, since the choice of surface emissivity shifts the line of regression for predicting ΔT_{AC} data in Figures 4.16 and 4.17 along the y-axis (the magnitude of ΔT_{AC} decreases towards zero as the surface emissivity increases towards unity). The results from Figures 4.16 and 4.17 do not fully explain the seasonal distribution of the dBT data from Figures 4.7 and 4.8, which were the stimulus for this investigation into

the impact of the atmosphere upon the atmospheric correction process. Some seasonal variation is captured in Figures 4.16 and 4.17 since both figures show that ΔT_{AC} for the nadir and forward views of the sensor change with SBT, which does vary seasonally. However, the variability in ΔT_{AC} described by figures 4.16 and 4.17 alone is not enough to account for the variability seen in the seasonal plots of dBT. This highlights that the equation for predicting ΔT_{AC} from SBT is dependent upon the choice of surface emissivity, however, and the challenge to explain the observed distributions of dBT data for the two field sites then necessitates investigation of surface effects on satellite-retrieval of LST. This approach is appropriate since the land surface and atmosphere are connected through radiative transfer theory, as shown by (4.1). With this in mind, the current chapter concludes by noting that the magnitude of the atmospheric correction term for satellite TIR data, ΔT_{AC}, may be estimated from a simple linear equation based upon an estimate of the SBT and knowledge of the atmospheric state derived via modelling of the radiative transfer between the land surface and the satellite sensor. However, the exact linear equation for predicting ΔT_{AC} which is applicable for a particular satellite viewing geometry of the land surface is dependent upon the surface emissivity of the scene. In this chapter the accuracy with which ΔT_{AC} may be defined has been calculated as an average over the range of surface emissivity values between 0.90 and 1.0 to be 3–4 K for the Amburla field site. If the range of possible emissivity values can be narrowed, for example from 0.1 to 0.02, then the accuracy with which ΔT_{AC} may be predicted is improved to 1–2 K under the atmospheric conditions characteristic of the Amburla field site.

Chapter 5 then investigates the angular distribution of SBT and surface emissivity in more detail using *in situ* measurements made by the scanning infrared radiometer at the Amburla field site with the aims of applying the results of the investigation to; i) developing a method of obtaining a high quality dataset for validation of satellite-based estimates of LST, and; ii) the development of physics-based algorithms for the satellite retrieval of LST.

Chapter 5

In Situ Measurements From the Amburla Field Site

5.1 The Scanning Radiometer

The scanning TASCO radiometer installed at the Amburla field site is the primary instrument for validation of satellite-derived LST at the site. It sits atop a five metre high pole (see Figures 3.2 and 3.6 in Section 1.1), and is oriented such that it scans from a zenith angle of 70° in a southward-looking direction, through nadir to 70° in the northward-looking direction. The instrument scans continuously, taking approximately 10 minutes to complete a full scan cycle.

The construction of the scanning radiometer instrumentation is shown in Figure 5.1. The optics contained within the head of the radiometer are aligned with the scan mirror, which rotates so as to receive the surface-leaving radiance through the surface-view aperture in the housing. The surface-leaving radiance is reflected from the scan mirror into the field of view of the radiometer. The scan mirror is driven by a motor, the mirror's position and the duration is preset in the controlling electronics. The radiometer and controlling electronics are inserted into the protective housing and bolted to the top of the pole.

The temperature of the Hot Blackbody (HBB) and the Cold Blackbody (CBB)

are both monitored independently of the radiometric view so that calibration of the radiometer data may be performed. The temperature of the blackbodies is known to within ±50mK and is stable over the scanning cycle of the radiometer, while the accuracy with which 'off-the-shelf' models of TASCO radiometer (Model THI–500L) may measure surface temperature has been assessed as ±0.2 K (Barton and Minnett, 2001). Further technical description of the radiometer may be found in Prata et al. (2003). The installation runs autonomously and is powered by solar panels during the day which also charge a battery that powers the installation during nighttime operation. The data are transmitted back to a central site several hundred metres away, where the data stream is logged, and may be periodically downloaded via a mobile telephone link.

5.1.1   Calibration of the Radiometer

The radiometer scans continuously day and night, and by utilizing the CBB and HBB, calibration of the data is also continuous. The temperatures of the CBB and HBB are continually monitored in the form of raw counts from the two blackbodies, and, as noted earlier, the temperature of each blackbody is known to within ±50 mK. In one scan cycle, the radiometer scans from a zenith angle of -70° to 70° in increments of 10°, stopping at each position for approximately 30 seconds. Following the measurement made at 70°, the radiometer views the CBB, then makes a sky temperature measurement, and completes the scan cycle with a measurement of the HBB.

Figure 5.2 shows a flow diagram representing the calibration process of radiometer measurements from raw counts through to the production of well-calibrated SBT data. The calibration cycle begins after the TASCO radiometer has viewed the cold and hot blackbodies in sequence, measuring the brightness temperature (BT) of each. At the time coincident with the view of the radiometer, the raw counts from the CBB and HBB blackbodies are used to derive; i) a counts-to-radiance relationship from which the CBB and HBB temperature equivalent radiances are
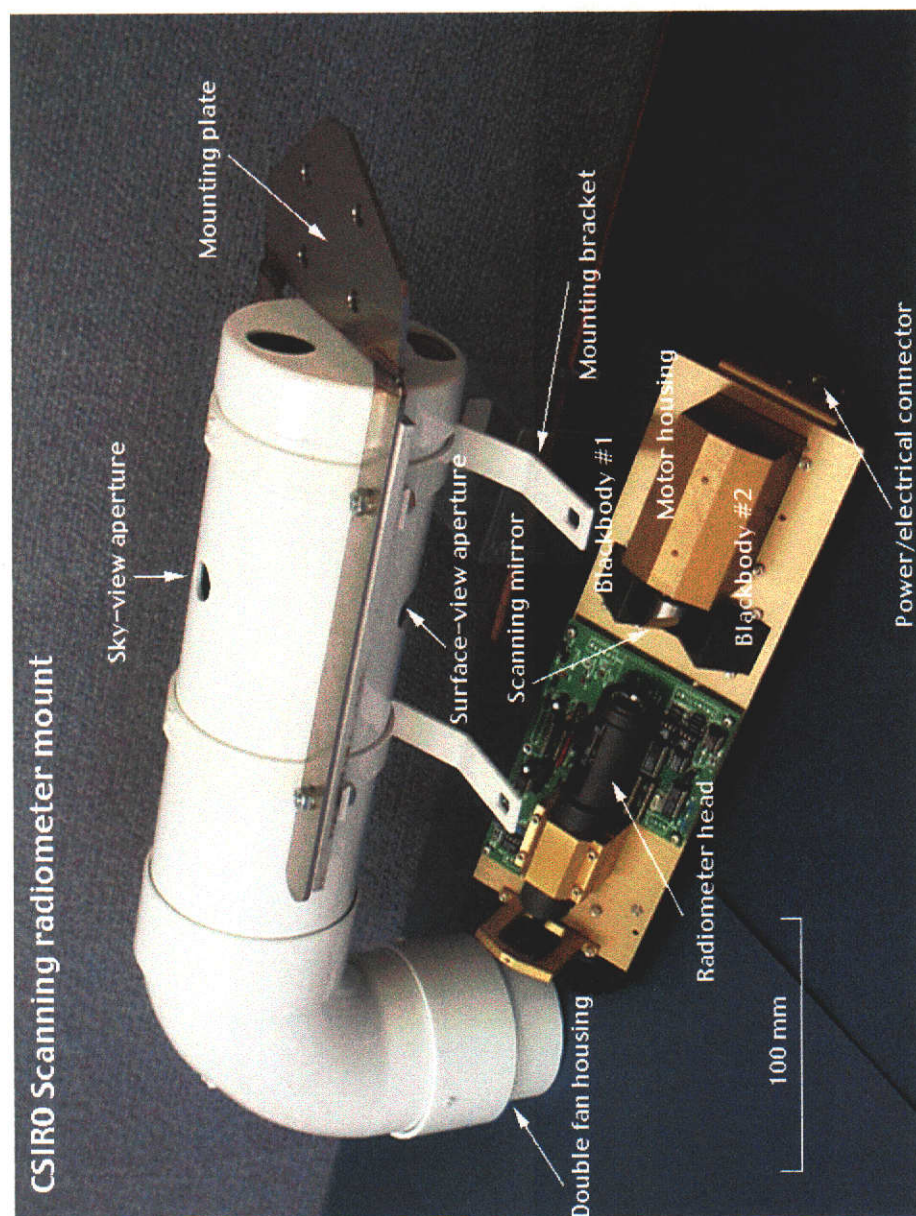
Figure 5.1: Diagram of the major components of the scanning TASCO radiometer instrumentation.
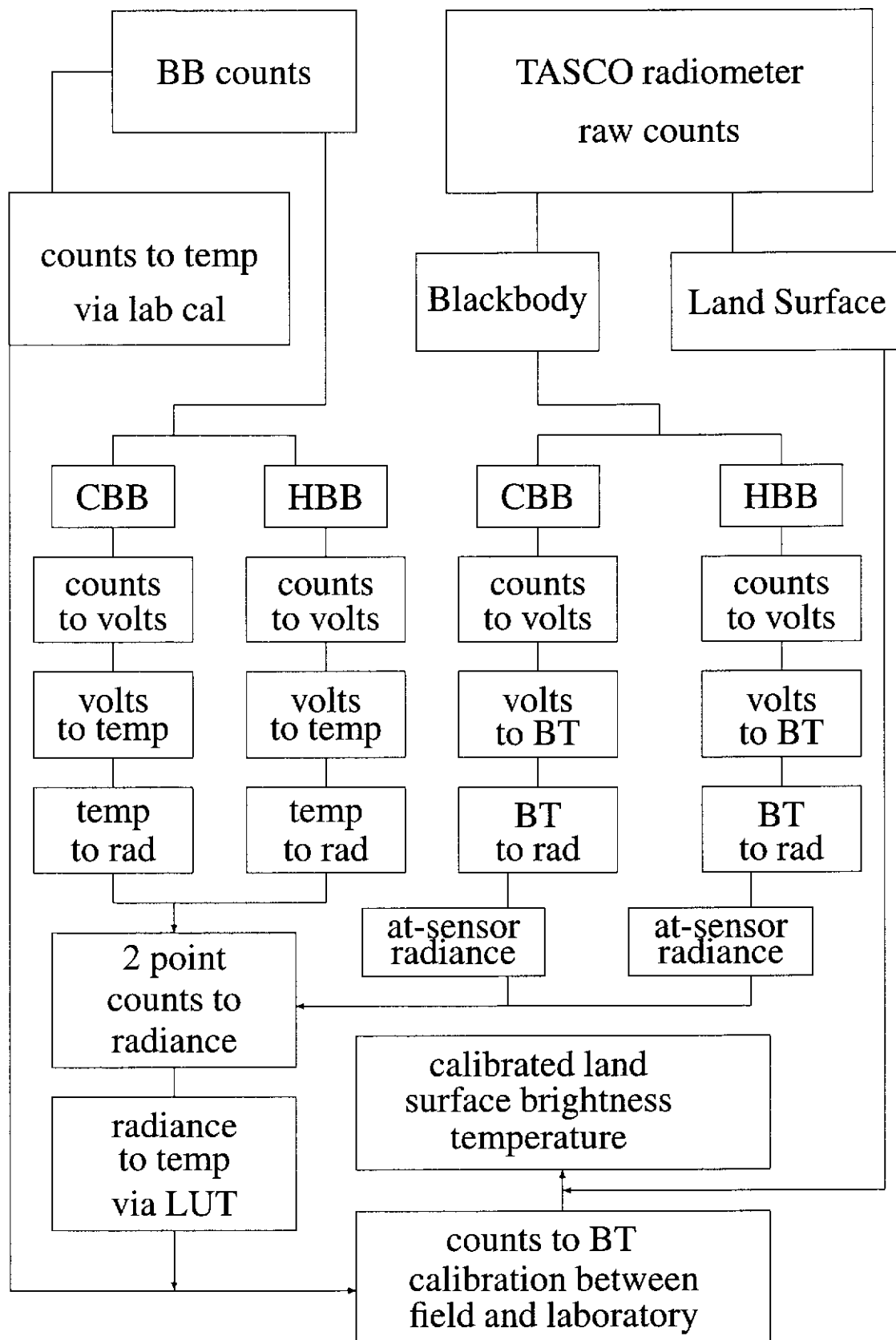
Figure 5.2: Flow diagram showing sequence of steps in the counts-to-brightness temperature calibration process for TASCO radiometer data from the Amburla field site.

subsequently converted to a counts-to-BT relationship via the radiance-to-BT LUT for the radiometer, and; ii) a laboratory-to-field calibration, utilizing the predefined laboratory calibration of the instrument.

Because a complete scan cycle takes approximately 10 minutes, a linear interpolation is performed between the gain and offset of the counts-to-BT relationship developed from the scan cycle just completed and the gain and offset derived from the prior scan cycle. In this way the calibration of the radiometer most appropriate to the BT measurement made at each zenith angle may be determined. Each set of calibration data is quality controlled, and if the latest calibration data appear erroneous the data from the previous scan cycle only are used. If the old calibration data are erroneous no interpolation is performed. In the event no 'good' calibration data are available for either the current of previous scan cycle the last set of acceptable calibration data are used to define the counts-to-BT relationship. The default calibration of the radiometer is the counts-to-BT relationship defined in the laboratory.

The quality control procedure essentially monitors the difference in temperature between the HBB and CBB, as measured by both sensors built into the controlling electronics and the radiometer. The HBB is maintained at approximately 60°C, while the CBB is essentially at ambient temperature. Measurements of the CBB show that the maximum ambient temperature reached at the field site is approximately 320 K during the day in the summer months, while the minimum is around 280–290 K during nighttime operation in winter. As a result, the criteria used for accepting calibration data was when the difference between the HBB and CBB temperature estimates, made by both the blackbody sensors and the radiometer, were between 10 and 60 K. Analysis of the calibration of the radiometer showed that only about 0.06% of the HBB and CBB data fell outside these constraints.

In the final step, a laboratory-to-field calibration between the BT derived from the radiometric view of the blackbodies and the BT estimates derived directly via the fixed laboratory calibration (based upon the predefined counts-to-BT relation-

134

ship) is performed so as to relate all field measurements back to the laboratory calibration. The laboratory calibration of the radiometer may be traced back to a NIST blackbody standard so that referencing all field measurements back to the laboratory calibration then provides a link between *in situ* measurements and the blackbody standard. As for the calibration of the instrument described previously, a linear interpolation between the gain and offset of the laboratory-to-field calibration for the current scan cycle and the previous scan cycle is performed so that each measurement made by the radiometer over the 10 minute scan cycle may be calibrated as accurately as possible. Quality control of this process runs as previously described, and the default laboratory-to-field calibration is described by a gain of 1.0 and an offset of 0.0 K.

The continual referencing of the field calibration to the laboratory calibration allows the effects of the changing environmental conditions over seasonal and diurnal cycles to be monitored. The process relates all *in situ* measurements back to the laboratory calibration giving an estimate of the SBT that would be measured by the TASCO radiometer under laboratory conditions. Through compensating for any changes to the response of the radiometer, this process ensures that *in situ* measurements made by the TASCO radiometer are not biased by changing environmental conditions.

Figure 5.3 compares the response of the TASCO radiometer over the period from June to December of 2000 to the fixed laboratory calibration. The changing response of the radiometer is represented in the figure by the gain and offset derived from the laboratory-to-field calibration. The data set consists of 213 days of data, each comprising some 150 scan cycles. The gain and offset plotted in the figure are those calculated while the radiometer makes a nadir measurement, giving approximately 30,000 data points in total. When field conditions are similar to those in the laboratory, in particular the ambient temperature at the the time when the laboratory calibration of the radiometer was performed, the *in situ* counts-to-BT relationship gives similar estimates of the blackbody temperature to the predefined relationship.

When this is the case, the gain calculated for the laboratory-to-field relationship should be approximately one, and the offset near zero. However, diurnal and seasonal variation in the ambient temperature affects the response of the radiometer. An increase in the ambient temperature in which the TASCO radiometer operates causes it to overestimate the true surface temperature of the target it is observing. This overestimate is larger for warmer BTs, and results in a decrease of the gain of the laboratory-to-field calibration, and corresponding increase in the offset. When the ambient temperature is cooler than that in which the radiometer was calibrated in the laboratory the gain from the laboratory-to-field relationship increases and the offset decreases. This can be seen to occur in the late Spring and Summer months in Figure 5.3a, beginning around Julian day 300. As shown in Figure 5.3b, there is a corresponding change in the magnitude of the calibration offset when the gain decreases. Figures 5.3a and b show that the laboratory and field calibration of the TASCO radiometer remain very close through June and September, with the gain no more than 3–4% above unity and the offset between 0 and -10 K. This suggests that the ambient temperature of the field site throughout this period was slightly lower than when the radiometer was calibrated in the laboratory. At the beginning of October, however, the gain drops sharply and the offset correspondingly increases, suggesting that the ambient temperature warms up quickly, altering the response of the radiometer. There is a clear change in the calibration of the radiometer as the seasons move from Spring into Summer.

Within the data plotted in Figure 5.3, the seasonal variation in the calibration of the radiometer is clearly apparent, but the calibration of the radiometer also varies on a diurnal basis. Examples of this diurnal change in calibration are shown in Figure 5.4. Figures 5.4a and b are for 21 June 2000 and Figures 5.4c and d for 25 December 2000. The two days represent the calibration of the radiometer for the different temperature regimes between winter and summer at the field site. During winter, the average land surface and air temperature are lower, as shown by the plot of the ground temperature measured by an AD-590 contact temperature sensor in

Figure 5.4a. The gain of the radiometer shown in Figure 5.4b is around 1.01 during the day and 1.04 at night, while the offset is negative and may be as low as -10 K. In summer (Figure 5.4d), when the average temperature is warmer, the gain of the radiometer decreases to around 0.90 during the day and 0.91-0.92 at night. For the decreasing gain, there is a corresponding increase in the offset which may be between 30–40 K. In summer, when the gain of the radiometer is at its lowest at around 0.88, the offset, as may be as high as 50 K.

Tables 5.1 and 5.2 illustrate the importance of the laboratory-to-field calibration in ensuring an SBT dataset of high accuracy. Table 5.1 contains data on the gain and offset of the radiometer, representative of morning, midday and nighttime operation, taken from Figure 5.4b. The data show an example typical of how the response of the radiometer may vary over a diurnal cycle in the cooler months of the year at the field site. For each estimate of the SBT from the morning, midday and nighttime, given in the 'SBT_{field}' column of Table 5.1, the laboratory-to-field calibration has been performed to calculate the equivalent SBT estimate under laboratory conditions, given in the 'SBT_{lab}' column. The difference between the field and laboratory estimates of SBT is given in the 'ΔT' column. The data from the 'ΔT' column of Table 5.1 show that over the course of the diurnal cycle the response of the radiometer may vary from underestimating the SBT in the morning by -0.2 K, through an overestimate in the middle of the day of 0.9 K, back to an underestimate of -2.2 K at night. For warmer months the laboratory-to-field calibration varies differently. The data in the 'ΔT' of Table 5.2 shows that in the field during December the radiometer underestimates the SBT throughout the diurnal cycle by approximately -4 K, with the magnitude of the underestimate decreasing slightly from the morning throughout the day into the night.

Together, the data in Figures 5.3, 5.4 and Tables 5.1 and 5.2 show that the calibration of the radiometer varies diurnally, monthly and seasonally. Importantly, the calibration procedures described in this section accurately account for the observed changes in the calibration of the radiometer, which may be up to 4 K under some
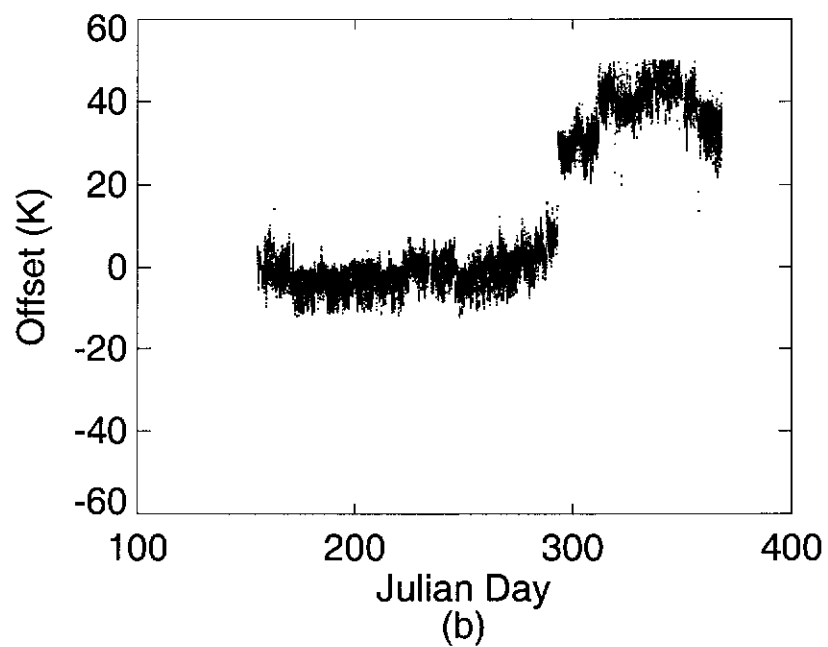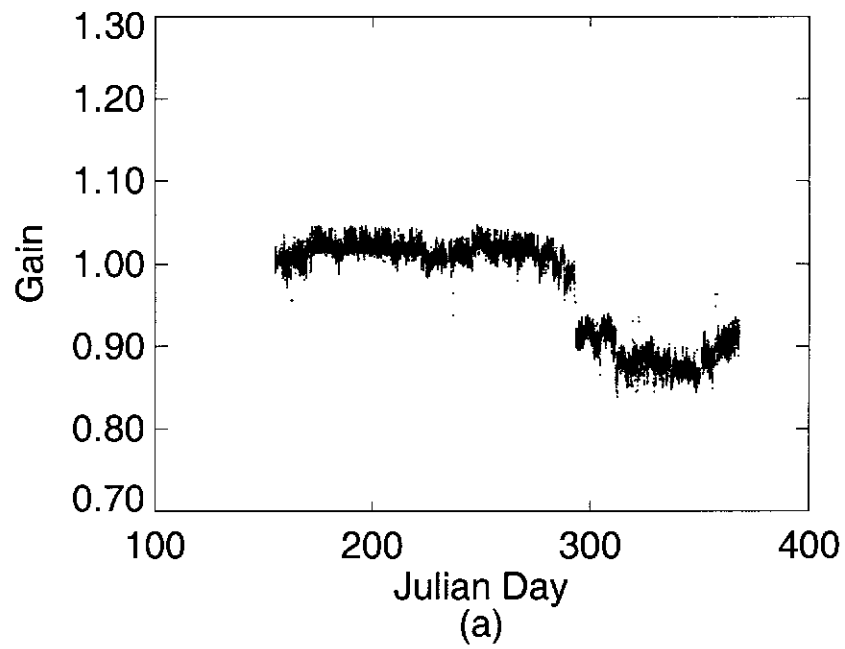
Figure 5.3: Seasonal variation in the calibration of the scanning TASCO radiometer for data from June to December 2000. a) gain. b) offset.

June	gain	offset (K)	SBT$_{field}$ (K)	SBT$_{ground}$	ΔT (K)
morning	1.035	-10	290.0	290.2	-0.2
midday	1.010	-4	310.0	309.1	0.9
night	1.035	-8	290.0	292.2	-2.2

Table 5.1: Sample of the effect of change in calibration of the TASCO radiometer over the diurnal cycle for June 2000. ΔT is the difference between the SBT measured by the radiometer *in situ* minus the temperature that would be measured by the radiometer in the laboratory.

December	gain	offset (K)	SBT$_{field}$ (K)	SBT$_{ground}$ (K)	ΔT (K)
morning	0.92	28	290.0	294.8	-4.8
midday	0.90	37	330.0	334.0	-4.0
night	0.91	30	290.0	293.9	-3.9

Table 5.2: Sample of the effect of change in calibration of the TASCO radiometer over the diurnal cycle for December 2000. ΔT is the difference between the SBT measured by the radiometer *in situ* minus the temperature that would be measured by the radiometer in the laboratory.

conditions. This high level of calibration then permits the acquisition of a good quality SBT dataset, to an accuracy limited by that of the TASCO radiometer itself, which is of the order of ±0.2 K. The radiometer ran continuously over the duration of the field study at the Amburla field site, between June and December 2000.

The continuous acquisition of SBT data by the radiometer reveals both diurnal and monthly cycles in the radiative properties of the land surface. Analysis and application of these *in situ* data to the estimation of LST is described in the following sections.

5.2 Surface Brightness Temperature Data

5.2.1 Diurnal Cycles of SBT

The calibration process described in the previous section ensures that the scanning radiometer acquires SBT data, over the range of zenith angles from -70–70° south

and north of nadir, to within ±0.2 K. Analysis of these data reveals strong cyclical patterns in the angular dependence of SBT. The variability is driven by solar influences during the day, which often contribute to an asymmetry in the data about nadir, while at night, once residual heating effects from the solar input during the day decline, the angular distribution of SBT about nadir becomes more symmetrical. The cyclical nature of the SBT distribution is illustrated by Figures 5.5, 5.6 and 5.7. The figures show a time series over three days from the 18 June to the 20 June 2000, illustrating the diurnal cycle of SBT, and the relationship of the variability to other geophysical variables. The three figures are placed in reverse order to capture the continuity of the cycles in SBT over the three day sequence.

Figures 5.5, 5.6 and 5.7a show the downwelling solar flux incident upon the surface, as measured by a pyranometer installed at the field site. Figures 5.5, 5.6 and 5.7b show the Ground Temperature (GT), measured by an AD-590 contact temperature sensor (plotted in red), the Air Temperature (AT) and relative humidity measured by the Vaisala instrument (plotted in yellow and blue respectively). Figures 5.5, 5.6 and 5.7c, show the angular dependence of SBT data acquired by the scanning radiometer. Figures 5.5, 5.6 and 5.7d show dBT data, calculated by subtracting the mean SBT over the set of observation zenith angles from each individual SBT estimate. The plots of dBT highlight the relative impact of changing zenith angle on the measurement of SBT in a way that is independent of the magnitude of the observed SBT.

The SBT and dBT plots in Figures 5.5, 5.6 and 5.7 are plotted over the scanning range of the radiometer, and have been interpolated to a 10 minute time grid in the y-direction which spans the 24 hour period equating to one day. The data have also been smoothed with a 3×3 boxcar filter. Figures 5.5, 5.6 and 5.7,c show a near-symmetric distribution in the absence of solar input, but as the sun rises, the angular distribution of SBT is altered. Initially, at sunrise, there are only small variations in SBT with zenith angle across the range of angles covered by the radiometer. The SBT appears to be almost independent of viewing angle, though the beginnings of

the asymmetric peak in BT, which occurs later in the day, are apparent between zenith angles of 10–30°.

As the sun rises further, and the scene warms, further structure in the angular distribution of SBT becomes evident. At peak solar input, during the middle of the day, a noticeable assymetry in the SBT distribution about nadir emerges, with the data measured in the anti-solar direction (north-looking) to a zenith angle up to 30° being a few degrees warmer than the data acquired at the equivalent zenith angle in the solar (south-looking) direction. The assymetry in the distribution is related to the solar zenith angle, with the distribution becoming more symmetrical about nadir when the sun is higher in the sky, particularly for data from months later in the year. The data in Figures 5.5, 5.6 and 5.7 are for days from June 2000, at a time nearing the winter solstice in the southern hemisphere, and as such, this is the time of year when the sun is at its largest zenith angle in the middle of the day. Discussion of the influence of solar zenith angle on the angular distribution of SBT is continued in Section 5.2.2. On the late afternoon side of the peak solar input, the SBT distribution becomes almost angularly independent once again. After sunset, as the residual from the day's solar heating fades away, the distribution reforms its near-symmetrical nature.

Examination of the plots of solar flux for the three days (Figures 5.5, 5.6 and 5.7a), in combination with the plots of GT (Figures 5.5, 5.6 and 5.7b) show that it is the solar flux incident upon the surface which drives the change in GT over the course of the day. The figures show that the response of the GT lags behind the solar input to the surface by approximately 1 hour. In contrast to this, the radiative response of the surface, illustrated by the contour plots of SBT and dBT in Figures 5.5, 5.6 and 5.7c and d, show that diurnal cycles in the GT and SBT are in phase to within a few minutes. This suggests that the slowly changing diurnal cycle of SBT is largely dependent upon the GT rather than the incoming solar flux. However, the emergence in the contour plots of SBT and dBT of asymmetry about nadir shows that there is also an impact on the SBT and dBT distributions which is directly

141
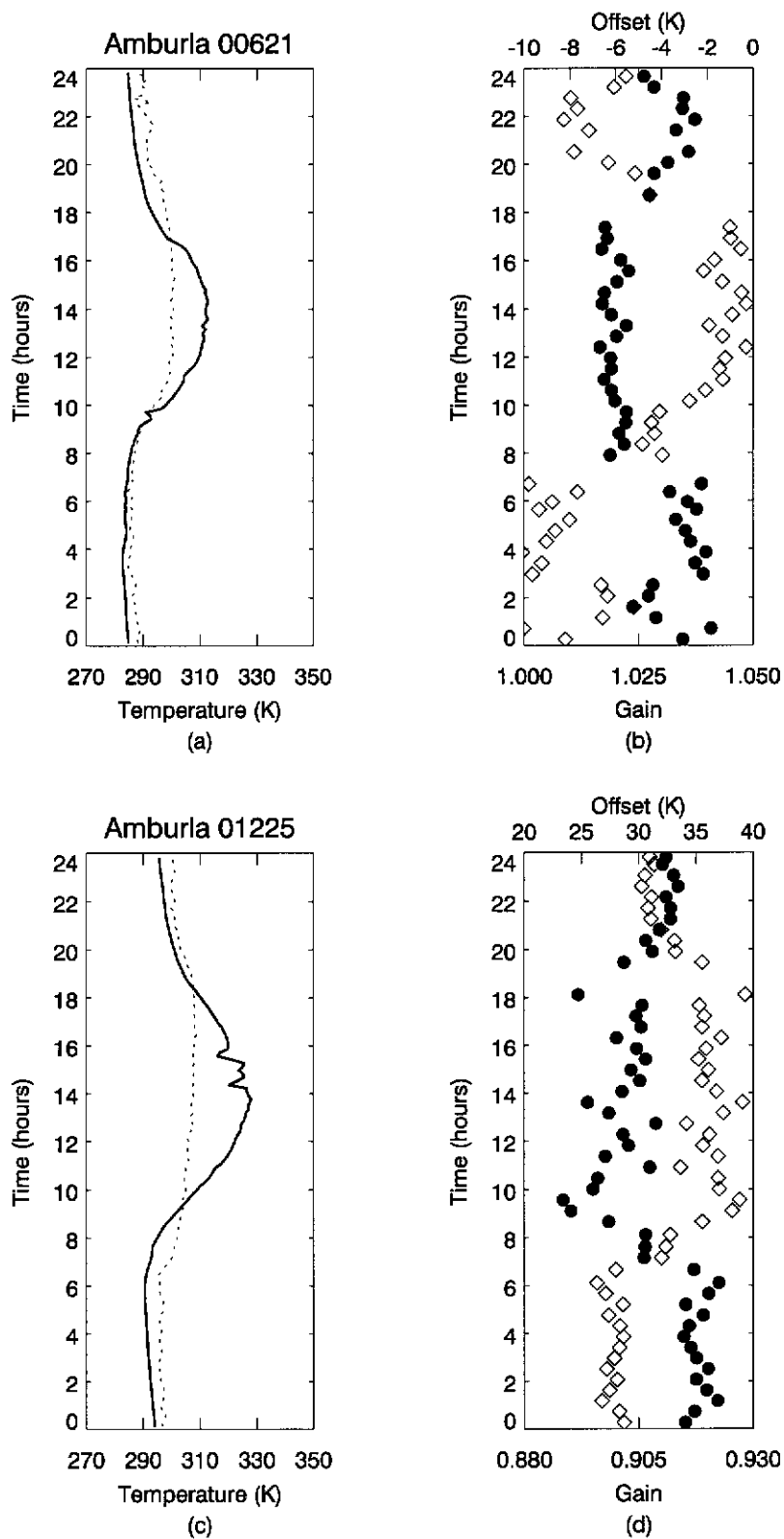
Figure 5.4: Diurnal variation in the calibration of the scanning TASCO radiometer for data from a) 21 June 2000, representing calibration during the winter temperature regime, and b) 25 December 2000 representing calibration during the summer temperature regime. In (a) and (c) the solid line shows ground temperature and the dashed line shows air temperature. In (b) and (d) filled circles show the gain. Diamonds show the offset.

142
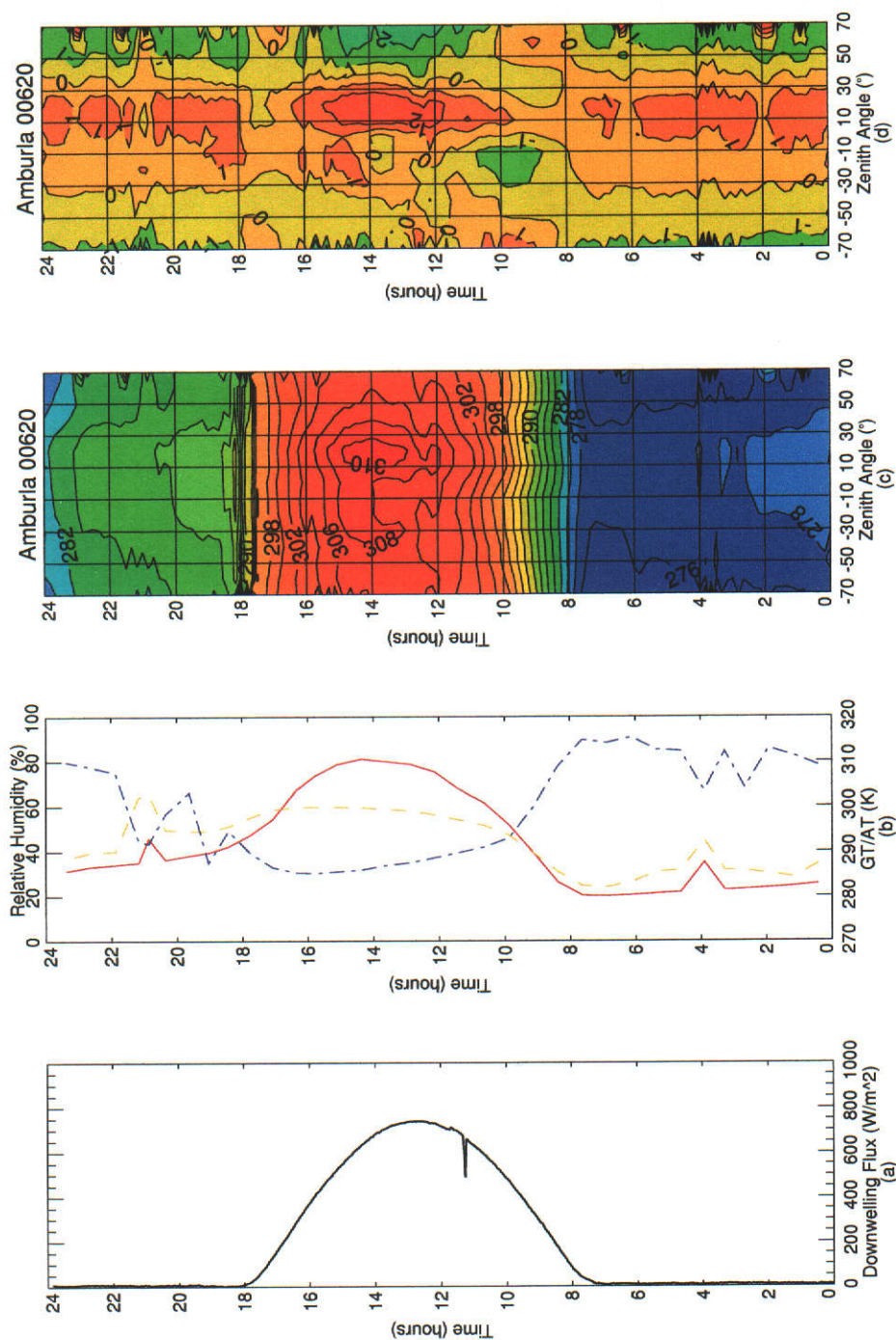
Figure 5.5: Cyclical nature of the angular distribution of SBT for 20 June 2000. The distribution is symmetrical at night and is driven by directional solar input during the day. Figure a) shows the downwelling solar flux. Figure b) shows the diurnal cycle of GT (plotted in red), AT (plotted in yellow) and the relative humidity (plotted in blue). Figure c) shows the angular distribution of SBT. Figure d) shows the difference in brightness temperature from the mean (dBT) along each scan cycle.
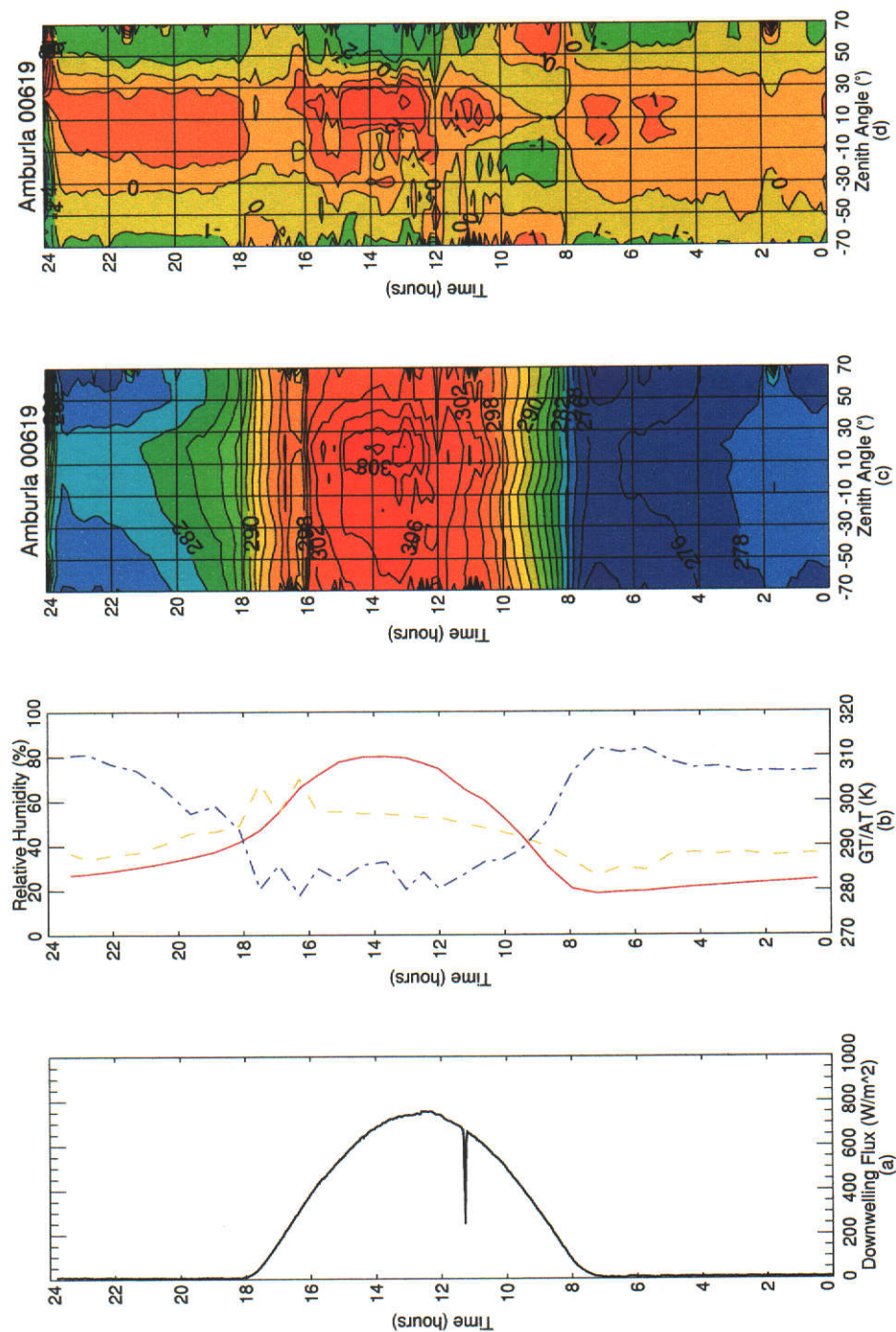
Figure 5.6: Cyclical nature of the angular distribution of SBT for 19 June 2000. The distribution is symmetrical at night and is driven by directional solar input during the day. Figure a) shows the downwelling solar flux. Figure b) shows the diurnal cycle of GT (plotted in red), AT (plotted in yellow) and the relative humidity (plotted in blue). Figure c) shows the angular distribution of SBT. Figure d) shows the difference in brightness temperature from the mean (dBT) along each scan cycle.
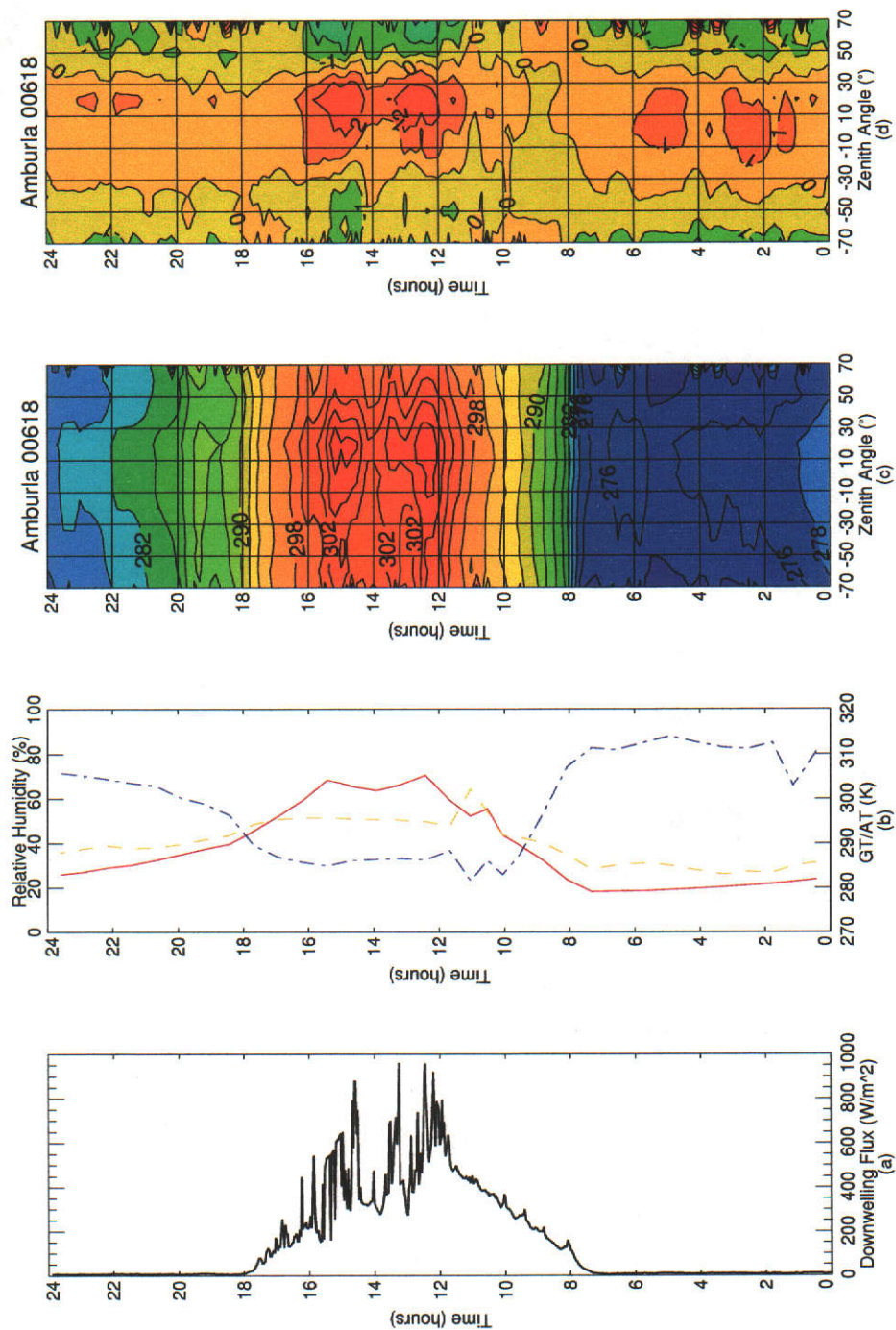
Figure 5.7: Cyclical nature of the angular distribution of SBT for 18 June 2000. The distribution is symmetrical at night and is driven by directional solar input during the day. Figure a) shows the downwelling solar flux. Figure b) shows the diurnal cycle of GT (plotted in red), AT (plotted in yellow) and the relative humidity (plotted in blue). Figure c) shows the angular distribution of SBT. Figure d) shows the difference in brightness temperature from the mean (dBT) along each scan cycle.

related to the incoming solar radiation. Comparison of Figures 5.5, 5.6 and 5.7a with the respective contour plots of SBT and dBT show that the asymmetric peak, apparent during the part of the day in which the solar input is a maximum, only lags behind the solar input by a few minutes.

This is highlighted by comparing the solar flux, SBT and dBT plots for the 18 June in Figure 5.7. The pyranometer data in Figure 5.7a shows that there was often significant cloud cover during the day. For clear days, the pyranometer data should form a smooth curve, as is the case in Figures 5.5 and 5.6a. For the 18 June, however, there are numerous peaks in the pyranometer data. When the occurrence time of these maxima and minima in solar input are correlated with the SBT and dBT distributions in Figures 5.7c and d, respectively, it may be seen that they correspond closely to the emergence and disappearance of the asymmetry about nadir in the SBT and dBT contours. When clouds are present, solar input to the surface is more diffuse than direct and the angular structure in the data largely disappears. When there are brief clear periods during the middle of the day on 18 June, where the downwelling solar flux approaches 1000 W/m^2, there are corresponding peaks in the SBT and dBT data and asymmetry reappears. The asymmetry about nadir in the angular dependence of SBT and dBT is then dependent upon the directional nature of the solar input to the surface.

On a daily basis, the data acquired by the scanning radiometer reveal well defined, complex, angular distributions of SBT. The analysis of data described in this section has shown that; i) at night, the angular distribution of SBT is nearly symmetric about nadir; ii) during the day, the distribution of SBT is primarily driven by incoming solar flux incident upon the surface, and; iii) during the middle of the day, when solar input to the surface is maximized, there exist directional solar-surface interactions which result in the anisotropy of the angular distribution of SBT and dBT about nadir. Both the night and daytime distributions of SBT have significance for remote sensing of LST, and the physical basis for the distributions observed in each case is discussed separately in the following sections of this chapter, beginning

with an analysis of the influence of the solar zenith angle on the asymmetry in the contour plots of dBT which occurs during the middle of the day.

5.2.2 Impact of the Solar Zenith Angle

In order to illustrate the impact of the solar zenith angle upon the angular distribution of SBT/dBT, dBT of the type shown in Figures 5.5, 5.6 and 5.7d of the previous section have been reprocessed by averaging over the period from 1200–1500 hours. During the middle of the day, the dBT data plotted in Figures 5.5, 5.6 and 5.7d, showed structure related to the solar heating of the land surface. The solar input causing the observed structure is directional, and in winter the solar zenith angle (SZA) is higher than in the summer months. The sun is more directly overhead in summer, and this change in solar geometry impacts upon the SBT distribution causing the single peak in the anti-solar direction, apparent mid-year (see Figures 5.8a and b), to become a dual peak nearly symmetrical about nadir (Figures 5.8c–g, as summer approaches.

The transformation of the SBT distribution is shown in Figure 5.8, where the angular profile of dBT data and the solar zenith angle have been plotted for the 22nd day of each month from June to November, and the 21st December 2000 (chosen instead of the 22nd as the midday profile appears cloud-affected for this date). The dBT profiles have been calculated by averaging the value of the dBT data at each zenith angle viewed by the scanning radiometer, over the period from 1200–1500 hrs for each day of the given month. This time period captures the impact of the SZA on the dBT profile at the time of peak solar input. The 22nd day of each month (21st in December) was chosen because the days in June and December coincide with the winter and summer solstices in the southern hemisphere, so the extremes in SZA are captured by the data. The SZA (represented by the asterisks in Figure 5.8 was calculated at 10 minute intervals using the '*Sun and Moon Altitude/Azimuth Table*' (USNO, 2001), for the latitude and longitude of the Amburla field site, over

147
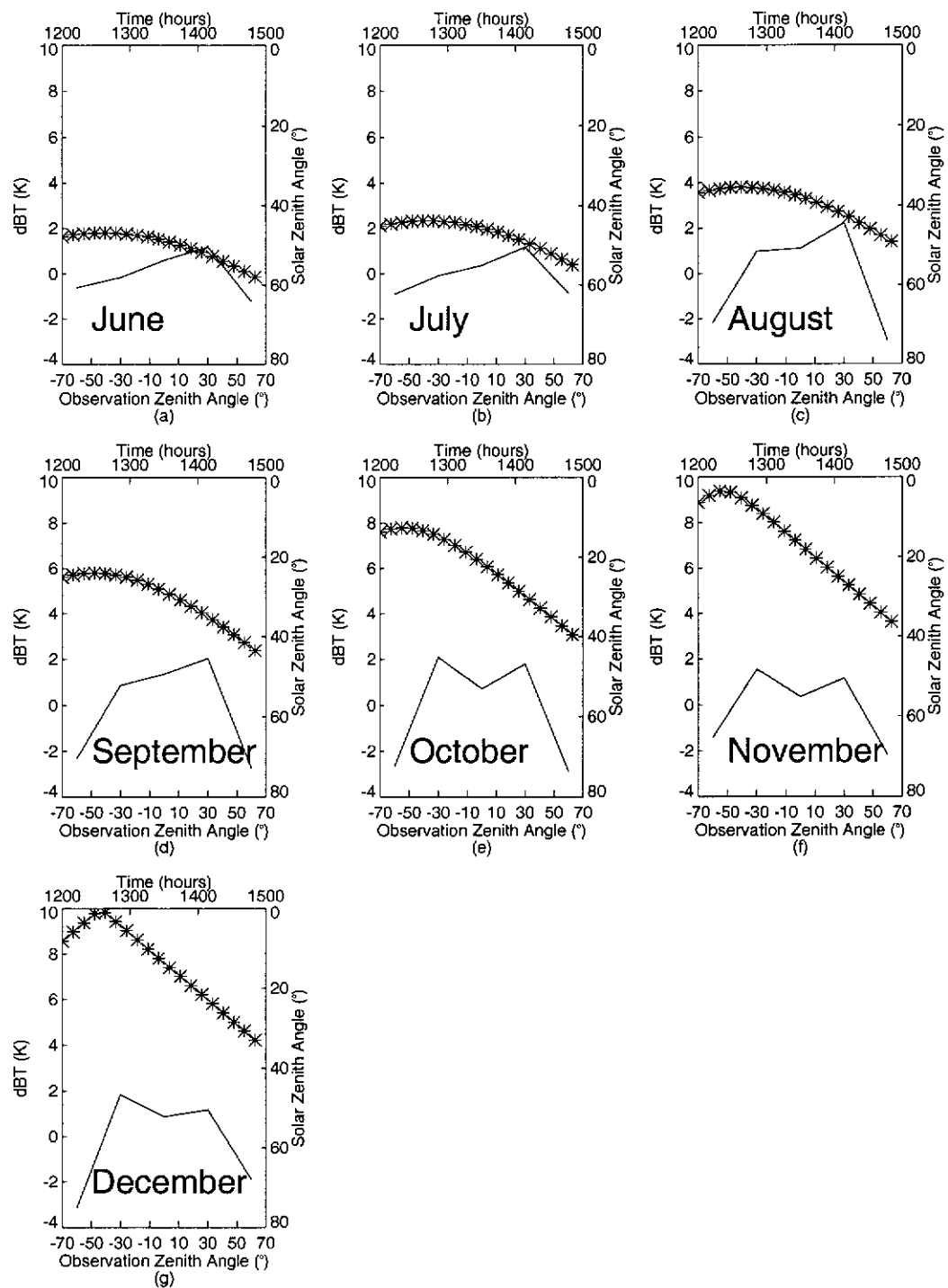
Figure 5.8: The impact of the solar zenith angle upon the dBT distribution averaged over the period of peak solar insolation between 1200 and 1500 hrs (top x-axis) as a function of observation zenith angle (bottom x-axis). The continuous line shows the dBT data (left y-axis). The asterisks show the solar zenith angle (right y-axis).

the same period for which the data at each zenith angle were averaged (1200–1500 hrs).

During June and July (Figures 5.8a and b), when the SZA is near its maximum for the diurnal cycle during the middle of the day, there is distinct asymmetry about nadir, with the data in the anti-solar direction (positive observation zenith angles) being warmer than for data at the equivalent zenith angle in the solar direction (negative observation zenith angles). As the SZA decreases, symmetry of dBT about nadir begins to emerge (Figures 5.8c and d). As the SZA progresses towards its minimum value through October, November and into December, dual peaks either side of nadir are established (Figures 5.8e, f and g). The magnitude of the dBT distribution also has increased as the months progress, suggesting that not only the form of the dBT distribution, but also the magnitude, is related to the annual cycle in the downwelling solar flux.

The nature of the interaction between the downwelling solar radiation and the surface is dependent upon the land surface 'architecture', particularly vegetation (Smith et al., 1997), though, for the Amburla site, vegetation is limited to small clumps of short grass (see Section 3.2). Previous studies of the distribution of land surface radiative properties, such as TIR exitance from the surface (Balick and Hutchinson, 1986; Smith et al., 1997), spectral reflectance and emissivity (Snyder et al., 1998a) and LST (Minnis and Khaiyer, 2000), suggest that anisotropy in the directional SBT may be expected. The angular distribution of SBT in Figures 5.8a and b shows similarities in form to results from the previous studies, most notably, there are similarities between the SBT profiles in Figures 5.8a and b and that which may be expected from the forward-scattering BRDF kernel for the thermal infrared developed by Snyder et al. (1998a). The correspondence between the in situ measurements from the Amburla field site, at least for June and July, and BRDF kernels for the TIR developed by Snyder and Wan suggest the existence of a TIR equivalent of the BRDF for the visible spectrum, as defined by Roujean et al. (1992). This is an important result impacting the interpretation of LST retrieval by scanning satellite

149

sensors.

The instrumentation installed at the field site measures macroscopic radiative properties only, which, by themselves, do not contain information on the smaller scale solar-surface interactions which most likely give rise to the observed SBT distributions. Although it is the case that the radiative properties at the macroscopic scale are likely to be due to interactions occurring at the microscopic level, this work concentrates on the impact which the field observations of SBT and dBT distributions have on the interpretation of satellite-based retrievals of LST from scanning sensors. The latter is particularly important for validation of satellite-based estimates of LST from sensors such as MODIS (Wan, 1999).

The results in the current chapter describe surface-related impacts on satellite estimation of LST in terms of the macroscopic form of physical quantities such as surface emissivity and SBT, since the instrumentation utilized for this study acquires data at these scales. Within the macroscopic measurements made by the radiometer there occur complex radiative interactions between the atmosphere and the surface which are impacted by both the surface architecture and the solar geometry. In the following sections of this thesis the dependence of SBT measurements upon i) the zenith angle of observation, and; ii) the directional nature of the surface emissivity, are investigated in more detail.

5.2.3 Angular Variation of Surface Brightness Temperature

5.2.3.1 Descending ATSR-2 Overpass

The scanning radiometer field data show that there exist well defined cycles in the angular distribution of SBT over the course of a day. The angular distribution of SBT is important for remote sensing of LST, since a satellite views the surface at varying geometries on successive overpasses of the same location. If such observations are to be compared, then the form of the angular distribution of SBT becomes important. Sections 5.2.1 and 5.2.2 have discussed the existence of well-defined

cycles in SBT, found to be present within the SBT data acquired by the scanning radiometer at the Amburla field site. Of importance to satellite remote sensing of LST is how reproducible such angular distributions of SBT and dBT may be between several scan cycles of the radiometer, and how consistent the observed profiles are over longer time periods. These factors will impact the accuracy with which it is possible to validate remotely sensed LST data. In this and the following section, dBT profiles characteristic of the Amburla field site during different periods of the diurnal cycle are extracted from the data acquired by the scanning radiometer and used to address; i) how the characteristic dBT profile varies between the descending and ascending passes of the ATSR-2 satellite sensor, and; ii) how accurately the dependence of dBT upon observation zenith angle may be defined at these times.

The ATSR-2 follows a sun-synchronous orbit, such that it passes over the Amburla field site within half an hour of the same local time every day, for both the descending (1030 hrs local time) and ascending passes (2330 hrs local time). The form of the dBT distribution is dependent upon the observation zenith angle at these times and is important for the accurate retrieval of satellite-derived LST. In the ideal case, the observed dBT at the time of the satellite overpass would be independent of viewing geometry. However, Figure 5.8 in Section 5.2.2 showed that the dBT distribution characteristic of of the middle of the day depends on; i) the observation zenith angle, and; ii) the solar zenith angle. As noted earlier, the descending ATSR-2 overpass occurs at approximately 1030 hrs local time, and even by this time of day the dBT profiles represented in Figure 5.8 are beginning to emerge (see Figures 5.5, 5.6 and 5.7 in Section 5.2.1). Figure 5.9 shows the angular distribution of dBT observations extracted from the scan cycle data sets between 1000 and 1100 hrs. This interval encompasses the descending overpass time of the ATSR-2. The data plotted in Figure 5.9 are the time averaged values of the dBT data at each observation zenith angle, for all scan cycles between 1000–1100 hrs, coinciding with the descending pass of the ATSR-2. The data have been smoothed with a three point moving average over the range of zenith angles scanned by the radiometer.

Figure 5.9: Plot of the angular dependence of dBT on observation zenith angle averaged over each of the months from June to December 2000, at the time of the descending overpass of the ATSR-2, derived from measurements made by the scanning TASCO radiometer.

The dBT data for each month in Figure 5.9 are very similar to the simplified dBT profiles shown previously in Figure 5.8. Figures 5.9a–g show a time series from June to December 2000 which captures the transformation of the dBT distribution from the single peak in the anti-solar direction in June and July (Figures 5.9a and b), to the emergence of the nearly symmetrical dual peak, positioned about nadir (Figures 5.9d–f). The emergence of the peak in the solar direction (negative zenith angles) is clearly noticeable in the plot of dBT for August. As the months progress it becomes more pronounced, while the dBT peak in the anti-solar direction remains relatively constant.

For the descending pass, the ATSR-2 is south-looking. In each of the dBT profiles in Figure 5.9, the error bars at each zenith angle scanned by the radiometer represent one standard deviation of the monthly mean data averaged over the number of scan cycles between 1000 and 1100 hrs. In one hour the radiometer usually completes between 5 and 6 scan cycles, giving some 150 to 180 samples in a month for each zenith angle. Any given plot in Figure 5.9 shows that the variability in the profile at each zenith angle is about the same. In Table 5.3 the mean standard deviation over the set of dBT estimates for all zenith angles scanned by the radiometer, for the number of scan cycles between 1000 and 1100 hrs is given for each month in the column headed 'Daily'. This column in the table shows that the dBT profile may be measured to within 1 K over a few scan cycles on most occasions. As noted in the description of the Amburla field site (Section 3.2), there was significant rainfall during October, November and December and this is believed to have some impact on the form of the dBT profile. Such impacts on the zenith angle dependence of the dBT profile are evident in the 'Daily' column of Table 5.9 for November, for which the standard deviation is 1.37 K.

The data in the 'Daily' column of Table 5.3 show that because the duration of the scan cycle is approximately 10 minutes, and the overpass of the field site by the ATSR-2 sensor occurs within a fraction of one scan cycle, the accuracy with which the dBT profile may be measured is limited to about 1 K. The columns headed

153

Month	Daily	Weekly	Monthly	3-Monthly
June	0.94	0.28	0.54	0.65
July	0.76	0.55	0.45	0.87
August	0.86	0.39	0.56	0.92
September	0.82	0.66	0.72	0.85
October	1.03	0.87	0.82	0.87
November	1.37	0.83	1.16	0.92
December	0.97	0.53	0.50	0.85

Table 5.3: Standard deviation of data for the mean distribution of dBT with observation zenith angle at the time of the descending overpass of the ATSR-2 for months from June to December 2000, over time periods from one day to three months.

'Weekly', 'Monthly' and '3-Monthly' show how dBT may be expected to vary over time periods longer than just a few cycles. While the data in the 'Daily' column have been derived from the standard deviation in dBT over 5 or 6 measurement cycles. Data in the other columns show the standard deviation of the set of mean dBT estimates calculated on a daily basis, at each zenith angle, but for each day within the different time periods. The data in Table 5.3 show that the dBT profile may be defined most accurately on a daily basis, and that over time the profile slowly changes, as illustrated by the increase in the standard deviation between weekly, monthly and 3-monthly estimates. From the table, definition of the angular distribution of dBT on a daily basis may be made to within 1 K. When the angular dependence of dBT is examined over the longer time periods, the accuracy with which the distribution may be defined is calculated from the data in Table 5.3 as the sum of the standard deviation from the daily measurement and the standard deviation of the angular distribution over the appropriate time period. For example, in June the dBT estimate at each zenith angle within the angular distribution for a given descending overpass of ATSR-2 may be defined to within ± 0.94 K. The dBT estimate at each zenith angle for a dBT distribution measured over a week may then be defined to within $0.94 + 0.28 = \pm 1.22 K$. Similarly, over a month the standard deviation of a dBT estimate for a given observation zenith angle would be $0.94 + 0.54 = \pm 1.49 K$ over a month. If measured over a 3-month period the standard

deviation would be $0.94 + 0.65 = \pm 1.59K$. The representative angular distribution of dBT profile for the descending overpass of the ATSR-2 is then consistent over a few scan cycles of the radiometer to within 1 K, and is slowly changing over longer time periods.

5.2.3.2 Ascending ATSR-2 Overpass

The dBT data from 2300–2400 hrs, the time period which encompasses the range of times of the ascending ATSR-2 overpass are plotted in Figure 5.10. These show that, for June to September, the angular distribution of dBT is similar for each month, but that the dBT distribution begins to show significantly less variability with zenith angle for the months from October to December. Again, this change in the form of the angular distribution of dBT profiles may be related to the unusually high rainfall and associated cloud cover during these months. The nighttime data plotted in Figures 5.10a, b and c show different distributions of dBT for each month at night than for the daytime case (shown previously in Figure 5.9).

In the nighttime case, the dBT profile does not display any off-nadir peaks, as are seen during the day, and the dBT data generally decrease monotonically from nadir in a smoothly varying fashion, with the exception of the dBT estimate at a zenith angle 70°, which is often slightly warmer than the estimate at 60°. The absence of any off-nadir peaks in the nighttime data supports the case that the off-nadir structure observed in the data during the day is related to the directional factors associated with the solar input to the surface.

The profiles in Figure 5.10 are notably less variable than during the day. Whereas, for the daytime case, the dBT data for a given observation zenith angle could be defined to within 1 K on a daily basis, at night the standard deviation was closer to 0.5 K. Table 5.4 gives the standard deviation data for the daily, weekly, monthly and 3 monthly cases for the dBT profiles coincident with the ascending overpass of ATSR-2, as was given in Table 5.3 for the descending case. The standard deviation data show that the nighttime distributions are less variable than the dBT profiles

155

observed during the day. In fact, from the data given in Table 5.4, the angular dependence of dBT over a month may be defined to within a standard deviation of 1 K at night (calculated from the sum of the standard deviations in the 'Daily' and 'Monthly' columns for each month), which is equivalent to the level of accuracy achieved by measurements of the angular dependence dBT acquired during the day on a daily basis. Such a result shows that the land surface is radiatively more complex during the day. This is a positive result for achieving remotely sensed estimates of LST to within 1 K at night. However, to do so it is likely that knowledge of the underlying physical processes which give rise to the angular distributions of SBT, and subsequently dBT, observed by the radiometer at night will be necessary, so that the form of the distribution may be modelled given knowledge of the satellite viewing geometry and the properties of the land surface. Development of a similar model during the day will also require complementary knowledge of the solar geometry.

5.2.3.3 The Case For An Isothermal Surface

Comparison of the standard deviation data from radiometric measurements of dBT data between day and nighttime (Tables 5.3 and 5.4 respectively) shows that the angular distribution of dBT representative of the surface may be defined more accurately at night than during the day. As noted previously, dBT data for these two cases were extracted over hourly periods encompassing the possible range of descending and ascending overpass times of the of ATSR-2 satellite sensor over the Amburla field site. Interestingly, when a larger time period of dBT data is selected at night, where night is defined as lying between 0000 and 0600 hrs, the dBT at each observation zenith angle may be defined even more accurately than for the dBT profile representative of the land surface during the ascending overpass of ATSR-2. The distribution of dBT for the nighttime case for each month from June to December of 2000 are plotted in Figure 5.11. The figures show that the observed distributions do not change much from those in Figure 5.11. However, from the standard deviation

156
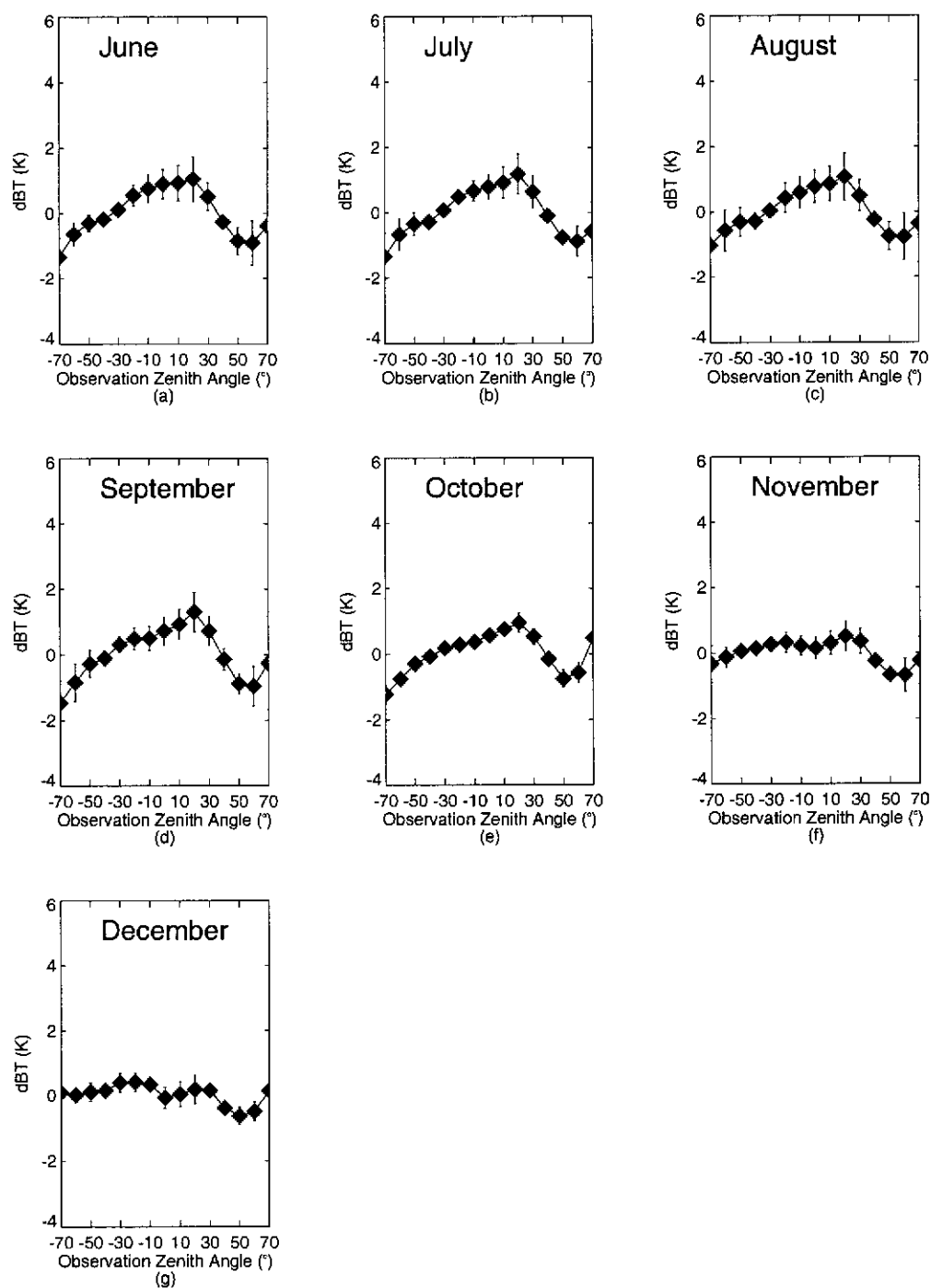
Figure 5.10: Plot of the angular dependence of dBT on observation zenith angle averaged over each of the months from June to December 2000, at the time of the ascending (nighttime) overpass of ATSR-2, derived from measurements made by the scanning TASCO radiometer.

157

Month	Daily	Weekly	Monthly	3-Monthly
June	0.57	0.29	0.52	0.87
July	0.60	0.30	0.36	0.89
August	0.45	0.53	0.54	0.77
September	0.68	0.40	0.54	0.66
October	0.57	0.47	0.44	0.89
November	0.34	0.44	0.33	0.77
December	0.45	0.33	0.40	0.66

Table 5.4: [Standard deviation of data for the mean distribution of dBT with observation zenith angle of the ascending (nighttime) overpass of the ATSR-2 for months from June to December 2000, over time periods from one day to three months.

data for the nighttime case given in Table 5.5, it is evident that the data for the 'Daily' case for each month are slightly larger than the equivalent data for the case corresponding to the time of the ascending overpass from Table 5.4. This is understandable since there are six times as many cycles taken into account for the nighttime case in Table 5.5. However, even given this larger sample size, the data in Table 5.5 for the weekly, monthly and 3-monthly cases show smaller variability than for the ascending overpass data. This result suggests that much of the variability in the dBT profiles for the descending and ascending overpasses of ATSR-2 is due to uneven heating and cooling of the surface. During the day it is clear that there are directional effects present in the dBT data. Earlier in the night there is still some residual heating left in the profiles, though its influence on the distribution of dBT subsides as the night progresses. The period between 0000 and 0600 should be the time when the land surface is completely free from any influence of solar heating, so it well may be expected that the land surface exhibits the most well-defined profiles at this time. The data in Table 5.5 support this theory since they show smaller variability in the form of the dBT profile over the nighttime period.

In the absence of directional solar effects, such as those shown previously in Figure 5.8, and when the land surface at night is free from any residual heating from the previous day, the surface should approach an isothermal state. If the dBT profiles which are shown by Figure 5.11 are representative of an isothermal

surface then there must be underlying physical processes at work which act to decrease the surface-leaving radiance as the zenith angle at which the radiometer views the surface increases, since the SBT and dBT have been shown to decrease near-symmetrically about nadir at night. The surface emissivity is a key variable in surface-atmosphere interaction, and has been shown by previous studies to decrease with increasing zenith angle of observation (Takashima and Masuda, 1987; Masuda *et al.*, 1988; Sobrino and Cuenca, 1999; Bower, 2001) (among others). It is then possible that the decrease in surface emissivity may give rise to the observed variation in SBT and dBT with increasing zenith angle captured by the scanning radiometer. In fact, the distribution of the dBT data at night (0000–0600 hrs) from June to December, as shown in Figure 5.11, may be shown to be related to the decrease in the surface emissivity with zenith angle. The work confirming this result is described in the following sections of this thesis.

Month	Daily	Weekly	Monthly	3-Monthly
June	0.72	0.19	0.42	0.39
July	0.73	0.34	0.26	0.39
August	0.59	0.33	0.43	0.45
September	0.66	0.38	0.41	0.46
October	0.44	0.22	0.32	0.39
November	0.37	0.46	0.32	0.45
December	0.79	0.17	0.28	0.46

Table 5.5: Standard deviation of data for the mean distribution of dBT with observation zenith angle for the time interval between 0000 and 0600 hrs for months from June to December 2000, over time periods from one day to three months.
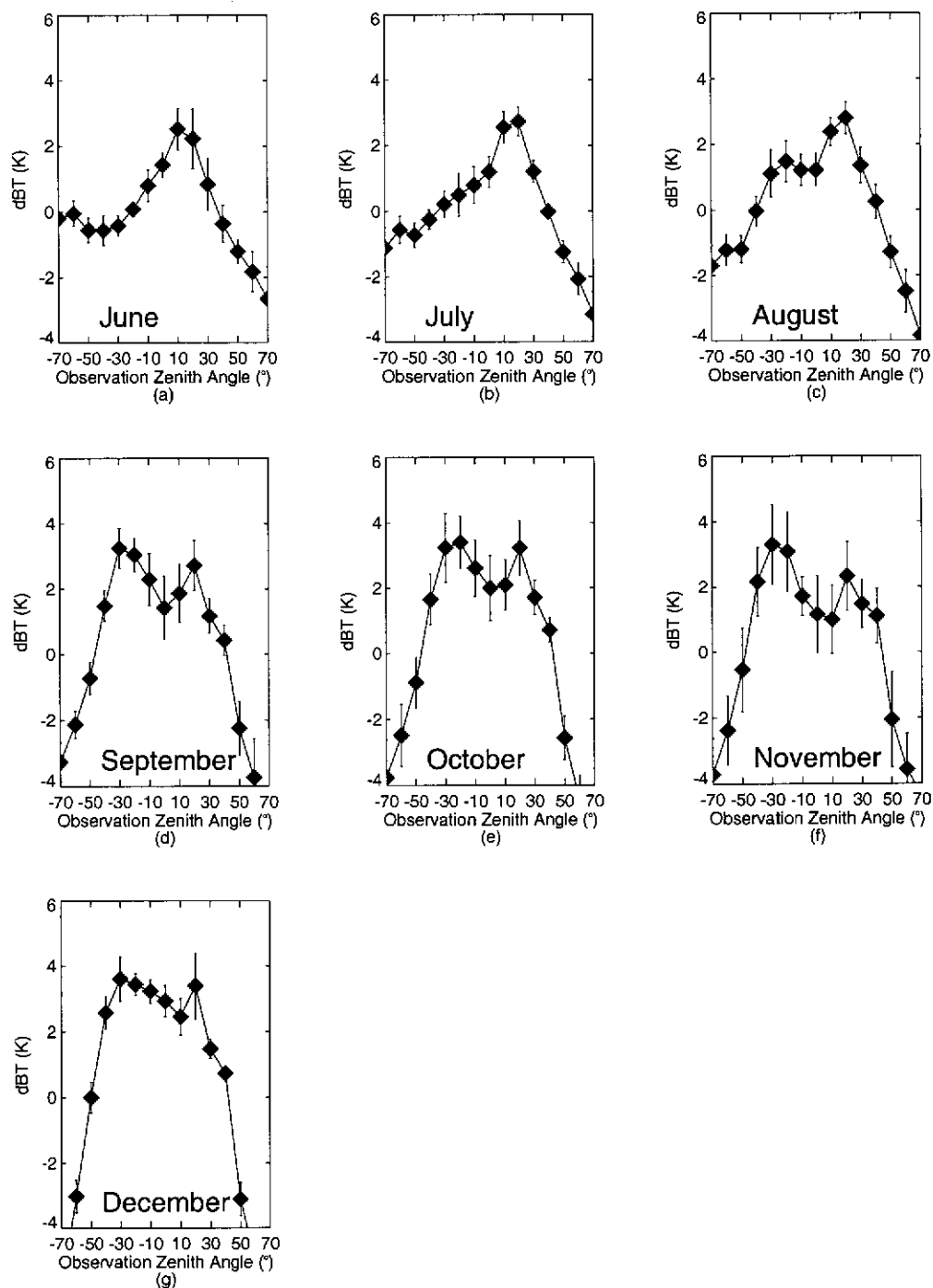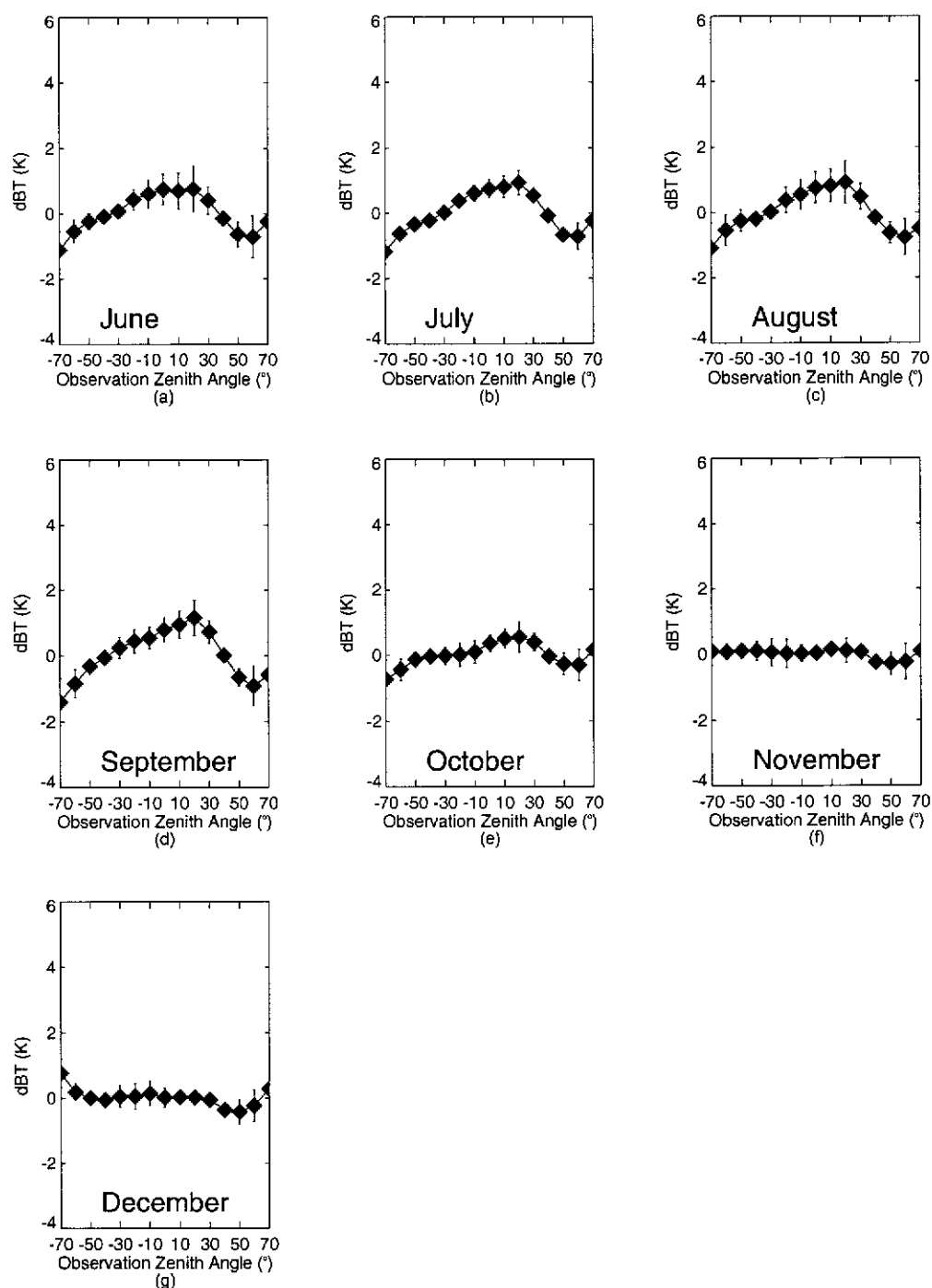
Figure 5.11: Plot of the angular dependence of dBT on observation zenith angle averaged over each of the months from June to December 2000, for the period between 0000 and 0600 hours, derived from measurements made by the scanning TASCO radiometer.

160

5.3 Modelling of Surface Emissivity

5.3.1 Application of a Theoretical Model For the Surface Emissivity

The variation in the value of the surface emissivity with zenith angle may be modelled from scattering theory. We evaluate the modelling approach developed by Wiscombe and Warren (1980) and applied by them to assess the spectral albedo of snow for any wavelength and at any zenith angle, which may be adapted to the estimation of surface emissivity of soil surfaces. The model is based on the δ-Eddington approximation for multiple scattering (Joseph et al., 1976) and Mie theory for single scattering. It accounts for the strong forward peak in scattering characteristic of quartz grains of radius greater than 2μm for wavelengths of radiation in the TIR (Takashima and Masuda, 1987), and assumes the scatterers to be independent spheres in a semi-infinite medium. Though the model was developed for snow, it is equally applicable to other surface types. The model requires information spectral estimates of the single-scattering albedo and the asymmetry factor to describe the anisotropic scattering of the radiation emergent from the surface. In this work, the scattering properties of quartz sand grains, the dominant soil type at the field site (Northcote and Wright, 1983), have been used to model the surface emissivity at the Amburla field site. More detail on the model itself may be found in Wiscombe and Warren (1980); Warren and Wiscombe (1980), and on the δ-Eddington approximation in Jospeh et al (1976). The emissivity model equations from Wiscombe and Warren model are given below;

$$\mu = \cos\theta,$$

$$g_s = \frac{g}{1+g},$$

$$\varpi_s = \frac{(1-g^2)\varpi}{1-g^2\varpi},$$

161

$$b_s = \frac{g_s}{1 - \varpi_s g_s},$$

$$\xi = [3(1 - \varpi_s g_s)(1 - \varpi_s)]^{\frac{1}{2}},$$

$$P = \frac{2\xi}{3(1 - \varpi_s g_s)},$$

$$\epsilon(\mu) = \frac{\xi\mu(\varpi_s b_s + 1 + P) + 1 + P - \varpi_s}{(1 + P)(1 + \xi\mu)}, \tag{5.1}$$

where;

g = the asymmetry factor,

ϖ = the single-scatter albedo,

θ = the zenith angle of surface-emitted radiation, and

ϵ = the spectral, directional emissivity.

The scattering parameters, g and ϖ may be calculated from Mie theory using refractive indices of quartz for a specified mean grain size. The spectral single-scatter albedo and asymmetry factor are integrated over the spectral response function of the radiometer and used in the model to estimate a band-averaged surface emissivity for the waveband of the TASCO radiometer.

The theoretical value of the surface emissivity has been calculated for each of the viewing angles of the scanning radiometer for three different grain sizes of mean radii 3μm, 1mm and 2.5mm. No surface or solar influence on the emissivity is taken into account here, so that the emissivity derived for viewing angles in the solar and anti-solar directions are equivalent. The theoretical emissivity distribution over the angular range scanned by the radiometer is therefore symmetrical about nadir. Further, the approach assumes that variations in SBT with viewing angle are due solely to the change in surface emissivity, and that the surface is therefore uniform and isothermal over the field of view of the radiometer. The work in this section describes the decrease in the surface emissivity relative to its nadir value, since it

162

is assumed in this analysis that the relative change in the surface emissivity with viewing angle that gives rise to the dBT distributions shown previously in Figure 5.11. Estimation of the absolute value of the surface emissivity is necessary for the atmospheric correction of remotely sensed SBT data. The component of the work for this thesis which deals with the estimation of the absolute value of the surface emissivity is described later in Section 5.3.4.

Normalized estimates of the surface emissivity for the three mean grain sizes, derived from the model, are given in Table 5.6. The data have been normalized so that $\epsilon_{\theta=0} = 1.0$, as assumed in the work of Sobrino and Cuenca (1999), to illustrate the relative change in the normalized surface emissivity with increasing zenith angle. The theoretical normalized emissivity data are compared to normalized estimates of surface emissivity given by Takashima and Masuda (1987) from their study of the emissivity of quartz powders in Figure 5.12a, and to the estimates of the relative surface emissivity for sand and gravel from the work of Sobrino and Cuenca (1999) in Figure 5.12b.

Figure 5.12a shows that, in general, the results from this work show a similar monotonic decrease in the normalized surface emissivity as the zenith angle increases, to the results from the study made by Takashima and Masuda. However, the results from the current study suggest a steeper decrease in the normalized surface emissivity for a given grain size than the Takashima and Masuda study. With respect to the apparent differences between the results from this and the Takashima and Masuda studies, it should be noted that; i) the surface emissivity is a spectral quantity; ii) the distribution of grain sizes, and; iii) chemical composition of the quartz samples affect estimates of the surface emissivity. In Figure 5.12a, the results from the Wiscombe and Warren model show that, for the 1 and 2.5mm samples, there is a significantly steeper decrease with zenith angle than for the Takashima and Masuda results for comparative grain sizes. The relative decrease of the 3μm sample appears close to the predicted result from Takashima and Masuda for the C_2 (radii between 0.1–37μm) sample. However, when compared to the C_1 sample

from Takashima and Masuda, which also contains grain sizes comparable to $3\mu m$, the modelled reults for the current work predict that the surface emissivity should decrease more slowly with increasing zenith angle than for the C_1 distribution. The results from Takashima and Masuda suggest that, for a given grain size, the decrease in the normalized surface emissivity with zenith angle is steeper at smaller wavelengths in the TIR. For the TASCO radiometer, the band-averaged wavelength is close to $10\mu m$, while the results from Takashima and Masuda used for comparison in Figure 5.12a are for the $10.5-11.5\mu m$ range and there is no spectral response function to consider, so the band-averaged wavelength assumed is $11.0\mu m$. This spectral difference may contribute to the apparent differences between the normalized spectral emissivity results from the two data sets, at least for the larger grain sizes. For smaller grain sizes, differences between the results from this work and that of Takashima and Masuda may also be related to the size distribution within the samples. In general, however, the results from the Wiscombe and Warren model show a decrease in the value of the normalized surface emissivity over the range of zenith angles scanned by the TASCO radiometer of around 20%, in agreement with the results of Takashima and Masuda.

Figure 5.12b shows that the relative decrease in surface emissivity is much greater over the angular range scanned by the radiometer for the surface at the Amburla field site than for the sand and gravel surfaces examined by Sobrino and Cuenca (1999). Sobrino and Cuenca observed decreases in the normalized surface emissivity of the order of only 5%. Clearly, the impact of zenith angle on the surface emissivity varies significantly both spectrally and with surface composition. These results reinforce the need for the surface emissivity to be accurately known on localized scales in order to accurately estimate LST from scanning sensors such as satellite radiometers.

Agreement between the results from the Wiscombe and Warren model and results from Takashima and Masuda suggest that the results from the modelling work described so far in this chapter may be justly applied to further investigate the rela-

mean radii	θ	0°	$\pm10^o$	$\pm20^o$	$\pm30^o$	$\pm40^o$	$\pm50^o$	$\pm60^o$	$\pm70^o$
3μm		1.000	0.997	0.988	0.973	0.951	0.920	0.880	0.827
1mm	$\epsilon(\theta)$	1.000	0.998	0.992	0.980	0.964	0.941	0.910	0.868
2.5mm		1.000	0.998	0.993	0.984	0.971	0.953	0.927	0.892

Table 5.6: Normalized surface emissivity values for the range of zenith angles scanned by the TASCO radiometer, derived from the Wiscombe and Warren model for emissivity using mean grain radii of 3μm , 1mm and 2.5mm.

tionship between decreasing surface emissivity with increasing zenith angle and the consequent SBT distributions observed by the scanning radiometer. Description of the application of the model to the explanation of the SBT distribution is continued in the following sections in this chapter.

5.3.2 The Impact of the Downwelling Sky Radiance

The definition of an appropriate value of the surface emissivity for a given view of the land surface is of great importance in improving the accuracy of satellite-derived LST. Whether a classification-based (Snyder *et al.*, 1998a), modelling (Li *et al.*, 1999), or statistical approach (Gillespie *et al.*, 1998) to the accurate estimation of surface emissivity is adopted, it is important that the method be based upon well understood physical interactions on the ground. The work described in this section relates the decrease in surface emissivity predicted by the Wiscombe and Warren model to the distributions of dBT data derived from observations made by the scanning radiometer.

In Figures 5.9, 5.10 and 5.11, and the contour plots of dBT in Figures 5.5, 5.6 and 5.7 the modelled angular difference in SBT, due to the decrease in surface emissivity with zenith angle, hereafter denoted ΔT_b , may be calculated via (2.4) (Chapter 2, p 8). The ΔT_b data are analagous to the dBT field data in Figures 5.9, 5.10 and 5.11. The distinction between dBT and ΔT_b is made because the ΔT_b data are derived from theoretical calculations of the relative decrease in surface emissivity with viewing angle (using the Wiscombe and Warren model), while dBT data

are estimated from actual measurements of SBT (satellite-derived estimates in the case of Chapter 4 and *in situ* measurements made by the scanning radiometer in the earlier sections of the current chapter). To calculate $T_b(\theta)$ at each zenith angle, T_s in (2.4) (restated below for convenience) is set to $T_b(\theta = 0)$. Under the constraint that the change in $T_b(\theta)$ with angle is due solely to the change in surface emissivity, the surface-leaving radiance at each zenith angle may be calculated using;

$$I_\nu^{surface}(\theta) = \varepsilon_\nu(\theta)B_\nu(T_s) + (1 - \varepsilon_\nu(\theta))\pi I_\nu \downarrow.$$

The surface-leaving radiance for each viewing angle is then converted to the equivalent blackbody temperature via the radiance-to-brightness temperature LUT for the TASCO radiometer, to form a modelled set of SBT data (here termed $T_b(\theta)$ so as to maintain the distinction between results derived from the theoretical model and field measurements) for a given scan cycle. The set of ΔT_b values is then derived by subtracting the mean from the set of $T_b(\theta)$, as described by (5.2);

$$\Delta T_b(\theta_i) = T_b(\theta_i) - \frac{1}{n}\sum_{i=1}^{n} T_b(\theta_i), \tag{5.2}$$

for the n zenith angles θ_i.

Because we are seeking to show the existence of an underlying surface emissivity effect, the data set we use must be independent of the maximum SBT since this will continually change. The ΔT_b data set for each scan cycle obtained using (5.2) meets this criteria. The data set therefore allows analysis of the angular distribution of SBT in a manner which should expose any underlying physical processes. The set of modelled ΔT_b derived using (5.2), for each scan cycle, are attributed to the changes in the value of the surface emissivity with observation zenith angle.

This approach also utilizes estimates of the directional components of the DWSR, derived via the regression relations developed to describe the characteristic angular
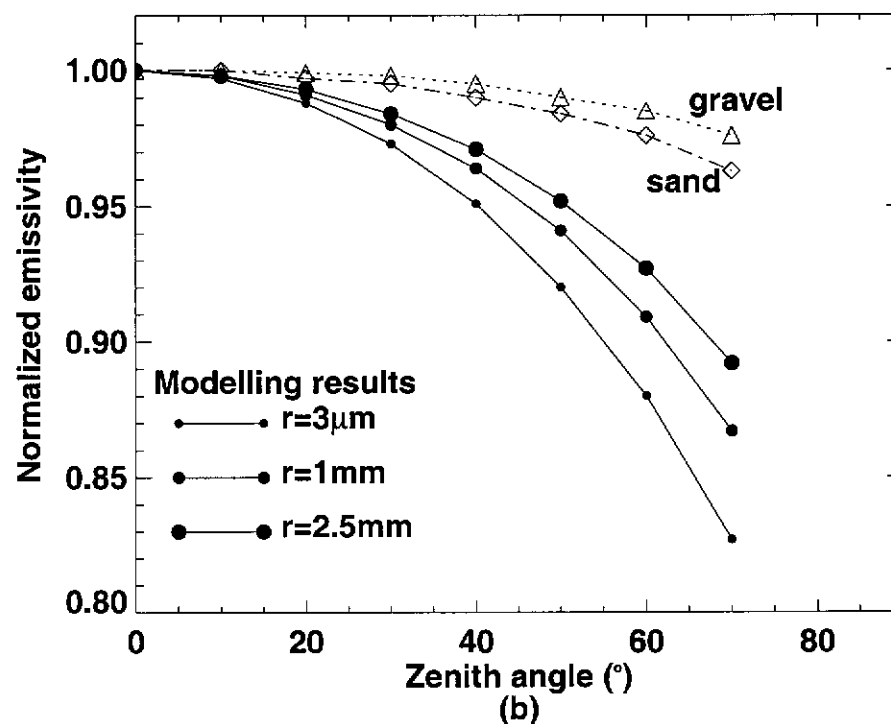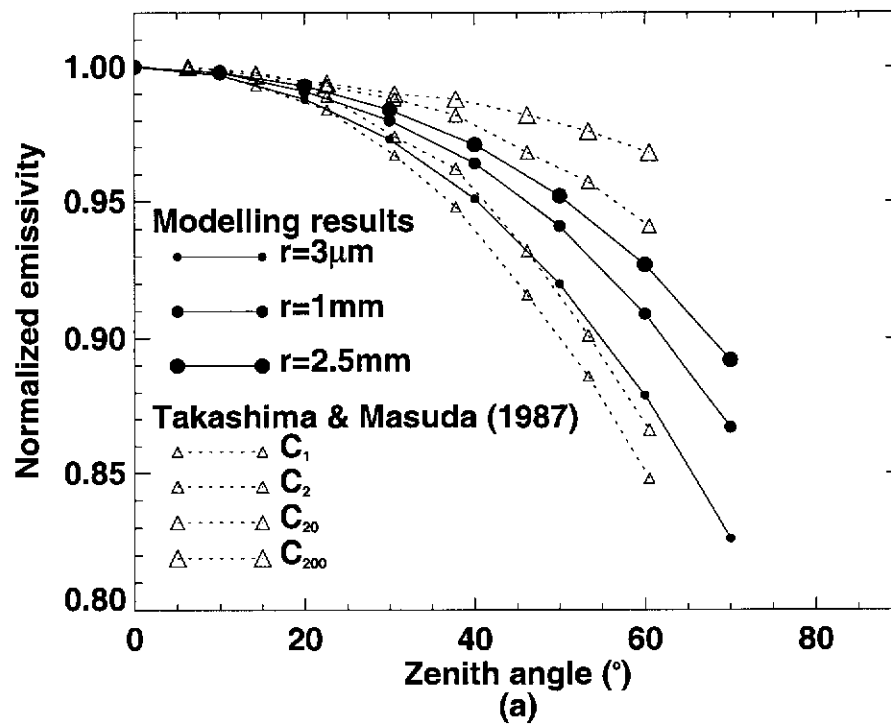
Figure 5.12: Comparison between angular variation of normalized surface emissivity estimates from the Amburla field site, using the Wiscombe and Warren (1980) model, and the results given by; a) Takashima and Masuda (1987) for grains of mean radii 0.05–18.5μm (C$_1$), 0.1–37μm (C$_2$), 1–370μm (C$_{20}$) and 10–3700μm (C$_{200}$), and; b) Sobrino and Cuenca (1999) for sand and gravel.

distribution of DWSR at the Amburla field site (see Chapter 4). These relations were developed using results from the atmospheric radiative transfer model LBLRTM (Clough *et al.*, 1996), described previously in Section 4.2. Importantly, application of these results requires that the surface exhibit specular properties, and this condition has been assumed for this work.

It is important to note that although the modelled angular distribution of the surface emissivity is fixed for a given grain size, the magnitude of the modelled set of ΔT_b is dependent upon the DWSR. As shown in Figure 5.13, the value of the DWSR has a marked impact upon the angular distribution of ΔT_b. The figure shows in each individual plot the modelled ΔT_b profiles for sky temperatures, which may be thought of as estimates of the mean temperature of the atmosphere, in the range 220–320 K, for separate values of T_s, over the same temperature range. It is evident from Figure 5.13 that the impact of the DWSR on the $T_b(\theta)$ distribution is dependent upon the relative magnitudes of surface emitted-radiance and the DWSR. For the Amburla field site at night, the conditions are such that the ΔT_b profile is characterized by Figure 5.13d. The surface temperature is generally in the range between 270 and 280 K (see Figures 5.5–5.7c), and the sky temperatures measured by the sky view of the TASCO radiometer range between 220 and 260 K. When the sky temperature is low ($\approx$ 220–240 K), the modelled ΔT_b distribution is concave, and decreases quickly with increasing zenith angle. As the sky temperature increases, the ΔT_b distribution becomes less dependent on the zenith angle of observation, and the vertical range of the data decreases. As the sky continues to warm, relative to T_s, the ΔT_b distribution continues to flatten, and the data at nadir changes from a maximum to a minimum at a sky temperature in the range of 260–280 K. Such conditions are representative of sky temperatures for significant cloud cover and rainfall scenarios. It is this DWSR effect which accounts for the change in the angular dependence of ΔT_b from a decreasing trend with increasing zenith angle in June–September, to near independence of zenith angle (for small to moderate zenith angles) between October–December (compare Figures 5.10 and

168

5.11a–d to e, f and g). Further, it is the change in the relative magnitudes of the surface-emitted radiance and the DWSR which causes the SBT profile (during the periods preceding and following the peak solar input to the surface) to be nearly constant with observation zenith angle. Consequently, the angular distribution of dBT also shows a similar independence of viewing angle over the range of zenith angles scanned by the radiometer.

For the range of sky and surface temperatures typical of the nighttime conditions at the field site, Figure 5.13d predicts the form of the dBT profiles which are shown by the monthly averages of ΔT_b profiles plotted in Figures 5.14 and 5.15. In these two figures, the modelled ΔT_b distribution predicted using the normalized surface emissivity profile for quartz grains of radii 1mm, and DWSR measurements from the TASCO radiometer are overlaid on the measured dBT distributions shown previously in Figures 5.11 and 5.10. Figure 5.14 shows the how well the modelled ΔT_b fit the dBT data measured by the scanning radiometer for nighttime data (0000-0600 hrs). Figure 5.15 shows comparison between ΔT_b and dBT for the time of the ascending ATSR-2 overpass (2300–2400 hrs). The data from the TASCO radiometer are represented by the filled diamonds, and the mean results from the model for each month are shown by the red dashed lines. The orange and blue curves respectively represent the ΔT_b profiles predicted by the model using the DWSR estimates one standard deviation above and below the mean value used to derive the mean results from the model for each month. Plots (a)–(d) in Figures 5.14 and 5.15 show that for nighttime conditions at the field site for June to September, there is a difference in dBT between zenith angles of 0 and 60° (a zenith angle range approximating that between forward and nadir views of the ATSR-2) of between 1 and 2 K. This is a consistent result over these four months because the dBT profile does not change significantly. However, between October and December the dBT profiles noticeably flatten out so that the dBT data are always near zero for zenith angles between 0 and 60° .

As noted previously in Section 3.2, the months of October, November and De-

169

cember 2000 were unseasonally wet, and, as a result, increased cloud cover and subsequently larger DWSR may be expected during these periods. The results from the Wiscombe and Warren model for the surface emissivity, combined with the results from the modelling of the DWSR using LBLRTM, accurately predict this change to the dBT distribution. It is this increase in the DWSR which causes the observed dBT distributions during these months rather than any change to the normalized surface emissivity distribution derived from the Wiscombe and Warren model.

The best agreement between the model and the field data is obtained for the nighttime period 0000–0600 hrs, as shown by the data in Figure 5.14. During this time the surface best meets the constraints on the emissivity model; namely, that the surface be isothermal. The agreement between the model and experimental data is still very strong at the time of the ATSR-2 overpass (Figure 5.15), in fact from both Figures 5.14 and 5.15 it is evident that the model easily predicts the dBT distribution to within 1 K (for several months better than 0.3 K) over the range of zenith angles and throughout the year. The largest difference between the measured dBT data and the mean result from the Wiscombe and Warren model occurs in July (Figures 5.14b and 5.15b). In this case, the measured dBT data are encompassed by the upper (orange curve) and lower (blue curve) bounds on the modelled results obtained by using the the maximum and minimum estimates of the DWSR, respectively, in the model. Since the measured dBT data appear symmetrical about nadir, it is likely that the choice of DWSR is the cause of the observed divergence between the data measured by the radiometer and the results predicted by the model. For September (Figures 5.14d and 5.15d), there are also some noticeable differences between the measured and modelled results. Some asymmetry is evident in the dBT data measured by the radiometer around an observation zenith angle of 20° where the model and field measurements diverge. Here, it may be that the land surface within the field of view of the radiometer at a zenith angle of 20° is warmer than surrounding areas because of vegetation or some other biophysical factor which modifies the properties of the land surface but, is not included in the Wiscombe and Warren

model. In general, however, the comparison between measured data and modelled results in Figures 5.14 and 5.15 show that significant divergence between the two datasets is rare, and that the Wiscombe and Warren model may be used to accurately predict the form of the dBT distribution at night.

Figures 5.16 and 5.17 show the performance of the modelled emissivity-derived ΔT_b profiles once solar input to the surface begins to impact upon the observed dBT distribution. The descending ATSR-2 overpass occurs around 1030 hrs local time. At this time of day, in the summer months, the sun is high in the sky. The solar geometry model used to calculate the solar zenith angles is in Figure 5.8. It gives the estimate of the closest zenith angles to nadir being approximately 30 degrees in November and December. Comparison of the form of the modelled and measured angular distributions of ΔT_b and dBT, respectively, at nighttime in Figures 5.14 and 5.16 shows the emergence of the more complex structures in the dBT distributions, as noted previously in Figures 5.5–5.7c and d, and Figure 5.8. The model does not capture the features that arise in the observed dBT profiles due to the solar influence, since it was developed for a specular surface under isothermal conditions and, as such, no mechanism for incorporating directional effects has been included. However, even though the asymmetric peak evident in plots (a), (b), and (c) of Figures 5.16 and 5.17, and the dual peaks approximately symmetrically positioned about nadir in Figures (d), (e), (f) and (g) of Figures 5.16 and 5.17 are not well captured by the model, the modelled ΔT_b between $\theta=0°$ and $\theta=10°$ zenith, which covers the range of zenith angles for the nadir view of ATSR-2, are most often within 1 K between June and August, and within 2 K from September to December when the dual peaks occur.

In Figure 5.16, between the months of September and December, Figures 5.16d–g, an additional (dashed green) curve is plotted. This curve represents the ΔT_b distribution predicted by the model using the sky temperature measured by the sky-view of the scanning radiometer. In these four months all sky temperature measurements were upward of 270 K and in some cases close to 300 K. For the Amburla
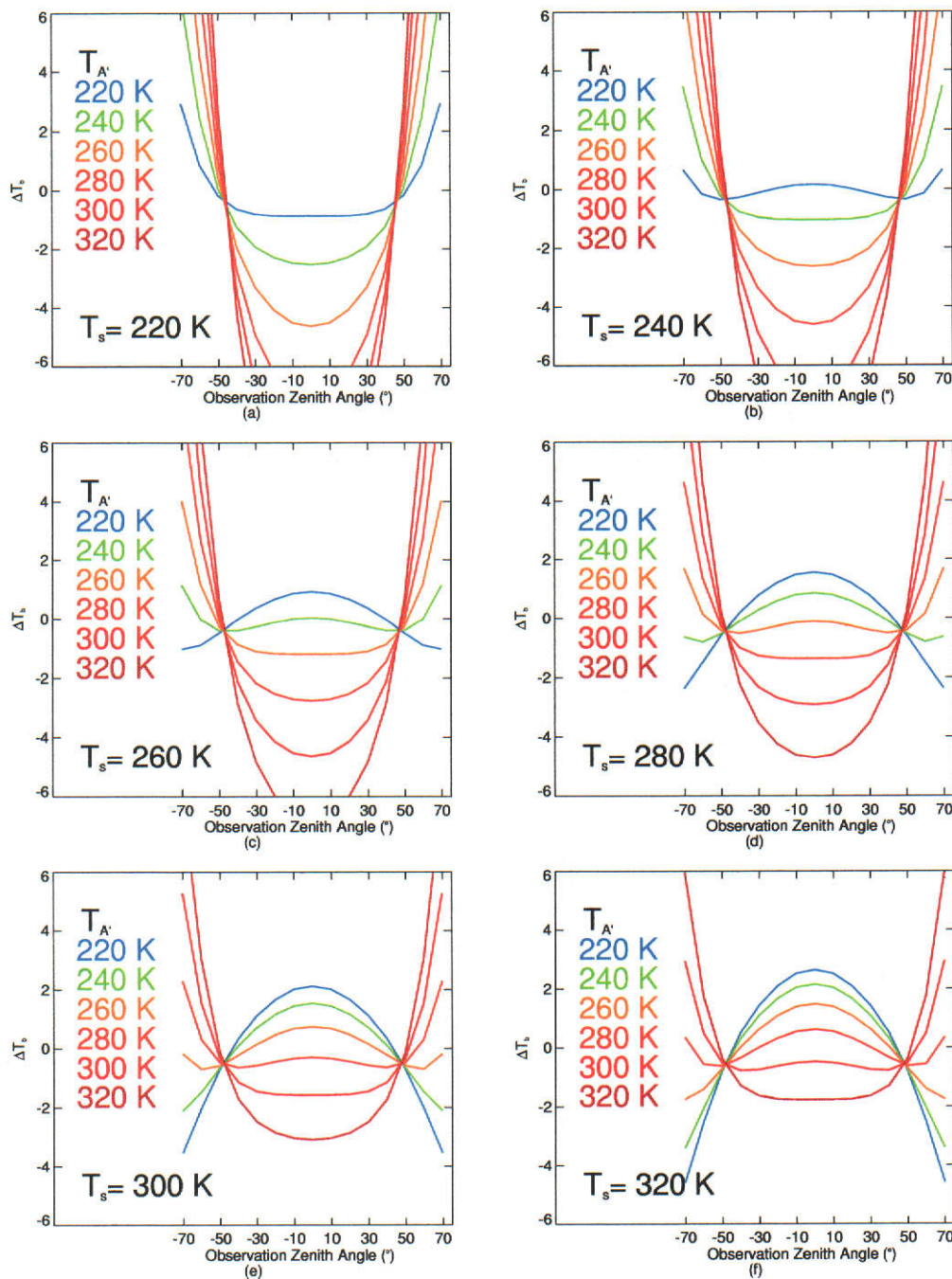
Figure 5.13: Predicted change in the form of the angular dependence of ΔT_b due to the relative magnitudes of the DWSR and surface-emitted radiance. Each panel corresponds to a specific surface temperature T_s and a set of six mean atmospheric temperatures, $T_{A'}$ (220–320 K).

field site, which has a typically dry atmosphere, these measurements of the sky temperature may be considered too high. Such measurements indicate that caution should be used, in some cases, when basing modelling of the ΔT_b distribution on DWSR estimates made by the radiometer. Extreme environmental conditions, either high temperatures or high rainfall, may introduce a warm bias into the sky-view measurements made by the radiometer (see Prata *et al.* (2003) for further description on operation and calibration of the scanning radiometer). In such cases, a better estimate of the DWSR may be obtained from radiosonde measurements such as those used to derive the relation between *in situ* and radiosonde-based estimates of the DWSR in Chapter 4 (see Section 4.2.4). In Figures 5.16d–g, and all following modelling work relating to the morning overpass of ATSR-2, the estimate of the DWSR made by the scanning radiometer has been replaced by the DWSR estimate (for the satellite view of the surface) derived from the relation between *in situ* and radiosonde DWSR estimates for 1030 hrs (see Figure 4.13b in Section 4.2.4 of Chapter 4). With this modification the model consistently describes ΔT_b at larger zenith angles to within an accuracy of 1 K throughout the year, which is an important result, since for scanning satellite sensors, zenith angles may extend out to 60°. For the descending overpass in the morning, the ATSR-2 is southbound so it views the field site at zenith angles equivalent to the south-looking half of the scanning radiometer cycle (the negative zenith angles in the Figures). For the ATSR-2 sensor, the zenith angle of the forward view is approximately 55° and the model predicts the observed dBT well at this zenith angle (see Figure 5.16). The choice to use the radiosonde-derived DWSR estimate instead of the radiometer measurement is made in this work as it is important for future LST validation work that the model accurately predicts the ΔT_b distribution for larger zenith angles (up to 55° for ATSR-2). The radiosonde-derived DWSR estimates for September–December were cooler than the corresponding estimates derived from the radiometer. Figure 5.13 showed that the ΔT_b curve tended to have a larger maximum at nadir for cooler sky temperatures at a set surface temperature. In the modelling work it was found

that the predicted ΔT_b distribution matched the dBT data measured by radiometer better when the colder radiosonde-derived DWSR estimate was used. It is important to note that the choice of DWSR has effects on the accuracy of the model, which will be discussed further in later sections relating to LST estimation.

In Figure 5.17, the progressive decrease in the SZA which occurs towards the middle of the day, as well as seasonally (from winter in June to summer in December), is shown to accentuate divergence of the model from the observations for both the asymmetrical cases in June, July and August (Figures 5.17a, b, c), and the dual-peak structure evident from September to December (Figures 5.17d–g). For the morning case (Figure 5.16), this structure is also not captured by the model. However, as before, the off-nadir angular variation is often very well described (within ± 1 K), and the nadir value of the ΔT_b distribution may still be predicted to an accuracy of ± 2 K.

The collection of data plotted in Figures 5.14 to 5.17 cover the range of conditions experienced on both a daily and monthly basis for the semi-arid soil conditions characteristic of the land surface of the field site. Together, the figures show that there is significant variation in the form of the ΔT_b profile over the diurnal cycle, and that only the part of the diurnal cycle, for which there is no solar influence, is accurately predicted by the model. The divergence between the ΔT_b distribution predicted using the Wiscombe and Warren model and the dBT data measured by the radiometer over the course of the day is illustrated in Figures 5.18 to 5.24. In these Figures, cycles of the measured dBT distribution have been extracted from the contour plots in Figures 5.18a to 5.24a, which show the mean dBT distribution for each month (June to December). These monthly mean radiometric zenith scans are plotted in Figures 5.18b to 5.24b for each month at the time at selected times (0200, 0600, 1000, 1400, 1800 and 2200 hrs). Each of these times is representative of the particular field conditions prevalent during these times of the day, and together the set of figures describe the performance of the model over a large proportion of the seasonal cycle. In Figures 5.18b– 5.24b, the ΔT_b distribution

predicted using the modelled normalized surface emissivity results (the red dashed line) is overlaid upon each cycle of mean dBT estimates extracted from the contour plot of the scanning radiometer data. As shown by previous plots, the agreement between the model and the field data is best when there is no solar input to the surface. This period has been loosely defined to lie between 0000-0600 hrs and the level of agreement between the model and field data in Figures 5.18b to 5.24b validates our assumption that the decrease in SBT/dbT observed at these times is due to the decrease in the surface emissivity as the zenith angle of observation increases. As the solar influence becomes more pronounced, the model and field data diverge, and the level of divergence is dependent upon the level of solar input to the surface.

The results described in the current section of this thesis have shown that the SBT/dBT distributions observed by the scanning radiometer at the Amburla field site are caused by the interaction between the angular distributions of surface emissivity and the DWSR. Figures 5.13 to 5.24 all show that the seemingly complex diurnal SBT/dBT cycle may be successfully modelled using the simple form of the RTE given by 2.4, with the change in the normalized surface emissivity with increased zenith angle being accurately described by the Wiscombe and Warren model, and the increase in DWSR with zenith angle being described by regression relations relating the nadir estimate of DWSR made by the TASCO radiometer to the DWSR which may be expected at larger zenith angles.

The DWSR regression relation for the TASCO radiometer was developed via the method previously described for the 11 and 12μm channels of the ATSR-2 in Chapter 4 (see Section 4.2.2; Figure 4.11). Figure 5.13 shows that the choice of DWSR is particularly important if the dBT profile is to be accurately predicted. Currently, the dBT profile may be modelled most accurately at night, where the model agrees with the scanning radiometer observations to within 1 K throughout the year for all zenith angles. During the day, the model predicts dBT at near-nadir zenith angles to within ± 1 K between June and August, and within ± 2 K from September to December, once the dual-peak dBT profile emerges. At zenith angles between 50° and

175

60°, the extent of the angular range of most scanning satellite sensors, the model predicts dBT to within ±1 K during the day throughout the annual cycle. However, although the model and measured data show good agreement at zenith angles in the range of the nadir and forward views of ATSR-2 (Figures 5.18 to 5.24), the model does not account for the structure which emerges in the measured dBT data across the full scan range of the radiometer during the day.

In the Wiscombe and Warren-based model there are no physical processes that permit such structure to occur. The explanation of these structures in dBT clearly are in need of further investigation. The consistent appearance over the monthly averaged data throughout the seven months suggest these are real features. This structure is believed to arise due to directional solar-surface interactions, and is discussed in more detail in the following section.

5.3.3   A Simple Empirical Model for the BEDF

At night, the ΔT_b distribution derived from the theoretical model for the normalized surface emissivity shows close agreement with the dBT distribution derived from the scanning radiometer data. However, during the day directional solar input to the surface causes the model and field data to diverge. This occurs most noticeably during the middle of the day when solar input to the surface is at its maximum. Either side of this solar maximum, as the solar influence wanes, the model and field data begin to converge once again. Such directional solar effects as those which appear to be impacting the filed measurements during the day are well known in the visible spectrum, and are described by the Bi-Directional Reflectance Distribution function (BRDF) (Roujean et al., 1992). More recently, work has been done by Snyder et al. (1998a) in extending the BRDF model into the TIR, a notion which then may describe the Bi-Directional Emission Distribution Function (BEDF) (Jupp, 1998). Models such as that developed by Li et al. (1999), as well as an array of other radiative transfer models describing intra-canopy interactions (Otterman et al., 1995a; Colton, 1996; Francois et al., 1997), among others, and the
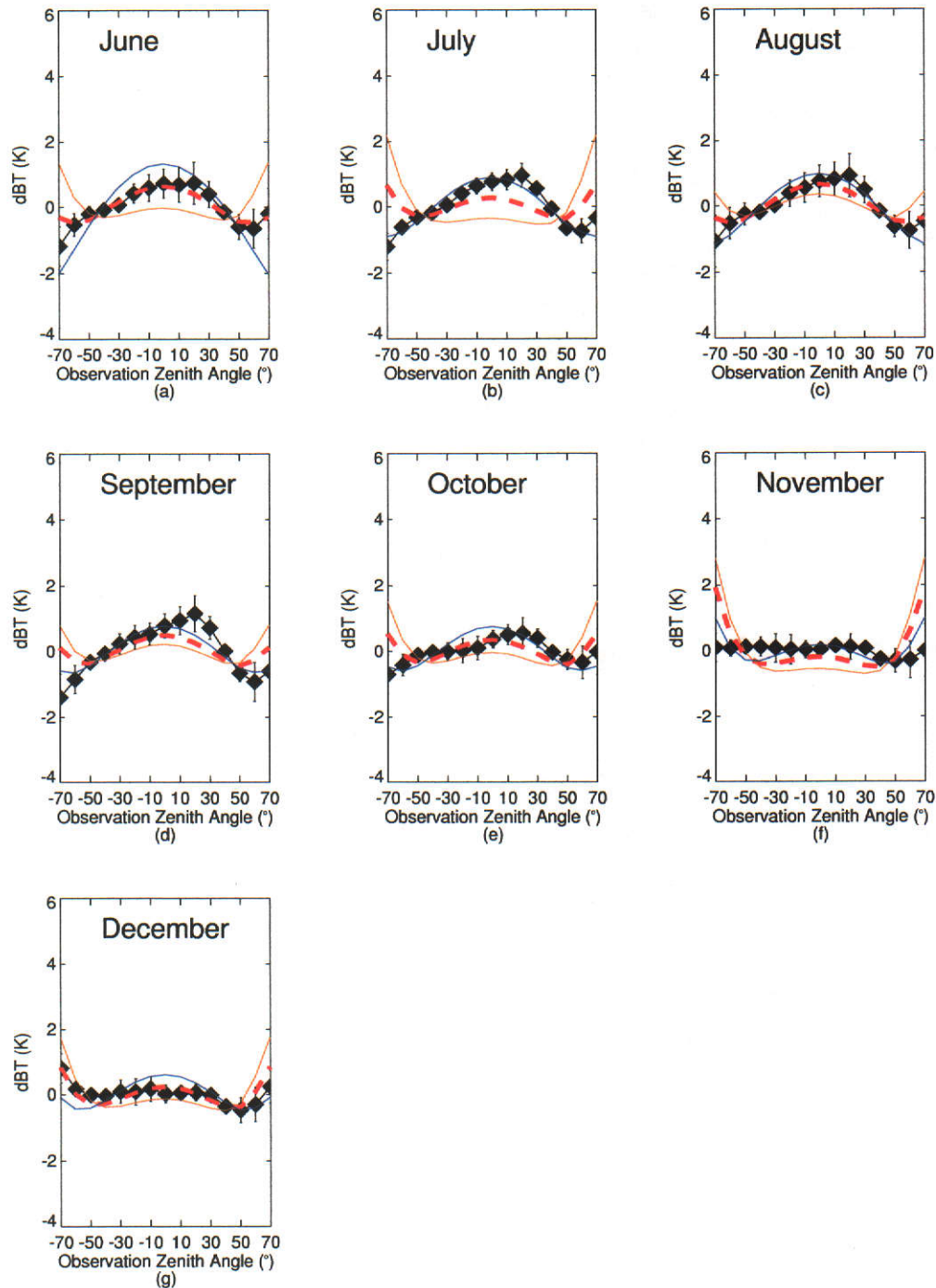
Figure 5.14: Comparison between the ΔT_b profile predicted using the theoretical emissivity model and the dBT profile measured by the TASCO radiometer for the night period (0000–0600 hrs). Filled diamonds show measured data. The red dashed line shows the mean result from the model. The blue line shows the results from the model using a DWSR one standard deviation below the mean value. The orange line shows the results using a DWSR one standard deviation above the mean.
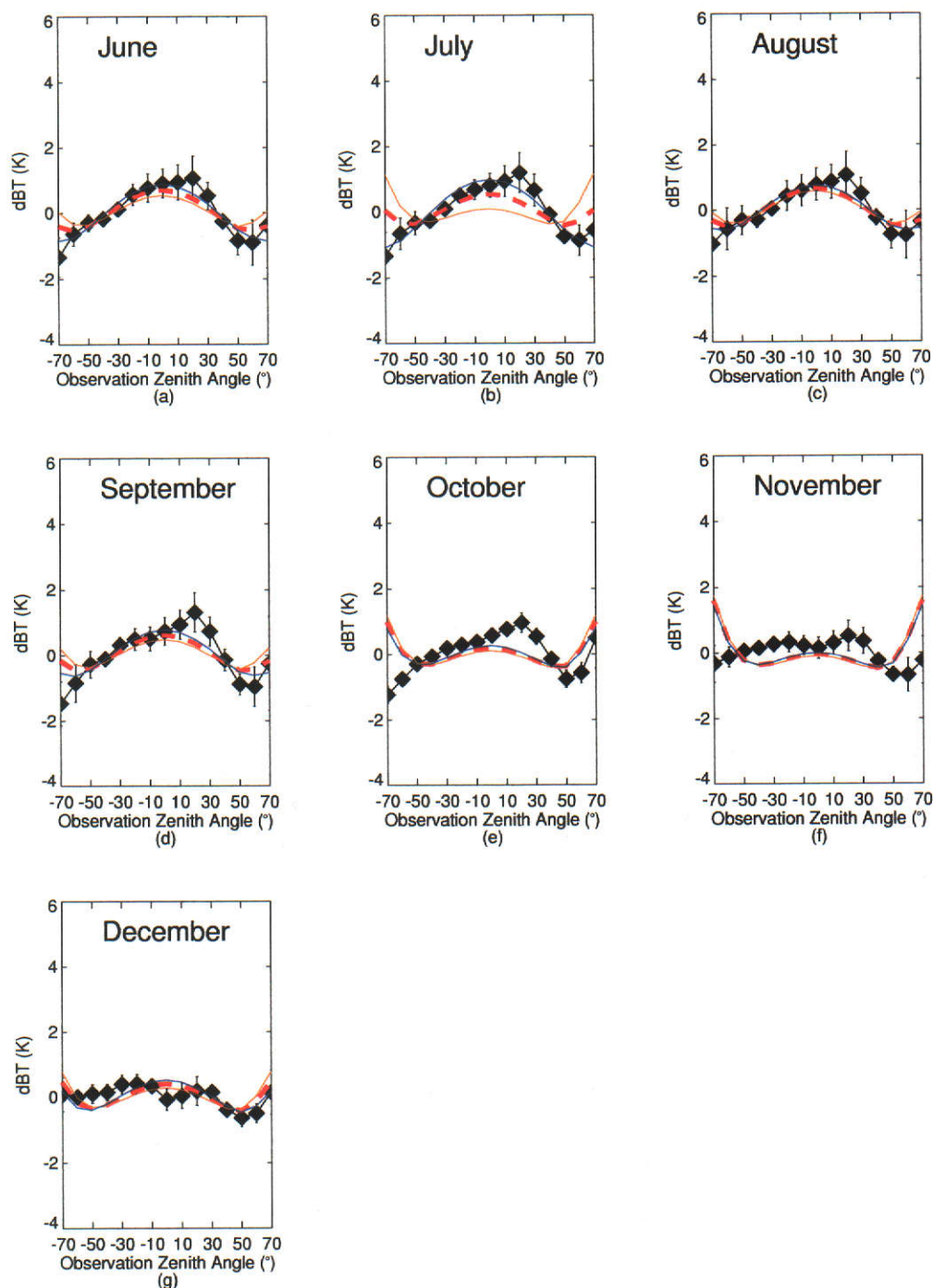
Figure 5.15: Comparison between the ΔT_b profile predicted using the theoretical emissivity model and the dBT profile measured by the TASCO radiometer for the period coinciding with the nighttime ATSR-2 overpass (2300–2400 hrs). Filled diamonds show measured data. The red dashed line shows the mean result from the model. The blue line shows the results from the model using a DWSR one standard deviation below the mean value. The orange line shows the results using a DWSR one standard deviation above the mean.

178
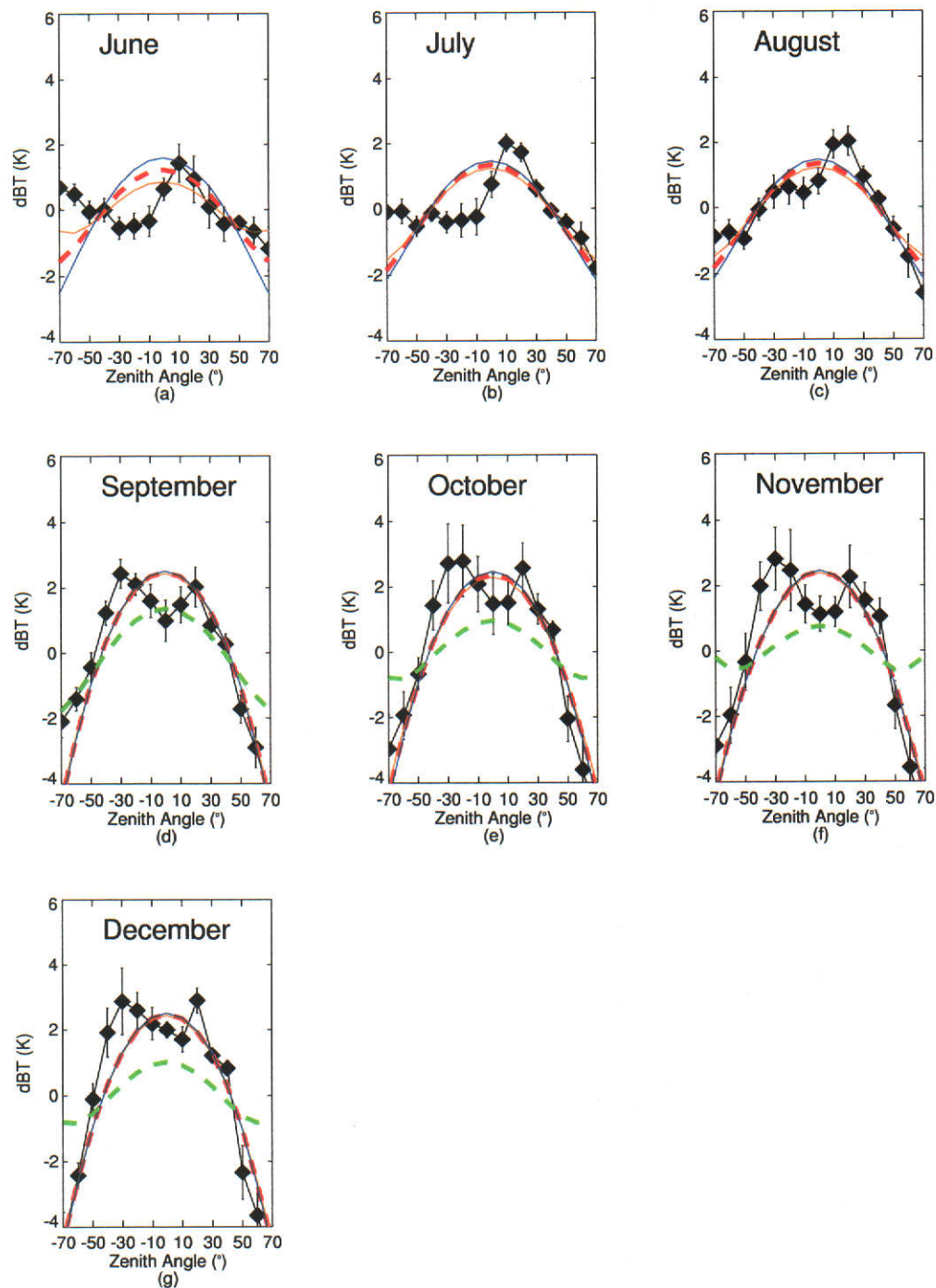
Figure 5.16: Comparison between the ΔT_b profile, predicted using the theoretical emissivity model, and the mean monthly dBT profile measured by the TASCO radiometer for the period coinciding with the morning ATSR-2 overpass (1000–1100 hrs).
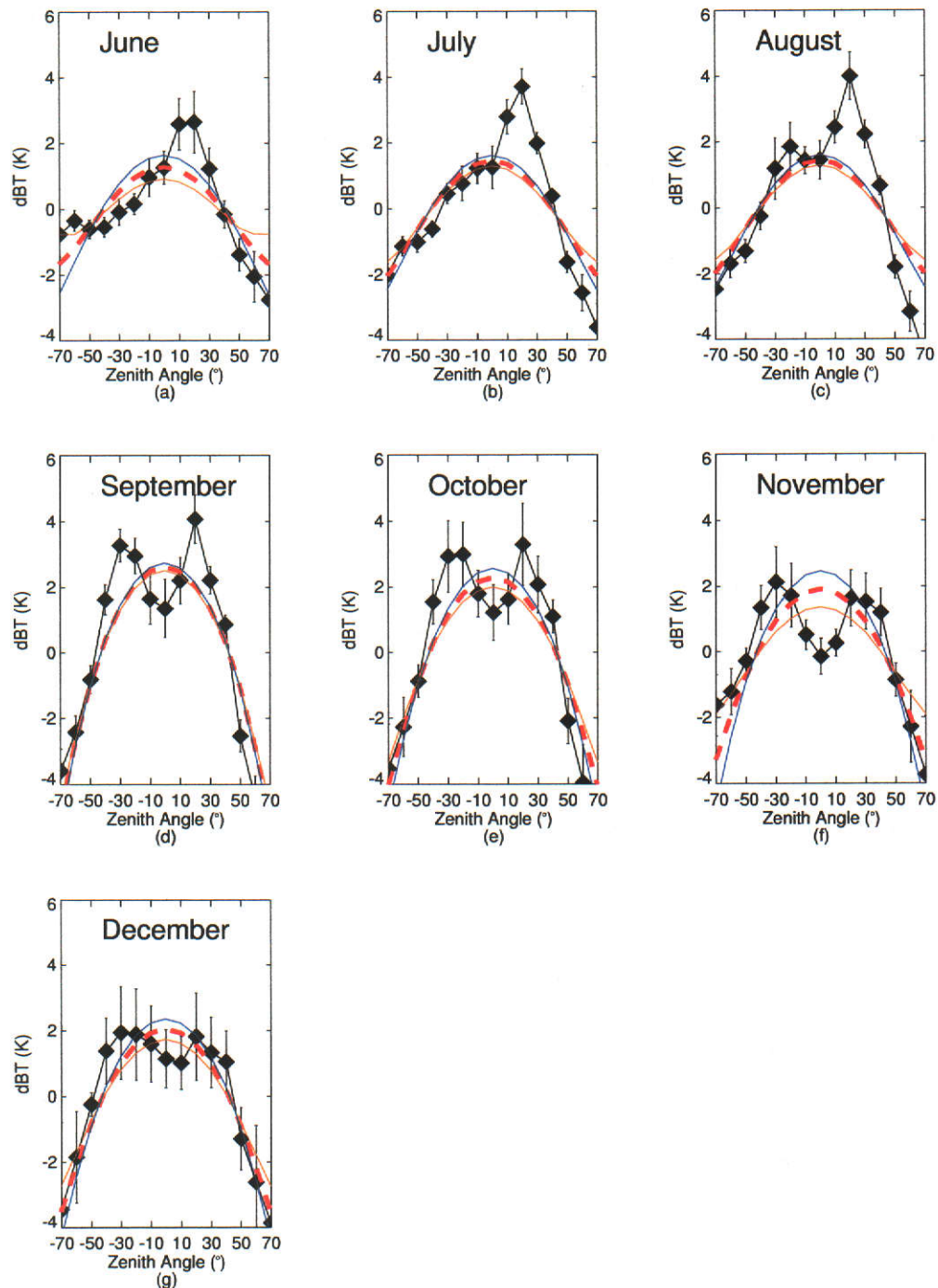
Figure 5.17: Comparison between the ΔT_b profile, predicted using the theoretical emissivity model, and the mean monthly dBT profile measured by the TASCO radiometer during the period of peak solar input (1200–1500 hrs).
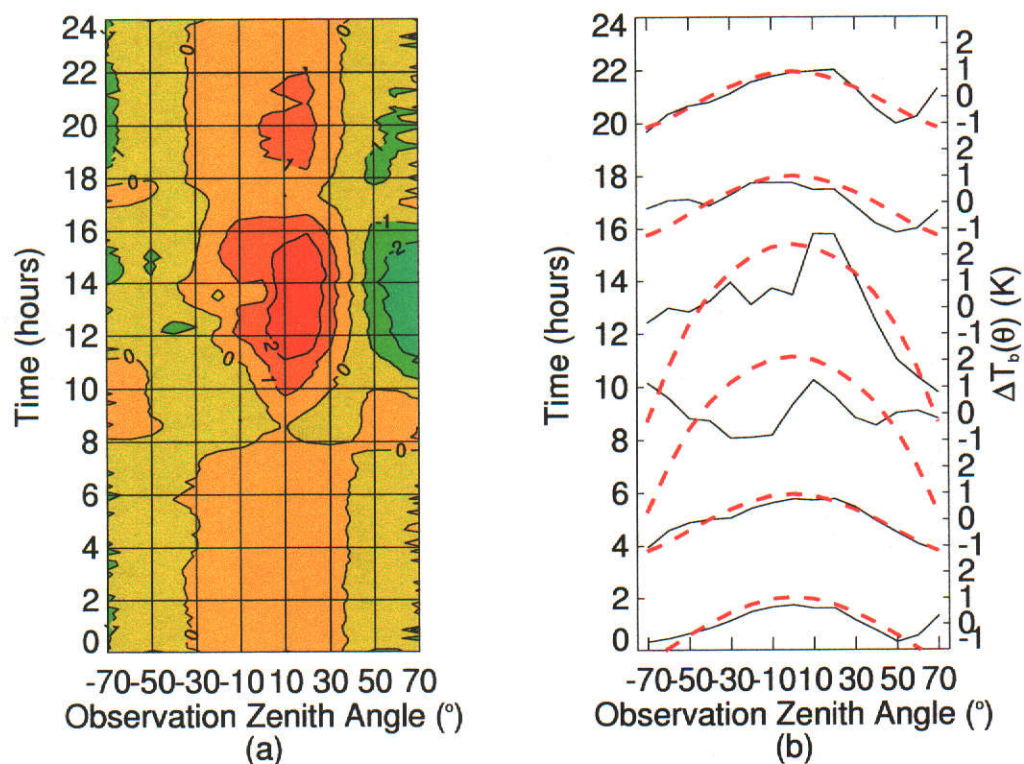
Figure 5.18: Illustration of the fit of the theoretical ΔT_b distribution to the measured dBT data over the diurnal cycle for June 2000. (a) Contour plot of the average dBT distribution measured by the scanning radiometer over the diurnal cycle for the month of June. (b) The dBT profile (solid line) extracted from the contour plot for selected times of the day. The ΔT_b distribution predicted by the model (red dashed line) at the coincident time is overlaid upon each extracted cycle.
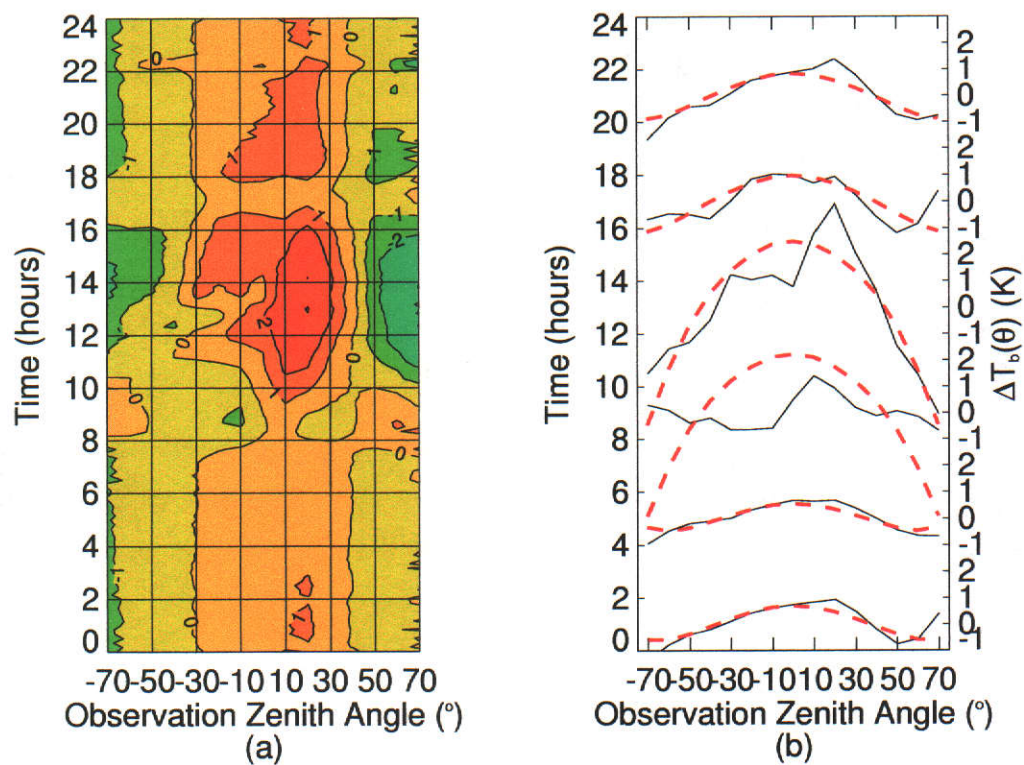
Figure 5.19: Illustration of the fit of the theoretical ΔT_b distribution to the measured dBT data over the diurnal cycle for July 2000. (a) Contour plot of the average dBT distribution measured by the scanning radiometer over the diurnal cycle for the month of July. (b) The dBT profile (solid line) extracted from the contour plot for selected times of the day. The ΔT_b distribution predicted by the model (red dashed line) at the coincident time is overlaid upon each extracted cycle.
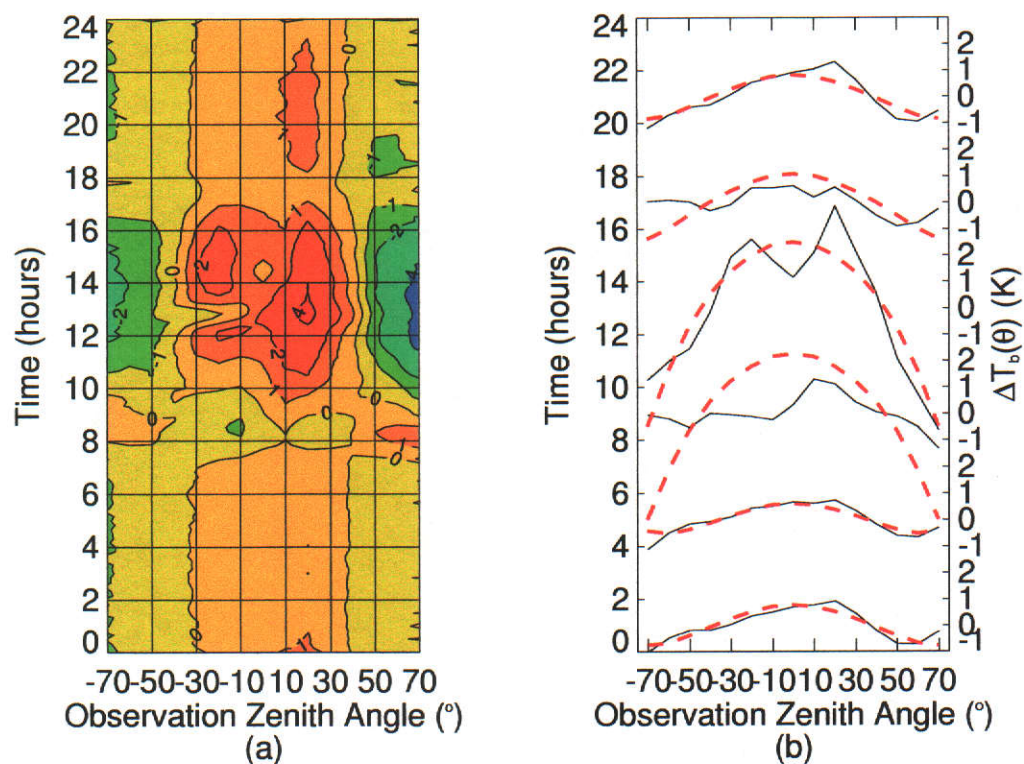
Figure 5.20: Illustration of the fit of the theoretical ΔT_b distribution to the measured dBT data over the diurnal cycle for August 2000. (a) Contour plot of the average dBT distribution measured by the scanning radiometer over the diurnal cycle for the month of August. (b) The dBT profile (solid line) extracted from the contour plot for selected times of the day. The ΔT_b distribution predicted by the model (red dashed line) at the coincident time is overlaid upon each extracted cycle.
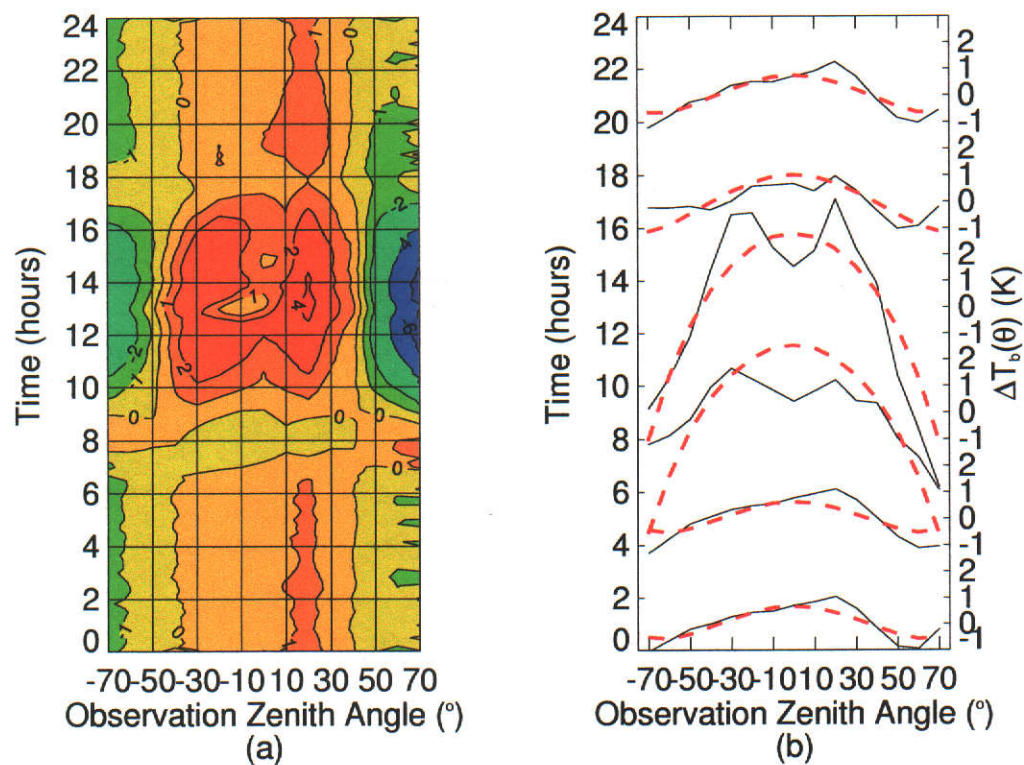
Figure 5.21: Illustration of the fit of the theoretical ΔT_b distribution to the measured dBT data over the diurnal cycle for September 2000. (a) Contour plot of the average dBT distribution measured by the scanning radiometer over the diurnal cycle for the month of September. (b) The dBT profile (solid line) extracted from the contour plot for selected times of the day. The ΔT_b distribution predicted by the model (red dashed line) at the coincident time is overlaid upon each extracted cycle.
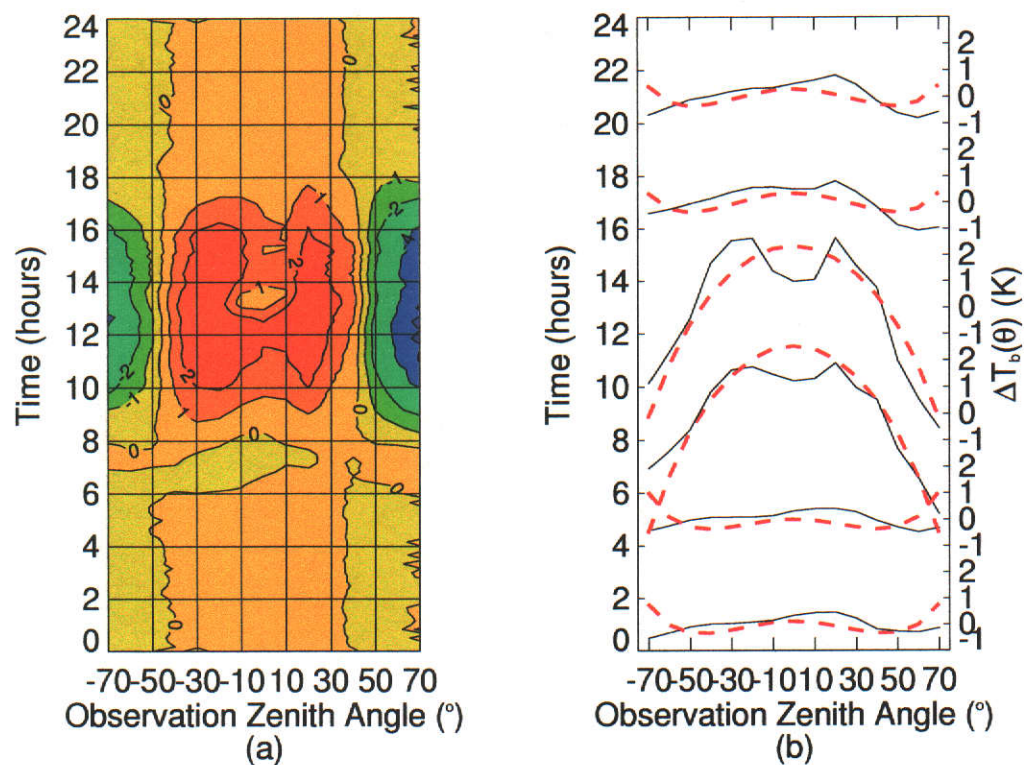
Figure 5.22: Illustration of the fit of the theoretical ΔT_b distribution to the measured dBT data over the diurnal cycle for October 2000. (a) Contour plot of the average dBT distribution measured by the scanning radiometer over the diurnal cycle for the month of October. (b) The dBT profile (solid line) extracted from the contour plot for selected times of the day. The ΔT_b distribution predicted by the model (red dashed line) at the coincident time is overlaid upon each extracted cycle.
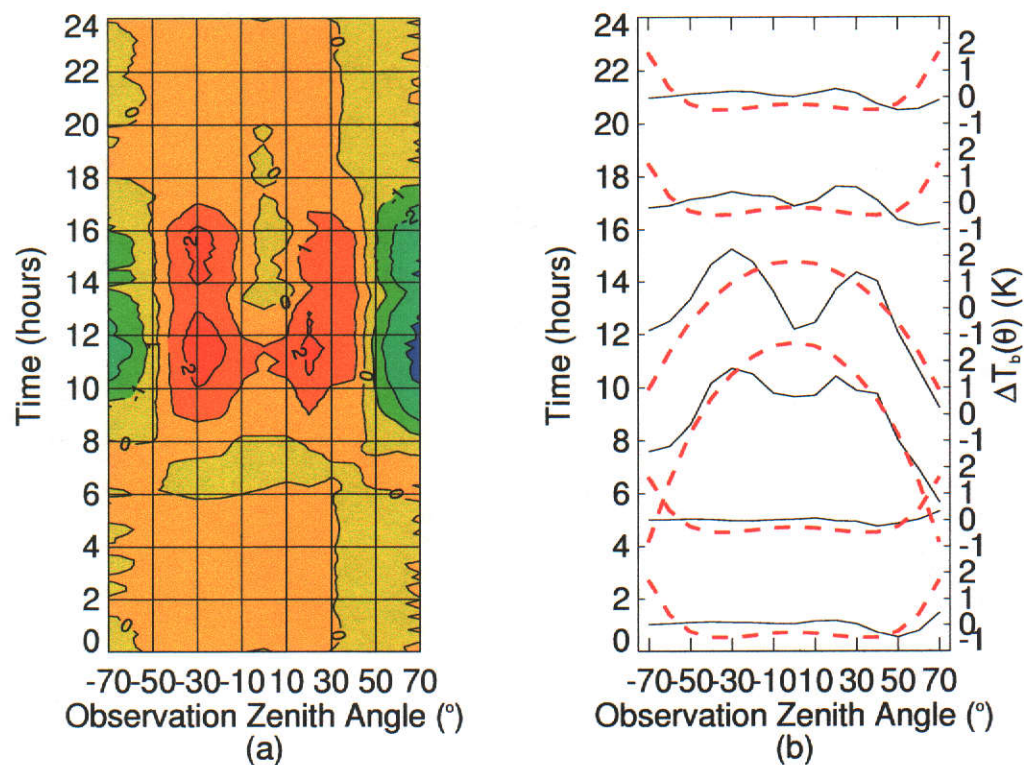
Figure 5.23: Illustration of the fit of the theoretical ΔT_b distribution to the measured dBT data over the diurnal cycle for November 2000. (a) Contour plot of the average dBT distribution measured by the scanning radiometer over the diurnal cycle for the month of November. (b) The dBT profile (solid line) extracted from the contour plot for selected times of the day. The ΔT_b distribution predicted by the model (red dashed line) at the coincident time is overlaid upon each extracted cycle.
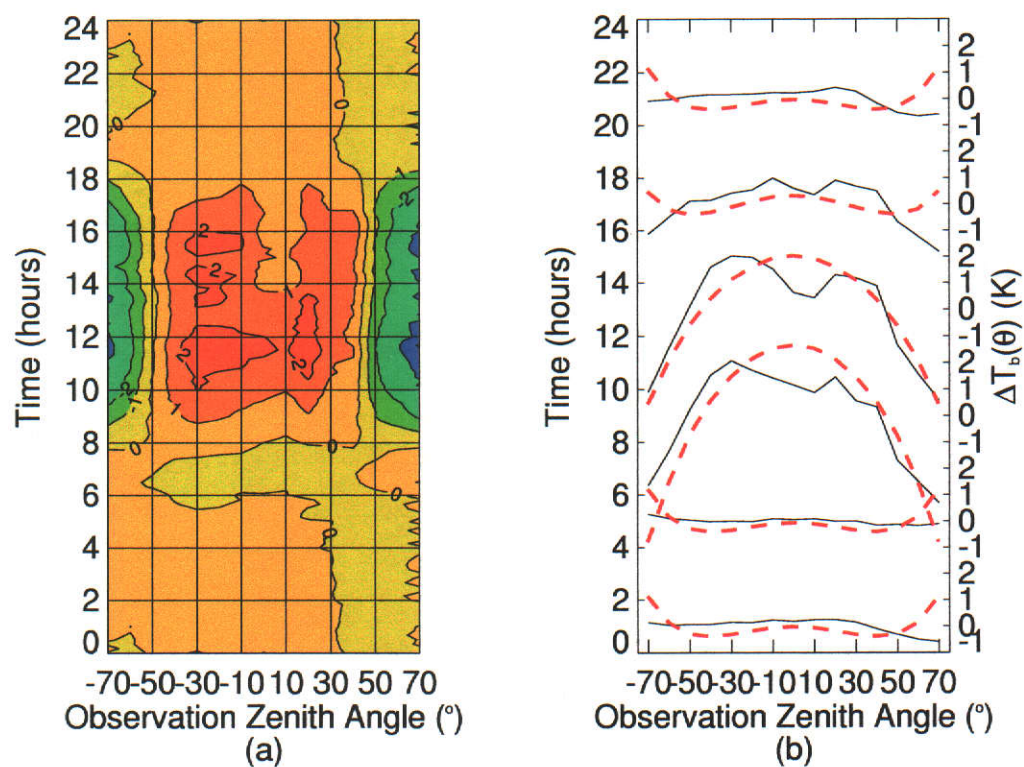
Figure 5.24: Illustration of the fit of the theoretical ΔT_b distribution to the measured dBT data over the diurnal cycle for December 2000. (a) Contour plot of the average dBT distribution measured by the scanning radiometer over the diurnal cycle for the month of December. (b) The dBT profile (solid line) extracted from the contour plot for selected times of the day. The ΔT_b distribution predicted by the model (red dashed line) at the coincident time is overlaid upon each extracted cycle.

measurements by Sobrino and Caselles (1990); Smith *et al.* (1997) and Minnis and Khaiyer (2000) predict anisotropy in the surface-leaving radiance between equivalent zenith angles in the solar and anti-solar directions. Such effects are apparent in the data plotted in Figures 5.18b to 5.24b, particularly in the middle of the day. During the day, the dBT distribution no longer exhibits the monotonic decrease with increasing zenith angle predicted by the ΔT_b distribution. The modelled ΔT_b distribution consistently underestimates the observed dBT data during the day at specific viewing angles. This occurs most notably where the single peak exists in the dBT data from June to August ($\theta=10^o$, see Figure 5.9a–c), and for the observations of dual-peak structure from September to December ($\theta=\pm30^o$, see Figure 5.9d–g). At other zenith angles the modelled ΔT_b distribution overestimates the observed dBT values.

If a fixed LST is assumed for the segment of the field site in which the scanning radiometer is located, the divergence between the measured dBT data and the modelled data, at zenith angles of observation for which the anisotropic peak is observed, for example, may be attributed to an underestimate of the effective surface emissivity, as in the work of Li *et al.* (1999), rather than a change in the temperature of the land surface. It is clear from Figures 5.5–5.7 and Figures 5.18 to 5.24 that the brightness temperature of the land surface of the Amburla field site measured by the scanning radiometer is not constant with observation zenith angle. As such, the theoretical model for the normalized surface emissivity used to derive the ΔT_b distribution, as described previously in Sections 4.3.1 and 4.3.2, is no longer appropriate. However, an effective surface emissivity (Li *et al.*, 1999) for each zenith angle may be defined. The approach would make use of the fact that the divergence between the modelled ΔT_b distributions (predicted using the Wiscombe and Warren (1980) model for the theoretical emissivity) and the observed field data (evident in Figures such as 5.16, 5.17 and 5.18b to 5.24b) appear to occur consistently over timescales of the order of a month. The Wiscombe and Warren model for the theoretical emissivity alone cannot account for the directional nature of the radiative

interactions between the surface and atmosphere illustrated by these figures.

Collectively, directional effects on the surface-emitted radiance may be described by a modelled BEDF (Jupp, 1998). The BEDF may include contributions from surface structure or anisotropies in DWSR caused by directional airmass temperature (Jupp, 1998) in the form of a correction to the normalized surface emissivity predicted by the Wiscombe and Warren model for each observation zenith angle. Such an empirical approach assumes both a Lambertian and specular component to the surface-emitted radiance, as described by the RTE. Expressions for the radiative transfer between surface and atmosphere for the modelled and measured cases may then be defined to describe the observed differences between the the angular distribution of ΔT_b predicted by the Wiscombe and Warren model and the dBT data acquired by the scanning radiometer. These equations are written in the form of (2.4) utilizing a 'normalized' surface emissivity from the Wiscombe and Warren model and an effective 'field' emissivity, such that;

$$B(T_T)(\theta)_{norm} = \epsilon(\theta)_{norm}B(T_{\theta=0}) + (1 - \epsilon(\theta)_{norm})B(T_{sky})(\theta), \qquad (5.3)$$

and;

$$B(T_T)(\theta)_{field} = \epsilon(\theta)_{field}B(T_{\theta=0}) + (1 - \epsilon(\theta)_{field})B(T_{sky})(\theta), \qquad (5.4)$$

where,

$B(T_T)(\theta)_{field}$ = the equivalent blackbody radiance for the SBT measured by a radiometer at each zenith angle θ,

$B(T_T)(\theta)_{norm}$ = the equivalent blackbody radiance for the SBT predicted using the Wiscombe and Warren model at each zenith angle θ,

$\epsilon(\theta)_{field}$ = the effective surface emissivity at each zenith angle θ, and

$\epsilon(\theta)_{norm}$ = the normalized surface emissivity predicted by the Wiscombe and Warren model for each zenith angle θ.

189

By combining (5.3) and (5.4) an expression for $\Delta\epsilon_{BEDF}$, the difference between $\epsilon(\theta)_{field}$ and $\epsilon(\theta)_{norm}$ for each observation zenith angle, may be derived;

$$\Delta\epsilon_{BEDF} = \epsilon(\theta)_{field} - \epsilon(\theta)_{norm}, \tag{5.5}$$

$$\Delta\epsilon_{BEDF} = \frac{B(T_T)(\theta)_{field} - B(T_T)_{norm}}{B(T_{\theta=0}) - B(T_{sky})(\theta)}, \tag{5.6}$$

where three of the four measurements on the right hand side of (5.6) are made by the radiometer and one is modelled. $\Delta\epsilon_{BEDF}$ represents the correction to the normalized theoretical emissivity derived from the model and is designed to account for the directional variation of the observed SBT. By applying ϵ_{BEDF}, the effective normalized surface emissivity of the land surface, ϵ_{field}, may be given by;

$$\epsilon(\theta)_{field} = \epsilon(\theta)_{norm} + \Delta\epsilon_{BEDF}, \tag{5.7}$$

where $\Delta\epsilon_{BEDF}$ is calculated via (5.6) and $\epsilon(\theta)_{norm}$ is predicted by the Wiscombe and Warren model. $\Delta\epsilon_{BEDF}$ for each month is given in Table 5.7 and is plotted in Figure 5.25.

When $\Delta\epsilon_{BEDF}$ is applied to value of $\epsilon(\theta)_{norm}$, derived from the Wiscombe and Warren model, the modelled ΔT_b distribution may be seen to match much more closely with the observed dBT data in Figure 5.26. After application of the correction term, the modelled data capture both the anisotropy between June and August (Figures 5.26a–c) and the dual-peak structure observed in the data between September and December (Figures 5.26d–g). The empirical derivation of the BEDF described here, as noted, is analagous to the conceptual model for surface emissivity

190

developed by Li *et al.* (1999). In their work, Li *et al.* define a characteristic surface temperature, which is directionally and spectrally invariant, and show that observed variations in surface temperature with viewing angle may be described by a correction to the r-emissivity (Norman and Becker, 1995) which encompasses directional effects such as those referred to by Jupp (1998).

The $\Delta\epsilon_{BEDF}$ term developed in this work forms a practical example of the correction term proposed by Li *et al.* (1999). However, it should be noted that, in the derivation given previously, $\Delta\epsilon_{BEDF}$ is a correction to the normalized surface emissivity derived from the Wiscombe and Warren model only. If the absolute value of the surface emissivity (see Section 5.3.4) were to be used in (5.3) and (5.7) in place of $\epsilon(\theta)_{norm}$ then $\epsilon(\theta)_{field}$ would be the effective absolute surface emissivity rather than the effective normalized surface emissivity as in (5.3) and (5.4). The absolute value of both the surface emissivity and the effective surface emissivity, due to the consideration of the directional effects, may only be defined once; i) the difference between the true surface temperature (T_s in (2.4)) and $T_{\theta=0}$ from (5.4) and (5.3) is known, or; ii) an estimate of the absolute value of the surface emissivity at nadir can be obtained from an independent source. The further application of the modelled description of the BEDF to the definition of the angular distribution of the absolute effective surface emissivity is described in the following Section.

It is clear from the work by Colton (1996), Francois *et al.* (1997) and Li *et al.* (1999) among others, that the effective surface emissivity (either normalized or absolute), $\epsilon(\theta)_{field}$, is dependent upon the geometry and spatial distribution of surface structure at a small scale through biophysical variables such as leaf area index and radiative anisotropy due to effects such as shadowing. The Amburla field site was chosen for this work as it was shown to be uniform at the scale of the FOV of the scanning radiometer and only sparsely vegetated (McAtee *et al.*, 2002). However, Figure 5.25 shows that well defined directional surface effects may still exist for this uniform, sparsely vegetated surface.

The suite of instruments at the Amburla field site measures area-averaged radia-

θ	June	July	Aug	Sept	Oct	Nov	Dec
-70	0.103	0.064	0.031	0.045	0.027	0.027	0.001
-60	0.037	0.013	-0.015	-0.008	-0.026	-0.022	-0.033
-50	0.040	0.042	0.030	0.027	0.031	0.026	0.039
-40	-0.013	-0.039	-0.040	0.006	0.007	0.027	0.035
-30	-0.008	-0.010	0.004	0.012	0.020	0.033	0.006
-20	-0.040	-0.025	0.024	0.040	0.049	0.020	0.038
-10	-0.045	-0.062	-0.057	-0.045	-0.023	-0.025	-0.013
0	-0.016	-0.022	-0.027	-0.034	-0.038	-0.040	-0.036
10	0.025	0.041	0.042	0.002	0.010	-0.003	0.021
20	0.025	0.038	0.029	-0.013	-0.014	-0.015	-0.021
30	-0.031	-0.025	0.000	0.014	0.038	0.035	0.047
40	0.010	-0.012	-0.004	-0.025	-0.022	-0.006	-0.031
50	0.019	0.035	0.024	0.006	0.001	0.008	0.008
60	0.008	-0.003	-0.024	-0.024	-0.041	-0.044	-0.052
70	0.041	-0.008	-0.040	0.001	-0.021	-0.024	-0.015

Table 5.7: Estimates of $\Delta\epsilon_{BEDF}$ for each month for the time period coincident with the morning overpass of the ATSR-2.

tive properties of the surface and does not provide information on such small-scale interactions. For this reason the current work acknowledges that the Wiscombe and Warren model fails to describe the angular distribution of surface emissivity during the day, and defines the BEDF to make use of the consistency in the divergence between the distribution of dBT observed by the scanning radiometer and the ΔT_b predicted by the model. It does not, however, seek to describe the underlying small-scale physical processes which give rise to the observed directional effects. Although, it should be noted that, in the future, investigations of such processes may prove valuable. More rigorous investigation of these processes requires additional data which may not be obtained from the larger-scale measurements made by the current instrumentation, but should be considered in the design of future field measurement progams.
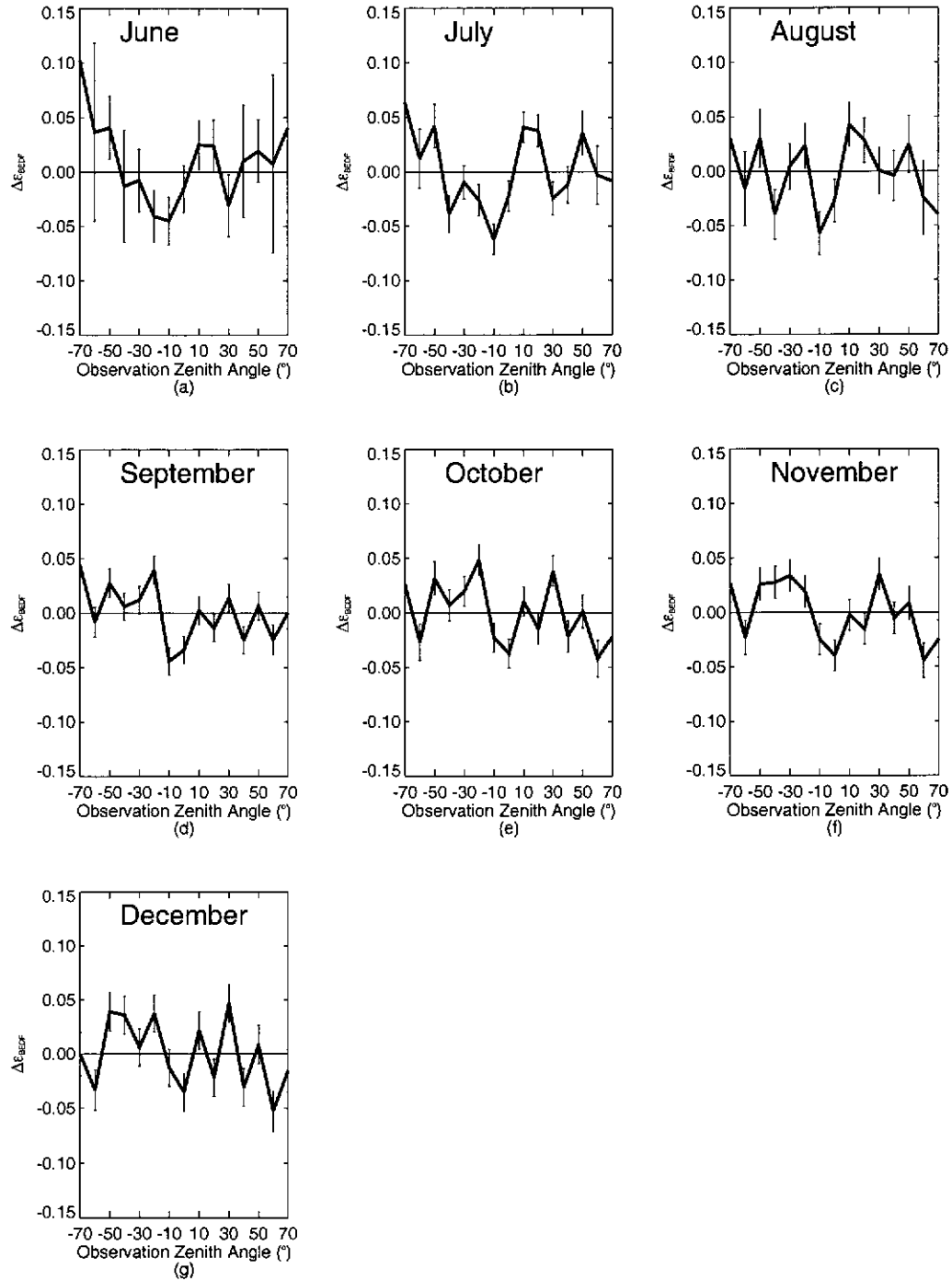
Figure 5.25: Estimates of $\Delta\epsilon_{BEDF}$ from the adjusted BEDF model for the time period coincident with the morning overpass of the ATSR-2.

5.3.4 Estimation of the Absolute Surface Emissivity

The preceding sections of this thesis have shown that the decrease in the SBT measured by the scanning radiometer may be related to the decrease in the surface emissivity which occurs with increasing zenith angle. Using (2.4) from Chapter 2 (p 8), the theoretical normalized emissivity distribution derived from the Wiscombe and Warren (1980) model combined with the regression relations developed in Chapter 4 (Section 4.2.2), to estimate the DWSR were shown to accurately describe the surface-atmosphere interactions resulting in the observed dBT distributions. However, for validation of satellite-derived estimates of LST it is necessary to know the absolute value of the surface emissivity in order to atmospherically correct the remotely sensed data. A method for estimating the atmospheric correction term, ΔT_{AC}, was described in Section 4.2.5 in Chapter 4. This method of atmospheric correction is applied to remotely sensed data from the Amburla field site in Section 5.4.2 of the current chapter, however, it is necessary, initially, to arrive at an estimate of the absolute value of the surface emissivity so that the LST prediction algorithms (developed in Chapter 4) may be adjusted to the conditions which exist at the Amburla field site.

McAtee *et al.* (2002) showed that the surface of the Amburla field site appears homogeneous at scales corresponding with the FOV of the scanning radiometer. However, it is pertinent to note that the effective surface emissivity for a given FOV of the scanning radiometer is dependent upon the composition of the FOV in terms of both its structural and material composition. For example, surface emissivity data acquired by a micro-Fourier Transform Interferometer (μ-FTIR) (Prata, 2002) show that substantially different emissivity spectra may be obtained for samples representative of a range of locations over the Amburla field site. Further, variability in the estimation of emissivity exists due to the spectral characteristics of the surface. Table 5.8 gives estimates of the surface emissivity derived from band averaging spectral measurements using the μ-FTIR made by Prata (2002) for different samples from the Amburla field site for; i) the scanning TASCO radiometer

194

Surface Type	TASCO	11μm	12μm
quartz rocks on clay soil	0.788	0.918	0.947
compacted clay soil	0.921	0.952	0.969
grassy cover over compacted clay soil	0.988	0.987	0.989

Table 5.8: Band-averaged estimates of the surface emissivity for three samples representative of the different locations within the Amburla field site for the TASCO radiometer and the 11 and 12μm channels of the ATSR-2.

installed at the field site; ii) the 11μm channel of the ATSR-2, and; iii) the 12μm channel of the ATSR-2.

The spectral response of the TASCO radiometer and the 11 and 12μm channels of the ATSR-2 were compared in Figure 4.10a in Section 4.2.2. As the spectral response functions for the TIR channels of the ATSR-2 are similar, so too are the relative values of the band-averaged surface emissivity. From previous studies of the emissivity of quartz grains by Takashima and Masuda (1987) and Salisbury and D'Aria (1992) the surface emissivity in the spectral range of the 11μm channel of the ATSR-2 is slightly lower than for the 12μm channel. For the samples of quartz rocks on compacted clay and bare compacted clay the band-averaged emissivity values for the 11 and 12μm channels given in Table 5.8 are higher in the 12μm channel than the 11μm channel as expected. The apparent difference between the band-averaged emissivity estimates for the 11 and 12μm channels of approximately 0.02 would give an error in the estimate of LST of approximately 0.7 K if one was substituted for the other. Further, following the work of Becker (1987) in the form of (2.27) from Section 2.3.1, a split-window algorithm utilizing the emissivities for the 11 and 12μm channels of the ATSR-2 given in Table 5.8 would underestimate the true LST by approximately 5 K due to spectral differences in emissivity. As such, the spectral effects of the emissivity on LST for these surface samples common to the Amburla field site are significant and need to be accounted for in algorithms for the retrieval of LST.

Because the spectral response function of the TASCO radiometer is so broad,

the band-averaged surface emissivity for the TASCO radiometer is lower than the equivalent estimate for the TIR channels from ATSR-2 for surface types where quartz is prominent. This occurs because the waveband of the TASCO radiometer covers wavelengths in the TIR at which Restrahlen bands in the spectral signature of quartz (Bower, 2001; Salisbury and D'Aria, 1992) occur. Hence, the lower emissivity at these wavelengths is incorporated in the band average over the spectral range of the TASCO radiometer and the result is lower than for the spectrally narrower TIR channels of the satellite sensors. The channels of the latter are centred at wavelengths outside these Restrahlen features. Interestingly, for those months when there exists a grass cover over the clay/quartz surface of the field site, the data in Table 5.8 show that spectral differences between the band-averaged emissivities for the TASCO radiometer and the 11 and 12μm channels of the ATSR-2 disappear. The impact of the Restrahlen bands upon the emissivity spectra may be reduced when there is a grass covering on the surface, and as a result the band-averaged estimates of the surface emissivity in Table 5.8 converge.

The μ-FTIR measurements were made at smaller spatial scales than the FOV of the scanning TASCO radiometer. In this work, based on the view of the field site from Figure 3.2 in Section 3.3, which shows some grass cover, the result from Table 5.8 (ϵ=0.988) for the grass-covered clay surface was chosen as being representative of the surface-emissivity of the field site for nadir viewing at the scale of the FOV of the radiometer. As noted earlier, the field site may be assumed to be homogeneous at scales of view of the FOV of the radiometer over its scan range. The estimate of the absolute surface emissivity for nadir may then be used to estimate the absolute surface emissivity for each zenith angle using the decrease in the normalized surface emissivity with increasing observation zenith angle obtained from the Wiscombe and Warren (1980) model.

The surface emissivity at each zenith angle for the TASCO radiometer and the 11 and 12μm channels of the ATSR-2 are given for the nighttime case in Table 5.9. An estimate of the accuracy with which the emissivity may be defined for the

mean radii	θ	0°	$\pm10^o$	$\pm20^o$	$\pm30^o$	$\pm40^o$	$\pm50^o$	$\pm60^o$	$\pm70^o$
TASCO		0.988	0.986	0.980	0.968	0.952	0.930	0.899	0.858
11μm	$\epsilon(\theta)$	0.987	0.985	0.979	0.967	0.951	0.929	0.898	0.857
12μm		0.989	0.987	0.981	0.969	0.953	0.931	0.900	0.858

Table 5.9: Band-averaged absolute surface emissivity values for the range of zenith angles scanned by the TASCO radiometer for; i) the TASCO radiometer; ii) the 11μm channel of the ATSR-2, and; iii) the 12μm channel of the ATSR-2 for night-time conditions, derived from band averaging emissivity spectra measured by μ-FTIR.

nighttime case for each month, and at each zenith angle, is given in Table 5.10. The uncertainty is derived from the variability in the angular distribution of dBT, as represented by the error bars in the data in Figure 5.14 in Section 5.3.2. For the majority of cases, in Figure 5.15, the mean result from the model predicted the dBT to within the uncertainty estimate (one standard deviation) at each zenith angle (except for some cases in July and September, and at some extreme zenith angles of observation). Because the Wiscombe and Warren model accurately predicts the dBT profiles at night, the emissivity may be estimated to within ±0.01 in most cases.

For the daytime case, the inclusion of the BEDF defined in Section 5.3.3 means the angular distribution of surface emissivity valid for the time of the descending overpass of the ATSR-2; i) is no longer symmetrical about nadir, and; ii) must be continuously updated (in the current work this is done on a monthly basis). The absolute values of the effective surface emissivity are given for each month at each zenith angle of observation for the TASCO radiometer in Table 5.11. The equivalent estimates of surface emissivity for the 11 and 12μm channels of the ATSR-2 are not tabulated here, but as is apparent from Table 5.9, it may be assumed that, for the grass-covered clay surface, the surface emissivity values for the 11μm channels are 0.001 lower and the estimate for the 12μm channel 0.001 higher than the estimate given for the TASCO radiometer for each month at each zenith angle in Table 5.12. As for the nighttime case, the predicted angular distribution of ΔT_b agrees closely

θ	June	July	Aug	Sept	Oct	Nov	Dec
-70	0.015	0.008	0.011	0.011	0.005	0.003	0.013
-60	0.011	0.007	0.010	0.010	0.005	0.004	0.010
-50	0.009	0.006	0.008	0.007	0.005	0.002	0.008
-40	0.010	0.006	0.007	0.006	0.003	0.002	0.006
-30	0.008	0.005	0.006	0.006	0.003	0.002	0.006
-20	0.010	0.006	0.007	0.007	0.003	0.002	0.009
-10	0.009	0.005	0.007	0.006	0.003	0.002	0.008
0	0.008	0.005	0.006	0.006	0.003	0.003	0.007
10	0.009	0.006	0.007	0.007	0.003	0.002	0.008
20	0.009	0.007	0.007	0.006	0.003	0.003	0.008
30	0.010	0.007	0.008	0.007	0.004	0.003	0.008
40	0.009	0.007	0.008	0.007	0.005	0.004	0.008
50	0.010	0.008	0.008	0.008	0.004	0.003	0.008
60	0.011	0.009	0.010	0.011	0.008	0.008	0.009
70	0.033	0.031	0.027	0.027	0.017	0.015	0.022

Table 5.10: Uncertainties in the estimates of the absolute surface emissivity for each month, at each observation zenith angle, over the time interval coincident with the nighttime overpass of the ATSR-2.

with the dBT data measured by the scanning radiometer in the morning at the time of the descending overpass of the ATSR-2, after inclusion of the correction factor due to the BEDF (see Figure 5.26 in Section 5.3.3). The accuracy of the estimates of the absolute value of the effective surface emissivity is also of the order of ± 0.01 in most cases.

Knowledge of the angular distribution of the surface emissivity now allows the estimation of LST from the data derived from both *in situ* measurements and from satellite-based sensors. The estimation of LST from *in situ* measurements and its application to the validation of satellite-based estimates of LST is described in the following section.

θ	June	July	Aug	Sept	Oct	Nov	Dec
-70	0.971	0.932	0.899	0.913	0.895	0.896	0.869
-60	0.947	0.923	0.895	0.902	0.884	0.888	0.877
-50	0.981	0.983	0.971	0.968	0.973	0.967	0.980
-40	0.951	0.925	0.924	0.970	0.971	0.991	0.999
-30	0.972	0.970	0.984	0.992	1.000	1.013	0.986
-20	0.952	0.967	1.016	1.032	1.041	1.012	1.030
-10	0.953	0.936	0.941	0.953	0.975	0.973	0.985
0	0.984	0.978	0.973	0.966	0.962	0.960	0.964
10	1.023	1.038	1.040	1.000	1.008	0.995	1.020
20	1.016	1.031	1.021	0.979	0.978	0.978	0.971
30	0.949	0.955	0.980	0.994	1.018	1.015	1.027
40	0.974	0.952	0.960	0.939	0.942	0.958	0.933
50	0.960	0.976	0.965	0.947	0.942	0.949	0.949
60	0.918	0.907	0.886	0.886	0.869	0.866	0.858
70	0.909	0.860	0.828	0.869	0.847	0.844	0.853

Table 5.11: Estimates of the effective absolute surface emissivity for each month, at each observation zenith angle, for the time interval coincident with the descending overpass of the ATSR-2.

θ	June	July	Aug	Sept	Oct	Nov	Dec
-70	0.088	0.050	0.060	0.020	0.024	0.021	0.025
-60	0.083	0.029	0.037	0.018	0.020	0.019	0.024
-50	0.031	0.022	0.029	0.017	0.018	0.018	0.022
-40	0.053	0.019	0.026	0.017	0.018	0.018	0.021
-30	0.031	0.018	0.025	0.018	0.017	0.017	0.022
-20	0.027	0.018	0.026	0.019	0.018	0.018	0.021
-10	0.025	0.016	0.023	0.016	0.016	0.016	0.021
0	0.025	0.017	0.024	0.016	0.017	0.017	0.021
10	0.026	0.018	0.024	0.016	0.016	0.017	0.022
20	0.028	0.018	0.024	0.016	0.017	0.018	0.021
30	0.031	0.018	0.025	0.017	0.018	0.018	0.021
40	0.053	0.019	0.026	0.016	0.017	0.017	0.021
50	0.031	0.023	0.030	0.018	0.018	0.019	0.022
60	0.083	0.030	0.037	0.019	0.020	0.019	0.024
70	0.088	0.050	0.061	0.021	0.023	0.024	0.026

Table 5.12: Uncertainty in the estimate of the surface emissivity for each month, at each observation zenith angle, over the time interval coincident with the descending overpass of the ATSR-2.
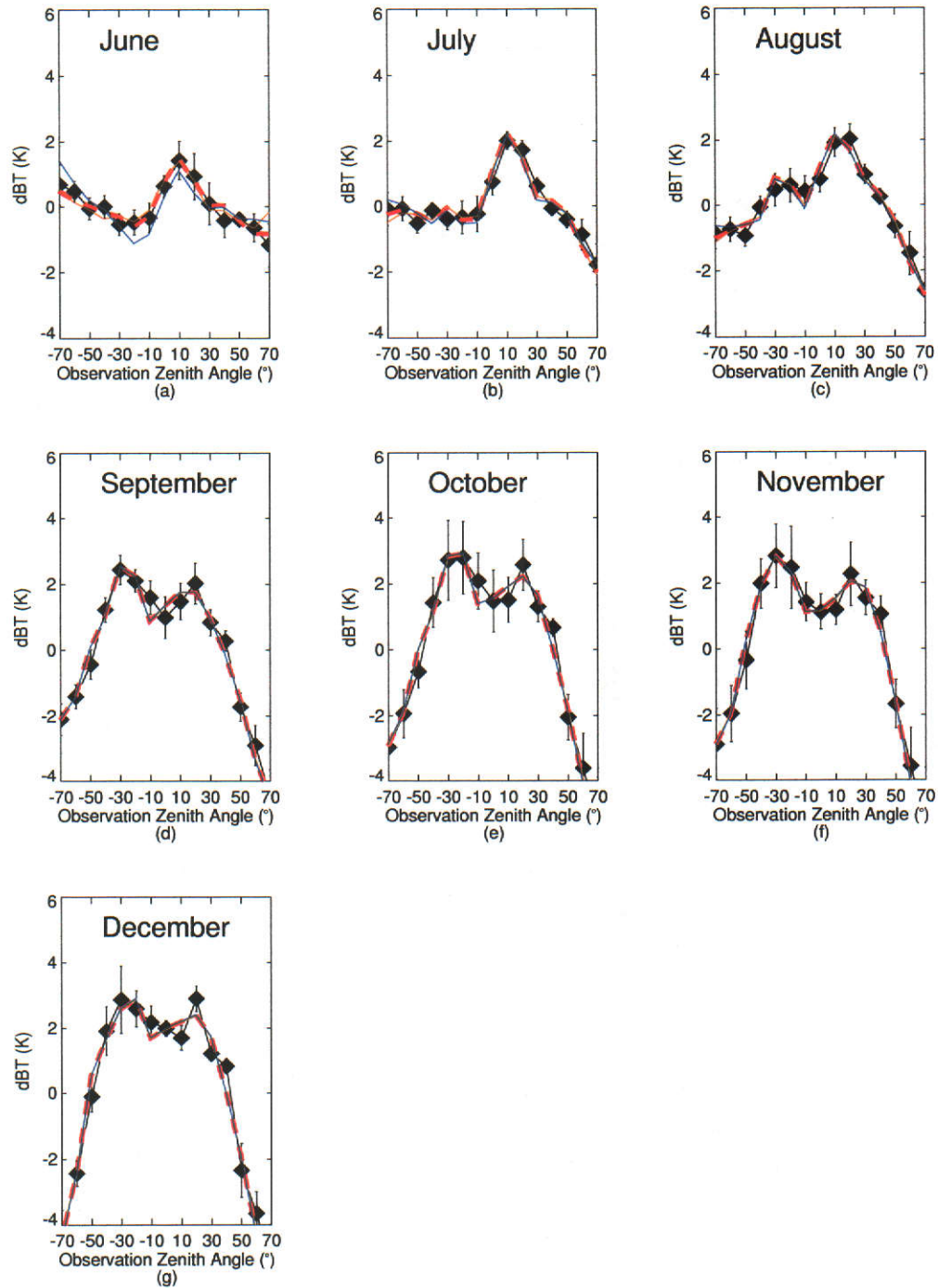
Figure 5.26: Improvement in the prediction of the ΔT_b distribution at the time of the morning ATSR-2 overpass, once the basic emissivity model is extended to include the empirical formulation of the BEDF. The model predicts the form of the dBT distribution much more accurately after application of the correction term.

5.4 Land Surface Temperature

5.4.1 *In Situ* Estimates

So far it has been shown that the land surface at the Amburla field site exhibits well-defined diurnal cycles in the angular distribution of SBT. The observed SBT structure has been shown to arise from the interaction of the surface emissivity distribution derived from the theoretical surface emissivity model developed by Wiscombe and Warren (1980) with the directional components of the DWSR, defined for each of the viewing angles utilized by the scanning radiometer.

At night, the characteristic dBT profiles extracted from the SBT data measured by the scanning radiometer have been shown to be attributable to the decrease in surface emissivity with increasing zenith angle. However, during the day, explanation of the observed dBT profiles does not appear so straight forward. There are well-defined, consistent cycles in the data, as for the nighttime case, but the angular distributions are no longer simply related to the theoretical normalized surface emissivity distribution from the Warren and Wiscombe model. The directional nature of the dBT profiles during the day is related to the solar geometry, which is not included in the Wiscombe and Warren model. Such directional effects were, however, incorporated into an empirical description of the observed daytime dBT distributions through the calculation of the correction term describing a BEDF (Jupp, 1998), $\Delta\epsilon_{BEDF}$, which was applied to the normalized surface emissivity derived from the Wiscombe and Warren model in Section 5.3.3. With the inclusion of this adjustment the model and the measurements exhibited a high degree of agreement.

In Sections 5.3.1–5.3.4 the characteristic dBT profiles for both night and day at the Amburla field site represent the residual after the mean has been extracted from the angular distribution of the SBT. The success in modelling the observed dBT in terms of the change with zenith angle of the surface emissivity then justifies the definition of a mean SBT over the angular range scanned by the radiometer, which may be derived by subtracting the dBT distribution from the observed SBT profile.

A characteristic LST for the surface may subsequently be defined after correcting for the effects of non-blackness.

In order to estimate the surface-emitted radiance in terms of quantities measured by the scanning radiometer, (2.4) from Section 2.1 may be rearranged and written as;

$$B(T_s)(\theta) = \frac{B(T_T)(\theta)(1 - \epsilon(\theta))B(T_{sky})(\theta)}{\epsilon(\theta)}, \tag{5.8}$$

where,

$B(T_s)(\theta)$ = the blackbody equivalent radiance for the LST,

$B(T_T)(\theta)$ = the blackbody equivalent radiance for the SBT measured by the scanning radiometer at zenith angle θ,

$\epsilon(\theta)$ = the band-averaged surface emissivity for the TASCO radiometer at

zenith angle θ (from Table 5.9 for the nighttime case and Table 5.11 for the daytime)

case, and

$B(T_{sky})(\theta)$ = the DWSR for zenith angle θ.

In terms of the same quantities averaged over the scanning range of the radiometer, (5.8) may be written;

$$\overline{B(T_s)(\theta)} = \frac{\overline{B(T_T)(\theta)(1 - \overline{\epsilon(\theta)})B(T_{sky})(\theta)}}{\overline{\epsilon(\theta)}}. \tag{5.9}$$

Although equations (5.8) and (5.9) are written in terms of blackbody equivalent radiance rather than temperature, $B(T_s)(\theta)$ and $\overline{B(T_s)(\theta)}$ may be converted to an estimate of the LST via a LUT. Because the range of brightness temperatures within the ΔT_b distribution is small, the impact of averaging brightness temperature rather than radiance is negligible.

By definition (see Section 2.2.1), the LST for a uniform surface determined from (5.8) and (5.9) should be independent of zenith angle. This condition is met using the approach described by (5.9), provided that the physical quantities important to the atmospheric correction process for ground-based measurements may be accurately estimated. Constraints on the validity and accuracy of the model in this work relating to the *in situ* estimation of LST are that; i) the spectral surface data used in the Wiscombe and Warren model to predict the surface emissivity distribution must be representative of the composition of the surface viewed by the radiometer; ii) the surface be grass-covered clay so that the band-averaged surface emissivity estimate for the TASCO radiometer is valid (see Section 5.3.4), and; iii) the DWSR should be accurately known and fluctuation in its magnitude over the time taken to complete several scan cycles should be minimal.

The work described so far in the current chapter has concentrated on monthly averages of data from the scanning radiometer in order to show the dBT distributions extracted from the observed SBT data are not purely transient effects due to the prevailing environmental conditions. Comparisons between modelled predictions and radiometer measurements, such as those depicted in Figures 5.18–5.24 from Section 5.3.2 and Figures 5.15 and 5.26, from Sections 5.3.2 and 5.3.3 confirm this to be the case and show that the dBT profile characteristic of specific periods of the diurnal cycle may be accurately predicted provided that the DWSR may be accurately estimated. The times of day used to illustrate the results derived from the modelling work were chosen so as to coincide with the descending (1030 hrs local time) and ascending (2330 hrs local time) overpasses of the ATSR-2 satellite sensor, as this work has applications to the validation of LST from such sensors.

Figure 5.27 shows the LST profile for each month at the time of the ascending overpass of the ATSR-2 derived using (5.9), with SBT measurements made by the TASCO radiometer, and the band-averaged surface emissivity, $\epsilon(\theta)$, for the radiometer from Table 5.9 as inputs. When the modelled surface emissivity distribution is representative of the surface viewed by the radiometer and an accurate esti-

mate of the DWSR is obtained, the modelled ΔT_b distribution may be seen to agree closely with the observations of dBT made by the radiometer, as in Figures 5.15a, c and g from June, August and December of 2000, respectively. When this is the case, application of (5.9) gives an estimate of the mean LST for these months which is nearly independent of observation zenith angle, as shown by Figures 5.27a,c and g. The estimates of mean LST for July, September, October and November, shown by Figures 5.27b, d, e and f do not show estimates of LST as close to being independent of the observation zenith angle of the radiometer as in the plots for June, August and December because the modelled ΔT_b distributions in Figures 5.15b, d, e and f do not fit the observed dBT profiles as closely. Figure 5.13 from Section 5.3.2 showed that for a given surface temperature the dBT profile may be expected to flatten near nadir and increase rapidly at extreme zenith angles as the sky temperature increases. From Figures 5.15b, d, e and f it is then likely that the DWSR has been overestimated in these cases since the modelled ΔT_b data underestimate the observed dBT near nadir and overestimate at larger zenith angle. Differences between the modelled ΔT_b and observed dBT distributions result in the estimates of LST derived via (5.9) being dependent upon the observation zenith angle, with the LST being underestimated in cases where ΔT_b overestimates the dBT data and the LST being overestimated where the ΔT_b underestimate the observed dBT data.

For the daytime case, at the time of the descending overpass of the ATSR-2, the estimates of the mean LST for each month derived using (5.9) are shown in Figure 5.28. Because the BEDF developed in Section 5.3.3 is derived from differences between the observed dBT and modelled ΔT_b profiles, the LST derived via (5.9) is closer to being independent of zenith angle in most cases during the day, compared to the nighttime case. Only slight variability in the mean LST may be observed over the scanning range of the radiometer during the day because, after the inclusion of the BEDF, the modelled ΔT_b closely fit the observed dBT distributions, as shown in Figure 5.16 from Section 5.3.3.

Figure 5.29 compares the LST estimates from (5.8) and (5.9) on a daily basis.
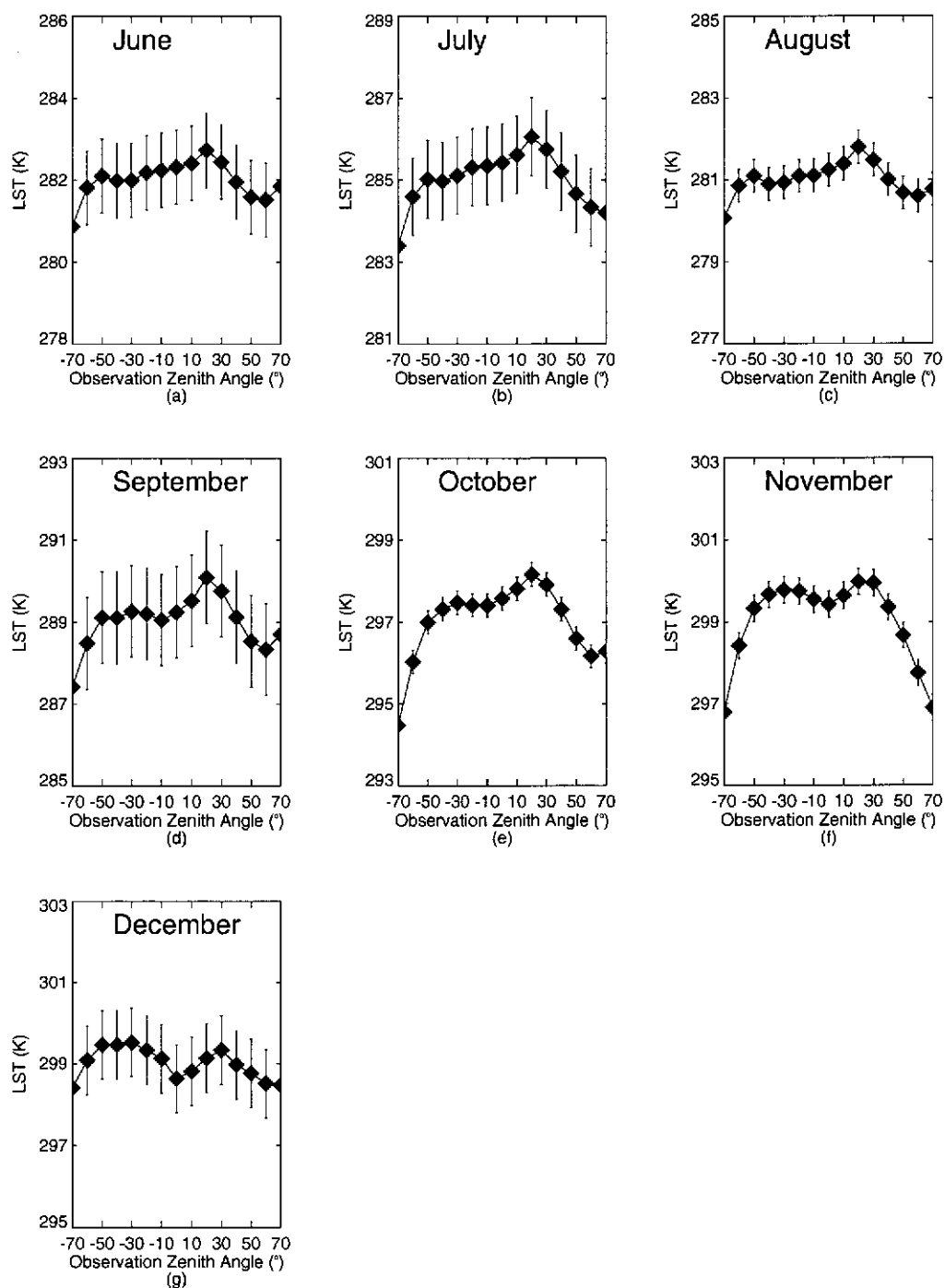
Figure 5.27: Average estimates of LST derived by applying the modelled ΔT_b distribution to the SBT data acquired by the TASCO radiometer for the nighttime overpass of ATSR-2.
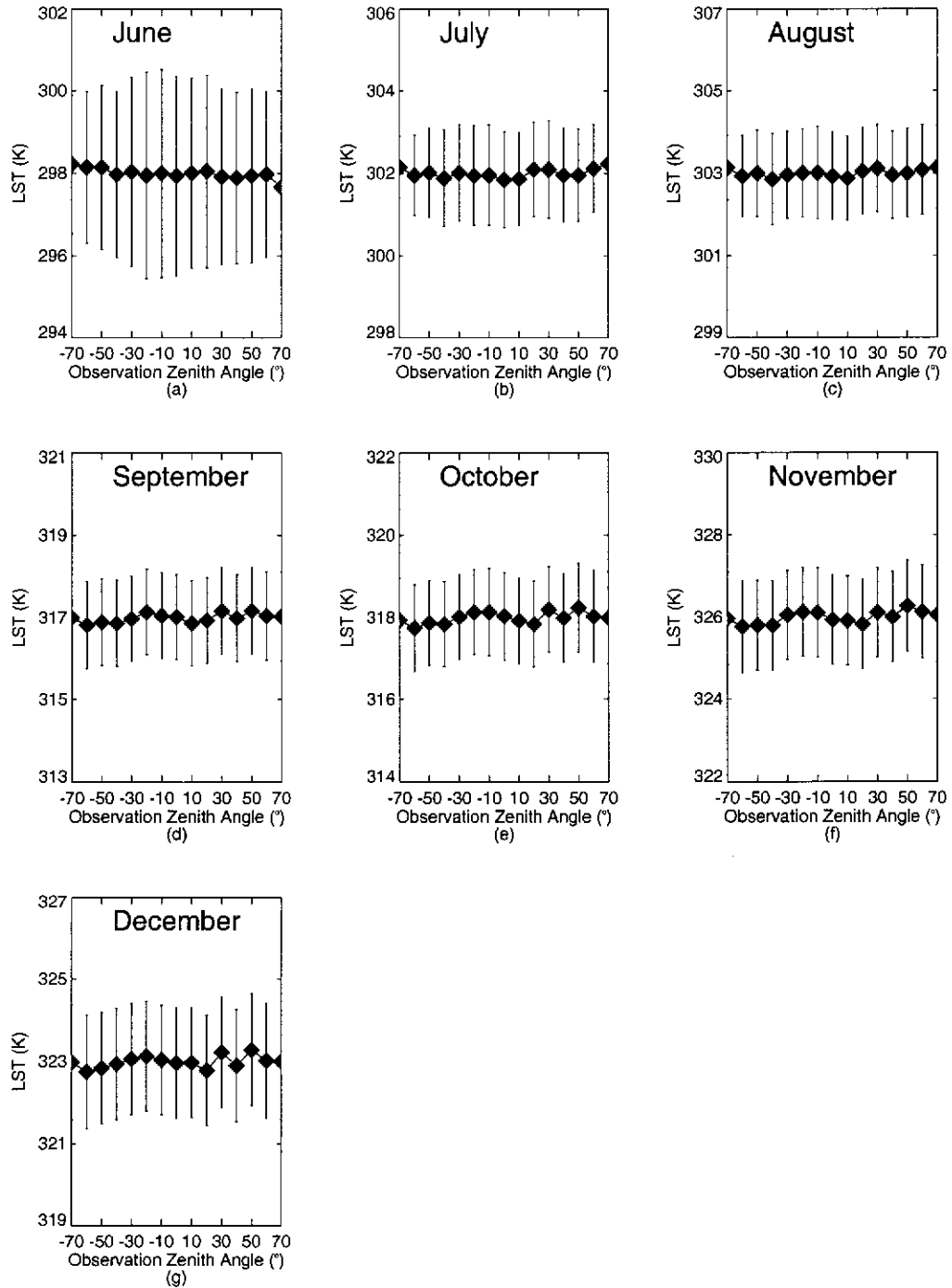
Figure 5.28: Average estimates of LST derived by applying the modelled ΔT_b distribution to the SBT data acquired by the TASCO radiometer for the morning overpass of ATSR-2.

On the x-axis 'mean LST^1' refers to the estimates of LST obtained for each zenith angle using (5.8), while 'mean LST^2' on the y-axis refers to the mean estimate of LST obtained by averaging the LST for each zenith angle given by (5.9) over the scan-angle range of the radiometer. For both the night and day cases the plots of the estimates of LST from (5.8) versus those from (5.9) fall on or very close to the line for which y=x. This confirms that two approaches measure the same physical quantity, and suggests that the choice of the best approach to LST estimation should then be based on the accuracy of the LST estimate.

A comparison of the results obtained using 5.8 and 5.9 is given in Tables 5.13 and 5.14 for the night and daytime cases respectively. As before 'mean LST^1' refers to the estimate of LST obtained using (5.8) and 'mean LST^2' refers to the mean estimate of LST obtained by averaging the LST for each zenith angle given by (5.9) over the scan-angle range of the radiometer. The results show that for both the night and daytime cases the estimates of LST obtained using the two approaches agree to within 0.5 K. At night, Table 5.13 shows that application of (5.9) permits estimation of LST to within ±1.01 K on average, a result which is an improvement of 0.6 K over using (5.8). During the day, the increased variability in the dBT profile compared to the nighttime case (see Tables 5.3 and 5.4 in Sections 2.3.3.1 and 2.3.3.2) limits the accuracy with which LST may be estimated using (5.9) to ±1.29 K on average over the seven months of the study, but this is still approximately 1 K better than the equivalent results using (5.8).

These results show that the accuracy with which LST may be retrieved *in situ* is increased when the extra angular information is included in the retrieval algorithm. Importantly, the work in this section has shown that it is possible to measure LST to within 1 K at night, and close to 1 K (±1.3 K) during the day using (5.9). Estimation of LST to within or close to 1 K is an important result since this is the desired level of accuracy for satellite remote sensing of LST (Wan, 1999), and is encouraging for the validation of algorithms for the satellite-based retrieval of LST. The accuracy with which LST may be estimated is, however, still limited by knowledge of the

207

surface emissivity. At night, the surface emissivity may be estimated to a level that allows LST to be calculated to within 1 K. During the day, the surface emissivity is more difficult to estimate accurately due to the increased variability in the observed dBT distributions which propagates into the LST calculation. For the daytime case LST may be estimated to within ± 1.3 K. The work in this section has concentrated on monthly averages of LST in oder to illustrate the method by which the estimates have been derived. For the validation of satellite-derived LST an estimate of the *in situ* LST is required at times coincident with the overpass of the satellite. Daily *in situ* estimates of the LST measured at times coincident with the nighttime ascending and morning descending overpasses of the Amburla field site by the ATSR-2 satellite sensor are given in Appendix B.

5.4.2 Algorithms for Satellite-Based Retrieval of LST

From this investigation of the radiative interaction between the land surface and the atmosphere it has been demonstrated that both the atmosphere (Chapter 4), and the land surface (the current chapter) impact in a complex manner the surface-leaving radiance that would be subsequently measured at the satellite sensor. This radiative interaction may be described by the RTE as given by (2.6) and (2.4) for the satellite and *in situ* cases respectively. The process of atmospheric correction utilizes the RTE so as to extract the surface-emitted radiance from the at-sensor radiance using knowledge of each of the important radiative components and the surface emissivity. For the derivation of algorithms for the satellite-based retrieval of LST, using a single channel approach it is necessary to be able to estimate the DWSR, UWSR and atmospheric transmittance as well as the surface emissivity. A method for estimating these radiative components was described in Chapter 4.

In Section 4.2.5 of Chapter 4 it was shown that the atmospheric correction term, ΔT_{AC}, could be linearly related to both the surface emissivity (see Figures 4.14 and 4.15), and the SBT measured by the satellite sensor (see Figures 4.16 and 4.17), where the linear relations illustrated implicitly incorporate knowledge of the

208
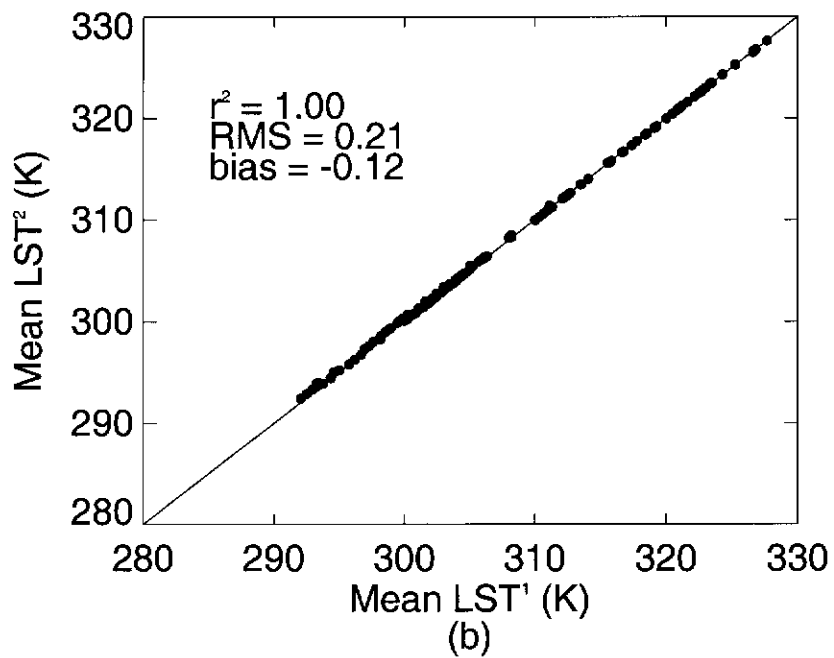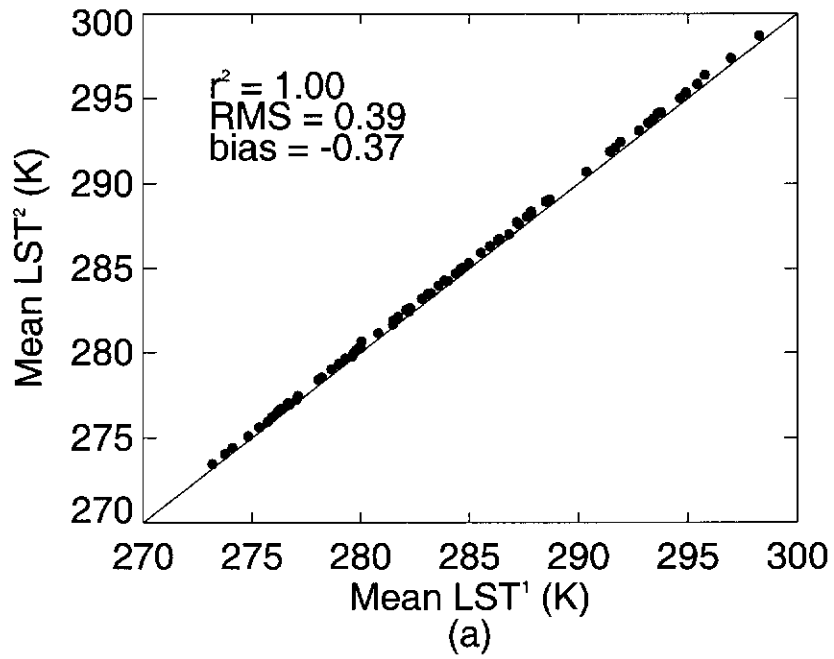
Figure 5.29: Estimates of the LST derived using (5.8) (mean LST[1]) and (5.9) (mean LST[2]) for; a) the nighttime, and; b) the daytime cases.

Month	mean LST^1	mean LST^2
June	281.37±1.11	281.53±1.01
July	284.57±0.85	284.91±1.17
August	280.51±3.31	281.41±0.58
September	287.89±2.47	288.52±1.29
October	296.28±0.62	296.59±0.99
November	298.52±1.94	299.14±1.11
December	298.56±0.97	298.93±0.93

Table 5.13: Monthly averaged values of LST for the nighttime interval correspond-ing with the time of the ascending ATSR-2 overpass.

Month	mean LST^1	mean LST^2
June	296.64±2.64	297.06±2.13
July	301.28±1.86	301.40±1.01
August	302.41±1.90	302.77±1.07
September	315.83±2.05	315.87±1.15
October	317.18±2.39	317.22±1.12
November	324.84±2.32	324.88±1.14
December	322.36±2.65	322.38±1.42

Table 5.14: Monthly averaged values of LST for the daytime interval corresponding to the time of the descending ATSR-2 overpass.

radiative properties of the atmosphere. Figures 4.16 and 4.17 suggest that separate linear algorithms for predicting ΔT_{AC} may be developed for the nadir and forward views of the ATSR-2 taking proper account of the important radiative components between the nadir and forward viewing geometries. Given the estimates of surface emissivity, in Figures 4.14 and 4.16, the results were generalized to encompass the range of values likely to be representative of the surface. In this case the range cho-sen was 0.90–1.00. By utilizing the successful modelling of the angular distribution of surface emissivity (described earlier in the current chapter), and incorporating the estimates of the absolute value of the surface emissivity (from Section 5.3), it is possible to develop relationships for predicting ΔT_{AC} for the Amburla field site (see Figure 4.16 in Chapter 4). Taking the nadir case in Figure 4.16 as an example, the linear relation for predicting ΔT_{AC} may be expressed as;

210

$$\Delta T_{AC} = a_n T_n + b_n, \tag{5.10}$$

for which n denotes the nadir viewing direction and T_n is the SBT measured by the satellite sensor for the nadir view. From the formulation for ΔT_{AC} given by (4.4) in Section 4.2.5, the LST may be expressed as;

$$T_s = T_n - \Delta T_{AC}, \tag{5.11}$$

where T_s is the estimate of the LST. Combining (5.10) and (5.11) gives;

$$T_s = (1 - a_n)T_n - b_n, \tag{5.12}$$

for the nadir case. By analogy;

$$T_s = (1 - a_f)T_f - b_f, \tag{5.13}$$

represents T_s for the forward view of the ATSR-2 (the forward viewing direction is denoted by f).

In Figures 4.16a and b, from Section 4.2.5, for the day and nighttime cases respectively, the linear relationship between the SBT measured by the satellite sensor and ΔT_{AC} was illustrated by combining ATSR-2 data for the Amburla field site for both years 1998 and 2000. The high correlation coefficients for each case (r^2= 0.914 and 0.877 for the nadir and forward views during the day and 0.895 and 0.892 respectively for the nighttime cases) show that the site has changed little over the two years and that atmospheric conditions characteristic of the field site were also

211

relatively unchanged over the same period. In Tables 5.15 and 5.16 the coefficients for the LST retrieval algorithms were generated using only ATSR-2 data from year 2000 combined with the estimates of the surface emissivity from Table 5.9 in Section 5.3.4. As such, the ATSR-2 data from 1998 form an independent data set which may be used to compare the performance of the retrieval algorithms derived using the year 2000 data both angularly and spectrally.

For the nighttime case, the results from Sections 5.3.1 and 5.3.2 show that the dBT profiles measured throughout the year by the radiometer may be described by the normalized surface emissivity distribution derived from the Wiscombe and Warren model. Using the estimates of the absolute value of the surface emissivity (given in Table 5.9) for the nighttime case and Table 5.11 for the daytime case from Section 5.3.4, algorithms for the estimation of LST for the nadir and forward views in the 11 and 12μm channels of the ATSR-2 may be defined which are valid throughout the year. At night, only a single algorithm for each spectral channel and viewing geometry is required as it was shown in Section 5.3.2 that the ΔT_b distribution derived using the Wiscombe and Warren model could be used to accurately predict the monthly mean dBT distributions observed by the radiometer (see Figures 5.14 and 5.15). The coefficients for the nighttime algorithms for the 11 and 12μm channels of the ATSR-2 are given in Table 5.15.

During the day, as was evident by the need to define the BEDF in Section 5.3.3 to account for the variation in the observed SBT/dBT profiles, the estimation of the effective surface emissivity is not as simple as for the nighttime case. Figure 5.8 from Section 5.2.2, Figures 5.16, 5.17 and 5.18–5.24 from Section 5.3.2 all show that the dBT distribution characteristic of the land surface at the time of the descending overpass of the ATSR-2 changes throughout the year. Consequently, so too does the BEDF (see Figure 5.25 in Section 5.3.3), and subsequently the effective surface emissivity. The variation in the effective surface emissivity, characterized monthly in this work, requires that separate algorithms be defined for each month for the nadir and forward views of the of the ATSR-2 and for the two TIR channels

11μm				12μm			
a_n	b_n	a_f	b_f	a_n	b_n	a_f	b_f
-0.049	13.00	-0.110	26.63	-0.046	12.23	-0.103	23.96

Table 5.15: Values of the coefficients 'a' and 'b' for (5.12) and (5.13) for the 11 and 12μm channels of the ATSR-2 for ascending overpasses for 2000. The subscript n denotes the nadir viewing direction. f denotes the forward viewing direction.

	11μm				12μm			
Month	a_n	b_n	a_f	b_f	a_n	b_n	a_f	b_f
June	-0.081	21.04	-0.137	36.38	-0.128	34.41	-0.216	59.98
July	-0.081	21.04	-0.137	36.38	-0.138	36.32	-0.216	58.98
August	-0.087	21.86	-0.144	36.92	-0.138	36.32	-0.242	65.80
September	-0.071	19.76	-0.143	36.85	-0.113	31.32	-0.240	65.06
October	-0.068	19.36	-0.145	37.06	-0.108	30.35	-0.248	67.20
November	-0.074	20.12	-0.146	37.06	-0.117	32.17	-0.249	67.28
December	-0.070	19.57	-0.146	37.07	-0.110	30.86	-0.248	67.36

Table 5.16: Values of the coefficients 'a' and 'b' for (5.12) and (5.13) for the 11 and 12μm channels of the ATSR-2 for descending overpasses in the months from June–December 2000. The subscript n denotes the nadir viewing direction. f denotes the forward viewing direction.

in order to optimize the accuracy of LST retrieval. The values of the coefficients for the LST retrieval algorithms derived for each month are given in Table 5.16.

In the ideal case the LST algorithms for the nadir and forward viewing geometries should give equivalent estimates of LST, and these estimates should also be equivalent between the 11 and 12μm channels for the same viewing geometries. However, a qualitative assessment of the results from the LST retrieval algorithms reveals that there is better agreement between different spectral estimates for the same viewing geometry at night, while during the day there is better agreement between different angular estimates in the same spectral channels.

At night, it is apparent that there is much closer agreement between different spectral estimates for the same viewing geometry (Figure 5.30b) than for different viewing geometries in the same spectral channels (Figure 5.30a). The large RMS error for the comparisons between LST estimates for different viewing ge-

ometries in the same spectral channel suggests that there may be variation in the absolute value of the surface emissivity over the seven month period of the study. The nadir value of the surface emissivity was chosen assuming that a grass covered clay surface was representative of the land surface in the FOV of the radiometer. It is possible that vegetation change throughout the year invalidates this estimate at some stages resulting in the uncertainty in the estimation of LST represented by the RMS error. The bias between the nadir and forward view estimates of LST of approximately -4 K (apparent in Figure 5.30a) may be explained by either; i) the surface emissivity estimate used in the derivation of the LST algorithms for the nighttime cases being underestimated in the forward view case, or; ii) a near-surface temperature inversion existing between the surface and the satellite such that its effect is not captured by the *in situ* measurements, and its differing impact between the nadir and forward viewing geometries of ATSR-2 has not been accounted for in the modelling of radiative transfer between the surface and the satellite sensor. Both of these possibilities, however, suggest that the angular structure observed in the *in situ* measurements does not translate to the larger FOV seen by the satellite at night. Interestingly, in Figure 4.16b for the nighttime case (from Section 4.2.5), where the same range of emissivity was assumed for both the nadir and forward cases (0.90–1.00), the relations describing ΔT_{AC} for the nadir and forward cases intersect near an SBT estimate of 285 K. This causes the the magnitude of the atmospheric correction term, ΔT_{AC}, to the nadir SBT estimate to be equal to larger than that for the forward viewing geometry for SBT estimates in this range. In such a scenario, the bias observed in Figure 5.30a would be closer to zero. It is therefore more likely that the decrease in the surface emissivity with increasing zenith angle observed *in situ* does not translate to the scale of view of the satellite, rather than the forward view of the sensor being impacted by an inversion layer.

Figure 5.30b shows very good agreement between the different spectral estimates for the two viewing geometries, both of which show and RMS of approximately 1 K. This is an encouraging result for the remote sensing of LST and sug-

214

gests that at night a multispectral approach to the retrieval of LST may achieve the best results. However, the LST retrieved by such an algorithm will still be in error if a temperature inversion layer exists, since the at-sensor radiance may not originate from the land surface. Further, if the surface emissivity estimate is incorrect or the decrease in the value of surface emissivity predicted by the modelling does not translate to the scale of view of the satellite, the retrieved LST will not be representative of the temperature of the land surface. Knowledge of the surface emissivity therefore still limits the accuracy with which LST may be estimated remotely via satellite using the algorithms developed in this work.

For the daytime case, Figure 5.31 shows that better agreement is obtained between the LST estimates for different viewing geometries in each spectral channel (Figure 5.31a) than between the same viewing geometries in different spectral channels (Figure 5.31b). This is most likely due to the facts that; i) any variability in the surface emissivity in the data set has been largely characterized by by the BEDF, enhancing the agreement between LST estimates in the nadir and forward viewing directions, and; ii) spectral differences in the surface emissivity at different observation zenith angles may be more prominent during the day. Differences between spectral estimates of LST may be increased if such spectral variation is not accounted for. Table 5.8 from Section 5.3.3 shows that the spectral nature of the surface emissivity may cause differences in the band-averaged quantities between the 11 and 12μm channels depending on the structure and composition of the surface. Such spectral variation has been noted in previous studies by Takashima and Masuda (1987) and Bower (2001) among others. The good agreement between the 11 and 12μm estimates of LST for near-nadir viewing in Figure 5.31b, when compared to the case for the forward view, does, however, suggest that spectral differences in the surface emissivity may be more pronounced at larger zenith angles, and as such a multispectral algorithm may still be useful for near-nadir viewing during the day. In summary, Figure 5.31 suggests that, in contrast to the nighttime case, LST may be estimated more accurately during the day using a multi-angle approach so as to

215

avoid any spectral impacts related to the surface emissivity. From Figure 5.31 such a multi-angle approach may be expected to retrieve LST to within an accuracy of ±1.5 K. However, this result, as for the 1 K RMS for the nighttime case, is only a relative estimate of the accuracy of LST retrieval using the algorithms derived in this section, and represents a lower bound on the accuracy which it may be possible to achieve under ideal conditions. In order to obtain an assessment of the retrieval accuracy using the algorithms developed in this work it is necessary to validate the retrieved LST against the *in situ* estimates of LST derived using the method described in Section 5.4.1.

Over the seven months of year 2000 for which field measurements have been analysed in this chapter the number of coincident satellite measurements was unfortunately limited. Only ATSR-2 data between June and September could be obtained, permitting a maximum of 40 ascending and descending overpasses of the field site under the 3-day cycle for global coverage of the ATSR-2. Further restrictions on the number of suitable passes for validation work came from the field site often being located just outside the FOV of the satellite during an overpass and the impact of cloud cover over the site. Due to these restrictions the amount of available ATSR-2 data was limited to three passes for the daytime and nine for the nighttime cases in total. The small amount of data available for validation of the retrieval algorithms allowed only a qualitative assessment of the retrieval accuracy to be made. This limited study showed that; i) good correlations exist between the *in situ* LST data derived via the method described in Section 5.4.1, and; ii) the RMS differences between the *in situ* and satellite-derived LST were of the order of the accuracy with which ΔT_{AC} could be estimated (3–4 K, see Section 4.2.5) using the available atmospheric data with generalized estimates of the surface emissivity. The results of the limited validation study are summarized in Table 5.17.

Though the data in Table 5.17 show that the accuracy with which LST may currently be retrieved using the algorithms is low, there are several areas in which improvements may be made to the retrieval scheme in the future. i) The inclusion of

216

more well-known and perhaps more representative atmospheric data may provide scope to improve the accuracy of the satellite-derived estimate. For example, simulations have suggested that using atmospheric data of the accuracy achievable by the AIRS instrument (BAE Systems, 2002) may permit the estimation of LST to within a theoretical accuracy of 1–2 K using the algorithms derived in this section. ii) How well *in situ* estimates of the surface emissivity translate to the scale of view of the FOV of the satellite sensor may also impact the satellite-based retrieval scheme. It was evident from Figure 5.30 in Section 5.4.1 that the decrease in surface emissivity with increasing zenith angle observed *in situ* may not translate to the scenario for the satellite sensor. Further investigation of the impact of such questions of scale in the future may help to improve the satellite-based retrieval of LST described in this work. iii) It should be noted that the retrieval algorithms were developed for generalized nadir and forward viewing geometries, and did not consider any angular variation within these two categories (in the nadir case the zenith angle may vary between 0 and 20° for example). Inclusion of the viewing geometry of individual overpasses into algorithm development may improve the accuracy of LST retrieval in the future. iv) There is currently no consideration of the azimuth angle of the satellite view of the surface included in the algorithm development since the instrumentation for the *in situ* measurement of LST was only designed for the study of the effects of zenith angle variation. Azimuthal variation may, however, also be an important factor and future investigation of the impact of changing azimuth angle on LST retrieval may also prove beneficial in improving the accuracy of LST retrieval in the future. v) The validation results are also limited by the accuracy with which LST may be estimated *in situ*. The limiting factors in the *in situ* case are knowledge of the true surface emissivity and measurement of the DWSR. The choice of surface emissivity was based upon the μ-FTIR estimates from Table 5.8, which are only assumed to be representative of the true surface emissivity for the FOV of the radiometer at nadir.
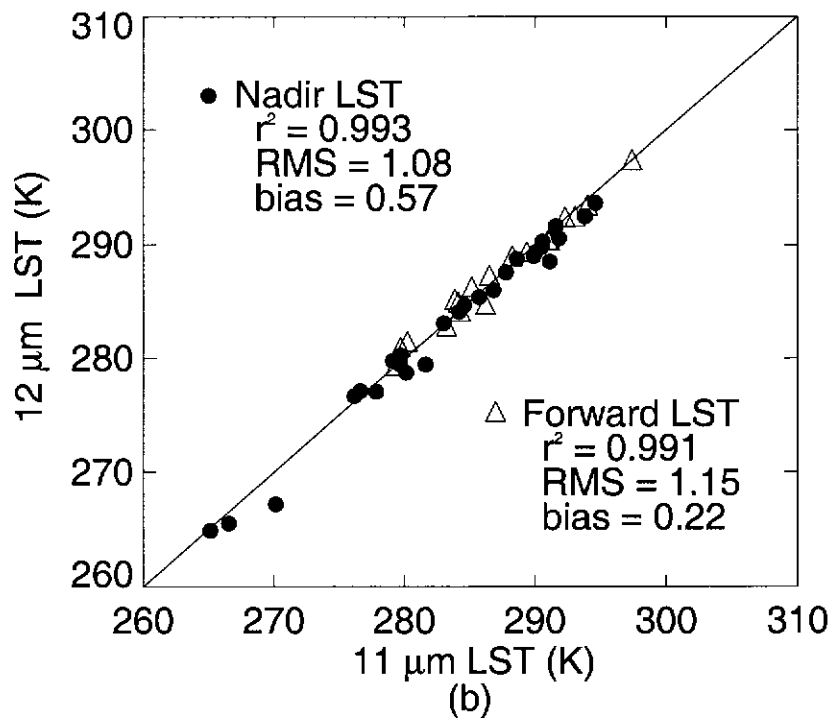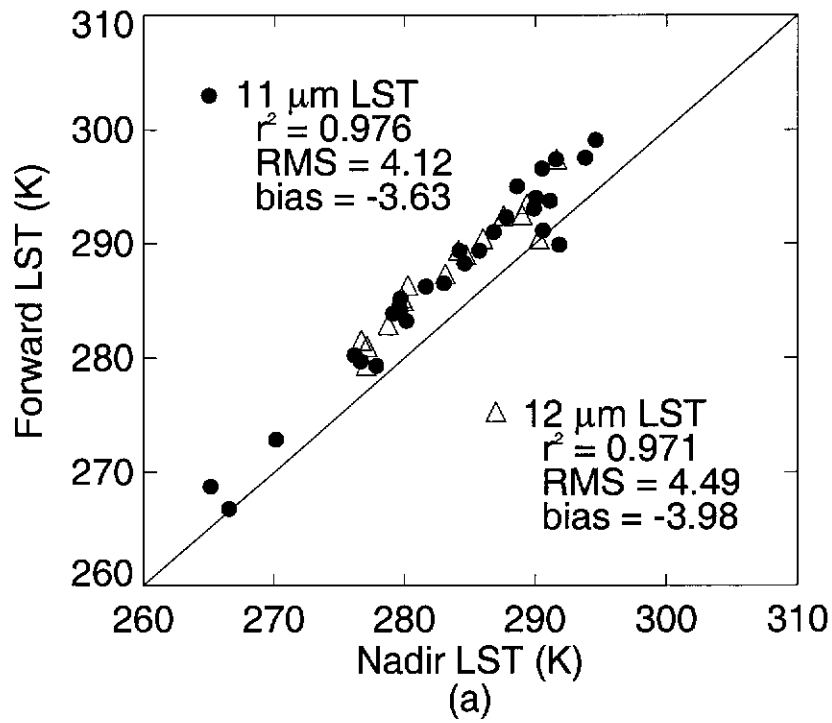
Figure 5.30: Comparisons of the LST retrieved using the LST algorithm for the nighttime case with coefficients given in Table 5.15. a) Comparison between results from the nadir and forward viewing geometries separately for both the 11 and 12μm spectral channels. b) Comparison between results in both the 11 and 12μm spectral channels for the same viewing geometry.
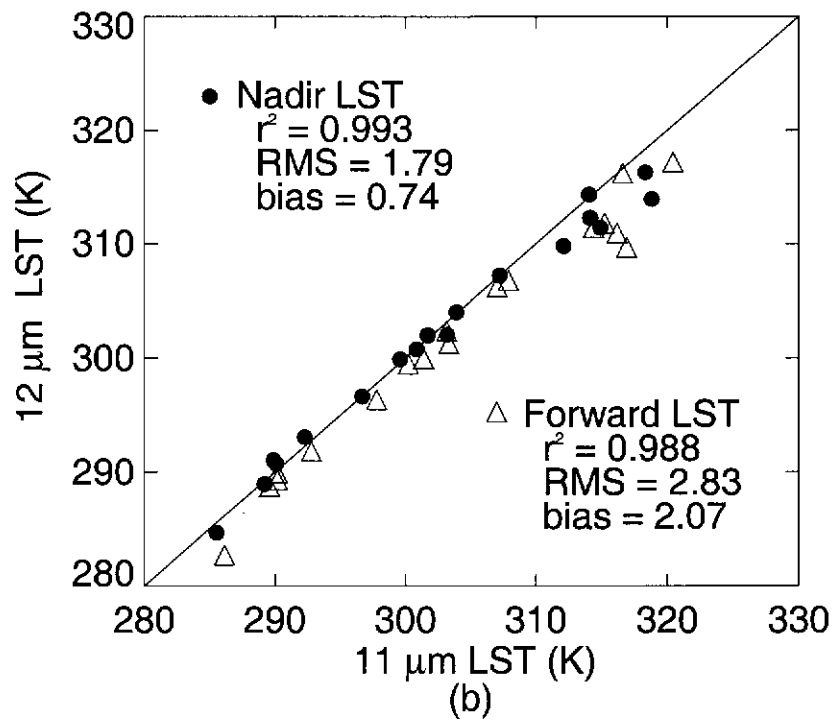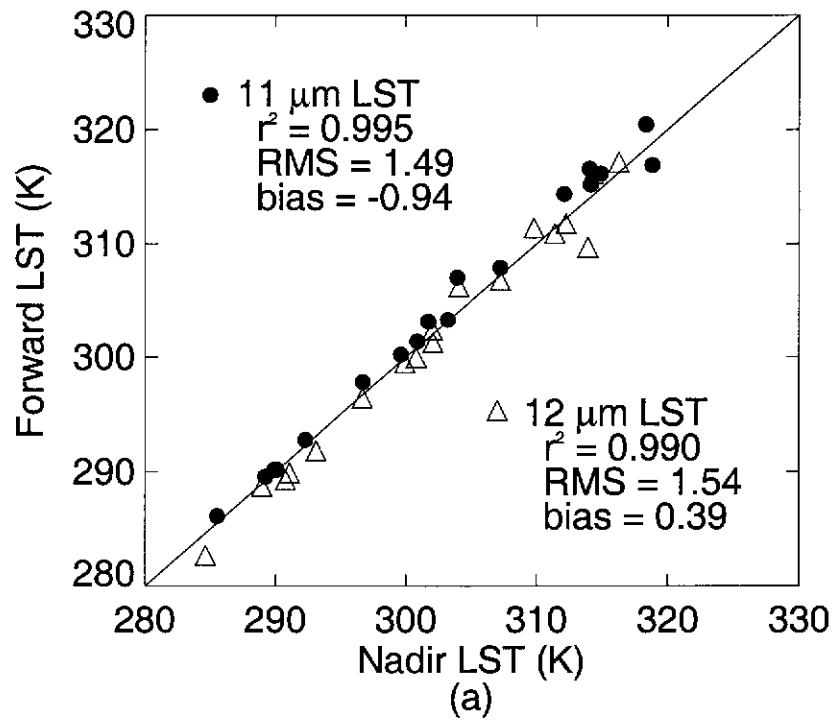
Figure 5.31: Comparisons of the LST retrieved using the LST algorithm for the daytime case with coefficients given in Table 5.16. a) Comparison between results from the nadir and forward viewing geometries separately for both the 11 and $12\mu m$ spectral channels. b) Comparison between results in both the 11 and $12\mu m$ spectral channels for the same viewing geometry.

	Night				Day			
	11μm		12μm		11μm		12μm	
	nad	fwrd	nad	fwrd	nad	fwrd	nad	fwrd
r^2	0.983	0.882	0.980	0.873	0.994	0.997	0.990	0.993
bias (K)	2.64	-2.13	3.32	-1.92	3.30	3.03	3.79	4.00
RMS (K)	2.89	3.67	3.76	3.62	3.28	3.09	3.87	4.05

Table 5.17: Statistical data from the limited validation study describing accuracy of LST retrieved using algorithms with coefficients given in Tables 5.15 and 5.16.

This estimate may not representative at all times, and in such cases incorrect estimates of the surface emissivity will cause errors in the estimation of the *in situ* LST which propagate into the validation results. In general, however, although there are still some improvements which may be made to the retrieval algorithms in their current form, the analysis of the results obtained so far in this work are definitely encouraging and will only improve in the future as modifications to the algorithms are made based on further work, and the expansion of the validation data set.

The current chapter began with a description of the scanning TASCO radiometer installed at the Amburla field site in Section 5.1. The radiometer sits atop a 5m high pole and continuously scans back and forth through the angular range of -70° (the south-looking direction) to 70° (the north looking direction) in 10 degree increments. It measures the surface-leaving radiance at each zenith angle over the angular range for approximately 30 seconds, giving a scan time for one cycle of approximately 10 minutes. Included in each scan cycle is a measurement of an ambient blackbody, a hot blackbody and a vertical view of the sky to give an estimate of the sky brightness temperature and hence the DWSR. The temperature of the black-bodies is known to an accuracy of ±50 mK, and through the calibration process described in Section 5.1, provide continuous well-calibrated measurements of the SBT. Through this calibration process the measurements made by the radiometer may be traced back to a NIST standard blackbody via a fixed laboratory calibration (Section 5.1). The sky-view is a particularly useful measurement as it provides the basis of the method for atmospheric correction of the radiometer measurements

which was described in Chapter 4. From the measurements of the angular distribution of SBT made by the radiometer, described in Section 5.2, continuous, well defined, diurnal cycles of SBT were shown to exist (see Figures 5.5–5.7 in Section 5.2.1). In general, the diurnal cycle of SBT described in Section 5.2.1 showed a consistent monotonic decrease from nadir in both off-nadir viewing directions at night. As the sun rose and the surface warmed a period occurred in which the SBT appeared to be nearly independent of zenith angle. Continuing into the middle of the day, zenith angle dependent structure about in SBT emerged during peak solar input to the surface. As the solar influence waned, the diurnal cycle of SBT was shown to pass though another period of near-zenith angle independence and returned to the nighttime state. The diurnal cycle was also well described by the quantity termed the dBT which was derived by subtracting the mean SBT over the scan-angle range of the radiometer from the SBT data for each scan cycle. Analysis of the observed SBT distributions began in Section 5.2.2 by noting that the form of the dBT peak observed during the middle of the day varied throughout the year and was related to the solar geometry. In Section 5.2.3, more detailed investigation of the dBT distributions characteristic of different periods of the diurnal cycle was undertaken with emphasis on those times coincident with overpasses of the field site by the ATSR-2 satellite sensor. In Section 5.2.3.1 this work showed that mean dBT distributions could be defined over a few scan cycles encompassing the time of the morning or descending overpass of the ATSR-2, at 1030 hrs local time, to within ± 1 K (see Table 5.3). In Section 5.2.3.2, for the time coincident with the ascending overpass of the ATSR-2 (2330 hrs local time), the dBT distribution was shown to be defined to within ± 0.5 K (see Table 5.4). This estimate was comparable to the accuracy with which a dBT profile for the whole night (defined as lying between 0000 and 0600 hrs) could be defined in Section 5.2.3.3.

In Section 5.3.1 a physical basis for the observed dBT distributions for the nighttime from Section 5.2.3.3 was developed based upon the the Wiscombe and Warren (1980) model for the surface emissivity. The Wiscombe and Warren model, orig-

221

inally developed to describe the spectral albedo of snow, was adapted to the characteristic quartz-dominated surface of the Amburla field site. The Wiscombe and Warren model describes the emergent TIR radiation from the surface using Mie theory for single scattering and the δ-Eddington approximation for multiple scattering. Spectral estimates of the single scatter albedo and the assymetry factor for quartz samples from the field site for mean radii 3μm , 1 mm and 2.5 mm were band-averaged over the spectral response function of the TASCO radiometer and used in the Wiscombe and Warren model to predict the decrease in the normalized surface emissivity over the range of zenith angles scanned by the radiometer. The decrease in the normalized surface emissivity over the scanning range of the radiometer was found to decrease as the grain size increased. The results obtained were comparable to the results from similar studies by Takashima and Masuda (1987) and Sobrino and Cuenca (1999) (see Figure 5.12), and predicted a decrease of around 20% in the value of the normalized surface emissivity over the scan-angle range of the radiometer.

In Section 5.3.2 it was shown that the RTE given by (2.4) could be used to accurately model the dBT distribution over the scan-angle range of the radiometer by; i) incorporating the theoretical normalized surface emissivity distribution from the Wiscombe and Warren model; ii) using the DWSR estimated from the sky-view of the radiometer, and; iii) applying the regression relations developed in Chapter 4 to subsequently preidct the DWSR for any zenith angle of observation. By choosing different values for the sky temperature and surface temperature, as in Figure 5.13, it was shown that in the absence of solar input to the surface the relative magnitudes of the surface-emitted radiance and the DWSR determine the form of the dBT profile. The combinations of DWSR and surface-emitted radiance covered in Figure 5.13 show that the observed dBT profiles are due to the interaction between the DWSR and surface-emitted radiance as described by (2.4). Figures 5.14, 5.15 and Figures 5.18–5.24 from Section 5.3.2 show that with accurate estimates of the DWSR from the sky view of the scanning radiometer, (2.4), where the surface emissivity is given

by the theoretical distribution for the normalized surface emissivity, may be used to accurately predict the dBT distribution. Importantly, the result from Section 5.3.2 showed that the mean dBT distributions at night, for each month in Figures 5.14, 5.15, may be explained by the decrease in the surface emissivity with increasing zenith angle.

Figures 5.18–5.24, from Section 5.3.2, clearly illustrate that the model works well at night, but that the field measurements of dBT diverge from the modelled ΔT_b distribution during the day. In Section 5.3.3 this fact was used to empirically describe a BEDF function (Jupp, 1998), which accounts for the difference between the dBT and ΔT_b distributions at each zenith angle. The difference between the two distributions at each zenith angle was described by an increment to the normalized surface emissivity, as given by (5.6). This empirical description of the BEDF is analagous to the effective emissivity proposed by Li *et al.* (1999) to allow definition of a characteristic surface temperature. Inclusion of the BEDF (defined in Section 5.3.3) in the model allowed the characteristic dBT profiles for each month at the time of the ATSR-2 overpass to be accurately modelled, as shown by Figure 5.26.

In order to estimate LST from the SBT measured by the radiometer it is necessary to have an estimate of the absolute surface emissivity. Such estimates were obtained in Section 5.3.4 by band-averaging spectral measurements of the surface emissivity made by a μ-FTIR (Prata, 2002) over an interval corresponding to the spectral response function of the TASCO radiometer. Table 5.8 shows that the surface emissivity may vary greatly between different samples from the field site. For the TASCO radiometer, the surface emissivity may range over 20% at nadir for different surface types, while the surface emissivity for the TIR channels of the ATSR-2 may range over 10%. The choice of a surface emissivity value representative of the surface viewed by the radiometer is then particularly important for accurate *in situ* estimation of LST. Figure 3.2 from Section 3.2 showed the site to be grass covered during August 2000. Accordingly, a band-averaged surface emissivity of 0.988 at nadir taken from Table 5.8 was used in this work.

In Section 5.4.1 two methods of estimating the LST for the purpose of validating satellite-based measurements of LST were compared. At night, the LST estimates given by (5.8) and by (5.9) were found to be in very close agreement (within 0.5 K), however, the accuracy of the method described by (5.9) was found to give results of superior accuracy by about 0.3 K. The increase in accuracy may be attributed to the extra angular information incorporated into (5.9). In most cases it was possible to estimate the *in situ* LST to within 1 K at night. During the day the method described by (5.9) was found to measure LST to an accuracy of between 1 and 1.5 K in most cases, approximately 1 K better than the equivalent results obtained using (5.8). Importantly, the work in this section has shown that it is possible to measure LST to within 1 K at night, and close to 1 K during the day using (5.9). Estimation of LST, based on angular measurements of SBT, to within, or close to, 1 K is an important result since this is the desired level of accuracy for satellite remote sensing of LST (Wan, 1999), and is encouraging for the validation of algorithms for the satellite-based retrieval of LST.

In Section 5.4.2, the estimates of the surface emissivity given in Section 5.3.4 were used to develop the relations for predicting ΔT_{AC} from the SBT measurements for the nadir and forward viewing geometries of the ATSR-2. The latter were developed in Section 4.2.5 from Chapter 4, for generalized estimates of the surface emissivity (see Figure 4.16). Because it was shown, in Section 5.3.2, that it is possible to accurately model the dBT distribution using (2.4) throughout the year at night, a single LST algorithm for each viewing geometry and spectral channel was defined for the nighttime case, the coefficients for which were given in Table 5.15. During the day however, for the descending overpass of the ATSR-2, LST retrieval algorithms were defined monthly so as to account for the change in the characteristic dBT distribution for each month. The coefficients for each of the monthly algorithms for the nadir and forward viewing geometries and the two spectral channels were given in Table 5.16. Comparison of the results from each algorithm for the day and nighttime cases, (see Figures 5.30 and 5.31) suggests that, at night,

LST may be best retrieved using a multispectral algorithm. For the daytime case, the angular and spectral comparisons in Figures 5.31a and b suggest that LST may retrieved more accurately using a multi-angle approach. The spectral nature of the surface emissivity, as shown by the Table 5.8 suggests that LST is likely to be retrieved more accurately during the day using a multi-angle algorithm as spectral effects appear more prominent at larger zenith angles. In summary, Figures 5.30 and 5.31 show that, in the ideal case, the algorithms developed in this chapter for the retrieval of LST may be expected to provide estimates accurate to within 1 K at night and to within 1.5 K during the day. The validation of the LST estimates obtained using the retrieval algorithms in this chapter carried out using the limited data set of LST estimates from the ATSR-2 satellite sensor coincident with *in situ* measurements from the scanning radiometer, however, showed that under real conditions the accuracy with which LST may be estimated is of the order of 3–4 K, as predicted from estimates of the accuracy with which ΔT_{AC} may be estimated from Chapter 4. Areas in which the accuracy of LST retrieval may be improved in the future using these algorithms include; i) the use of more accurate and representative atmospheric data; ii) investigation of the how well *in situ* estimates of the surface emissivity translate to the scale of the FOV of the satellite sensor; iii) development of algorithms based upon the viewing geometry of individual satellite overpasses of the field site; iv) investigation of the impact of the azimuth angle on both *in situ* and satellite estimation of LST, and; v) further investigation into accurate *in situ* estimation of the surface emissivity.

In conclusion, Chapter 5 has described how *in situ* measurements of the angular distribution of SBT may be utilized to derive estimates of the LST to within 1 K at night and to within 1.5 K during the day (in most cases). These results complement the development of the algorithms for satellite-based retrieval of LST, also developed in this chapter, and show that field measurements of SBT made by the scanning radiometer may be useful in the future in an intensive validation study of LST estimated via satellite remote sensing. As such, the work described in this chapter

has increased understanding of surface-atmosphere properties and interactions and achieved the objectives of this research and represents a useful step forward for the remote sensing of LST.

Chapter 6

Conclusions and Further Work

For long term studies of global climate using remotely sensed data, the desired accuracy for satellite-based LST retrieval is 1 K (Wan, 1999). Because such a wide variety of climatic types and surface properties exist around the globe, in order to move towards achieving the desired accuracy for LST retrieval, investigation of the underlying physical processes which impact upon the satellite retrieval of LST needs to be carried out. The next challenge is to develop methods by which the radiative interaction between the land surface and the atmosphere may be accurately described in relation to; i) the surface properties of the target surface viewed by the satellite sensor, and; ii) the prevailing atmospheric conditions through which the satellite-based sensor views the surface. This thesis describes such an investigation into the physical basis of the radiative interaction between the surface and the atmosphere, focusing on the impacts of changing viewing geometry, with the results being; i) the development of a method for estimating LST from *in situ* measurements of SBT made by a scanning radiometer to within 1 K at night and 1–2 K during the day, and; ii) the derivation of physics-based algorithms for the remote sensing of LST which are characteristic of the field site for which the *in situ* measurements were made.

In Chapter 3 of this study of surface-atmosphere interaction, two field sites used as validation sites for satellite-derived estimates of LST are described. The first site

is located at Amburla Station near Alice Springs in the Northern Territory, while the second site is situated on Thangoo station near Broome in the Kimberley region of Western Australia. The Amburla site is semi-arid with a characteristically dry atmosphere, while the Thangoo site is sub-tropical with a typically humid atmosphere and well-defined dry and wet seasons. These two sites characterize markedly different climatic and surface regimes and were chosen in the investigation because they represent extremes in global environmental conditions under which satellite-derived LST must be validated. For the Amburla site, *in situ* instrumentation provides ground-based estimates of SBT which are complimentary to satellite-derived SBT data. For the Thangoo site, only ATSR-2 data is used as the *in situ* instrumentation was affected by the harsh environmental conditions characteristic of the subtropical climate.

In Chapter 4, the impacts of the two different atmospheric types, characteristic of each field site, upon the surface-leaving radiance are investigated. Initial investigation of measurements of SBT from the ATSR-2 sensor for the two field sites gave little insight into the radiative interaction between the surface and atmosphere (Figures 4.1 and 4.2 for the Amburla site and 4.3 for the Thangoo site). ATSR-2 data is used in this section with the aim of examining the angular nature of radiative interactions in the belief that the unique dual-look possessed by the ATSR-2 may give some insight into the underlying physical processes. However, no significant progress may be made by solely investigating the difference in SBT estimates between the nadir and forward viewing geometries of the ATSR-2, termed dBT data, until the data are plotted against their Julian day of acquisition (Figures 4.7 and 4.8). From the dBT data plotted in this way it is possible to see definite seasonal cycles begin to emerge, which exhibit a mid-year minimum during the day at both field sites and also for the Thangoo dBT data acquired during the nighttime. The dBT data at night for the Amburla site, however, remain relatively constant throughout the year.

These findings provided the impetus for investigation of the atmospheric cor-

rection of remotely sensed LST data from the ATSR-2 sensor, which begins in Section 4.2 in order to understand the physical basis of the observed seasonal cycles. In Section 4.2.1 a single channel approach to atmospheric correction of the remotely sensed SBT data is developed based on (2.6). The important radiative components in the atmospheric correction process described by (4.1), namely the DWSR, UWSR and atmospheric transmittance, are simulated using the radiative transfer model LBLRTM with vertical atmospheric profile data derived from radiosondes launched from the closest available sites as input. Simulations show that, in the ideal case, the RC approach to atmospheric correction given by (4.1) could be applied to retrieve LST to within ±0.01 K. Importantly, the surface was assumed to exhibit spectral properties and the DWSR component reflected from the surface may be calculated from the directional DWSR for the zenith angle of the satellite view of the surface.

For application of the RC method of atmospheric correction to remotely sensed data, an algorithm for estimating each of the important radiative components for the 11 and 12μm channels of the ATSR-2 is developed for the Amburla field site in Section 4.2.2, based upon a combination of *in situ* measurements of the DWSR made by the TASCO radiometer and vertical atmospheric profile data from radiosonde launches from the Alice Springs airport. In the case of the Thangoo field site, because there were no *in situ* measurements of the DWSR, only radiosonde data are used in the investigation of atmospheric correction. In Sections 4.2.3 and 4.2.4 the accuracy with which the radiative components could be estimated is assessed. In this Section, it is found that due to; i) the uncertainty in the atmospheric data measured by the radiosonde; ii) spatial differences between the location of the field site and the location of the radiosonde launch site, and; iii) temporal differences between the sonde launch time and the overpass of ATSR-2 over the field site, that the DWSR and UWSR may only be estimated to within an accuracy of 20% and the atmospheric transmittance to within 5%.

In Section 4.2.5 the atmospheric correction term ΔT_{AC} was developed and used

229

to illustrate linear relationships between the magnitude of atmospheric correction and both surface emissivity (Figures 4.14 and 4.15) and the initial SBT estimates made by ATSR-2, for the nadir and forward viewing geometries (Figures 4.16 and 4.17). Due to the uncertainty in the estimates of the radiative components used to derive the relationships between ΔT_{AC}, the surface emissivity and the SBT based on the RC approach to atmospheric correction, it is only possible to estimate ΔT_{AC} to within 3–4 K for the Amburla field site and 4.5–9.5 K for the Thangoo site due to the level of uncertainty in the estimates of the radiative components. Importantly, however, in the future the method may be generalized to accommodate atmospheric data from other sources. For example, more accurate atmospheric data from instruments such as AIRS has the potential to improve the accuracy with which ΔT_{AC} may be estimated to within 1–2 K using the method described in this work. Further, narrowing the range of the possible values which the surface emissivity may assume from 0.1 (as used in this work) to 0.02 (eg 0.98±0.01) may also increase the accuracy with which ΔT_{AC} may be estimated, in atmospheric conditions characteristic of the Amburla field site, to within 1–2 K.

The investigation of the atmospheric correction process represented by the relationship of ΔT_{AC} to the surface emissivity and satellite-SBT estimate showed that; i) the magnitude of ΔT_{AC} was zenith angle dependent, and; ii) for the case where the same range in surface emissivity is assumed for the nadir and forward viewing geometries of ATSR-2, an SBT threshold exists at which the SBT measured by the forward view of the ATSR-2 is warmer than the nadir view; a phenomena often seen in the nighttime SBT data from ATSR-2 for the two field sites.

The linear equations developed in Section 4.2.5 to predict ΔT_{AC} are generalized, in that the range of surface emissivities used is 0.90 to 1.00. It was noted in this section that estimating the surface emissivity which was representative of a given FOV of the ATSR-2 permits the generalized algorithms from Section 4.2.5 to be localized to a specific region. Chapter 5 describes a method through which this may be achieved, using *in situ* measurements of SBT made by the scanning

radiometer installed at the Amburla field site.

Section 5.1 of Chapter 5 describes the scanning TASCO radiometer at the Amburla field site. The radiometer is calibrated to within ±50 mK using in-built hot and cold blackbodies and continuously scans over the range zenith angles from -70 (in the south-looking direction) to +70° (in the north-looking direction). From the measurements of the angular distribution of SBT made by the radiometer, in Section 5.2.1 well defined, continuous diurnal cycles of SBT are shown to exist. At night, a consistent monotonic decrease from nadir is apparent in both viewing directions for most months. As the sun rises and the surface warms, a period occurrs in which the SBT appears to be nearly independent of zenith angle. In the middle of the day, structure in the angular dependence of SBT about nadir emerges during peak solar input to the surface. As the solar influence wanes, the diurnal cycle of SBT passes though a second period of near-zenith angle independence and returns to the characteristic nighttime state after sunset. The diurnal cycle is also well described by the quantity termed the dBT (derived by subtracting the mean SBT over the scan-angle range of the radiometer from the SBT data for each scan cycle). The structure in the dBT data about nadir during the day is shown to be related to the solar geometry (Figure 5.8) in Section 5.2.2 and the directional nature of solar input to the surface. More detailed investigation of the characteristic dBT distributions observed at times coincident with overpasses of the field site by the ATSR-2 satellite sensor shows that a dBT profile representative of the mean dBT distribution over a few scan cycles may be defined to within ±0.5 K at night and ±1 K during the day.

In Section 5.3.1 a physical basis for the observed dBT distributions for the nighttime from Section 5.2.3.3 is developed based upon the the model for the surface emissivity developed by Wiscombe and Warren (1980). The Wiscombe and Warren model for the spectral albedo of snow is adapted to the characteristic quartz-dominated surface of the Amburla field site. The model describes the emergent TIR radiation from the surface using Mie theory for single scattering and the δ-Eddington approximation for multiple scattering (Joseph et al., 1976; Takashima

231

and Masuda, 1987). Spectral estimates of the single scatter albedo and the assymetry factor for quartz samples from the field site for mean radii 3 μm, 1 mm and 2.5 mm are band-averaged over the spectral response function of the TASCO radiometer and used in the Wiscombe and Warren model to predict the decrease in the normalized surface emissivity over the range of zenith angles scanned by the radiometer. The rate at which the normalized surface emissivity decreases as the observation zenith angle of the radiometer increases is found to slow as the grain size increases. The best agreement between the dBT data and the modelled ΔT_b distributions is found to be given by the model for a mean grain size of radii 1 mm, for which there is a decrease in the normalized surface emissivity of approximately 20% from nadir over the scan-angle range of the radiometer.

In Section 5.3.2 it is shown that using the Wiscombe and Warren model to describe the change in surface emissivity with angle, combined with the regression relations developed in Chapter 4 to estimate the DWSR for each zenith angle, through the form of the RTE given by (2.4), the dBT profile measured by the radiometer may be accurately predicted in the absence of solar input to the surface (Figures 5.14 and 5.15). During the day, the modelled ΔT_b distribution diverges from the field measurements (Figures 5.16, 5.17 and 5.18–5.24) and a BEDF function is empirically defined to account for the differences between the model and the observations in Section 5.3.3. The increments to the surface emissivity given by the BEDF describe the directional variation in SBT in a manner similar to that proposed by Li *et al.* (1999).

In order to apply the results from the successful modelling of the normalized surface emissivity and the observed dBT profiles to the estimation of LST, in Section 5.3.4 estimates of the effective surface emissivity, characteristic of the land surface of the field site, are derived from spectral measurements of the surface emissivity for several samples from different parts of the Amburla site. The μ-FTIR measurements show that there may be significant spectral variation in the surface emissivity depending on the composition and structure of the surface. For the spectral range

232

of the TASCO radiometer, the effective surface emissivity may vary by over 20%, while for the narrower spectral ranges for the TIR channels of ATSR-2 the surface emissivity may vary by 10% between samples from different locations within the field site. For a grass-covered clay surface, representative of the land surface of the Amburla field site for August 2000 (Figure 3.2 from Section 3.2), the surface emissivity at nadir is 0.988. From this result the angular distribution of the effective surface emissivity may be determined for the night and daytime cases, since the normalized surface emissivity distribution relative to the nadir estimate is known from the Wiscombe and Warren model. The absolute value of the surface emissivity calculated in this way may then be used to estimate LST from the estimates of SBT made by the radiometer using (5.8) and (5.9).

In Section 5.4.1 the angular distribution of surface emissivity for then night and daytime cases from Section 5.3.4 are used to compare the accuracy of two approaches to the estimation of LST; i) direct estimation of the LST using the inverted form of the RTE given by (5.8), and; ii) estimation of the LST using knowledge of the dBT distribution to define a mean SBT over the scan-angle range of the radiometer via (5.9). The estimates of LST given by (5.8) and (5.9) are found to be in very close agreement (within 0.5 K) for both the night and daytime cases. At night, both algorithms permit the LST to be estimated to within 1 K in most cases, with the results from (5.9) improving on the accuracy with which (5.8) may be used to estimate LST by 0.3 K. During the day the method described by (5.9) is found to give the best results, permitting estimation of LST to an accuracy of between 1 and 1.5 K in most cases. The use of (5.9) shows that LST may be estimated with an approximate improvement of 1 K over (5.8).

Finally, in Section 5.4.2, using the modelled change in the normalized surface emissivity with increasing zenith angle given by the Wiscombe and Warren model from Section 5.3.1, and the estimate of the absolute surface emissivity from Section 5.3.4, localized forms of the generalized relations describing the atmospheric correction term, ΔT_{AC}, developed in Section 4.2.5, are derived. Using the range

in surface emissivity predicted from the modelling work for the nadir and forward viewing geometries of the ATSR-2, at night, a single algorithm may be defined for each viewing geometry and spectral channel, while during the day algorithms are best defined on a monthly basis to account for the observed change in the dBT distribution at the time of the descending overpass of the ATSR-2 throughout the year.

Comparison of the results from each algorithm for the day and nighttime cases, (see Figures 5.30 and 5.31) suggests that; i) at night, LST may be best retrieved using a multispectral algorithm, and; ii) for the daytime case LST may retrieved more accurately using a multi-angle approach. At night, although the RMS errors in the LST retrieved for each viewing geometry within each spectral band are close to 1 K (Figure 5.30b) there is also a bias of approximately -4 K between the nadir and forward-view LST estimates (Figure 5.30a). This suggests that, at night, although the dBT profiles are highly reproduceable throughout the year, the decrease in the surface emissivity with viewing angle observed *in situ* may not translate to the scale of view of the satellite. During the day, the spectral nature of the surface emissivity appears more prominent, particularly at larger zenith angles, and causes the comparisons between different viewing geometries (Figure 5.31a) to exhibit a lower RMS error than for the spectral comparison in Figure 5.31b.

In the ideal case, the algorithms developed in this chapter for the retrieval of LST may be expected to provide estimates accurate to within 1 K at night and to within 1.5 K during the day. These results are comparable to the accuracy of LST retrieval achieved by Prata (1994) and Sobrino *et al.* (1996). However, the limited validation study utilizing the methods for *in situ* estimation of LST and derivation of retrieval algorithms developed in the work for this thesis, under real conditions, has shown that the accuracy with which LST may be estimated is of the order of 3–4 K RMS. This is a result comparable to the estimated accuracy of the generalized equations for predicting ΔT_{AC} from Chapter 4. This result suggests that, although this research has realized some interesting and useful results, there is still work to

do in order to fully understand the radiative interactions which occur between the land surface and the atmosphere.

Following on from this, in addition to the results summarized in the current chapter, this research has identified a number of issues which may warrant further study in the future in order to continue to improve the accuracy with which LST may be estimated remotely;

- i) A more comprehensive validation study utilizing the methods for *in situ* and satellite-based estimation of LST developed in this work should be undertaken to confirm the preliminary findings from the limited validation study. A methodology for the acquisition of high-accuracy *in situ* LST data has been described in this work, and a dataset comprising of some 200 day and nighttime LST estimates coincident with ascending and descending overpasses of the Amburla field site has been compiled (see Appendix B). The method may be generalized to other sensors apart from ATSR-2 used in this work, such as MODIS. *in situ* acquisition is ongoing, so this research provides a basis for such a study in the future.

- ii) The accuracy with which LST may be estimated remotely, both *in situ* and via satellite, is still limited by knowledge of the surface emissivity. It appears from this research that it is difficult to choose an absolute value of the surface emissivity appropriate to the scales of view of both *in situ* and satellite measurements. In particular, this work has highlighted possible difficulties including the prominence of spectral impacts, and problems with defining a representative surface type during the day. The comparisons between nadir and forward viewing geometries in each spectral band from Figure 5.30a strongly suggest that the decrease in the surface emissivity with increasing zenith angle observed *in situ* does not translate to the scale of view of the satellite sensor at night. Although Figure 5.31a, for the daytime case, does not show the same bias between nadir and forward viewing geometries as for the nighttime case, spectral emissivity effects appear to dominate the nadir-forward comparisons, and largely contribute to the estimated 3–4 K RMS error between *in situ* and satellite-based estimates of LST. These results suggest the

235

need for further investigation of the effects of scale on surface emissivity and LST estimates. There is scope for such investigation in the future utilizing TIR data from satellite-based sensors with smaller FOV than that which the ATSR-2 uses in this work, including the ASTER and Multispectral Thermal Imager (MTI) instruments with spatial resolutions of the order of 90 m (Gillespie *et al.*, 1999) and 20–40 m (Clodius, 1999), respectively.

- iii) Investigation of surface properties at the small scale was limited in this research. The SBT and dBT distributions obtained from the scanning radiometer clearly showed the existence of directional effects during the day. In this work, these directional effects were incorporated into the empirical description of the BEDF (see Section 5.3.3) rather than undertaking an investigation of the relationship between vegetation size and distribution, for example, to the observed directionality. Such field study in this work was restricted by the remote location of the site and time and budget constraints. In the future, however, it may be beneficial to investigate the observed directional interaction at the surface in relation to such surface structure. Such a field study may provide insight into the physical factors which give rise to the observed directionality on the small scale and either lead towards development of a model for predicting SBT/surface emissivity anisotropy given knowledge of the surface structure and solar-satellite viewing geometry, or validate the numerous models which have already been developed for such purposes (see Section 2.2.2.3). Such an analytically derived model may find wider application than the empirically defined BEDF derived in this work for the Amburla field site.

- iv) The construction of the scanning radiometer used in this work was such that it scanned in a south-north direction only. For this reason, azimuthal variation of SBT was not addressed. It is highly likely, however, that azimuthal variation in viewing geometry is also important in interpreting remotely sensed SBT measurements, and, as such, azimuthal impacts should be included in research of this nature in the future.

236

• v) The algorithms derived in this work for the satellite-based retrieval of LST separated viewing geometry into the broad classes of nadir and forward views only. Within the nadir category, zenith angles may range between 0 and 20°, and, as such, significant variation in ΔT_{AC} may be expected within LST estimates for nadir viewing. In the future, derivation of retrieval algorithms customized for the viewing geometry of individual satellite overpasses should be a goal. Although the methodology for the development of such an algorithm may be complex, it would be likely to further improve the accuracy with which LST may be estimated globally via satellite-based sensors.

In conclusion, the investigation into the radiative interaction between the surface and atmosphere, based upon angular measurement of SBT at both the scales of measurement of the *in situ* radiometer and the satellite sensor has led to some interesting results from which conclusions beneficial for the remote sensing of LST may be drawn. In Section 4.2.1, it was shown that there exist seasonal cycles in the difference between the SBT measured by the nadir and forward viewing geometries of the ATSR-2 (dBT data) for the daytime case at the Amburla and Thangoo field sites, as well as for the nighttime case at the Thangoo site. The subsequent analysis of *in situ* measurements inspired by these findings showed that there were indeed cycles, both diurnal and seasonal in the angular distribution of SBT/dBT at the Amburla field site, and that these cycles were related to the seasonal variation in dBT shown by satellite measurements during the day. At night, the *in situ* measurements confirmed that there was no seasonal cycle in the dBT at the Amburla field site, in agreement with the satellite observations.

During the analysis of the data acquired by the scanning radiometer which led to these findings;

• i) the change in the value of the surface emissivity with increasing zenith angle in combination with the DWSR was shown to account for the dBT distributions observed by the scanning radiometer.

• ii) a method of estimating the LST based on knowledge of the dBT distri-

237

bution was developed from modelling work which allowed the definition of LST to within ±1 K at night and within ±1–2 K during the day in most cases.

- iii) a set of LST retrieval algorithms based on the physical processes which cause the observed angular distribution of SBT were derived. The definition of the *in situ* LST to within 1–2 K in most cases is a particularly encouraging result for the validation of remotely sensed LST, while the method for the derivation of the algorithms allows for improvements in the accuracy of the LST retrievals towards 1–2 K in the future as more representative and well-known atmospheric and surface emissivity data are incorporated into the derivation of the retrieval algorithms.

The results from this research, as summarized by the three points above, show that this thesis has been successful in achieving its objectives. Through the investigation of surface-atmosphere interaction using angular measurements, new insights into the radiative interaction between the land surface and the atmosphere have been gained, and it has been demonstrated how these findings may be applied to improve retrieval schemes for the remote sensing of LST as well as the validation of results from such algorithms. Although there is still considerable work to do in the field of remote sensing of LST in the future, the research undertaken for this thesis has made a significant and original contribution to the field, and may be described as being both worthwhile and satisfying.

References

Anding, D. and Kauth, R. (1970). Estimation of sea-surface temperature from space. *Remote Sens. Environ.*, 1(4), 217–220.

ATSR Homepage (2002). The ATSR Project. http://www.atsr.rl.ac.uk/index.shtml. Accessed 28-06-02.

BAE Systems (2002). Atmospheric Infrared Sounder. http://www.iews.na.baesystems.com/iris/airs.htm. Accessed 18-03-02.

Bailey, P. (1995). SADIST-2 v100 products. Report ER-TN-RAL-AT-2164, Space Science Dept., Rutherford Appleton Laboratory, Oxfordshire, U.K.

Balick, L. and Hutchinson, B. (1986). Directional thermal infrared exitance distributions from a leafless deciduous forest. *IEEE. Trans. Geosci. Remote Sens.*, **GE-24**, 693–698.

Barton, I. and Minnett, P. (2001). The second international infrared radiometer calibration and inter-comparison. Report from WGCV to the 15th CEOS Plenary.

Barton, I. J. (1995). Satellite-derived sea surface temperatures: Current status. *J. Geophys. Res.*, **100**(C5), 8777–8790.

Barton, I. J. and Takashima, T. (1987). An AVHRR investigation of surface emissivity near Lake Eyre, Australia. *Remote Sens. Environ.*, **20**, 153–163.

Becker, F. (1987). The impact of spectral emissivity on the measurement of land surface temperature from a satellite. *Int. J. Rem. Sens.*, **8**(10), 1509–1522.

239

Becker, F. and Li, Z. (1990). Towards a local split window method over land surfaces. *Int. J. Rem. Sens.*, **11**(3), 369–393.

Becker, F. and Li, Z. (1995). Surface temperature and emissivity at various scales: definition, measurement and related problems. *Remote Sens. Reviews*, **12**, 225–253.

Berk, A., Bemstein, L. S., and Roberts, D. C. (1989). MODTRAN: a moderate resolution model for Lowtran-7. TReport GL-TR-89-0122, Spectral Sciences Inc., Burlington, Massachusetts, U.S.A.

Bower, N. (2001). *Measurement of land surface emissivity and temperature in the thermal infrared using a ground-based interferometer.* Ph.D. thesis, School of Physical Sciences, Curtin University of Technology, GPO Box U1987, Perth Western Australia 6845.

Bureau of Meteorology (2001). Climate averages. www.bom.gov.au/climate/averages/tables/cw_015590.shtml.

Bureau of Meteorology, Northern Territory (2001). Daily rainfall maps. FTP://ftp.bom.gov.au/anon/home/ncc/www/rainfall/totals/daily/colour/history/nt.

Caselles, V., Sobrino, J. A., and Becker, F. (1988). Determination of the effective emissivity and temperature under vertical observation of a citrus orchard. application to frost nowcasting. *Int. J. Rem. Sens.*, **9**(4), 715–727.

Caselles, V., Sobrino, J. A., and Coll, C. (1992). A physical model for interpreting the land surface temperature obtained by remote sensors over incomplete canopies. *Remote Sens. Environ.*, **39**, 203–211.

Cechet, R. P. (2001). Vaisala rs80 technical specifications (private communication).

240

Chedin, A., Scott, M. A., Wahiche, C., and Moulinier, P. (1985). The improved initialization inversion method: a high resolution physical method for temperature retrievals from the TIROS-N series. *Journal of Climate and Applied Meteorology*, **24**, 124–143.

Clodius, W. B. (1999). The MTI data reference guide for level 1 imagery. Technical Report Draft, Los Alamos National Laboratory, Los Alamos, NM.

Clough, S. A., Brown, P. D., Liljegren, J. C., Shippert, T. R., Turner, D., Miller, N. E., Knuteson, R. O., Revercomb, H. E., and Smith, W. L. (1996). Implications for atmospheric state specification from the AERI/LBLRTM QME and the MWR/LBLRTM QME. In *Proc. International Radiation Symposium*, pages 396–399.

Coll, C. and Caselles, V. (1994). Analysis of the atmospheric and emissivity influence on the split-window equation for sea surface temperature. *Int. J. Rem. Sens.*, **15**(9), 1915–1932.

Coll, C. and Caselles, V. (1997). A spli-window algorithm for land surface temperature from Advanced Very High Resolution Radiometer data: validation and algorithm coparison. *J. Geophys. Res.*, **102**, 16697–16713.

Coll, C., Caselles, V., Sobrino, J. A., and Valor, E. (1994). On the atmospheric dependence of the split window equation for land surface temperature. *Int. J. Rem. Sens.*, **15**(1), 105–122.

Colton, A. L. (1996). Effective thermal parameters for a heterogeneous land surface. *Remote Sens. Environ.*, **57**, 143–160.

Conel, J. E. (1969). Infrared emissivities of silicates:Experimental results and a cloudy atmopshere model of spectral emission from condensed particulate mediums. *J. Geophys. Res.*, **74**, 1614–1634.

Dozier, J. and Warren, S. G. (1982). Effect of viewing angle on the infrared brightness temperature of snow. *Water Resources Research*, **18**, 1424–1434.

Francois, C., Ottle, C., and Prevot, L. (1997). Analytical parameterization of canopy directional emissivity and directional radiance in the thermal infrared. application on the retrieval of soil and foliage temperatures using two directional measurements. *Int. J. Rem. Sens.*, **18**(12), 2587–2621.

Friedl, M. A. and Davis, F. W. (1994). Sources of variation in radiometric surface temperature over a tallgrass prairie. *Remote Sens. Environ.*, **48**, 1–17.

Gillespie, A., Rokugawa, S., Matsunaga, T., Cothern, J. S., Hook, S., and Kahle, A. B. (1998). A temperature and emissivity separation algorithm for Advanced Spaceborne Thermal Emission and Reflection Radiometer (ATSER images. *IEEE. Trans. Geosci. Remote Sens.*, **36**(4), 1113–1126.

Gillespie, A., Rokugawa, S., Matsunaga, T., Cothern, J. S., Hook, S., and Kahle, A. B. (1999). Temperature/emsiivity separation algorithm theoretical basis document. Technical Report Version 2.4, Jet Propulsion Laboratory, Pasadena, CA.

Hall, F. G., Huemmerich, K. F., Goetz, S. J., Sellers, P. J., and Nickerson, J. E. (1992). Satellite remote sensing of surface energy balance: success, failures, and unresolved issues in FIFE. *J. Geophys. Res.*, **97**(D17), 19061–19089.

Ishida, T., Ando, A., and Fukuhara, M. (1991). Estimation of the compex refractive index of soil and its dependence on soil chemical properties. *Remote Sens. Environ.*, **38**, 173–182.

Joseph, J. H., Wiscombe, W. J., and Weinman, J. A. (1976). The delta-eddington approximation for radiative flux transfer. *Journal of the Atmospheric Sciences*, **33**, 2452–2459.

Jupp, D. L. B. (1998). Directional radiance and emissivity measurement models

for remote sensing and surfac energy balance. *Environmnetal Modelling and Software*, **13**, 341–351.

Karnieli, T.-Z. Q. A. (1999). Progress in the remote sensing of land surface temperature and ground emissivity using NOAA-AVHRR data. *Int. J. Rem. Sens.*, **99**(C9), 2369–2393.

Kerr, Y. H., Lagouarde, J. P., and Imbernon, J. (1992). Accurate land surface temperature retrieval from AVHRR data with use of an improved split window algorithm. *Remote Sens. Environ.*, **41**, 197–209.

Kimes, D. S. (1983). Remote sensing of row crop structure and component temperatures using directional radiometric temperatures and inversion techniques. *Remote Sens. Environ.*, **13**, 33–55.

Kimes, D. S., Smith, J. A., and Link, L. E. (1981). Thermal IR exitance model of a plant canopy. *Appl. Opt.*, **20**(4), 623–632.

Kirkup, L. (1994). *Experimental Methods*. Jihn Wiley and Sons, 33 Park Road, Milton, Qld 4064.

Kneizys, F. X., Shettle, E. P., Gallery, W., Chetwynd, J. H., Abreu, L. W., Selby, J. E. A., Clough, S. A., and Fenn, R. W. (1983). Atmospheric transmittance/radiance: copmuter code Lowtran-6. Technical Report AFGL-TR-83-0187, Optical Physics Division, U.S. Airforce Geophysics Laboratory, Hanscom Airforce Base, Massachusetts, U.S.A.

Kneizys, F. X., Shettle, E. P., Abreu, L. W., Chetwynd, J. H., Anderson, G. P., Gallery, W., Selby, J. E. A., Clough, S. A., and Fenn, R. W. (1988). Users guide to Lowtran-7. Technical Report AFGL-TR-88-0177, Airforce Geophysics Laboratory, Bedford, Massachusetts, U.S.A.

Korb, A. R., Salisbury, J. W., and D'Aria, D. (1994). Thermal-infrared remote sensing and Kirchoff's law 2. Laboratory measurements. *J. Geophys. Res.*, **104**(B7), 15339–15350.

Kustas, W. P., Choudhury, B. J., Inoue, Y., Pinter, P. J., Jackson, R. D., and Reginato, R. J. (1990). Ground and aircraft infrared observations over a partially-vegetated area. *Int. J. Rem. Sens.*, **11**(3), 409–427.

Labed, J. and Stoll, M. P. (1991a). Angular variation of land surface spectral emissivity in the thermal infrared: laboratory investigations on bare soils. *Int. J. Rem. Sens.*, **12**(11), 2299–2310.

Labed, J. and Stoll, M. P. (1991b). Spatial variability of land surface emissivity in the thermal infrared band: spectral signature and effective surface temperature. *Remote Sens. Environ.*, **38**, 1–17.

Lagouarde, J. P., Kerr, Y. H., and Brunet, Y. (1995). An experimental study of angular effects on surface temperature for various plant canopies and bare soils. *Agricultural and Forest Meteorology*, **77**, 167–190.

Lagouarde, J. P., Ballans, H., Moreau, P., Guyon, D., and Coraboeuf, D. (2000). Experimental study brightness surface temperatureo angular variations of maritime pine (*pimus pinaster* stands. *Remote Sens. Environ.*, **72**, 17–34.

Li, X. and Strahler, A. H. (1992). Geometric-optical bidirectional reflectance modeling of the discrete crown vegetation canopy: effect of crown shape and mutual shadowing. *IEEE. Trans. Geosci. Remote Sens.*, **20**, 276–291.

Li, X., Strahler, A. H., and Friedl, M. A. (1999). A conceptual model for effective directional emissivity from nonisothermal surfaces. *IEEE. Trans. Geosci. Remote Sens.*, **37**(5), 2508–2517.

Li, Z. and Becker, F. (1993). Feasibility of land suface temperature and emissivity determination from AVHRR data. *Remote Sens. Environ.*, **43**, 67–85.

244

Li, Z. R. and McDonnell, M. J. (1988). Atmopsheric correction of thermal infrared images. *Int. J. Rem. Sens.*, **1**, 107–121.

Ma, X. L., Wan, Z., Moeller, C. C., Menzel, W. P., and Gumley, L. E. (2002). Simultaneous retrieval of atmospheric profiles, land-surface temperature, and surface emissivity from Moderate-Resolution Imaging Spectroradiometer thermal infrared data: extension of a two-step physical algorithm. *Appl. Opt.*, **41**(5), 909–924.

Maher, J. V. and Lee, D. M. (1977). *Upper Air Statistics Australia.Surface to 5 mb 1957 to 1975.* Australian Government Publishing Service, Canberra, Australia.

Masuda, K. T., Takashima, T., and Takayama, Y. (1988). Emissivity of pure and sea waters for the model seas surface in the infrared window regions. *Remote Sens. Environ.*, **24**, 313–329.

Maul, G. A. (1983). Zenith angle effects in multichannel infrared sea surface remote sensing. *Remote Sens. Environ.*, **13**, 439–451.

Maul, G. A. and Sidran, M. (1972). Comment on Anding and Kauth. *Remote Sens. Environ.*, **2**, 165–169.

McAtee, B. K., Prata, A. J., and Lynch, M. J. (2002). The angular behaviour of emitted thermal infrared radiation (8–12μm) at a semi-arid site. *Journal of Applied Meteorology. Submitted to Journal of Applied Meteorology.*

McMillin, L. M. (1975). Estimation of sea surface temperatures from two infrared window measurements with different absorption. *J. Geophys. Res.*, **80**(36), 5113–5117.

McMillin, L. M. and Crosby, D. S. (1984). Theory and validation of the multiple window sea surface temperature technique. *J. Geophys. Res.*, **89**(C3), 3655–3661.

245

Menzel, W. P. (2001). Applications with meteorological satellites. Technical Document WMO/TD No.1078, World Meteorological Organization.

Minnett, P. (1990). The regional optimization of sea surface temperature from space. *J. Geophys. Res.*, **95**(13), 13497–13510.

Minnis, P. and Khaiyer, M. M. (2000). Anisotropy of land surface skin temperature derived from satellite data. *Journal of Applied Meteorology*, **39**, 1117–1129.

Mutlow, C., Murray, J., Bailey, P., Birks, A., and Smith, D. (1999). ATSR-1/2 user guide. Technical Report Issue 1.0, Rutherford Appleton Laboratories, Oxford, United Kingdom.

Mutlow, C. T., Zavody, A., Barton, I. J., and LLewellyn-Jones, D. (1994). Sea-surface temperature-measurements by the along-track scanning radiometer on the ERS-1 satellite - early results. *J. Geophys. Res.*, **99**(C11), 22575–22588.

NASA (2002). TERRA: The EOS Flagship. http://terra.nasa.gov/. Accessed 26-02-02.

Nerry, F., Labed, J., and Stoll, M. P. (1990a). Spectral properties of land surfaces in the thermal infrared 1. laboratory measuremenst of absolute spectral emissivity signatures). *J. Geophys. Res.*, **95**(B5), 7027–7044.

Nerry, F., Labed, J., and Stoll, M. P. (1990b). Spectral properties of land surfaces in the thermal infrared 2. spectrally averaged emissivity measurements). *J. Geophys. Res.*, **95**(B5), 7045–7054.

Ninomiya, Y., Matsunaga, T., Yamaguchi, Y., Ogawa, K., Rokugawa, S., Uchida, K., Muraoka, H., and Kaku, M. (1997). A comparison of thermal infrared emissivity spectra measured insitu, in the laboratory, and derived from thermal infrared multispectral scanner (TIMS) data in Cuprite, Nevada, U.S.A. *Int. J. Rem. Sens.*, **18**(7), 1571–1581.

Norman, J. M. and Becker, F. (1995). Terminology in the thermal infrared remote sensing of natural surfaces. *Remote Sens. Reviews*, **12**, 159–173.

Northcote, K. H. and Wright, M. J. (1983). *Soils: an Australian viewpoint*, chapter 13, pages 173–178. CSIRO (Melbourne).

Otterman, J. (1981). Plane with protrusions as an atmospheric boundary. *J. Geophys. Res.*, **86**(B7), 6627–6630.

Otterman, J., Brakke, T. W., and Susskind, J. (1992). A model for inferring canopy and underlying soil temperatures from multi-directional measurements. *Boundary-Layer Meteorology*, **61**, 81–97.

Otterman, J., Brakke, T. W., and Smith, J. (1995a). Effects of leaf-transmittance versus leaf reflectance on bidirectional scattering from canopy/soil surface: an analytical study. *Remote Sens. Environ.*, **54**, 49–60.

Otterman, J., Susskind, J., Brakke, T. W., Kimes, D., Pielke, R., and Lee, T. J. (1995b). Inferring the thermal hemispheric emission from a sparsely-vegetated surface by directional measurements. *Boundary-Layer Meteorology*, **74**, 163–180.

Otterman, J., Brakke, T. W., Fuchs, M., Lakshmi, V., and Cadeddu, M. (1999). Longwave emission from a plant/soil surface as a function of the view direction: dependence on the canopy architecture. *Int. J. Rem. Sens.*, **20**(11), 2195–2201.

Ottle, C. and Stolle, M. (1993). Effect of atmospheric absorption and surface emissivity on the determination of land surface temperature from infrared satellite data. *Int. J. Rem. Sens.*, **14**(10), 2025–2037.

Ottle, C. and Vidal-Madjar, D. (1992). Estimation of land surface temperature with NOAA9 data. *Remote Sens. Environ.*, **40**, 27–41.

247

Prabhakara, C., Dalu, G., and Kunde, Y. G. (1974). Estimation of sea surface temperature from remote sensing in 11 to 13μm window region. *J. Geophys. Res.*, **79**(33), 5039–5044.

Prata, A. J. (1993). Land surface temperatures derived from the advanced very high resolution radiometer and the along-track scanning radiometer 1.Theory. *J. Geophys. Res.*, **98**(D9), 16689–16702.

Prata, A. J. (1994). Land surface temperatures derived from the advanced very high resolution radiometer and the along-track scanning radiometer 2.Experimental results and validation of AVHRR algorithms. *J. Geophys. Res.*, **99**(D9), 13025–13058.

Prata, A. J. (2002). Emissivity spectra measured using a μ-ftir at the Amburla field site. private communication.

Prata, A. J. and Cechet, R. P. (1999). An assessment of the accuracy of land surface temperature determination from the GMS-5 VISSR. *Remote Sens. Environ.*, **67**, 1–14.

Prata, A. J., Cechet, R. P., Barton, I. J., and Llewellyn-Jones, D. T. (1990). The along track scanning radiometer for ERS-1 - scan geometry and data simulation. *IEEE. Trans. Geosci. Remote Sens.*, **28**(1), 3–13.

Prata, A. J., Caselles, V., Coll, C., Sobrino, J., and Ottl, C. (1995). Thermal remote sesning of land surface temperature from satellites: current status and future prospects. *Remote Sensing Reviews*, **12**, 175–224.

Prata, A. J., Cechet, R. P., Grant, I. F., and Barton, I. J. (1997). Investigation of land surface radiation budgets using ATSR/ATSR-2 data. *Proc. 3rd ERS Symp. on Space at the Service of our Environ.*, **3**(ESA SP-414), 1795–1807.

Prata, A. J., Rutter, G. R., and Lynch, M. J. (1998). Thangoo field site survey, 18–29 July, 1998. Site survey, CSIRO Atmospheric Research, Aspendale, Victoria, Australia.

Prata, A. J., Bennett, J., Petraitis, B., Rutter, G., and McAtee, B. (2003). A self-calibrating zenith scanning infrared radiometer for satellite validation studies. *Appl. Opt. Submitted to Applied Optics*.

Price, J. C. (1983). Estimating surface temperatures from satellite thermal infrared data- a simple formulation for the atmospheric effect. *Remote Sens. Environ.*, **13**, 353–361.

Price, J. C. (1984). land surface temperature measurements from the split window channels of the advanced very high resolution radiometer. *J. Geophys. Res.*, **85**(D5), 7231–7237.

Rees, W. G. and James, S. P. (1992). Angular variation of the infrared emissivity of ice and water surfaces. *Int. J. Rem. Sens.*, **13**(15), 2873–2886.

Roujean, J.-L., Leroy, M., and Deschamps, P.-Y. (1992). A bidirectional reflectance model of the Earth's surface for the correction of remote sensing data. *J. Geophys. Res.*, **97**(D18), 20455–20468.

Rubio, E., Caselles, V., and Badenas, C. (1997). Emissivity measurements of several soils and vegetation types in the 8–14μm wave band: Analysis of two field methods. *Remote Sens. Environ.*, **59**, 490–521.

Running, S. W., Justice, C. O., Salomonson, V., Hall, D., Barker, J., Kaufmann, Y. J., Strahler, A. H., Heute, A. R., Muller, J. P., Vanderbilt, V., Wan, Z. M., Teillet, P., and Carneggie, D. (1994). Terrestrial remote sensing science and algorithms planned for EOS/MODIS. *Int. J. Rem. Sens.*, **15**(17), 3587–3620.

Rustana, C. E., Lynch, M. J., and Prata, A. J. (1994a). Development and validation of algorithms for land surface temperature measurement from NOAA-

11/AVHRR satellite data. In *Technical Proceedings of the Second Pacific Ocean Remote Sensing Conference*, pages 161–168.

Rustana, C. E., Lynch, M. J., Foster, I., and Prata, A. J. (1994b). The performance of satellite estimates of LST in the WA agricultural region. In *Technical Proceedings of the Second Pacific Ocean Remote Sensing Conference*, pages 153–160.

Salisbury, J. W. and D'Aria, D. M. (1992). Emissivity of terestrial materials in the 8–14μ m atmospheric window. *Remote Sens. Environ.*, **42**, 83–106.

Salisbury, J. W. and Walter, L. S. (1989). Thermal infrared (2.5–3.5μm) spectroscopic remote sensing of igneous rock tpyes on particulate planetary surfaces. *J. Geophys. Res.*, **94**(B7), 9192–9202.

Salisbury, J. W., Wald, A., and D'Aria, D. (1994). Thermal-infrared remote sensing and Kirchoff's law 1. Laboratory measurements. *J. Geophys. Res.*, **99**(B6), 11897–11911.

Schmugge, T. J., Becker, F., and Li, Z.-L. (1991). Spectral emissivity variations observed in airborne surface temperature measurements. *Int. J. Rem. Sens.*, **35**, 95–105.

Sidran, M. (1980). Infrared sensing of sea surface temperature from space. *Remote Sens. Environ.*, **10**, 101–114.

Smith, J. A., Ballard, M. R., and Pedelty, J. A. (1997). Effect of three-dimensional canopy architecture on thermal infrared exitance. *Optical Engineereing*, **36**(11), 3093–3111.

Smith, W. L., Knuteson, R. O., Revercomb, H. E., Feltz, W., Howell, H. B., Menzel, W. P., Nalli, N. R., Brown, O., Brown, J., Minnett, P., and McKeown, W. (1996). Observations of the infrared radiative properties of the ocean- implications for the measurement of sea surface temperature via satellite remote sensing. *Bull. Amer. Meteor. Soc.*, **77**(1), 41–51.

Snyder, W. C. and Wan, Z. (1998). BRDF models to predict spectral reflectance and emissivity in the thermal infrared. *IEEE. Trans. Geosci. Remote Sens.*, **36**(1), 214–225.

Snyder, W. C., Wan, Z., Zhang, Y., and Feng, Y. Z. (1998a). Classification-based emissivity for land surface temperature measurement from space. *Int. J. Rem. Sens.*, **19**(14), 2753–2774.

Snyder, W. C., Wan, Z., and Li, X. (1998b). Thermodynamic constraints on reflectance reciprocity and kirchhoff's law. *Appl. Opt.*, **37**(16), 3464–3470.

Sobrino, J. and Cuenca, J. (1999). Angular varaition of thermal infrared emissivity for some natural surfaces from experimental measurements. *Appl. Opt.*, **38**(18), 3931–3936.

Sobrino, J., Coll, C., and Caselles, V. (1991). Atmospheric correction for land surface temperature using NOAA-11 AVHRR channels 4 and 5. *Remote Sens. Environ.*, **38**, 19–34.

Sobrino, J. A. and Caselles, V. (1990). Thermal infrared radiance model for interpreting the directional radiometric temperature of a vegetative surface. *Remote Sens. Environ.*, **33**, 193–199.

Sobrino, J. A. and Caselles, V. (1993). A field method for measuring the thermal infrared emissivity. *ISPRS Journal of Photogrammetry and Remote Sensing*, **48**(3), 24–31.

Sobrino, J. A., Caselles, V., and Becker, F. (1990). Siginificance of the remotely sensed thermal infrared measurement obtained over a citrus orchard. *ISPRS Journal of Photogrammetry and Remote Sensing*, **44**, 343–354.

Sobrino, J. A., Li, Z.-L., Stoll, M. P., and Becker, F. (1996). Multi-channel and multi-angle algorithms for estimating sea and land surface temperature with atsr data. *Int. J. Rem. Sens.*, **17**(11), 2089–2114.

251

Susskind, J., Rosenfield, J., Reuter, D., and Chahine, M. T. (1984). Remote sensing of weather and climate parameters from HIRS2/MSU on TIROS-N. *J. Geophys. Res.*, **89**(D3), 4677–4697.

Takashima, T. and Masuda, K. (1987). Emissivity of quartz and Sahara dust powders in the infrared region (7–17 μm). *Remote Sens. Environ.*, **23**, 51–63.

Teggi, S., Bogliolo, M. P., Buongiorno, M. F., and Pugnaghi, S. (1998). Influence of non-representative atmospheric profiles on estimates of land surface temperature by MIVIS data ubing radiative transfer models. *Journal of Atmospheric and Solar-Terrestrial Physics*, **60**, 1059–1070.

Zavody, A. M., Mutlow, C. T., and Llewellyn-Jones, D. T. (1995). A radiative transfer model for sea surface temperature retrieval for the along-track scanning radiometer. *J. Geophys. Res.*, **100**(C1), 937–952.

USNO (2001). U.S. Naval Observatory sun and moon altitude\ azimuth table. http://aa.usno.navy.mil / data / docs / AltAz.html.

van Burgel, L. (1999). Bureau of Meteorology radiosonde-derived mixing ratio algorithm (private communication).

Vidal, A. (1991). Atmospheric and emissivity correction of land surface temperature measured from satellite using ground measurements or satellite data. *Int. J. Rem. Sens.*, **12**(12), 2449–2460.

Walton, C. C., Pichel, W. G., Sapper, J. F., and May, D. A. (1998). The development and operational application of nonlinear algorithms for the measurement of sea surface temperatures with the NOAA polar-orbiting environmental satellites. *J. Geophys. Res.*, **103**(C12), 27999–28012.

Wan, Z. (1999). MODIS land-surface temperature algorithm theoretical basis document (LST ATBD). Technical Report Version 3.3, Institute for Computational Earth System Science, University of California, Santa Barbara.

Wan, Z. and Dozier, J. (1989). Land-surface temperature measurement from space:physical principles and inverse modeling. *IEEE. Trans. Geosci. Remote Sens.*, **27**(3), 268–278.

Wan, Z. and Dozier, J. (1996). A generalized split-window algorithm for retrieving land-surface temperature from space. *IEEE. Trans. Geosci. Remote Sens.*, **34**, 892–905.

Wan, Z. and Li, Z. (1997). A physics-based algorithm for retrieving land-surface emissivity and temperature from EOS/MODIS data. *IEEE. Trans. Geosci. Remote Sens.*, **35**, 980–996.

Warren, S. G. and Wiscombe, W. J. (1980). A model for the spectral albedo of snow. ii: snow containing atmospheric aerosols. *Journal of the Atmospheric Sciences*, **37**, 2734–2744.

WCRP (1984). Report on the TOGA workshop on sea surface temperature and net radiation. World Climate Programme Report WCP-92, World Climate Research Programme, World Metorological Organization, Geneva, Switzerland.

Wiscombe, W. J. and Warren, S. G. (1980). A model for the spectral albedo of snow. i: pure snow. *Journal of the Atmospheric Sciences*, **37**, 2712–2733.

Wu, X. and Smith, W. L. (1997). Emissivity of rough sea surface for 8–13μm: modeling and verification. *Appl. Opt.*, **36**(21), 2609–2619.

Appendix A

Acronym	Definition
AATSR	Advanced Along Track Scanning Radiometer
AIRS	Atmospheric Infrared Sounder
AMI	Active Microwave Instrument
AMSU	Advanced Microwave Sounding Unit
ASTER	Advanced Spaceborne Thermal Emission and Reflection Radiometer
AT	Air Temperature
ATSR	Along Track Scanning Radiometer
AVHRR	Advanced Very High Resolution Radiometer
BEDF	Bidirectional Emission Distribution Function
BRDF	Bidirectional Reflectance Distribution Function
BT	Brightness Temperature
CAL/VAL	Calibration and Validation
CAR	CSIRO Atmospheric Research
CBB	Cold Blackbody
CIGSN	Continental Integrated Ground-truth Site Network
CSIRO	Commonwealth Scientific and Industrial Research Organization
DA	Dual-Angle
dBT	Difference in Brightness Temperature measured by a sensor between two different zenith angles
DHR	Directional-Hemispherical Reflectance
DRST	Directional Radiometric Surface Temperature
DWSR	Downwelling Sky Radiance
EDRST	Ensemble Directional Radiometric Surface Temperature
ESA	European Space Agency
FOV	Field-Of-View
FTIR	Fourier Transform Interferometer

Acronym	Definition
GCM	Global Climate Model
GMS	Geostationary Meteorological Satellite
GOES	Geostationary Operational Environmental Satellite
GT	Ground Temperature
HBB	Hot Blackbody
HDR	Hemispherical-Directional Reflectance
HIRS	High Resolution Infrared Sounder
IGBP	International Geosphere-Biosphere Program
LBLRTM	Line-By-Line Radiative Transfer Model
LST	Land Surface Temperature
LUT	Look-Up Table
MODIS	Moderate Resolution Imaging Spectroradiometer
MTI	Multispectral Thermal Imager
NASA	National Aeronautics and Space Administration
NOAA	National Oceanic and Atmospheric Administration
NIST	National Institute of Standards and Technology
PTRH	Pressure, Temperature and Relative Humidity
PW	Precipitable Water
RC	Radiative Component
RTE	Radiative Transfer Equation
RMS	Root Mean Square
SBT	Surface Brightness Temperature
SC	Single Channel
SST	Sea Surface Temperature
SW	Split-Window
SZA	Solar Zenith Angle
TES	Temperature/Emisivity Separation

Acronym	Definition
TIR	Thermal Infrared
TOVS	TIROS-N Vertical Sounder
UWSR	Upwelling Sky Radiance
VISSR	Visible and Infrared Spin Scan Radiometer

Appendix B

Nighttime Estimates (2230hrs Central Australian Time)

01 July — LST (K) — Observation Zenith Angle (°) — LST = 284.32 +/- 3.14 K

02 July — LST (K) — Observation Zenith Angle (°) — LST = 279.42 +/- 3.87 K

03 July — LST (K) — Observation Zenith Angle (°) — LST = 278.33 +/- 0.83 K

04 July — LST (K) — Observation Zenith Angle (°) — LST = 279.04 +/- 0.70 K

06 July — LST (K) — Observation Zenith Angle (°) — LST = 283.27 +/- 1.94 K

07 July — LST (K) — Observation Zenith Angle (°) — LST = 285.82 +/- 0.68 K

08 July — LST (K) — Observation Zenith Angle (°) — LST = 279.95 +/- 0.95 K

09 July — LST (K) — Observation Zenith Angle (°) — LST = 283.51 +/- 3.71 K

10 July — LST (K) — Observation Zenith Angle (°) — LST = 279.82 +/- 1.79 K

11 July — LST (K) — Observation Zenith Angle (°) — LST = 289.56 +/- 2.21 K

12 July — LST (K) — Observation Zenith Angle (°) — LST = 287.72 +/- 1.19 K

13 July — LST (K) — Observation Zenith Angle (°) — LST = 286.68 +/- 2.47 K

14 July — LST (K) — Observation Zenith Angle (°) — LST = 285.97 +/- 1.84 K

15 July — LST (K) — Observation Zenith Angle (°) — LST = 288.54 +/- 0.68 K

16 July — LST (K) — Observation Zenith Angle (°) — LST = 286.90 +/- 0.70 K

17 July — LST (K) — Observation Zenith Angle (°) — LST = 285.50 +/- 2.24 K

18 July — LST (K) — Observation Zenith Angle (°) — LST = 285.98 +/- 1.19 K

19 July — LST (K) — Observation Zenith Angle (°) — LST = 286.15 +/- 1.00 K

20 July — LST (K) — Observation Zenith Angle (°) — LST = 289.22 +/- 0.57 K

21 July — LST (K) — Observation Zenith Angle (°) — LST = 288.02 +/- 1.98 K

22 July — LST (K) — Observation Zenith Angle (°) — LST = 286.75 +/- 1.05 K

23 July — LST (K) — Observation Zenith Angle (°) — LST = 284.94 +/- 1.07 K

24 July — LST (K) — Observation Zenith Angle (°) — LST = 285.16 +/- 0.98 K

26 July — LST (K) — Observation Zenith Angle (°) — LST = 275.55 +/- 0.83 K

261

20 August

LST = 280.93 +/- 0.97 K

LST (K)

Observation Zenith Angle (°)

21 August

LST = 283.19 +/- 0.81 K

22 August

LST = 286.33 +/- 1.37 K

23 August

LST = 280.08 +/- 0.73 K

24 August

LST = 276.57 +/- 1.09 K

25 August

LST = 283.43 +/- 1.28 K

26 August

LST = 282.38 +/- 0.82 K

27 August

LST = 289.77 +/- 0.60 K

28 August

LST = 286.07 +/- 0.90 K

29 August

LST = 296.97 +/- 1.15 K

30 August

LST = 291.97 +/- 2.19 K

31 August

LST = 292.41 +/- 0.85 K

01 September

LST = 289.21 +/- 1.11 K

02 September

LST = 281.45 +/- 1.33 K

03 September

LST = 282.48 +/- 1.03 K

04 September

LST = 292.62 +/- 1.96 K

05 September

LST = 294.09 +/- 0.61 K

06 September

LST = 300.85 +/- 0.93 K

07 September

LST = 284.98 +/- 0.83 K

08 September

LST = 287.47 +/- 0.74 K

09 September

LST = 289.70 +/- 0.98 K

10 September

LST = 284.30 +/- 1.00 K

11 September

LST = 286.52 +/- 0.62 K

12 September

LST = 284.18 +/- 0.94 K

01 November — LST = 294.41 +/- 1.17 K
02 November — LST = 299.31 +/- 1.07 K
03 November — LST = 300.18 +/- 1.38 K
04 November — LST = 295.65 +/- 2.05 K
05 November — LST = 294.77 +/- 2.53 K
06 November — LST = 299.11 +/- 1.98 K
07 November — LST = 298.90 +/- 0.88 K
08 November — LST = 299.64 +/- 0.85 K
09 November — LST = 299.57 +/- 1.02 K
10 November — LST = 301.89 +/- 1.24 K
11 November — LST = 299.17 +/- 0.84 K
12 November — LST = 299.39 +/- 2.09 K
13 November — LST = 298.36 +/- 1.45 K
14 November — LST = 297.46 +/- 1.92 K
15 November — LST = 294.93 +/- 2.70 K
16 November — LST = 297.71 +/- 2.18 K
17 November — LST = 297.52 +/- 1.35 K
18 November — LST = 299.08 +/- 1.42 K
19 November — LST = 299.01 +/- 1.99 K
20 November — LST = 301.27 +/- 0.58 K
21 November — LST = 299.99 +/- 2.02 K
22 November — LST = 298.52 +/- 3.33 K
23 November — LST = 297.04 +/- 2.21 K
24 November — LST = 297.44 +/- 0.80 K

21 December

LST (K)

LST = 305.20 +/- 1.98 K

-70 -50 -30 -10 10 30 50 70
Observation Zenith Angle (°)

22 December

LST (K)

LST = 300.48 +/- 2.34 K

-70 -50 -30 -10 10 30 50 70
Observation Zenith Angle (°)

23 December

LST (K)

LST = 300.81 +/- 1.42 K

-70 -50 -30 -10 10 30 50 70
Observation Zenith Angle (°)

24 December

LST (K)

LST = 297.91 +/- 1.11 K

-70 -50 -30 -10 10 30 50 70
Observation Zenith Angle (°)

25 December

LST (K)

LST = 299.36 +/- 1.16 K

-70 -50 -30 -10 10 30 50 70
Observation Zenith Angle (°)

26 December

LST (K)

LST = 300.29 +/- 0.41 K

-70 -50 -30 -10 10 30 50 70
Observation Zenith Angle (°)

27 December

LST (K)

LST = 299.36 +/- 1.01 K

-70 -50 -30 -10 10 30 50 70
Observation Zenith Angle (°)

28 December

LST (K)

LST = 296.51 +/- 1.15 K

-70 -50 -30 -10 10 30 50 70
Observation Zenith Angle (°)

29 December

LST (K)

LST = 295.42 +/- 0.99 K

-70 -50 -30 -10 10 30 50 70
Observation Zenith Angle (°)

30 December

LST (K)

LST = 300.37 +/- 0.97 K

-70 -50 -30 -10 10 30 50 70
Observation Zenith Angle (°)

31 December

LST (K)

LST = 302.69 +/- 1.05 K

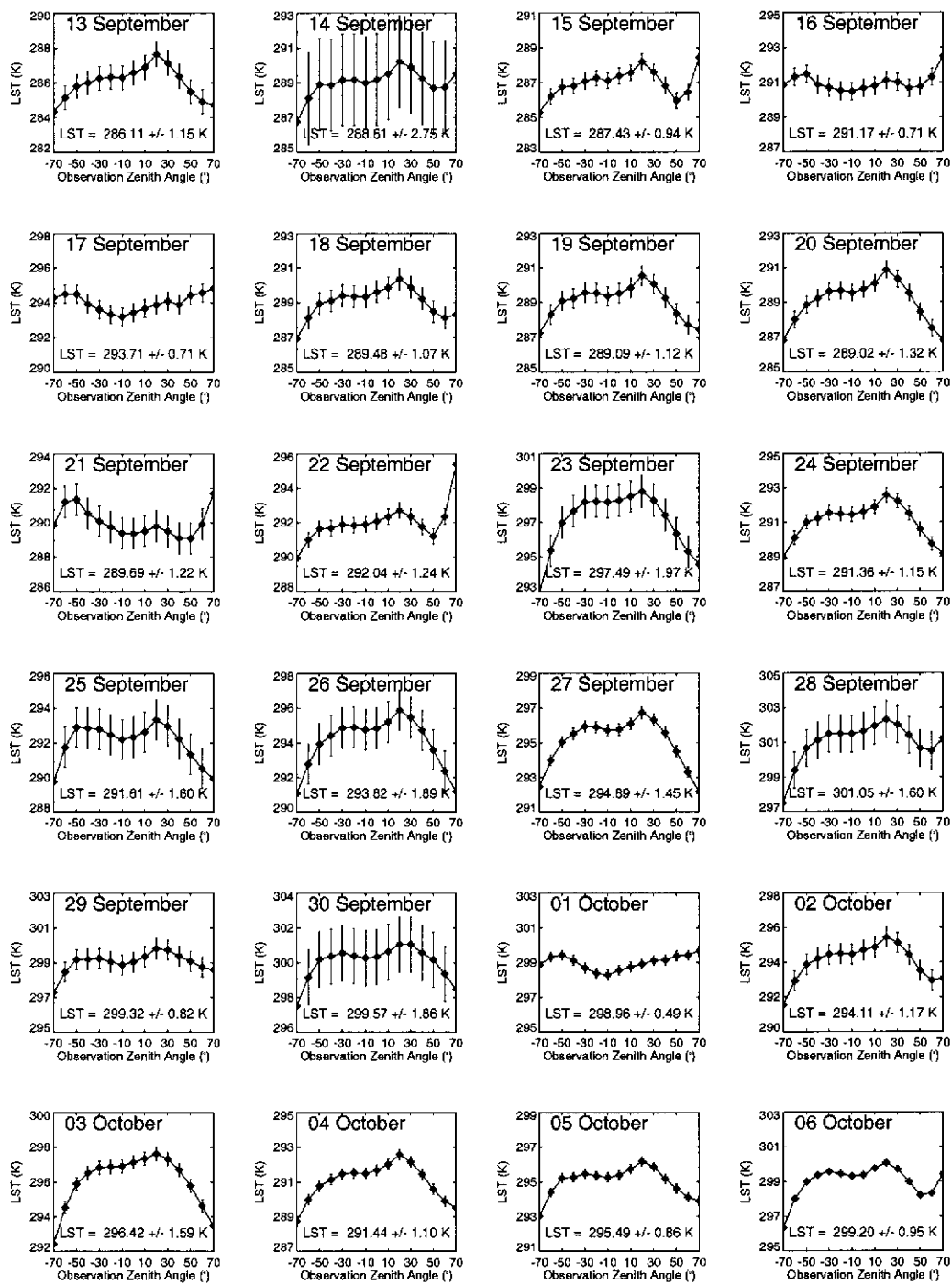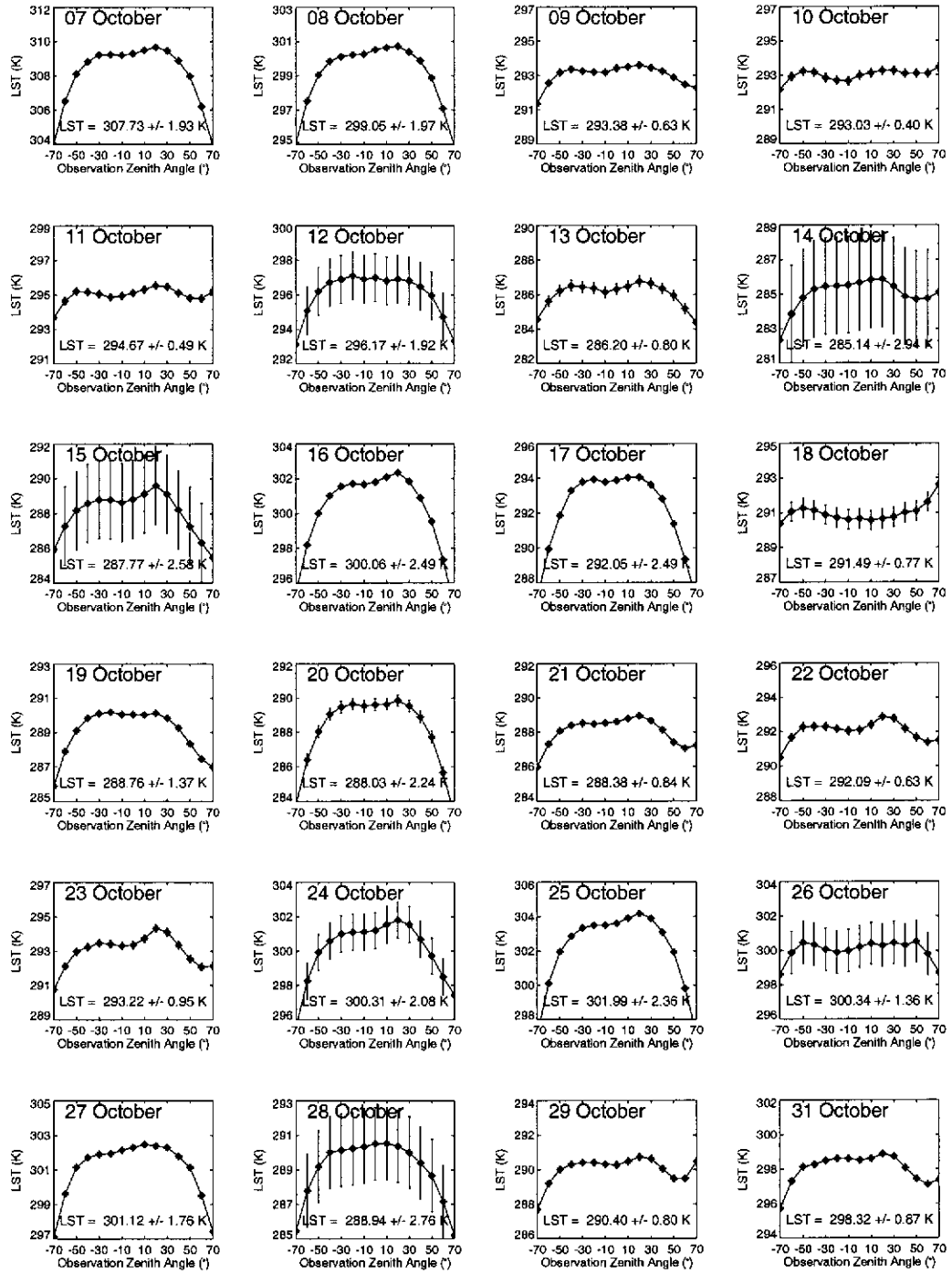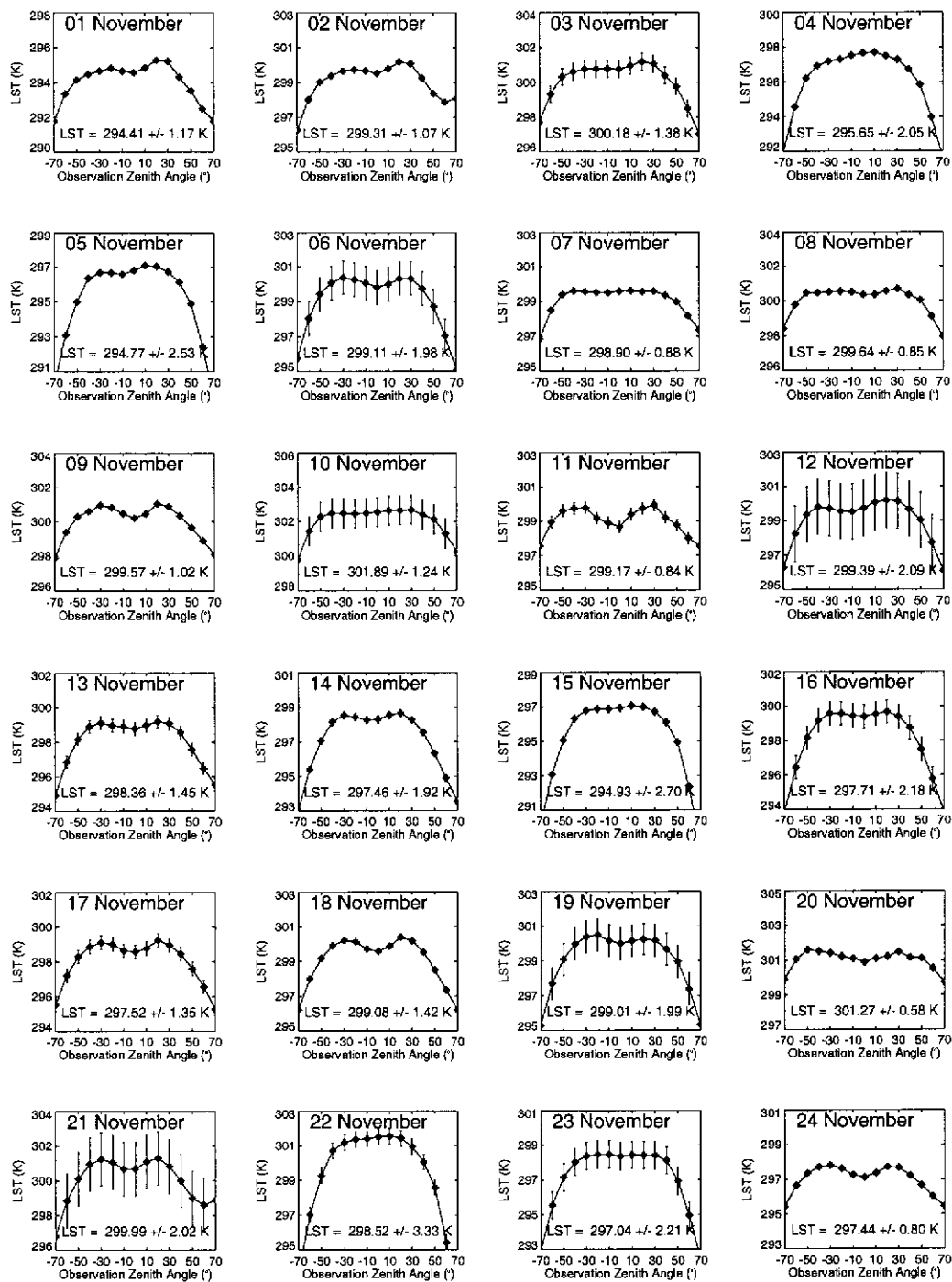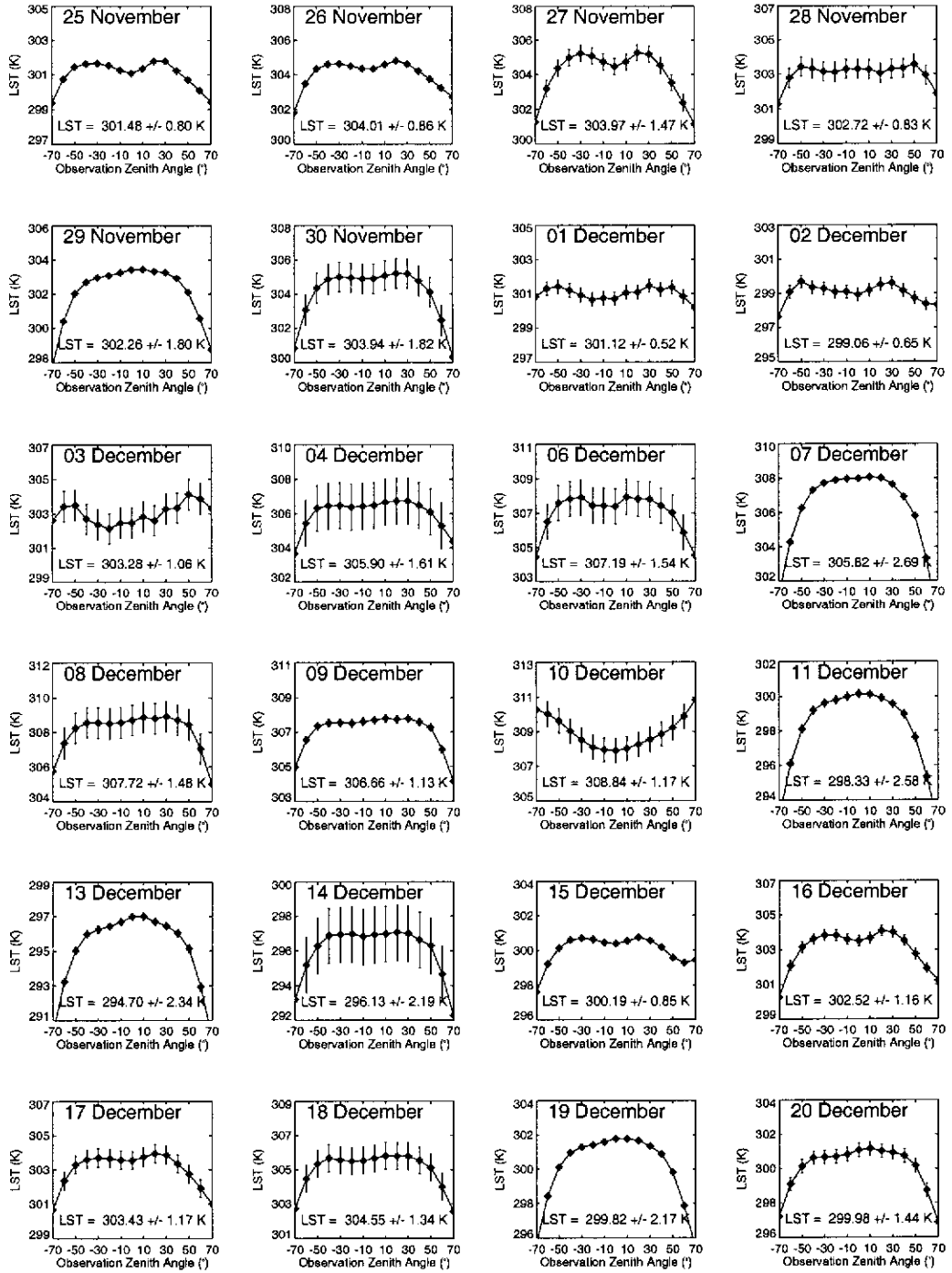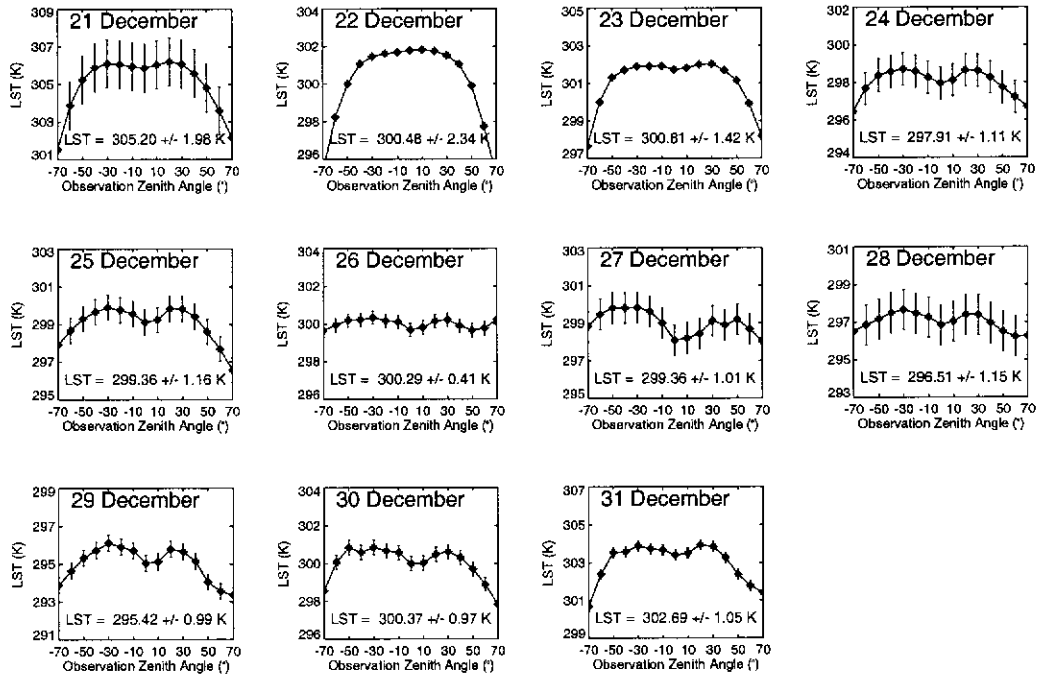-70 -50 -30 -10 10 30 50 70
Observation Zenith Angle (°)

268

Dayttime Estimates (1030hrs Central Australian Time)